ICE ACCRETION SIMULATION AND SCALING ANALYSIS FOR
CONCEPTUAL DESIGN OF AN ICING WIND TUNNEL

A THESIS SUBMITTED TO
THE GRADUATE SCHOOL OF NATURAL AND APPLIED SCIENCES
OF
MIDDLE EAST TECHNICAL UNIVERSITY

BY

MEHMET HARUN ÖZKANAKTI

IN PARTIAL FULFILLMENT OF THE REQUIREMENTS
FOR
THE DEGREE OF DOCTOR OF PHILOSOPHY
IN
AEROSPACE ENGINEERING

AUGUST 2023

Approval of the thesis:

ICE ACCRETION SIMULATION AND SCALING ANALYSIS FOR CONCEPTUAL DESIGN OF AN ICING WIND TUNNEL

submitted by **Mehmet Harun Özkanaktı** in partial fulfillment of the requirements for the degree of **Doctor of Philosophy** i**n Aerospace Engineering, Middle East Technical University** by,

Prof. Dr. Halil Kalıpçılar
Dean, Graduate School of **Natural and Applied Sciences**   _____

Prof. Dr. Serkan Özgen
Head of the Department, **Aerospace Engineering, METU**   _____

Prof. Dr. Serkan Özgen
Supervisor, **Aerospace Engineering, METU**   _____

Examining Committee Members:

Prof. Dr. Yavuz Yaman
Aerospace Engineering, METU   _____

Prof. Dr. Serkan Özgen
Aerospace Engineering, METU   _____

Assoc. Prof. Dr. Özge Başkan Perçin
Aerospace Engineering, METU   _____

Prof. Dr. Nafiz Alemdaroğlu
School of Civil Aviation, Atılım Uni.   _____

Assoc. Prof. Dr. Mustafa Kaya
Aerospace Engineering, Ankara Yıldırım Beyazıt Uni.   _____

Date: 08.08.2023

I hereby declare that all information in this document has been obtained and presented in accordance with academic rules and ethical conduct. I also declare that, as required by these rules and conduct, I have fully cited and referenced all material and results that are not original to this work.

Name Last name : Mehmet Harun Özkanaktı

Signature :

ABSTRACT

ICE ACCRETION SIMULATION AND SCALING ANALYSIS FOR CONCEPTUAL DESIGN OF AN ICING WIND TUNNEL

Özkanaktı, Mehmet Harun
Doctor of Philosophy, Aerospace Engineering
Supervisor : Prof. Dr. Serkan Özgen

August 2023, 232 pages

Icing in aerodynamic structures is one of the most important problems to be considered due to its negative impact on the performance of aerodynamic components and its potential to cause fatal accidents. Hence, it is necessary to conduct experimental studies to investigate the causes, intensity, and physics of icing. Additionally, certification processes and compliance with these processes are inevitable in the development of aircraft. For these reasons, icing wind tunnel (IWT) studies are the most suitable method in terms of cost, safety, and feasibility for icing prediction and certification. However, since the dimensions of these components are often large for existing IWTs, it is necessary to conduct a scaling study to directly obtain in-flight icing. In this study, a similitude model was developed that matches the geometry, flow-field, droplet trajectory, total water catch, energy balance, and surface-water dynamics. Based on the terms in this similitude model, a scaling calculation was performed using the Modified Ruff Method due to its superior accuracy and inclusion of more scaling terms. The outputs of these calculations were used to analyze different reference conditions using the Aeromsice-2D icing prediction code, and the experimental data was compared with the reference and scaled icing results. The technical specifications of the icing wind tunnel were determined based on the limitations and physical requirements of these calculations

and the requirements specified in 14 CFR Appendix C to Part 25. Various scenarios consisting of different air velocity, droplet sizes, temperatures, and ice accumulation conditions, as well as the technical information and limitations obtained from the scaling, were used to perform the conceptual design of an IWT and its verification was carried out using the commercial computational fluid dynamics software ANSYS Fluent. The design process was revised based on the results obtained and the IWT design reached its final form.

ÖZ

BUZLANMA RÜZGAR TÜNELİNİN KAVRAMSAL TASARIMI İÇİN BUZ OLUŞUMU SİMÜLASYONU VE ÖLÇEKLENDİRME ANALİZİ

Özkanaktı, Mehmet Harun
Doktora, Havacılık ve Uzay Mühendisliği
Tez Yöneticisi: Prof. Dr. Serkan Özgen

Ağustos 2023, 232 sayfa

Aerodinamik yapılarda buzlanma, aerodinamik bileşenin performansını düşürmesi ve ölümcül kazalara neden olması sebebiyle dikkate alınması gereken en önemli problemlerden biridir. Bu nedenle, buzlanmanın sebeplerini, yoğunluğunu ve fiziğini araştırabilmek amacıyla deneysel çalışmaların yapılması zaruridir. Ayrıca, hava araçlarının geliştirilmesinde sertifikasyon süreçleri ve bu süreçlere uyum kaçınılmazdır. Bu nedenlerden dolayı, buzlanma rüzgar tüneli (BRT) çalışmaları, buzlanma tahmini ve sertifikasyon için maliyet, güvenlik ve uygulanabilirlik açısından en uygun yöntemdir. Ancak bu bileşenlerin boyutları çoğu varolan BRT için büyük olduğundan ötürü uçuş durumunda oluşan buzlanmayı birebir elde edebileceği buz ölçeklendirme çalışmasının yapılması gereklidir. Bu çalışma dahilinde geometri, akış, damlacık hareket, toplam yakalanan su, enerji dengesi ve yüzey-su dinamiklerini eşleştiren bir benzetim modeli oluşturulmuştur. Bu benzetim modelindeki parametreler baz alınarak, ölçeklendirmedeki üstün doğruluğu ve daha fazla ölçeklendirme terimi içermesi nedeniyle Modified Ruff Metodu ile bir ölçeklendirme hesaplaması yapılmıştır. Bu hesaplamaların çıktıları ile AEROMSICE-2D buzlanma tahmin kodu ile farklı referans durumları için analizler yapılmış, deneysel veriler ile referans ve ölçeklendirilmiş buzlanma sonuçları karşılaştırılmıştır. Bu hesaplamalardaki sınırlamalar ve fiziksel gereksinimler

kullanılarak ile 14 CFR Appendix C to Part 25 standartında bulunan gereksinimler, buzlanma rüzgar tünelinin teknik özellikleri belirlenmiştir. Farklı rüzgar hızları, su damlacık boyutları, sıcaklıklar ve buz birikim koşullarından oluşan durumlar ve ölçeklendirilmesinden elde edilen teknik bilgi ve sınırlamalar bir BRT'nin kavramsal tasarımı yapılmış ve doğrulanması amacıyla ticari hesaplamalı akışkanlar dinamiği yazılımı olan ANSYS Fluent ile analizleri icra edilmiştir. Ortaya çıkan sonuçlar ile tasarım süreçleri tekrar düzenlenilmiş ve BRT tasarımı nihai haline getirilmiştir.

Anahtar Kelimeler: Buzlanma Rüzgar Tüneli, Deneysel Aerodinamik, Buzlanma Birikimi, Buzlanma Benzeşimi, Buzlanma Ölçeklendirme, Uçuş Buzlanması
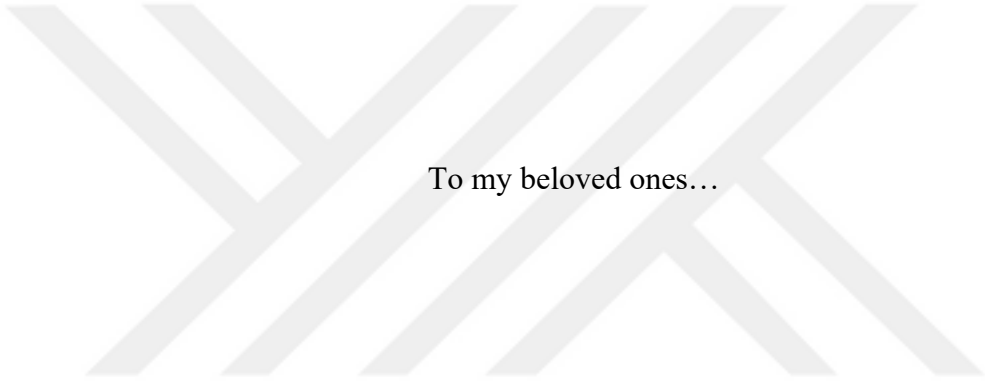
To my beloved ones…

ACKNOWLEDGMENTS

TABLE OF CONTENTS

LIST OF TABLES

TABLES

LIST OF FIGURES

FIGURES

LIST OF ABBREVIATIONS

ABBREVIATIONS

2D	Two Dimensional
AC	Air Conditioning
AEDC	Arnold Engineering Development Center
AGL	Above Ground Level
AOA	Angle of Attack
CB	Cumulonimbus
CFD	Computational Fluid Dynamics
CFR	Code of Federal Regulations
COP	Coefficient of Performance
CRM	Common Research Model
CU	Cumulus
CWT	Climatic Wind Tunnel
DLR	German Aerospace Center
EASA	The European Aviation Safety Agency
FAA	Federal Aviation Administration
FEA	Finite Element Analysis
IRT	Institute for Research in Technology
IWT	Icing Wind Tunnel
LWC	Liquid Water Content
MVD	Median Volumetric Diameter
NACA	National Advisory Committee for Aeronautics
NASA	National Aeronautics and Space Administration
NIST	National Institute of Standards and Technology
ONERA	Office National d'Etudes et Recherches Aérospatiales
RMS	Root Mean Square
RPM	Revolutions per Minute

SC	Stratiform Clouds
SLD	Supercooled Large Droplets
TRF	Turbulence Reduction Factor
TWC	Total Water Content
USA	United States of America
VFD	Variable Frequency Driver

LIST OF SYMBOLS

SYMBOLS

A_c	Accumulation parameter	
C_D	Drag Coefficient	
D_h	Hydraulic Diameter	
K_0	Modified inertia parameter	
L_F	Latent heat of solidification	
h_G	Gas phase mass transfer coefficient	
h_c	Convective heat transfer coefficient	
$\dot{m}$	Mass flow rate	
n_0	Freezing fraction at stagnation point	
p_w	Vapor Pressure	
A	Area	
B	Ice layer thickness	
H	Height	Chapter 4
K	Inertia parameter	
K	Pressure Loss Coefficient	Chapter 4
L	Characteristic Length	
L	Length	Chapter 4
M	Mach Number	
P	Pressure	Chapter 4
Pr	Prandtl Number	
Q	Heat loss/gain (energy)	
Re	Reynolds Number	
S	Surface area	Chapter 4
T	Temperature	

V	Velocity	
W	Width	Chapter 4
We	Weber number	
b	Relative heat factor	
d	Airfoil leading edge diameter	
g	Gravitational acceleration	
h	Thickness of water film	
k	Thermal conductivity	
l	Span-wise length	
p	Pressure	
q	Dynamics pressure	Chapter 4

GREEK SYMBOLS

Λ	Latent heat (subscript s for sublimation, v for vaporization, f for freezing)	
λ	friction factor	Chapter 4
Δ	Ice thickness, the total mass	
α	Angle in wind tunnel components in horizontal	Chapter 4
β	Droplet Collection efficiency	
β	Angle in wind tunnel components in vertical	Chapter 4 (wind tunnel components)
β	Porosity	Chapter 4 (mesh & honeycomb)
γ	Specific heat ratio	
δ	Droplet Median Volume Diameter (MVD)	
δ	Roughness	Chapter 4
ε	Surface emissivity	

θ	Air energy transfer parameter	
λ	Drop range	
μ	Dynamics viscosity	
ξ	Chord-wise dimension	
ρ	Density	
σ	Stefan-Boltzman constant	
σ	Solidity	Chapter 4
τ	Exposure time	
ϕ	Drop energy transfer parameter.	

SUBSCRIPTS

∞	Freestream
R	Reference condition
S	Scaled condition
a	Air
bl	At boundary layer
c	Airfoil chord
$cont$	Contraction cone
$corner$	Corner
$diff$	Diffuser
ew	Wire
f	Freezing point (0 degree Celsius)
$flow$	flow
$honey$	honeycomb
i	Ice
in	inlet
$mesh$	Mesh screen
out	Outlet

p	Droplet
rel	Relative
s	Surface
$sheet$	Sheet
st	Static
sur	ice surface (for rime ice)
$test$	Test section
tot	Total
$vane$	vane
w	Water
ws	Water on surface of model
0	Stagnation

CHAPTER 1

INTRODUCTION

Physical and climatic research on in-flight icing should be recognized as a crucial operational condition in many of the relevant engineering disciplines, particularly aviation. The consequences of the effects of these in-flight icing conditions on aerodynamic components can be catastrophic. In particular, this condition can occur on wings' leading edges, control surfaces and engine inlets, resulting in performance degradation or even failure of these components. In order to avoid such in-flight icing conditions, or at least to be aware of the threat when the possibility of the condition presence, the physics of these icing conditions must be thoroughly understood and accounted. It is of great importance that the aircraft is designed and operated taking into account the limits and behavior of the aircraft in icing conditions. During the design and certification phases of the aircraft, the assessment of performance degradation due to icing and operational limits in icing conditions has become a necessary part of the process. For conceptual design phases, the results of computational analysis for in-flight icing are acceptable, however, for detailed design and certification phases, tests simulating actual in-flight icing conditions should be conducted to validate the computational results and examine the actual behavior of the aircraft. Civil Aviation Authorities, such as the Federal Aviation Administration (FAA) and European Union Aviation Safety Agency (EASA), play a crucial role in addressing the challenges posed by aircraft icing. These organizations are responsible for ensuring that both commercial and general aviation operations are conducted with the highest level of safety. In light of the potential risks associated with icing, authorities have developed guidelines, protocols, and regulations that govern the design, maintenance, and operation of aircraft under icing

conditions. These regulations have been shaped through extensive research and experimental studies. The international aviation authorities FAA and EASA require atmospheric icing certification conditions 14 CFR Appendix C to Part 25 and EASA CS-25 to certify an aircraft to fly safely [1], [2].

For the aforementioned reasons, experimental studies need to be carried out to thoroughly understand the icing conditions and to ensure that the certification conditions can be met. Testing of aerodynamic components exposed to in-flight icing can be performed by flight tests, icing tanks or ground tests. Flight tests are the most realistic of these methods, but flights in hazardous conditions are risky, expensive, and it is not always possible to establish the conditions required for certification. Another method is testing with in-flight icing tankers. In this test, an icing condition is created for a flight created by a tanker spraying water and icing parameters can be controlled, but this method is effective for local parts of the exposed component and other atmospheric conditions are not completely controlled. At the same time, the issue of flight safety also applies to this test method.

However, among all these methods, the icing wind tunnel is the most applicable method. The icing wind tunnel can create the necessary environmental conditions for icing in a closed and controlled environment. In this way, tests can be carried out at reasonable costs, taking into account flight safety and physical icing conditions, with limitations on liquid water content (LWC), median volumetric diameter (MVD) and the size of the test object. It is often not feasible to perform actual size tests in an icing wind tunnel. For this reason, scaled models can be tested by matching the similitude parameters of icing. In addition, the implementation of the scaling method is performed in the wind tunnel. However, it is necessary to verify the outputs of the scaling calculations beforehand to verify the reliability and validity of the tests.

This thesis conducts the conceptual design of an icing wind tunnel through icing simulation and scaling studies, and the identification of constraints and parameters of the physical environmental conditions derived from their outputs. In addition, a comprehensive overview of the simulation of reference and scaling case study with

experimental data is presented. Subsequently, the technical requirements and conceptual design of the icing wind tunnel with the resulting limitations are be determined. The step-by-step process of this study is shown below.

- o Defining icing similitude parameters
- o Conducting icing scaling calculations
- o Determining limitations for the icing wind tunnel design
- o Defining requirements for icing wind tunnels
- o Icing wind tunnel design and calculations
- o Icing wind tunnel conceptual design in computer aided design.
- o Icing wind tunnel Computational Fluid Dynamics (CFD) analysis
- o Validation of the icing wind tunnel

In summary, conceptual design of an icing wind tunnel with all components is carried out. In addition, a model test case is determined and scaled to provide suitable conditions for the wind tunnel that is designed as part of this thesis.

1.1   Scope

The research commences by conducting a comprehensive review of existing academic literature and technical reports that pertain to the design and operational parameters of icing wind tunnels. Additionally, the research provides an overview of the current understanding of icing scaling limitations and their implications on wind tunnel testing applications. The study then proceed to the methodology and design phase, where a detailed discussion of the design of an icing wind tunnel on component base is presented. This discussion specifically focuses on the selection and determination of design parameters of icing wind tunnel, and the theoretical justifications for these design decisions. The primary objective of this focus is to address the challenge posed by icing scaling limitations in terms of test and icing similitude conditions and improve the validity and reliability of scaling techniques using available experimental data and to provide a better understanding of the physical and thermal phenomena related to atmospheric icing.

1.2 Literature Survey

Previous studies on in-flight icing have used different methods to obtain a scaled ice shape that matches the reference ice shape. The analogies mentioned in the literature for ice scaling analysis are geometry similarity, flow field similarity, droplet trajectory similarity, water catch similarity, energy balance and surface water dynamics similarity. The similitudes of the these is achieved by deriving the scaling parameters for each variable and matching them for the scaled and reference cases. However, the correct definition of scaling terms and the decision on their importance has been developed over many years and is still in progress. However, various similitude parameters for icing physics and scaling is suggested and employed for prediction of icing shapes through scaling methods. The parameters introduced as follows, K_0; modified inertia parameter, A_c; accumulation parameter, n_0; freezing fraction, We_L; weber number based on length for surface water dynamics, ϕ; droplet energy transfer parameter, θ; air energy transfer parameter, b;relative heat factor. Through the years, different and various combinations of scaling parameters for icing have been proposed depending on the simulation requirements to be met and to enhance the accuracy of icing scaling.

According to the authors affiliated with Lockheed Aircraft Corporation, a novel scaling approach has been introduced. This approach involves a series of parameters that need to be aligned in order to achieve similarities in droplet trajectory, water catch, and energy balance, represented using notation related to icing physics, such as, K_0, A_c, n_0, b [3].

Dodson et al. from Boeing Airplane company conducted a work [4], which involved the scaling method with droplet trajectory and water catch similarity that leads to the scaling parameters sufficient for icing scaling.

Another scaling approach was introduced and developed by Dr. Earl Olsen in the 1950s and is based on the temperature and humidity conditions in the atmosphere which require the knowledge on the ambient temperature, relative humidity, and wind speed at the altitude where the aircraft is flying [5]. Also, Olsen and Newton

4

enhanced this method by refining the $LWC \times \tau = constant'$ method. This method suggesting that the product of exposure time and LWC should be the same for both cases and this method can be utilized for size scaling and test condition scaling [5], [6].

The Ingelman-Sundberg method, as described by the Swedish-Soviet Working Group on Aircraft Safety, is a size-scaling approach that primarily focuses on matching the similarity parameters K_0 and A_c, as well as the test conditions τ and LWC. This method allows the user to specify the size and velocity of the scale model. With model size and velocity given, the drop size can be determined by matching scaled and reference K_0, and, with LWC$_S$ and V_s known, icing time can be found by matching A_c [7].

The other scaling method known as the ONERA technique [8], [9] was developed by Charpin et al. for wind tunnels where temperature and pressure are not controlled. This method requires the terms of K_0, A_c, n_0 and b from the energy balance equations. The droplet size is calculated by matching K_0, and the LWC is calculated by matching b. This method is conducted in Modane wind tunnel facilities with different scaling ratios, and it is reported that this method is useful [8], [9]. In this technique, the scaling speed is generally lower than the speed before scaling, and improvement by matching the Weber number [10] which is named as Method I of Ruff (AEDC) [11]. Parameters that need to be matched are K_0 and A_c, for the Method II is K_0, A_c and n_0.

Similar to prior methods, several scaling methods have been proposed by Ruff, which are combinations of similitudes of droplet trajectory, water catch and energy balance. Different combinations of energy balance parameters provide similarity of the energy balance. Some other scaling methods are suggested, where different number of similarity parameters are involved such as K_0 and A_c constant; K_0, A_c and n_0 constant; K_0, A_c, n_0 and b constant and K_0, A_c, n_0, ϕ and θ constant [11].

A novel scaling method by Ruff et al. was investigated at the Arnold Engineering Development Centre engine test facility [11]. This work includes scaled and full-

scale versions of cylinder and airfoil sections. As a result of this work, ice accumulation on the specimen was compared to real-case conditions to prove the accuracy of the scaling method. The scaling method include size scaling and scaling of icing conditions, and the similitude is examined by providing similitude of droplet trajectory, flow field and impact attribute to the amount of impinging water, and thermodynamics of the ice accretion process.

A study proposed by Anderson [10] suggests that is the most precise to obtain the proper outer geometry of scaled ice shapes. The limitation of the scaling method is the airflow velocity since the velocities leading to a Reynolds number of less than $2 * 10^5$ and beyond the critical Mach number have unique characteristics that only allow scaling with further work. A scaling method is developed by identifying the scaling parameters by analyzing icing and similitude physics in airflow and gathering the knowledge from previous studies on icing scaling methods.

Numerous empirical studies conducted in the NASA Glenn Icing Research Tunnel have demonstrated compelling outcomes. The similitude is provided by the similarity of geometry, energy balance, droplet trajectory, flow field, water catch, and surface water dynamics [12]. These similitude parameters are used for scaling test conditions in this intensive work, and the effects of the scaling parameters on the final geometry of the ice shape and the physical phenomena containing the icing parameters were deduced during the runs.

The Modified Ruff Method was proposed with a constant We_L ($Weber\ number$) approach which is an important parameter is to determine the characteristics of water flow onto model's surface. Weber number, is used to compute velocity and obtain reference ice shape with a scaled size model, which is also employed in the current study. This method requires tuning of energy balance, water catch, surface water dynamics, the droplet trajectory, as well as scaling of the geometry and angle of attack [11]. This research was further developed by Wang et al. who used the modified Ruff method to optimize the speed of the simulation to obtain more accurate results in the icing wind tunnel [13].

In the present work, the primary intention of the scaling method is to extend the effect of surface water dynamics, which is contained in the scaling method by modifying the conditions of We_L. The scaling parameters to be matched are chosen as K_0, A_c, n_0, ϕ, θ, b and We_L for tunnels with altitude adjustment capability or K_0, A_c, n_0, We_L and one of the ϕ and θ parameters for atmospheric tunnels. The We_L parameter drives the selection of scaled velocity. In this work, the practical limitations of size scaling due to physical and spatial constraints are as follows; a scale ratio smaller than ¼ is not feasible for effective scaling, and there are other limitations for test condition scaling.

1.2.1   Icing Wind Tunnels in The World

Icing wind tunnels are specialized testing facilities used to evaluate the impact of ice on aircraft performance. These tunnels are designed to replicate the conditions of flight through icing clouds, allowing engineers to assess how ice accumulates on an exposed surface and how it affects the aircraft's aerodynamics. Icing wind tunnels are used by aircraft manufacturers, airlines, and research institutions around the world to ensure the safety and performance of aircraft in icing conditions.

In the field of aerospace research, the icing wind tunnel is emerging as a crucial tool designed to rigorously simulate the conditions under which aircraft components struggle with the phenomenon of atmospheric ice accumulation. The essence of these tunnels is to understand the methods of ice formation on aircraft under various conditions, to facilitate subsequent evaluations of anti-icing and de-icing systems, and to investigate the aerodynamic consequences of these ice formations.

The key principle in the design of an icing wind tunnel is, firstly, to organize a controlled airflow over the test object, similar to conventional wind tunnels. Secondly, by conditioning the air inside the icing wind tunnel, providing the atmospheric conditions in which icing occurs, and having the ability to maintain temperatures below the freezing threshold. Finally, by spraying water into the

airflow through a calibrated spray bar, it simulates the accuracy of flight in cloud or high humidity environments.

From a design perspective, there is a multivariable design problem to consider. The uniformity and velocity of the airflow stand out as they critically affect the way ice forms. Given that the transformation of water into various forms of ice (rime or glaze) is closely linked to these temperatures, ensuring precision in the control of both air and water temperatures is another challenge. Furthermore, the spray bar must offer flexibility in terms of droplet size and distribution, mimicking the variations observed in real-world conditions. The spatial dimensions of the test section need to be calibrated to the object under investigation, such as a large wing section or a small probe. Furthermore, the instrumentation requires sophisticated instrumentation, including cameras, to meticulously observe and measure ice formations and the resulting aerodynamic nuances.

However, the procedure from designing to realizing an icing wind tunnel is full of challenges. Achieving a consistent and repeatable set of conditions can also be a challenging endeavor. While the size of larger aircraft components requires scaling down for testing, this action introduces scale-induced deviations not present in the original component. Maintenance also emerges as a concern as various areas of the tunnel become vulnerable to ice accumulation. Furthermore, the presence of support structures for the model, such as studs or ties, increases turbulence by disrupting airflow and can effect ice accumulation. With all these concerns and design needs in mind, several icing wind tunnels are in operation around the world, some examples of which are detailed below.

• The National Research Council of Canada's Icing Research Tunnel in Ottawa, Canada: This tunnel is one of the largest and most advanced icing wind tunnels in the world and is used to test aircraft of all sizes and types. The tunnel is equipped with A/C (air conditioning) system and sophisticated spray bar system to replicate the conditions of an icing cloud and has a variety of measurement instruments to assess the performance of the aircraft being tested [14].

• The Icing Research Tunnel, formerly known as the Lewis Research Center, is a facility located in Cleveland, Ohio, USA, operated by the National Aeronautics and Space Administration (NASA). Its primary purpose is to investigate the effects of ice on aircraft performance, as well as various aspects of aircraft design and performance. The tunnel is equipped with a climatic conditioning system and spray bar system, which allow for the replication of icing cloud conditions. Additionally, the facility is equipped with a range of measurement instruments that are used to evaluate the performance of the aircraft being tested [12]. It is worth noting that the renowned ice prediction code LEWICE has been developed as a result of the extensive research conducted in this wind tunnel.

• The DLR Institute of Aerodynamics and Flow Technology's Icing Wind Tunnel in Braunschweig, Germany: This tunnel is operated by the German Aerospace Center (DLR) and is used to study the impact of ice on aircraft performance, as well as other aspects of aircraft design and performance. The tunnel is equipped with A/C system and a spray bar system to replicate the conditions of an icing cloud and has a variety of measurement instruments to assess the performance of the aircraft being tested [15].

These are just a few examples of the many icing wind tunnels located around the world. These facilities play a vital role in the design and safety of aircraft, helping to ensure that aircraft are capable of performing safely and reliably in icing conditions.

Table 1 below lists the existing icing wind tunnels with their specifications. It is obvious that they are insufficient for the aerospace industry. Moreover, it should be noted that there are no icing wind tunnels in Turkey, although the Turkish Aerospace Industry has considerably in the last ten years.

Table 1: Icing Wind Tunnels Around the World

Company, Location	Name	Test Section (m)	Velocity at test section (m/s)	MVD (µm)	LWC (g/m³)	Min. temp (⁰C)
Regional Ecological Center, Latvia[16][17]	T-4	2 x 1.5	70	8 –35	0.25 – 3	
Regional Ecological Center, Latvia[16][17]	T-5	3.4 x 2.6	100	10 - 40	0.3 – 2	-12
CIAM, Turaevo[17]	S-1A	1.5 (Dia)	0.5 Mach	30	2.5	-30
NASA, USA[18]	IRT	2.74 x 1.83	175	15 – 50	0.2 – 2.5	-32
NRC, Canada[14]	PIWT	3.1 x 6.1	54	15 – 50	0.15 – 2.5	-30
CIRA, Italy[19]	IWT	2.35 x 1.15	150	15–250	0.15 – 2	-40
Boeing, USA[20]	BRAIT	1.22 x 1.83	128.6	15 – 40	0.2 – 3	-32
NASA, USA[12]	Glenn	1.8 x 2.7	168	15–275	0.15 – 4	-30
RTO, Vienna[21]	IWT	3.5 x 4.6	80	15 – 40	0.9 – 5	-30
BF Goodrich, USA[22]	IWT	0.56 x 1.12	268	10 – 50	0.4 – 3	-32
Collins Aerospace, USA	IWT	0.56 x 1.52	102	5 – 50	0.1 – 3	-43
AECD, TN USA	R-1D	0,914 (Dia)	268	15 - 40	0.2 - 3.9	-29
Le Clerc Icing Laboratory, NY USA[23]	LIRL	0.71 x1.17	98,5	15 - 50	0.25 - 3	-30
Le Clerc Icing Laboratory, NY USA[23]		1.22 x1.22	54	15 - 50	0.25 - 3	-30
FluiDyne, MN USA	IRT	0.55 x0.55	273	10 - 35	0.1 - 5	Amb.
Rosemount, MN USA [15]	IWT	0.254 (Dia)	94	15 - 40	0.1 - 3	-30

Figure 1: NASA Icing Wind Tunnel In-flight Icing Test [24]

In the initial phase of this thesis, a comprehensive review of existing literature on icing wind tunnels, wind tunnels, and icing studies worldwide is conducted. The subsequent chapter is aimed to establish an understanding of the physics of icing and the formation of ice on aerodynamic structures. This involves exploration of cloud types, microphysics of icing, icing envelope, and various physical factors that influence icing. Additionally, general parameters and information pertaining to icing were presented.

Chapter 3 focuses on modeling and scaling studies related to icing accumulation. Initially, the similitude approach for icing is discussed, followed by an examination of scaling methods and types. Subsequently, the most suitable scaling method for this study is selected, and calculations are performed accordingly. The solutions are then compared based on their physical properties, and limitations are identified. These limitations are subsequently incorporated as design inputs for the planned wind tunnel.

In Chapter 4, the conceptual design of the icing wind tunnel is developed for component-wise, and a collective analysis of all components is conducted. These analyses are compared, and the accuracy of the procedures employed is demonstrated.

CHAPTER 2

ICING PHYSICS

It is important to understand the physics of clouds and the atmosphere in order to fully comprehend the behavior of ice formation on air vehicles. Therefore, in this chapter, icing physics coupled with atmospheric constituents will be explained in detail.

The atmosphere comprises a combination of many gases which are nitrogen, oxygen, and carbon dioxide, mainly. However, beyond this gaseous mixture, air contains, vast number of particles of liquid or solid masses. Also, air mixture contains water vapor in three phases depending on the psychometric conditions of atmosphere apart from the most abundant gases [1], [25].

The upper atmosphere has ions and electronically excited particles. Composition of the air is approximately, 78% nitrogen, 21% oxygen, ~1% argon and 0.03% of carbon dioxide [1], [25]. These combinations of air can differ with location and time. So that, moisture in the air can be altered up to 4% of air volume and it can be easily said that water vapor is carried by clouds in the lowest atmosphere. The atmosphere also comprises different types of particles such as salt crystals, dust, and smoke particles carried with wind. Most of these small constituents in the air work as nuclei around which water droplet or ice crystals form. These microscopic residuals are crucial for aerospace because they play an important role in the condensation process. The water vapor in the air condenses on particles present in the atmosphere, which are called condensation nuclei [26]. Table 2 provides a comprehensive breakdown of the composition of atmospheric air, including the range of diameters and concentrations of its constituents. Furthermore, the table also presents the terminal velocities of these components, as they have the potential to precipitate.

Table 2: Constituents of Air [26]

Type	Diameter range (mm)	Concentration range (no./cm^3)	Approx. terminal velocity (cm/sec)
Small ions	$(0.15\text{--}1)\times10^{-5}$	$(1\text{--}7)\times10^2$	
Large ions	$(1\text{--}20)\times10^{-5}$	$(2\text{--}20)\times10^3$	
Small Aitken	$(0.1\text{--}4)\times10^{-4}$	$10\text{--}10^5$	$10^{-5}\text{--}10^{-3}$
Large nuclei	$(4\text{--}20)\times10^{-4}$	$1\text{--}10^3$	$10^{-3}\text{--}0.07$
Giant nuclei	$(20\text{--}1000)\times10^{-4}$	$10^{-4}\text{--}10$	$0.07\text{--}0.7$
Fog & cloud droplets	$(1\text{--}200)\times10^{-3}$	$25\text{--}600$	$0.01\text{--}70$
Drizzle	$(2\text{--}40)\times10^{-2}$	$1\text{--}10$	$1\text{--}170$
Raindrops	$0.4\text{--}4$	$10^{-3}\text{--}1$	$170\text{--}900$
Snow crystals	$0.5\text{--}5$	<10	$30\text{--}100$
Snow flakes	$4\text{--}20$	$10^{-3}\text{--}1$	$80\text{-}200$
Hail	$5\text{--}75+$ (largest: 140)	$10^{-6}\text{--}10^{-1}$	$800\text{--}3500+$

2.1   Cloud Formation And Classification

2.1.1   Cloud Formation

Clouds come into existence by condensation of water vapor resulting in the formation of visible water droplets, snow, or ice crystals with combination of various particles as it can also be seen in Table 2. This condensation process requires a sufficient adequate amount of vapor, cooling, and the existence of nuclei in the air. The cooling of the atmosphere can be initiated through various processes, including convection, orographic lifting caused by geographical features like mountains, frontal lifting where warm air displaces cold air, and turbulence-induced lifting due to friction between the air and the Earth's surface [26], [27]. These meteorological phenomena come into existence mostly in troposphere layer of the whole atmosphere which can be seen in Figure 2.
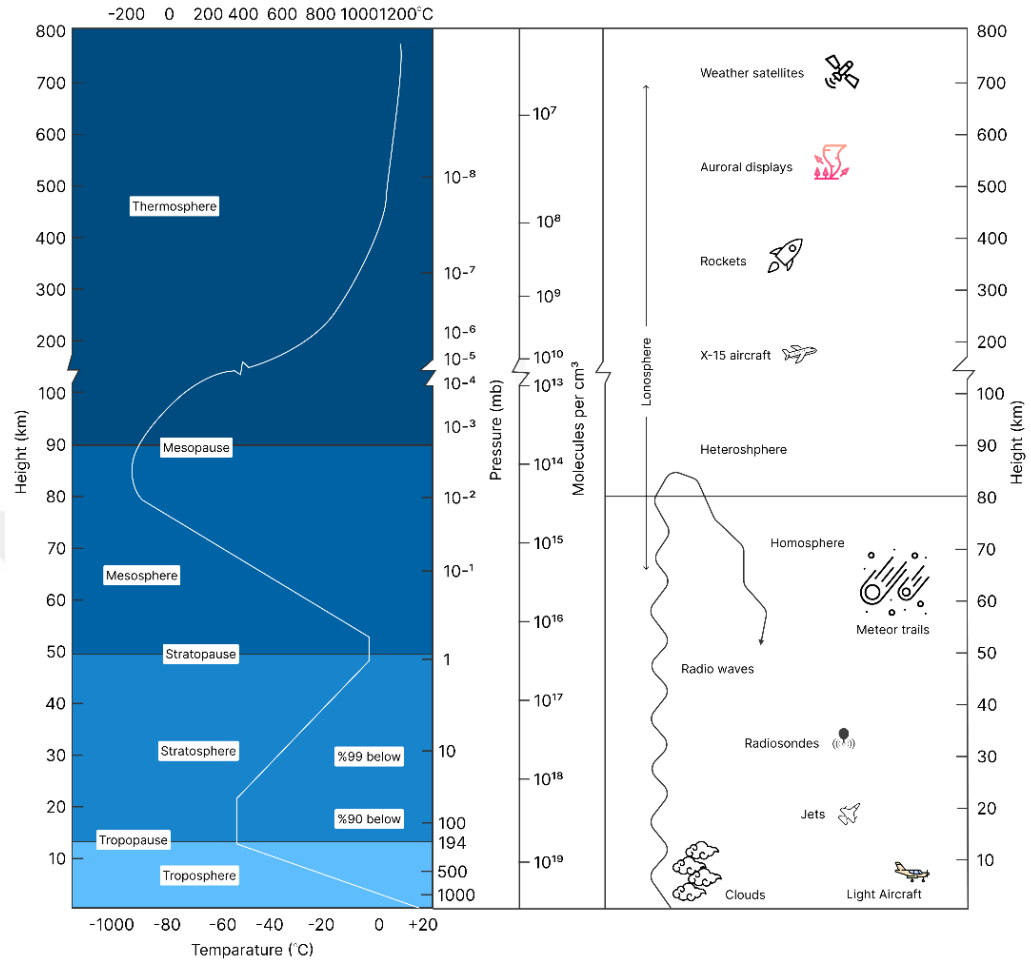
Figure 2: Vertical Atmospheric Properties [26].

2.1.2 Cloud Classification

Clouds consist of liquid water droplets, supercooled droplets, and solid particles (ice crystals). Studying these clouds is crucial for understanding atmospheric conditions and predicting weather patterns in the troposphere. The clouds can be classified into three segments as high (above 6 km), middle (2 km to 6 km), low (below 2 km) and vertically developing clouds. Figure 3 provides a visual representation of the most frequently observed cloud types with respect to altitude [1], [25], [26]. Clouds are identified according to their form and average height above ground level (AGL). Cloud names are categorized based on specific roots. Cirrus refers to clouds that have a feathery or fibrous appearance. Stratus denotes clouds that are stratified or arranged

in layers. Cumulus describes clouds that are heaped up or have a puffy shape. Lastly, Nimbus refers to clouds that are associated with rain.
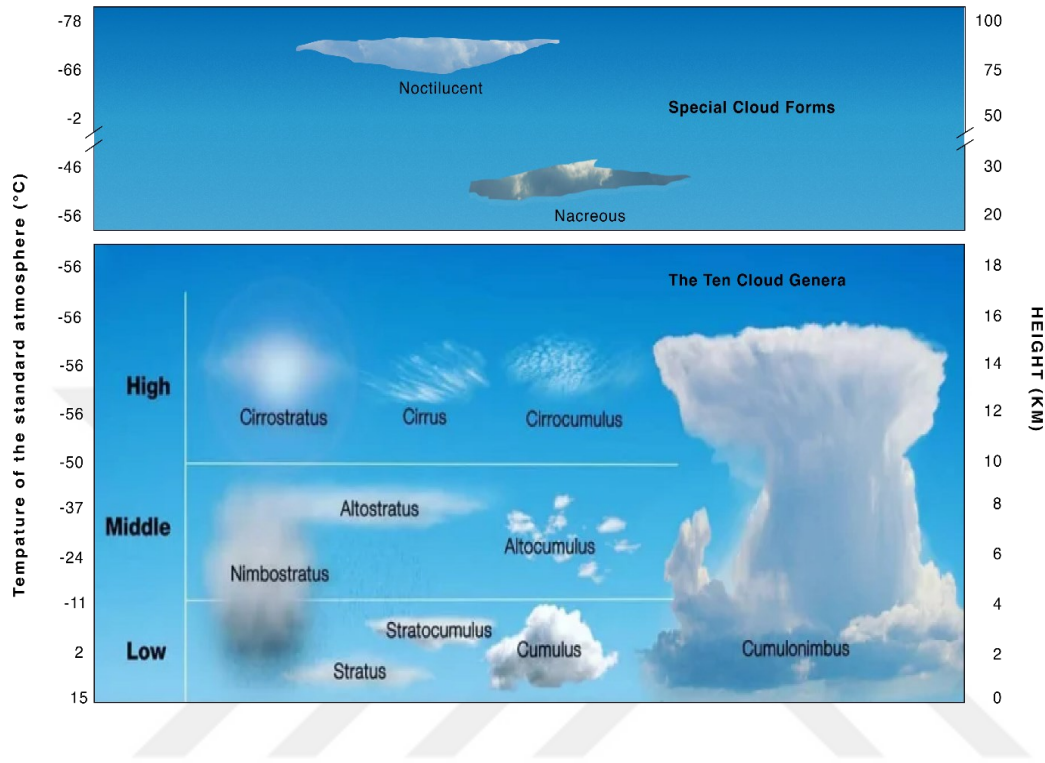
Figure 3: Cloud Classification with Different Altitude [25].

2.1.2.1 Icing Clouds

Two different cloud types are responsible for icing occurrence: stratiform clouds and cumuliform clouds. Beyond these two cloud types, there is another meteorological phenomenon that causes aerodynamic icing, although it is not a cloud. This phenomenon, called icing precipitation or drizzle, also causes severe icing. This phenomenon occurs when rain or drizzle encounters a layer of very cold air as it falls towards the ground and the precipitation droplets turn into large, supercooled droplets. These droplets are then called supercooled large droplets (SLD) and can cause a very rapid accumulation of ice. This type of icing is outside 14 CFR Parts 25, Appendix C range of conditions. The existence of this deficiency was recognized after the ATR-72 accident at Roselawn in 1994. Subsequently, in 2015, the FAA and EASA published new rules, Appendix O, required for certification including SLD conditions [28], [29].

Table 3: Continuous and Intermittent Maximum Icing Conditions [1]

Condition	Stratiform Clouds (Continuous Maximum)	Cumuliform Clouds (Intermittent Maximum)
Temperature Range	0 to -30 ℃	0 to -30 ℃ (possibly to -40 ℃)
Droplet Range	15 to 40 μm	15 to 50 μm
LWC Range	0.04 to 0.8 g/m^3	0.1 to 2.9 g/m^3
Pressure Altitude Range	0 to 22,000 feet	4,000 to 22,000 feet
Reference Horizontal Extent	17.4 nm	2.6 nm
Horizontal Extent Range	5 to 300 nm	0.26 to 5.21 nm

2.1.2.1.1 Stratiform Clouds

As it can be deducted from the name of the cloud, this type of cloud has the shape of horizontal layers. For this cloud type, icing conditions are generally less severe than cumuliform clouds. However, this cloud has the largest of horizontal extent in the air. This type of clouds has LWC ranging from 0.1 to 0.8 g/m³ and MVD from 5 to 50 μm [30], [31]. Stratiform clouds are responsible mostly for formation of rime ice due to relatively low temperature and low LWC.

The stratiform clouds can be high, middle, and low-level clouds. In the high-level occurrence of SC, above 6 km (20,000 ft), this cloud contains only ice crystals therefore, there would be no icing problem.

Middle level and low level SCs are important for icing since both ice crystals and liquid water droplets are present. As it is stated in the beginning of this chapter, under 2 km altitude (6,500 ft) icing is very crucial due to the presence of high liquid water content. Apart from the LWC issue, turbulence also increases the severity of icing, especially when the cumuliform and stratiform clouds overlap. Stratiform clouds

form continuous icing conditions as designated in the FAA envelope of 14 CFR Part 25, Appendix C.
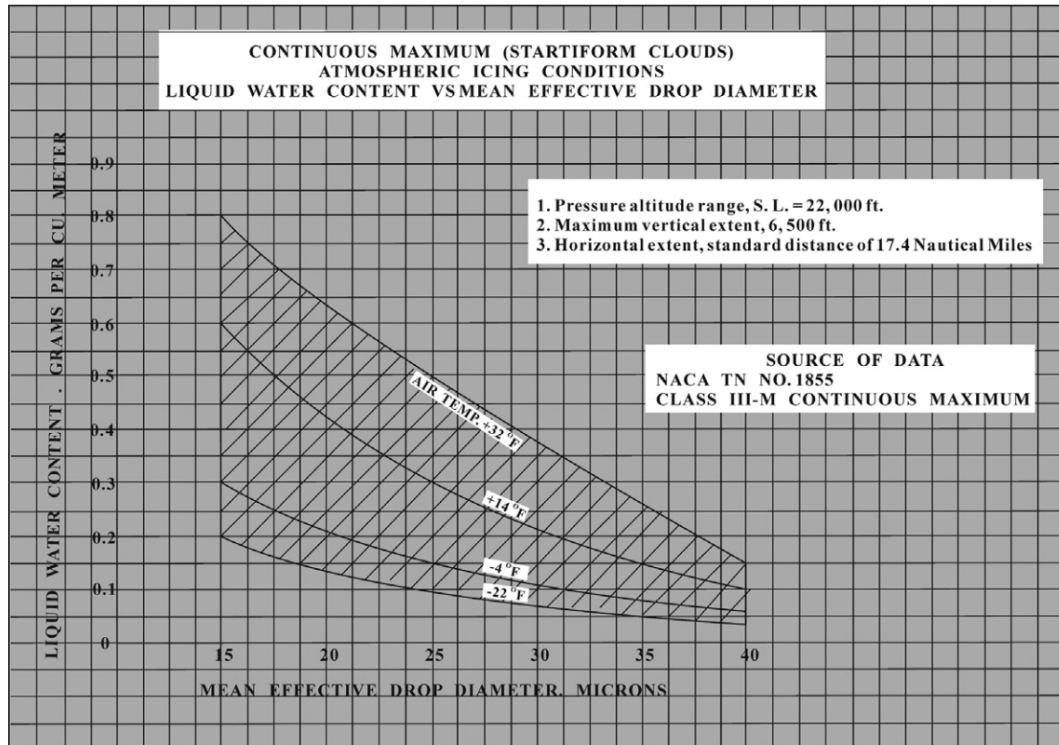
Figure 4: Continuous Maximum Atmospheric Icing Conditions [2]

2.1.2.1.2 Cumuliform Clouds

Cumuliform types of clouds contains higher quantities of water. In this cloud type, LWC ranges from 0.1 to 3.0 g/m^3 and some clouds can have 3.9 g/m^3 of LWC for a short extent [30], [31]. In cumuliform clouds, vertical air movement causes turbulence, which may enhance the formation of SLD. These droplets form glaze ice on exposed surfaces. This causes serious icing formation in a short time. Cumuliform clouds consists of cumulus (CU) and cumulonimbus (CB) formation. These clouds have a relative smaller horizontal coverage ranging from 3.7 to 11 km [31] but exhibit significant vertical growth, which can result in intermittent icing.
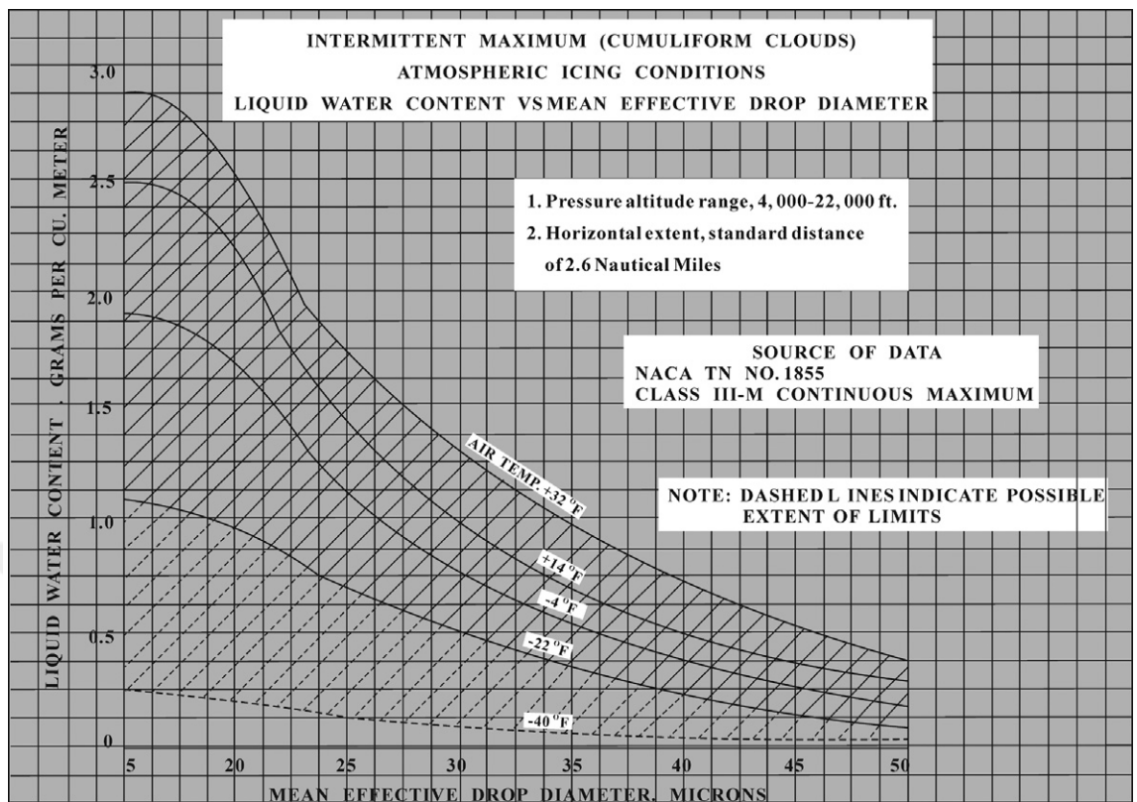
Figure 5: Intermittent Maximum Atmospheric Icing Conditions [2]

2.2   Icing Envelopes

National Advisory Committee for Aeronautics formerly known as NACA, placed extensive work on icing investigations in understanding icing behavior in atmospheric conditions both experimentally and theoretically in 40's and 50's [25], [32]. These works have been used and led to the FAA to create new regulations for operating aircraft in atmospheric icing conditions [1].

FAA accepted two standard envelopes for the certification of transport and category aircraft, which are the continuous and intermittent icing envelopes. The design criteria for icing protection systems are based on the parameters which are LWC, droplet diameter, temperature, altitude, horizontal extent, and the type of cloud.

In Figure 4 and Figure 5, distribution of LWC versus droplet diameter for different ambient air temperatures can be seen. Cumuliform clouds represents intermittent

maximum icing and stratiform clouds represents continuous maximum icing conditions.

2.3   Ice Accumulation Mechanism

Icing poses a significant hazard during flight and can have detrimental effect on aircraft. The formation of ice in the atmosphere requires two conditions to be met: the ambient temperature must be below 0°C and there must be supercooled water droplets present. When an aircraft flies through clouds containing supercooled droplets, which have a temperature slightly below freezing point, ice can accumulate on the outer surface of the aircraft. This occurs when the supercooled droplets freeze upon contact with the aircraft's surface, resulting in the accumulation of ice on the exposed frontal areas of the aircraft.

Rime ice represented in Figure 6, typically occurs at low temperatures and low liquid water content. Cloud droplets freeze immediately upon impingement. Rime ice is opaque and usually follows the surface contour. It is easier to detect and remove.
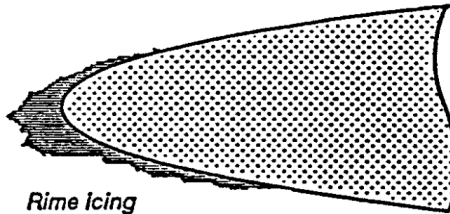
Rime Icing

Figure 6: Rime Ice on airfoil section [33]

Glaze ice represented in Figure 7 is transparent. This type of icing forms typically at temperatures around freezing point with high LWC. Glaze ice forms when only a part of the water droplets freeze with impact and the rest of the droplets run back and flow along the surfaces or freeze downstream. Glaze ice forms in irregular shapes and for this reason it distorts the aerodynamic shape of the aircraft and causes intense

performance degradation. Glaze ice is more dangerous than rime ice. Also, it is harder to detect and remove.
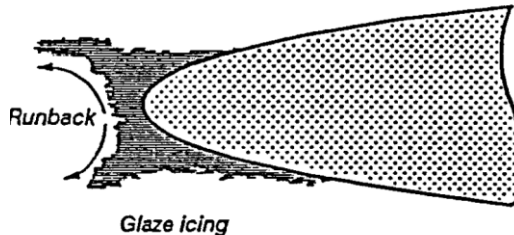
Figure 7: Glaze Ice on airfoil section [33]

Table 4: Rime and Glaze Ice Formation Comparison [26]

Icing Types	Rime Ice	Glaze Ice
Air Temperature	Low	High
Airspeed	Low	High
LWC	Low	High
Water Droplets	Freeze on impact	Only a fraction freezes on impact, rest flow on the surface
Color	Milky/opaque	Glossy / Clear
Texture	Rough	Smooth
MVD	Small	Large
Airfoil ice shape	Streamlined	Single or Double Horn

2.4 Physical Factors Affecting Ice Accumulation

The ice accumulation risk on the aircraft depends on several factors that can be named as icing intensity. These aerodynamics and meteorological factors consists LWC, MVD, ambient temperature, velocity, size/geometry of the exposed surface, exposure time, pressure altitude, horizontal extent of a cloud, terrain factors and seasonal climate. Beyond these factors, water catch, and collection efficiency are

derived parameters that determining ice accumulation. Water catch is the quantity of water that impinges the surface of aircraft and is the combination of LWC, freestream velocity and exposure time. Total collection efficiency can be stated as the ratio of the droplets' mass impinges on a body in unit time over droplets' mass that impinges the surface of aircraft component. Visual representation of trajectories of the impinging droplets is shown in Figure 8.
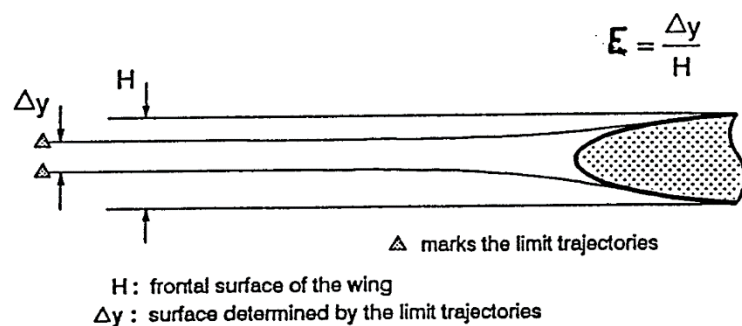
Figure 8: Total Collection Efficiency

2.4.1   Icing Intensity

Icing can be classified as trace light, moderate and intense. This classification have been defined in 1964 according to meteorological and operation conditions [34]. Table 5 summarizes icing intensities according to ice accumulation rate also same definitions in other way represented in Table 6.

Table 5: Icing Intensity and Time [34]

Icing Intensity	Time to Accumulate ¼ inch of Ice
Trace	Over 1 hour
Light	15 to 60 minutes
Moderate	5 to 15 minutes
Intense	5 minutes or less

In Figure 9, classification of the icing types introduced by Makkonen et al [35]. The term "Critical Liquid Water Content" is not commonly recognized within standard terminology, but it could denote a specific value of LWC where a transition from

liquid form to ice form based on a critical LWC denotes as W_c while other physical parameters are fixed. Figure 9 is also, confirms the Table 4 with addition of icing intensity characteristics.
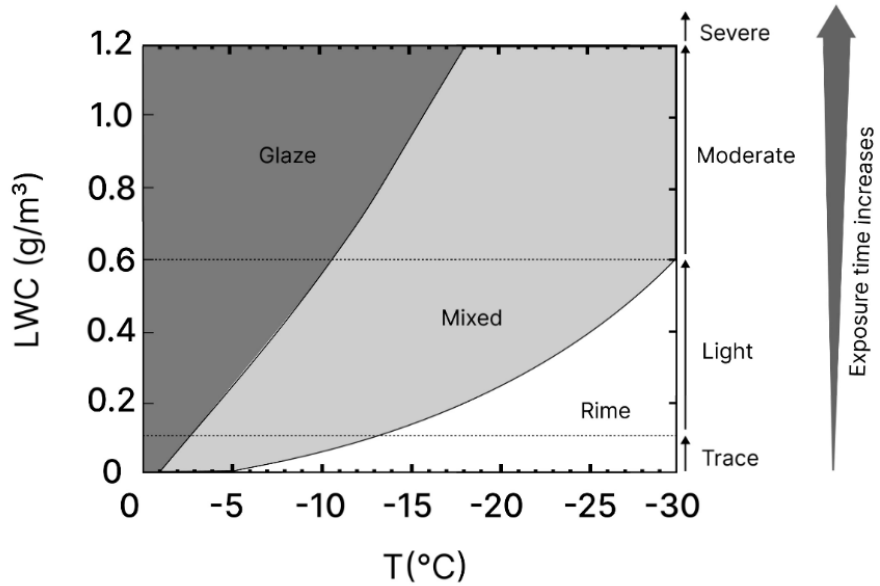
Figure 9: Ice Classification w.r.t. Critical LWC vs. Temperature [36].

The psychrometric diagrams depicted in Figure 10 and Figure 11 provide information on atmospheric conditions associated with cumuliform and stratiform clouds that are susceptible to icing. Upon careful examination of both figures, particularly within the high-risk region, it becomes evident that the temperature range conducive to icing formation lies between 0 and -15°C. This phenomenon can be attributed to the presence of a cold air mass, which fosters a more stable and low-energy environment. Additionally, during the impingement at lower temperatures than -30°C, the SLD exhibit a tendency to rebound rather than adhere to the model's surface. Consequently, the probability of ice formation on the surface is diminished.

In order to gain a deeper comprehension of the FAA icing envelope, Figure 10 and Figure 11 incorporate International Standard Atmosphere (ISA) temperature lines. The ISA model represents air that adheres to the principles of the ideal gas law and is considered a benchmark for atmospheric conditions. The temperature lines

depicted in Figure 10 and Figure 11 demonstrate the deviation from standard day conditions, indicating the altitude range within which icing conditions occur. For stratiform clouds, icing conditions are typically observed between ISA +8.5°C and ISA –40°C as represented with black dash and red line in Figure 10. On the other hand, the range for cumuliform clouds spans from ISA +5°C to ISA –20°C as represented with black dash and red line in Figure 11 [37].

If we examine each figure in more detail, the envelope of cumuliform clouds for Figure 10 is limited to the right side by the ISA values of 8.5°C. The high-risk region scans temperatures of -15°C and higher, while the medium-risk region encompasses atmospheric conditions of -15°C and colder. In summary, when the graph is examined, the region marked by the red line is seen as the continuous maximum icing envelope.
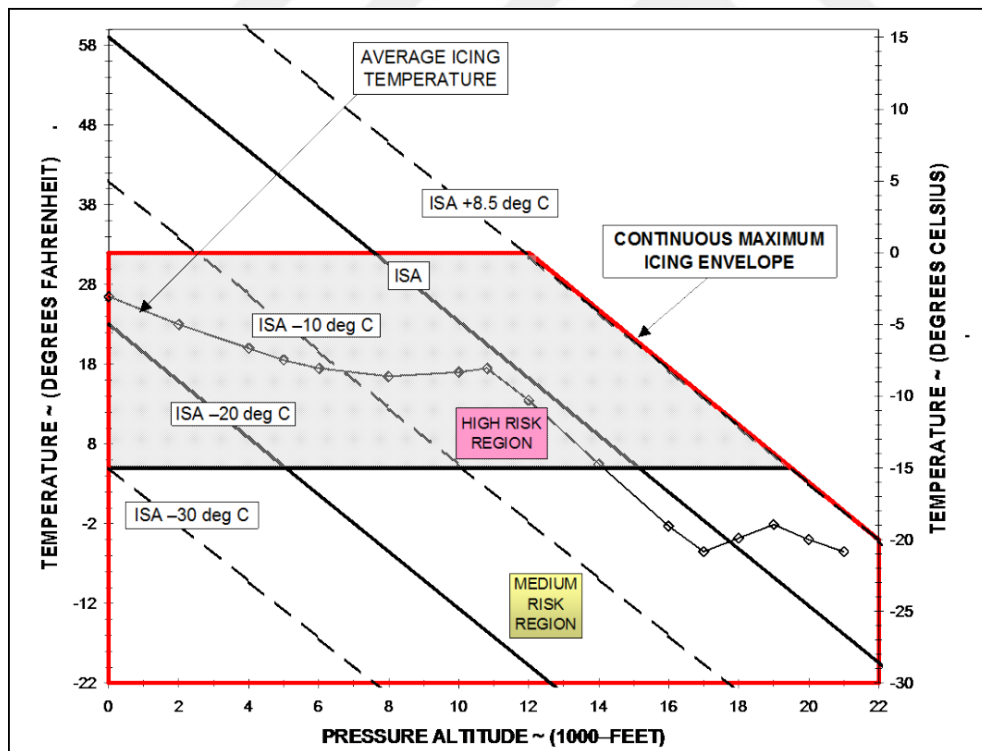
Figure 10: Stratiform Clouds Atmospheric Icing Conditions [37]

When examining the intermittent maximum atmospheric icing conditions shown in Figure 11, it can be observed that the ISA values limit the right side of the graph to +5°C. For the high-risk region, an upper limit of approximately -3°C is established. The left side of the graph is limited to an ISA value of -18°C for all risk regions. The icing risk regions for cumuliform clouds have lower limits of -20°C for high risk, -30°C for moderate risk, and -40°C for low risk.
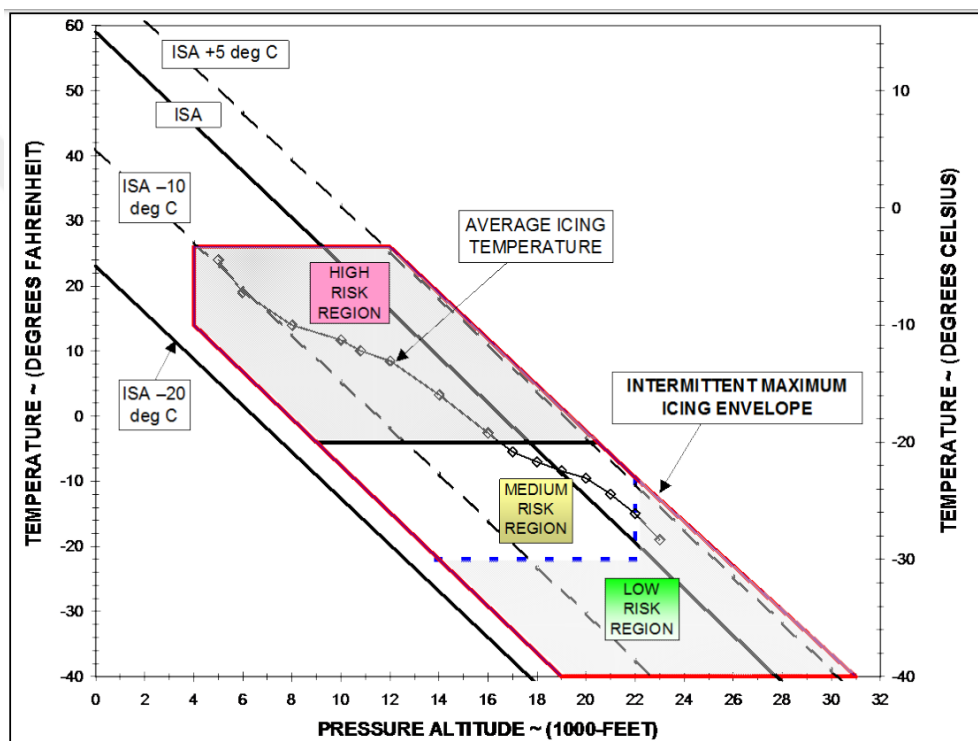
Figure 11: Cumuliform Clouds Atmospheric Icing Conditions [37]

Table 6 provides a detailed description of the physical characteristics and visual appearance associated with this level of icing intensity.

Table 6: Classification of Icing [33]

Ice Intensity	Description
Trace	Ice becomes perceptible. Rate of accumulation slightly greater than rate of sublimation. It is not a hazard even though except when deicing/anti-icing equipment is not utilized, unless encountered for an extended period of time (over one hour).
Light	The rate of accumulation may create a problem if flight is prolonged in this environment (over one hour). Occasional use of deicing/anti- icing equipment removes/prevents accumulation. It does not present a problem if deicing/anti-icing equipment is used.
Moderate	The rate of accumulation is such that even short encounters become potentially hazardous, and use of deicing/anti-icing equipment or diversion is necessary.
Severe	The rate of accumulation is such that deicing/anti-icing equipment fails to reduce or control the hazard. Immediate diversion is necessary.

2.4.2   Liquid Water Content (LWC)

The liquid water content (LWC) refers to the mass of water present in one cubic meter of dry air. Extensive research, as outlined in 14 CFR Parts 25, Appendix C, provides flight test data on LWC values for various cloud types and durations of exposure [1], [2]. The threat to aircraft increases as the LWC increases. The ability of air to hold liquid is determined by the available energy, and therefore the most significant risk of icing occurs at temperatures above -15°C for stratiform clouds and above -20°C for cumuliform clouds. Cumuliform clouds exhibit more turbulence compared to stratiform clouds, resulting in a higher level of energetic movement. This increased energy allows cumuliform clouds to hold a greater amount of supercooled liquid droplet (SLD) compared to stratiform clouds. Furthermore, the

LWC value also indicates the severity of icing, as well as the types and shapes of icing accumulation. Figure 12 provides a visual representation of the shape of icing accumulation for different LWC values.
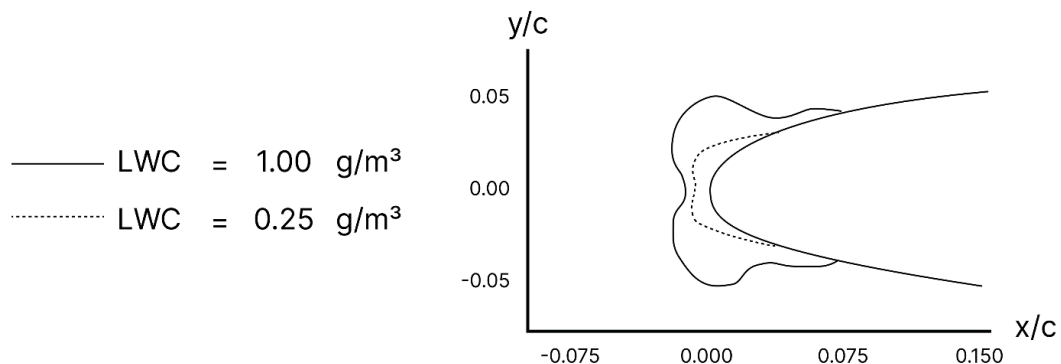
Figure 12: LWC on Airfoil [33]

2.4.3   Droplet Diameter (MVD)

The MVD is a term used to describe the size of water droplets present in the surrounding air. It is also a determining factor in the severity and type of icing, as it affects the droplet collection efficiency. When the droplet size increases, the kinetic energy of the impacting droplets also increases, resulting in a higher collection efficiency.

Droplet size is commonly measured in microns, with cloud droplets typically ranging from 2 to 50 μm in diameter. Droplets larger than approximately 100 μm tend to fall from the clouds as precipitation. In cloud formations, MVDs are generally less than 35 μm. Droplets smaller than 15 μm are so tiny that they are carried around aircraft surfaces by convection, and the minimal ice accretion that occurs does not significantly contribute to overall buildup. Consequently, droplets smaller than 15 μm are not considered in the Federal Aviation Regulations (FARs) [37].

Figure 13 illustrates the shape of icing accumulation for various MVD sizes. As the particle sizes increase, the likelihood of droplet impingement also increases.
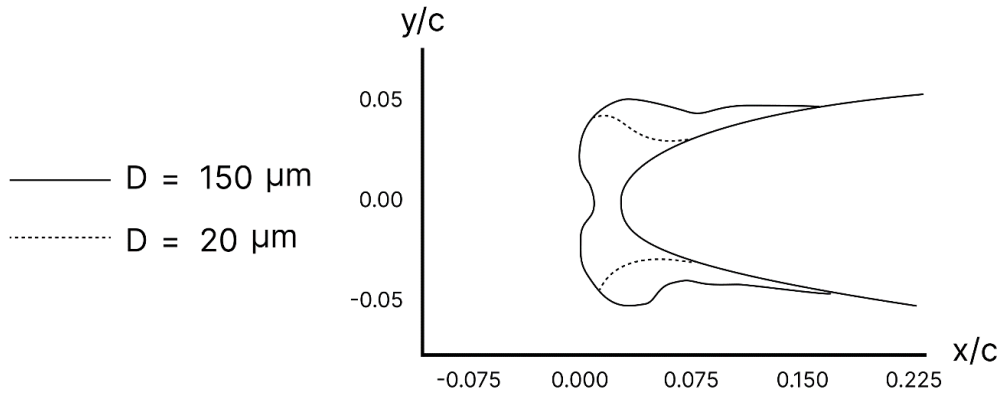
Figure 13: MVD Effect on Airfoil Icing [38]

2.4.4   Temperature

The ambient temperature plays a significant role in determining the type and severity of ice formation. Temperature serves as a measure of the thermal condition of the surrounding air. Hence higher temperatures correspond to greater thermal energy, enabling the air to hold more water vapor. Conversely, as the temperature decreases, water vapor condenses and precipitates out of the air. For SLD droplets, the outside air temperature range for ice formation spans from freezing to a minimum of -40°C. At -40°C, nearly all water is converted into ice crystals, resulting in a very low risk of structural icing. It is worth noting that as the temperature approaches 0°C, the phenomenon of runback, which refers to the movement of liquid water along the aircraft surface, becomes more pronounced. Consequently, the predictability of icing events diminishes. This decrease in predictability arises from the fact that during actual flight near freezing temperatures, minor local fluctuations can either increase or decrease the local energy, thereby altering the likelihood of freezing. Figure 14 provides a visual representation of the shape and characteristics of ice accumulation under different ambient temperature conditions.

○ AIRSPEED 209 km/hr LWC 1.3 g/m³ TIME 8 min.

TOTAL
TEMPERATURE -26°C -20°C -16°C -15°C -12°C -8°C -5°C -2°C -1°C 0°C

□ AIRSPEED 338 km/hr LWC 1.05 g/m³ TIME 6.2 min.

TOTAL
TEMPERATURE -26°C -17°C -12°C -8°C -2°C 0°C
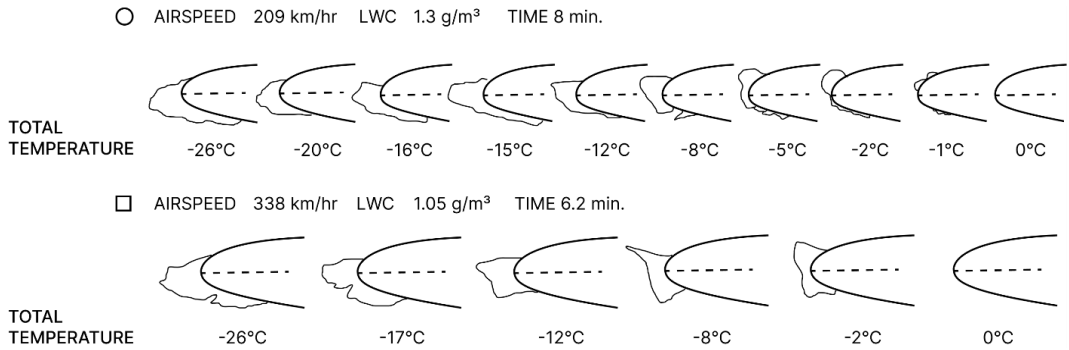
Figure 14: Temperature Effects on Airfoil Icing [33].

2.4.5   Velocity of Air

As the velocity of the air increases, the kinetic energy of the droplets also increases, resulting in a greater impingement. Consequently, as the speed of the air increases, the droplet collection efficiency level increases. Figure 15 illustrates the relationship between the collection efficiency of icing accumulation and different airspeed values. However, it should be noted that increasing the airspeed also leads to aerodynamic heating, which in turn raises the surface temperature and may potentially reduce ice accretion.
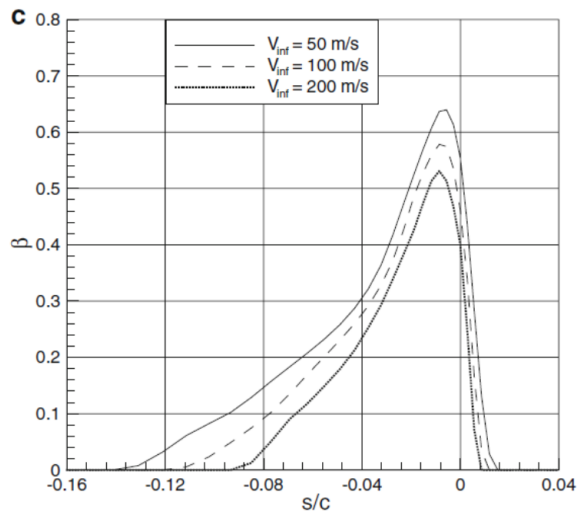
Figure 15: Velocity Effects on Airfoil Icing [38].

2.4.6 Exposure Time

The accumulation of ice is observed to increase with longer exposure times, specifically in relation to LWC. This is because the total amount of ice accretion is influenced by the increasing number of droplets that come into contact with the surface over time. The exposure time can also be influenced by the horizontal extent and airspeed of the aircraft. It is important to note that conditions with greater horizontal extent of clouds can result in higher levels of ice accretion. Also, as shown in the Table 5 and Figure 9, as the exposure time increases, the severity of the icing is increases.

2.4.7 Size of The Object

Larger aerodynamics components create more aerodynamics forces. Therefore, bigger deviation for the incoming droplets occurs and this causes less impingement that leads to a decrease in collection efficiency levels as it can be seen in Figure 16. Therefore, it can be said that bigger aircraft are less susceptible to icing occurrence.
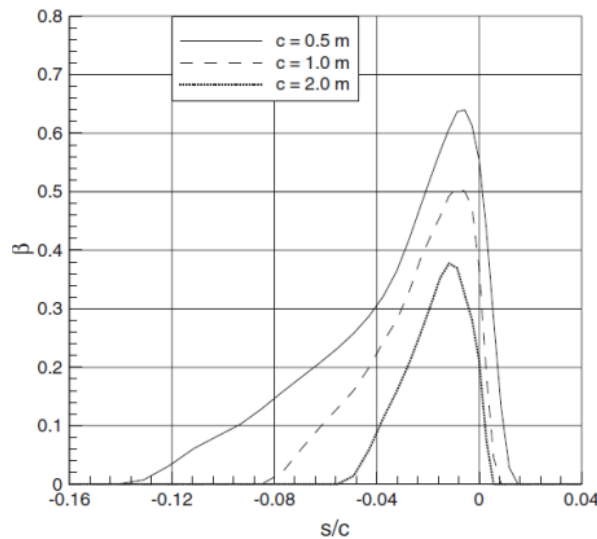
Figure 16: Collection Efficiency Effect on Airfoil Icing [38].

CHAPTER 3

MODELLING AND SCALING

The prediction of atmospheric ice formation, which is one of the critical issues in the field of aviation and has a significant role in many accidents and incidents, can be predicted by numerical methods. Although numerical methods give valuable information about this issue, the accuracy of these methods should be proven by experimental methods.

Icing experimental testing can be done in two different methods,

- Flight test
- Wind tunnel test

The most accurate and reliable testing is the flight test. However, this testing method is too expensive and risky to run, and besides, it is hard to replicate the exact natural conditions where icing occurs.

When a real-case model is too large for an existing wind tunnel facility and required test conditions exceed the operational limitations of the facility, a scaling method is required to provide scaled ice accretions for the desired test conditions. To ensure test reliability, the scaling method must be corrected for icing conditions prior to experimental wind tunnel testing.

Figure 17: In-flight Icing Test [39]

3.1 Icing Similitude Analysis

3.1.1 Dimensionless Parameters For Similitude

In fluid mechanics, a dimensionless number is a numerical value that describes a physical phenomenon or property of a fluid system in a way that is independent of the size or scale of the system. These numbers are used to predict the behavior of fluid systems under different conditions and to compare the results of different experiments or simulations.

3.1.1.1 Weber Number

The Weber number (We) is a non-dimensional parameter commonly employed in the field of fluid dynamics to investigate fluid flows involving the interface between two dissimilar fluids, particularly multiphase flows characterized by highly curved surfaces. It is named after Moritz Weber (1871-1951). The Weber number serves as an indicator of the relative significance of fluid inertia in relation to surface tension. This parameter proves valuable in the examination of phenomena such as thin film flow, as well as the formation of droplets. It is used to predict the likelihood of droplet formation and other phenomena in sprays and atomization. The Weber number indicates whether the kinetic or the surface tension energy is dominant.

$$We = \frac{\rho * v^2 * l}{\sigma} = \left(\frac{8}{C_D}\right) \frac{\left(\frac{\rho * v^2}{2} * C_D * \pi * \frac{l^2}{4}\right)}{(\pi * l * \sigma)}$$
$$= \frac{Drag\ Force}{Cohesion\ Force} \tag{1}$$

Where,

- C_D is the drag coefficient of the body cross-section.
- ρ is the density of the fluid (kg/m^3).
- v is its velocity (m/s).
- l is its characteristic length, typically the droplet diameter (m).
- σ is the surface tension (N/m).

In the field of aircraft icing, the Weber number plays a significant role in understanding the dynamics of interaction between supercooled water droplets and the aircraft surface. The behavior of these droplets upon impingement on the aircraft is greatly influenced by the Weber number. At higher values of the Weber number, the inertial effects can cause larger droplets to break upon impact, resulting in a different freezing pattern compared to single, unbroken droplets. This differential behavior, governed by the Weber number, also determines the type of ice formation. When droplets freeze rapidly upon impingement, rime ice forms, which is characterized by a rough and opaque structure. On the other hand, when droplets spread out before freezing due to greater inertial forces, glaze ice forms, which is a clear and glossy ice layer. The significance of the Weber number cannot be overstated, particularly due to its direct implications for aircraft performance and safety. Ice formations have the potential to alter aerodynamic properties, thereby affecting lift, drag, and overall control. Furthermore, studies have shown that maintaining the same Weber number in scaling analysis leads to successful prediction of icing, further highlighting the importance of the Weber number as a crucial parameter in understanding the physics of icing [40].

3.1.1.2 Nusselt Number

The Nusselt number is a dimensionless parameter that is used to predict the rate of heat transfer in convective heat transfer systems. It is defined as the ratio of the convective heat transfer coefficient to the conductive heat transfer coefficient and is used to predict the efficiency of heat transfer in systems involving fluid flow.

The Nusselt number is defined as:

$$Nu = \frac{hL}{k} \tag{2}$$

where:

- Nu is the Nusselt number.
- h is the convective heat transfer coefficient.
- L is a characteristic length, such as the diameter of a pipe or the height of a wall.
- k is the thermal conductivity of the fluid or solid.

The Nusselt number is used to predict the heat transfer rate in a wide range of applications, including the design of heat exchangers, boilers, and other heat transfer systems, the prediction of heat transfer in internal and external flows, and the analysis of heat transfer in porous media. It is an important parameter in the analysis and design of heat transfer systems and is widely used in engineering and scientific research.

The value of the Nusselt number depends on the specific conditions and geometry of the system and can be calculated using analytical or numerical methods. It is often used in conjunction with other dimensionless parameters, such as the Prandtl number and the Reynolds number, to predict the heat transfer rate in complex systems.

3.1.1.3　Prandtl Number

The Prandtl number is a dimensionless quantity that is used to describe the ratio of momentum diffusivity to thermal diffusivity in a fluid. It is often denoted by the symbol "Pr" and is defined as:

$$Pr = \frac{(viscosity \ * \ specific\ heat\ capacity)}{(thermal\ conductivity)} \tag{3}$$

$$Pr = \frac{c_p * \mu}{k} = \frac{momentum\ diffusivity}{thermal\ diffusivity} \tag{4}$$

Where:

- Pr is the Prandtl number.
- μ is the dynamic viscosity of the fluid $(Pa \cdot s \ = \ N \cdot s/m^2)$
- c_p is the specific heat capacity of the fluid at constant pressure $(J/(kg \cdot K))$
- k is the thermal conductivity of the fluid $(W/(m \cdot K))$

The Prandtl number is used to predict the behavior of fluids in various applications, such as heat transfer, fluid flow, and convection. It is particularly useful in the study of fluid dynamics, as it allows engineers and scientists to predict the behavior of fluids under different conditions.

For example, a high Prandtl number indicates that the momentum diffusivity is dominant, while a low Prandtl number indicates that the thermal diffusivity is dominant. The Prandtl number is also used to predict the behavior of turbulent flow, as it can affect the rate at which momentum and heat are transported in the fluid.

In general, the Prandtl number is an important parameter in fluid dynamics and is used to predict the behavior of fluids in a variety of applications.

3.1.2 Similitude Analysis Parameters

In order to simulate the model geometry in icing tests and achieve similarity in ice accretion conditions, it is imperative to scale the test geometry, flow field, droplet trajectory, total water capture, and heat transfer to simulate the desired icing encounter. Studies about icing similitude parameters and scaling studies have been investigated since the 1970's starting with deriving closed form equations that could be resolved for the model test conditions. For icing similarity and scaling studies, the calculations of the physical phenomena that cause aerodynamic icing formation are performed. The physical and thermal analyses are discussed in detail below. Further simplifications or derivations should be made if the solution requires a programmed numerical solution. The following similarities which can be seen in Figure 18 are defined by Anderson, D.N. [10].

Droplet Trajectory Similarity: Collection Efficiency, β_0	• Evaluate the possibility of water droplet impinging on the monitoring location
Water Catch Similarty: Accumulation parameter, A_c	• Evaluate normalized maximum local ice thickness
Energy balance Similarity: Freezing Fraction, n_0	• Evaluate how much of the impinged water is going to freeze upon impact
Geometry Similarity:	• Outer contour of the model geometry should be identical
Flow Field Similarity:	• Reynolds and Mach number should be matched
Surface water dynamics similarity: Weber number, We	• Evaluate surface running water behaviour

Figure 18: Similitude Parameters Definitions [41]

3.1.2.1 Geometric Similarity

Before any simulation parameters, the outer mold line of the scaled geometry must be equivalent to the reference (real model) geometry to ensure aerodynamic flow

similarity. This is a prerequisite for simulating the physics of icing in both cases. As ice accumulates on the test model, the accumulation shape of the ice must conform to the aerodynamic model's contour. So, the flow field similarity should be maintained.
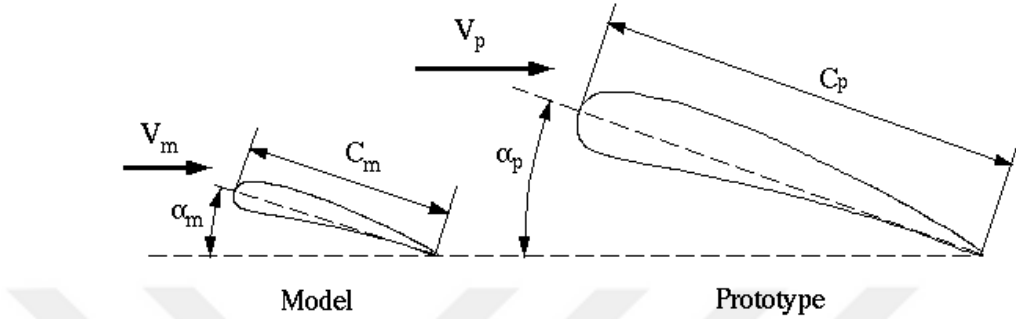
Figure 19: Geometric Similarity [42]

3.1.2.2   Flow Field Similarity

Not only for the icing wind tunnel experiments, but also, normal type wind tunnel experiments requires the matching of the Reynolds Number and Mach Number for reference and scaled conditions. This furnishes flight condition similitude.

In the following equations, the subscript a indicates that it represents air for the term in which it is used.

$$Re_a = \frac{V * L * \rho_a}{\mu_a} \tag{5}$$

$$M = \frac{V}{\sqrt{\gamma * R_a * T}} \tag{6}$$

For most of the cases regarding wind tunnel tests, characteristic length is taken as chord length; however, in this case, characteristic length is taken as leading-edge diameter of the airfoil because ice accumulation occurs in the region around the leading edge. So that, L is the airfoil leading edge radius in Equation 5, air density and viscosity can be calculated as follows,

$$\rho_a = \frac{P_{st}}{R_a * T_{st}} \qquad (7)$$

$$\mu_a = \frac{10^{-4}}{0.12764 + 124.38/T_{st}} \frac{g}{cm * s} \qquad (8)$$

Icing happens in the atmosphere in a specific range of psychrometric values of the ambient air. Therefore, matching Mach and Reynolds number together is hard to achieve simultaneously. When performing geometric similarity calculations, Reynolds and Mach numbers are ignored. Because of the conditions under which icing occurs, the Mach number is usually low so compressibility effects can be ignored, and the boundary layer is initially thin and viscous effects are negligible at the leading edge of the airfoil so the Reynolds number effect can also be neglected.

However, the flow field simulation needs to comply with the velocity, pressure, and temperature distributions for the scaled model, even though Reynolds and Mach numbers are not matched. Nevertheless, there is a condition that must be met for the flow to be considered as similar. If the Mach number and Reynolds number are in the $M_{Re=2x10^5} < M < M_{critical}$ range near the stagnation region, the flow field simulation is considered to be achieved at least for icing studies [11].

3.1.2.3   Droplet Trajectory Similarity

Similarity must be ensured as water droplets impinge the scaled and reference geometry. Furthermore, it is necessary to ensure that the impingement zones of the droplets and their trajectories are matched in order to accurately determine the specific impingement zone of the model. In order to achieve similitude in drop trajectory, it is imperative to ensure a harmonious match between the modified inertia parameter and the collection efficiency [10].

$$\left.\frac{C_D Re_{rel}}{24}\right)_S = \left.\frac{C_D Re_{rel}}{24}\right)_R \qquad (9)$$

Where Re_{rel} is Reynolds number of droplet calculated using droplet velocity relative to freestream velocity.

In order to satisfy the similitude condition for the droplet trajectory, modified inertia parameter (K_0) for both cases should be matched as it can be seen in Equation 10.

$$K_S = K_R \tag{10}$$

In addition, the Langmuir and Blodgett expression is used to calculate the modified inertia parameter, as shown in Equation 11 [43].

$$K_0 = \frac{1}{8} + \frac{\lambda}{\lambda_{Stokes}}\left(K - \frac{1}{8}\right) \quad for \ K > \frac{1}{8} \tag{11}$$

In the following equation, K is the non-dimensional inertia parameter defined by Langmuir and Blodgett [43].

$$K = \frac{\rho_w * \delta^2 * V}{18 * L * \mu_a} \tag{12}$$

where ρ_w is density of water and $\rho_w = 1 g/cm^3$

The ratio λ/λ_{stokes} is defined as [10]:

$$\frac{\lambda}{\lambda_{stokes}} = \frac{1}{0.8388 + 0.001483Re_\delta + 0.1847\sqrt{Re_\delta}}$$

$$or \tag{13}$$

$$= \frac{1}{Re_\delta}\int_0^{Re_\delta} \frac{24}{C_D * Re_{ref}} dRe_{ref}$$

where the Reynolds number for the droplet is defined as in Equation 14, where the δ term denotes the median volume diameter.

$$Re_\delta = \frac{V * \delta * \rho_a}{\mu_a} \tag{14}$$

Modified inertial parameters should be matched for both scaled case and reference case in order to gather similitude for droplet trajectory.

$$K_{0,S} = K_{0,R} \tag{15}$$

And it should be noted that, if a modified inertia parameter is lower than 1/8, impingement would not occur. Therefore, these calculations are only valid for K greater than 1/8.

3.1.2.4   Water catch Similarity.

The amount of ice accreted relies on the amount of water striking the surface. Water catch parameters should be matched in order to ensure ice accretion similitude. The freezing fraction concept, n, is introduced by Messinger et al [44]. For particular conditions, there is no local freezing of water. For that case, the n parameter is equal to zero. Otherwise, if all water droplets freeze on impact n parameter should be equal to 1. Also, if water droplets freeze partially upon impact, $0 < n < 1$. In the following calculation, n parameter is taken as 1 so that following equation is obtained.

In the following equation, n is taken as one:

$$\frac{d\Delta}{d\tau} = \frac{\dot{m}}{\rho_i} \tag{16}$$

The total mass of water impinging in a unit area per unit time is given as in Equation 17 where the LWC is liquid water content and β is the droplet collection efficiency.

$$\dot{m} = LWC * V * \beta \tag{17}$$

Integration of total mass equation over the accretion time for ice thickness is shown in Equation 18 and τ is the exposure time.

$$\Delta = \frac{LWC * V * \beta}{\rho_i} * \tau \tag{18}$$

The following equality should be established for water catch similarity:

$$\left.\frac{\Delta}{d}\right)_S = \left.\frac{\Delta}{d}\right)_R$$

$$\left.\frac{LWC * V * \beta * \tau}{\rho_i * d}\right)_S = \left.\frac{LWC * V * \beta * \tau}{\rho_i * d}\right)_R \qquad (19)$$

Additionally, the accumulation parameter, which is defined as follows should be matched for both reference and scaled conditions as can be seen in equation 21

$$A_c = \frac{LWC * V * \tau}{\rho_i * d} \qquad (20)$$

$$A_{c,S} = A_{c,R} \qquad (21)$$

For both cases if it is not possible to match the K_0 or β_0 parameters on the model., therefore in order to ensure matching both cases following equation must be followed.

$$\beta_{0,S} * A_{c,S} = \beta_{0,R} * A_{c,R} \qquad (22)$$

Where β_0 (collection efficiency at the stagnation point) is defined as follows [43]:

$$\beta_0 = \frac{1.40 * \left(K_0 - \frac{1}{8}\right)^{0.84}}{1 + 1.40 * \left(K_0 - \frac{1}{8}\right)^{0.84}} \qquad (23)$$

3.1.2.5   Energy Balance Similarity

Ice accretion occurs when the supercooled droplets strike the aircraft surface and freeze instantly (rime ice), or a fraction of them freezes upon impact, and the rest

freezes downstream (glaze ice). For the first case, the formation of rime ice, no similarity in the energy balance is required since all water freezes upon impingement. However, energy balance must be established for glaze ice conditions. These relevant terms are defined below and defined for the stagnation line. The energy balance of freezing is illustrated in Figure 20 to facilitate a better understanding of the physics involved.
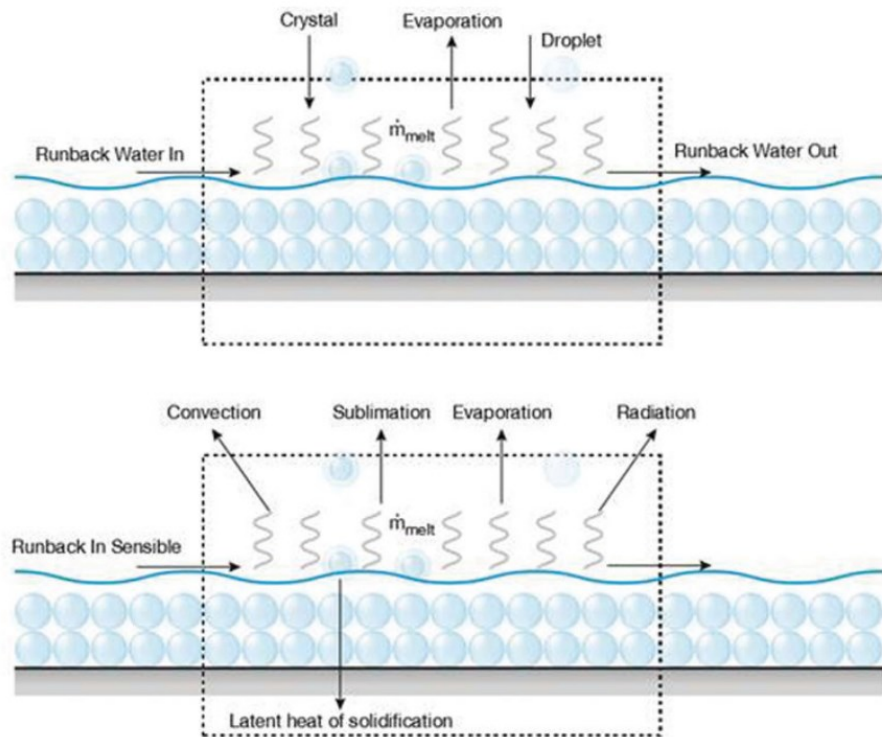
Figure 20: Mass and Energy Balance Diagram [45]

Heat dissipation from the surface by convection through the boundary layer [46]:

$$Q_c = h_c * (T_{sur} - T_a) \qquad (24)$$

Heat lost from the surface due to evaporation of water [10]:

$$Q_e = \dot{m}_e * \Lambda_v \qquad (25)$$

Heat lost from the surface due to sublimation of ice [10]:

$$Q_s = \dot{m}_s * \Lambda_s \qquad (26)$$

Where parameter Λ represents latent heat of vaporization or sublimation, and the subscripts v, s are used to denote vaporisation and sublimation, respectively.

Heat is lost from the surface due to radiation [10].

$$Q_r = \sigma * \varepsilon * (T_{sur}^4 - T_{st}^4) \tag{27}$$

Heat is dissipated from the surface to increase the temperature of the impinging liquid to the freezing point [10].

$$Q_w = \dot{m} * c_{pw} * (T_f - T_{st}) \tag{28}$$

Heat is dissipated from the surface by water flowing out of the control volume to a neighboring location [10]:

$$Q_{in} = [(1 - n) * \dot{m} - \dot{m}_e] * c_{pw} * (T_{sur} - T_f) \tag{29}$$

Heat conducted from ice to model [10]:

$$Q_{cond} = \frac{k_i * \Delta}{\xi * l} \left(T_{sur} - T_{st} - \frac{r * V^2}{2 * c_{p,a}} \right) \tag{30}$$

Heat is gained from the surface because of releasing the latent heat of fusion from the freezing water [10]:

$$Q_f = \dot{m} * n_0 * \Lambda_f \tag{31}$$

Heat is gained from the surface due to the release of sensible heat from the ice when cooling from the freezing temperature to the surface temperature [10]:

$$Q_i = \dot{m} * n_0 * c_{p,i} * (T_f - T_{sur}) \tag{32}$$

Heat gained from the kinetic energy of the water drops striking the surface [10]:

$$Q_k = \dot{m}(\frac{V^2}{2}) \tag{33}$$

Table 7: Energy Balance Components

1	Convective Heat Transfer	Q_c	
2	Evaporation	Q_e	
3	Sublimation	Q_s	Negligible
4	Radiation	Q_r	Negligible
5	Sensible Heat of Water	Q_w	
6	Conduction	Q_{cond}	Negligible
7	Runback	Q_{in}	Zero on stagnation line
8	Sensible Heat of Ice	Q_i	Discard for glaze ice; surface temperature is equal to freezing temperature.
9	Latent Heat of Fusion	Q_f	Only valid for rime ice
10	Drop Kinetic Energy	Q_k	
11	Water inflow		Zero on stagnation line

As clearly stated in Table 7, some of the components of the energy balance parameter cancel out due to its physical conditions. When the surface temperature converges to a point, heat transfer becomes zero. Therefore, the energy balance can be stated as follows [46].

$$Q_c + Q_e + Q_w = Q_f + Q_k \tag{34}$$

The above equation can be stated as follows.

$$
h_c \left(T_{sur} - T_{st} - \frac{V^2}{2c_{p,a}} \right) + h_G \left(\frac{\frac{p_{ww}}{T_{st}} - \frac{p_{tot}}{T_{tot}} * \frac{p_w}{p_{st}}}{\frac{1}{0.622} * \frac{p_{tot}}{T_{tot}} - \frac{p_{ww}}{T_{st}}} \right) \Lambda_v
$$
$$
+ \dot{m} c_{p,ws} (T_f - T_{st})
$$
$$
= \dot{m} n_0 \Lambda_f + \frac{\dot{m} V^2}{2} \tag{35}
$$

Where the p_{tot} is total pressure, p_w is vapour pressure and p_{ww} is vapour pressure of water.

The above equation has compressibility terms; in order to use this equation in incompressibility form, the energy equation is rearranged as follows.

$$h_c\left(T_{sur} - T_{st} - \frac{V^2}{2c_{p,a}}\right) + h_G\left(\frac{p_{ww} - p_w}{p_{st}}\right)\Lambda_v + \dot{m}c_{p,ws}\left(T_f - T_{st}\right)$$
$$= \dot{m}n_0\Lambda_f + \frac{\dot{m}V^2}{2} \tag{36}$$

Tribus et al. introduced the new dimensionless parameter b, named relative heat factor [47].

$$b = \frac{\dot{m} * c_{p,ws}}{h_c} = \frac{LWC * V * \beta_0 * c_{p,ws}}{h_c} \tag{37}$$

Two additional parameters frequently employed for the sake of convenience are temperature-based quantities, denoted as ϕ and θ. These parameters pertain to the transfer of energy between droplets and the surrounding air, respectively.

$$\phi = T_f - T_{st} - \frac{V^2}{2c_{p,ws}} \tag{38}$$

$$\theta = T_{sur} - T_{st} - \frac{V^2}{2c_{p,a}} + \frac{h_G}{h_c}\left(\frac{\frac{p_{ww}}{T_{st}} - \frac{p_{tot}}{T_{tot}} * \frac{p_w}{p_{st}}}{\frac{1}{0.622} * \frac{p_{tot}}{T_{tot}} - \frac{p_{ww}}{T_{st}}}\right)\Lambda_v \tag{39}$$

The low-speed form of the above equation is as follows,

$$\theta = T_{sur} - T_{st} - \frac{V^2}{2c_{p,a}} + \frac{h_G}{h_c}\left(\frac{p_{ww} - p_w}{p_{st}}\right)\Lambda_v \tag{40}$$

The energy balance, Equation 41, can be rearranged with parameters b, ϕ and θ. Then, the glaze ice energy balance becomes:

$$n_0 = \left(\frac{c_{p,ws}}{\Lambda_f}\right)\left(\phi + \frac{\theta}{b}\right) \tag{41}$$

Parameter n_0 should be matched for each case in order to yield ice accretion (freezing physics) similitude.

$$n_{0,S} = n_{0,R} \tag{42}$$

This representation of the freezing fraction incorporates simplifications and assessments that are specifically applicable to the stagnation line. Additionally, Equation 41 is only valid for a clean airfoil. It should be noted that as ice accumulates, the freezing fraction at the stagnation point is likely to vary due to the continuous alteration of the geometry.

3.1.2.6   Surface Water Dynamics Similarity

In order to achieve surface water dynamic similarity, Weber numbers should be matched for the reference and scaled geometries by considering water film presence for glaze ice conditions.

$$We_L = \frac{V^2 L \rho_a}{\sigma_{w/a}} \tag{43}$$

where $\sigma_{w/a}$ is surface tension between water and air with respect to water.

When the calculations of Weber's number for the scaled and reference cases are equalized and the terms that have the same value for both cases are discarded, by utilizing Equation 43, the equation 44 is obtained. The ratio of the velocities for both cases is inversely proportional to the square root of the leading-edge diameters.

$$V_S = V_R \left(\frac{d_R}{d_S}\right)^{\frac{1}{2}} \tag{44}$$

where the V_S, V_R are freestream velocities and d_S, d_R are leading edge diameters for scaled and reference geometries respectively.

3.2   Scaling Methods

Scaling methods are techniques used to reproduce the behavior of a full-scale aircraft in a wind tunnel at a reduced scale. This is necessary because it is often impractical or impossible to test a full-scale aircraft in a wind tunnel due to size or cost constraints. Scaling methods allow engineers to test smaller models of aircraft and extrapolate the results to predict the behavior of the full-scale aircraft.

There are several approaches to scaling methods in icing wind tunnels. One approach is to use geometric scaling, in which the dimensions of the aircraft model are scaled down in proportion to the size of the full-scale aircraft. For example, if the full-scale aircraft is twice the size of the model, the model would be scaled down by a factor of two in each dimension. This approach is based on the principle of similitude, which states that the behavior of a system is independent of size as long as the ratios of the relevant dimensions are maintained.

Another approach is to use dynamic scaling, where the model's dimensions are scaled down in proportion to the size of the full-scale aircraft. However, the model's mass and inertia are scaled up to maintain the same dynamic behavior as the full-scale aircraft. This approach is based on the principle of dynamic similitude, which states that the behavior of a system is independent of size as long as the ratios of the relevant dimensions, mass, and inertia are maintained.

Scaling methods in icing wind tunnels should take into account the effects of ice on the aircraft performance. Scaling can be challenging, as the behavior of ice on an aircraft's surfaces is highly dependent on the size and shape of the aircraft, as well as the temperature and humidity conditions. Engineers must carefully consider these factors when selecting a scaling method and applying it to test results.

Overall, scaling methods are essential in designing and testing aircraft in icing wind tunnels. They allow engineers to test smaller models and predict the behavior of full-scale aircraft under real icing conditions, which helps ensure flight safety and performance in real-world operations.

Previous studies have used various strategies to create a scaled ice shape that matches the reference ice shape. The simulation of geometry, flow field, droplet trajectory, water catch, energy balance, and surface water dynamics are mentioned in the literature in the context of scaling analysis of ice. The similitudes of the former are fulfilled by calculating scaling parameters for each similitude parameter and comparing them for scaled and reference situations. Defining the scaling factors and determining their strength and significance have proven challenging.

Nevertheless, following the procedure of the scaling study is only possible with a good understanding of the physics and calculations of similitude calculations. Scaling will start by solving a set of equations of the previously mentioned similitude parameters of the scaled and reference values to determine the scaled case. For the tests using a sea level wind tunnel, 5 test conditions need to be determined. These are temperature, air speed, MVD, LWC and exposure time. For pressure adjustable wind tunnels the number of parameters is 6, with the addition of pressure. In addition to these parameters, there are two parameters that are important to match but are not possible for icing conditions as mentioned in previous explanations, namely Reynolds number and Mach number. After these operations, droplet trajectory and water catch values are matched after keeping the external geometry of the model and AOA values the same. The remaining unmatched values are calculated by solving the energy balance equations.

Therefore, several icing scaling factors have been recommended based on the selected similitude parameters, and various combinations of these values have been used in scaling methods to generate similar ice accumulations. Those that have been selected for this study are,

- K_0; Modified inertia parameter,
- A_c; Accumulation parameter,
- β_0; collection efficiency,
- n_0; freezing fraction
- b; relative heat factor,
- ϕ; droplet energy transfer parameter

- θ; air energy transfer parameter,
- We_L; similitude of surface water dynamics.
- h_{film}/d; water film thickness.

When these six of nine parameters are matched geometry, flow field, energy balance, flow field, water catch, droplet trajectory, and surface-water dynamics are equivalent, which ensures similitude [48].

Most of the scaling methods and their researchers are mentioned in the literature review part of this study. However, one of the most important and reliable works has been selected in order to be utilized in the developed computer code in this thesis. Table 8 summarizes which parameters to be matched for specific works.

Table 8: Ice Scaling Literature Comparison [10]

	K_0	A_c	n_0	b	ϕ	θ	We_L
Hauger et al.	✓	✓					
Sibley et al.	✓	✓	✓	✓			
Jackson et al.	✓	✓	✓	✓			
Dodson et al.	✓	✓					
Armand et al.	✓	✓	✓	✓	✓	✓	
Ruff Sea Level Wind Tunnel	✓	✓	✓		✓	✓	✓
Ruff /with altitude capability	✓	✓	✓	✓	✓	✓	✓

3.3   Scaling Methods for Test Conditions

The most straightforward scaling method is LWC scaling and especially fulfills water-catch similarity [49]. For this application, scaled model dimensions, temperature, pressure, airspeed, and drop size are matched to the reference values. For the scaled case, model size and angle of attack should be same by reference geometry. When the scaled and reference numbers for the accumulation parameter

are correlated and constants revoked, the product of the liquid-water content emerges as follows:

$$LWC_S * \tau_S = LWC_R * \tau_R \qquad (45)$$

The user selects the scaled LWC, and the scaled accretion time can be determined from the equation. It is assumed that the leading-edge heat balance is fulfilled by adjusting the static temperature. K_0, which is the modified inertia parameter is matched through the model geometry, velocity, cloud drop size, and ambient pressure. The effect of liquid water content on the heat balance is neglected. Hence, this method is not sufficient for icing scaling as it does not take into account the heat balance [49].

The Olsen method is a method for predicting the formation of ice on aircraft surfaces during flight. It was developed by Dr. Earl Olsen in the 1950s and is based on the temperature and humidity conditions in the atmosphere. To use the Olsen method, one needs to know the ambient temperature, relative humidity, and wind speed at the altitude where the aircraft will be flying. [5]. Also, Olsen and Newton suggested refining the $'LWC \times \tau = constant'$ method. the scaled LWC is selected, while keeping chord length, velocity, MVD constant. Since model size, airspeed, and MVD size are not varied, $K_{0,S} = K_{0,R}$. Icing time for the scaled condition is found from equation $A_{c,S} = A_{c,R}$. But, in this method, the freezing fraction must be matched rather than static temperature. However, it has been discovered subsequently that when the size is scaled, there is a discrepancy between the scaled and reference velocity if surface water phenomena are accurately simulated. This approach is effective only when the scaled and the reference model dimensions are the same, due to the aforementioned factors.

Ruff's second method closely resembles the Olsen method. Nevertheless, his experimentation revealed that the replication of the glaze horns in terms of size and placement was insufficient. Consequently, it is determined that this particular approach is limited to simulating the ice type rather than its shape [11].

3.4   Scaling Methods for Model Size

Due to the nature of the wind tunnel, the test section's size is an important constraint for experimental testing. Unfortunately, real case sizes cannot be tested in the wind tunnel. Thus, real case models should be scaled down to the restriction of the facility under some conditions. These scaling rules applies for the test conditions which subscale model will produce the ice accumulation similar to real case model. Different models have been investigated over the years.

The Swedish-Soviet Working Group on Aircraft Safety proposed a method for scaling aircraft size that is primarily based on matching similarity parameters K_0 and A_c and test conditions t_{st} and LWC. The user specifies the scaled model size and air velocity. With model size and velocity given, the drop size can be determined by matching scale and reference K_0, and, with LWC_S and V_S known, icing time can be found by matching A_c. In the event that the scale and reference velocities are identical, the freezing fractions will match for both conditions as well. However, it should be noted that this method fails to acknowledge the significance of the freezing fraction, except in this particular scenario. Additionally, it has been established that velocity exerts a substantial influence on the shape of ice, thereby rendering arbitrary selection of velocity impractical.

The ONERA technique [8], [9] was developed for wind tunnels where temperature and pressure are not controlled. In the incompressible energy balance equation, the stagnation pressure and stagnation temperature are measured and substituted in the test unit inside the test facility. K_0 and A_c parameters with energy parameters n_0 and b should matched .The droplet size is calculated by matching the modified inertia coefficient, and the LWC is calculated by matching the relative thermal coefficient. In this technique, the scaling speed is generally lower than the speed before scaling, and improvement is needed in the direction of calculating by matching the Weber number [10] .

Among all aforementioned extensive scaling studies, the Modified Ruff Method (AEDC) differs from the others by matching the Weber number [11]. This particular method demonstrates superior alignment between the scale and reference ice shapes

in comparison to alternative methods. Consequently, this scaling technique is favored for the present dissertation and will be expounded upon extensively in a dedicated section.

3.4.1 Modified Ruff Method (AEDC)

The Modified Ruff method is a method for predicting the behavior of a full-scale aircraft based on testing a reduced-scale model in an icing wind tunnel. The method is based on the principle of similitude, which states that the behavior of a system is independent of size as long as the ratios of the relevant dimensions are maintained [11].

Modified Ruff Method is similitude analysis derivation of scaling method. Ruff Method is matching Weber number (surface tension) by adding surface water dynamics. For ice accretion similitude, the droplet trajectory similarity, the similarity of the total mass of liquid water impingement of the surface, the energy balance similarity, and surface-water dynamics similarity should be satisfied after the geometry and flow similarity are achieved. To provide that, modified inertia parameter (K_0), accumulation efficiency (β_0), accumulation parameter (A_C), freezing rate (n_0), and droplet energy transfer parameter(ϕ) and Weber number (We) are to be matched [50].
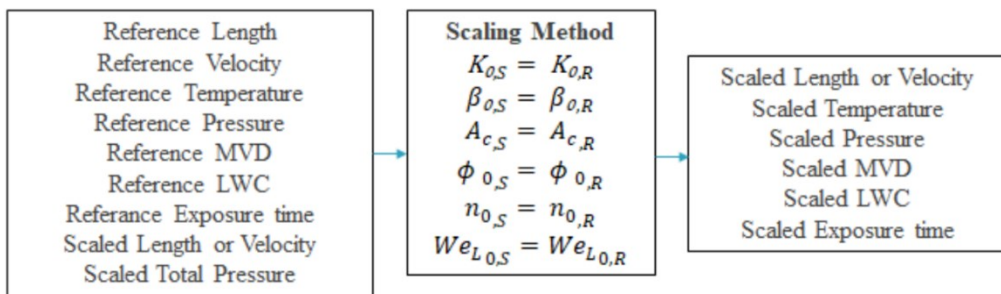
Figure 21: Modified Ruff Method Procedure [51]

The Modified Ruff method differentiated with constant We_L approach is suggested to compute velocity and for obtaining reference ice shape with a scaled size model which is the method employed in this dissertation. This method requires adjustment

of energy balance, water catch, surface water dynamics, the droplet trajectory as well as modelling of the nondimensional geometry and angle of attack. The scaling parameters to be matched are selected as K_0, A_c, n_0, b , ϕ and θ, We_L for tunnels with altitude capability or K_0, A_c, n_0, We_L and one of ϕ and θ for atmospheric tunnels. These findings are to be expected, as previous research has not demonstrated any independent influence of ϕ or θ on the shape of ice, apart from the freezing fraction. Therefore, it is likely that the scaled temperature can be selected arbitrarily, with the LWC determined by matching the scaled and reference values of n_0. This assertion is supported by experimental evidence presented by Anderson et al. [52].

Table 9: Modified Ruff Method Test and Similitude Parameters

Test Parameter	Modified Ruff Method
c_S	User Select
$t_{st,S}$	$\phi_S = \phi_R$
V_S	User Selects or $V_S = V_R \left(\dfrac{d_R}{d_S}\right)^{\frac{1}{2}}$
MVD_S	$K_{0,S} = K_{0,R}$
LWC_S	$n_{0,S} = n_{0,R}$
τ_S	$A_{c,S} = A_{c,R}$
$p_{st,S}$	User Selects or $\theta_S = \theta_R$

The Modified Ruff Method with a constant We_L is implemented using in house developed computer code. The test and scaling parameters are computed with respect to reference condition. To achieve size scaling, a specific scaled chord length is determined. By equating the We_L values for the reference and scaled cases, the scaled velocity can be obtained using equation 46.

$$V_S = V_R \left(\frac{d_R}{d_S}\right)^{\frac{1}{2}} \tag{46}$$

After determining the scaled velocity, the calculation of the T_{st} can be performed by equating the reference and scaled ϕ values, as described in equation 47.

$$\phi_S = T_f - T_{st,S} - \frac{V_S^2}{2c_{p,ws}} \tag{47}$$

In order to acquire the static temperature and airflow velocity, as well as the scaled Mach number, it is necessary to measure these parameters. Additionally, the total temperature and other associated terms can be determined through appropriate calculations.

MVD values for the scaled conditions can be determined by utilizing the results obtained from previous calculations.

$$K_0 = \frac{1}{8} + \frac{\lambda}{\lambda_{Stokes}}\left(K - \frac{1}{8}\right) \quad for \ K > \frac{1}{8} \tag{48}$$

In order to determine the MVD value, it is necessary to solve the following equations. However, due to their interdependence, they are solved iteratively within an inner loop. In this particular solution, a comprehensive non-linear generalized reduced gradient (GRG) method solver was employed, and the modified inertia parameter matching by optimizing multiple dependent parameters was carried out with minimal deviation.

$$\frac{\lambda}{\lambda_{stokes}} = \frac{1}{0.8388 + 0.001483Re_\delta + 0.1847\sqrt{Re_\delta}} \tag{49}$$

$$K = \frac{\rho_w \delta^2 V}{18L\mu_a} \tag{50}$$

The determination of the LWC for the scaled case, can be achieved by matching the scaled and reference freezing fraction, n_0. Similar to the solution for median volumetric diameter, an iterative approach is necessary.

$$n_0 = \left(\frac{c_{p,ws}}{\Lambda_f}\right)\left(\phi + \frac{\theta}{b}\right) \tag{51}$$

$$c_{p,ws} = 1.0074 \frac{cal}{gK} + 8.29 * \frac{10^{-5}cal}{gK^3} * (T_s - 273.15K)^2 \qquad (52)$$

According to Pruppacher and Klett, the energy released during the process of water freezing is referred to as latent heat is formulated as in equation 53.

$$\Lambda_f = 79.7 \frac{cal}{h} + 0.485 \frac{cal}{gK} * (T - 273.15K) -$$

$$2.5 * 10^{-3} \frac{cal}{gK^2} * (T - 273.15K)^2 \qquad (53)$$

ϕ value has been calculated in Equation 47, remaining parameter formulations are given in following equations. In order to calculate the θ, it is required to solve following equation. However, h_G, h_c, p_w, p_{ww} and Λ_v need to be calculated, which are defined as gas phase heat transfer coefficient, convective heat transfer coefficient, vapor pressure of water over ice, vapor pressure of water over liquid and latent heat of vaporization respectively.

$$\theta = T_s - T_{st} - \frac{V^2}{2c_{p,a}} + \frac{h_G}{h_c} \left(\frac{\frac{p_{ww}}{T_{st}} - \frac{p_{tot}}{T_{tot}} * \frac{p_w}{p_{st}}}{\frac{1}{0.622} * \frac{p_{tot}}{T_{tot}} - \frac{p_{ww}}{T_{st}}} \right) \Lambda_v \qquad (54)$$

$C_{p,a}$ is defined as constant pressure specific heat of air.

$$C_{p,a} = 1008 \ J * kg^{-1} * K^{-1} \qquad (55)$$

h_G is gas phase heat transfer coefficient and in order to compute this parameter, Prandtl number and Schmidt number of air should be calculated, and their formulas are given in equations 57 and 58.

$$h_G = \frac{h_c}{c_{p,a}} * \left(\frac{Pr_a}{Sc_a} \right)^{0.67} \qquad (56)$$

$$Pr_a = \frac{c_{p,a} * \mu_a}{k_a} \tag{57}$$

$$Sc_a = \frac{\mu_a}{\rho_a * D_v} \tag{58}$$

The relationship between the viscosity of air and temperature can be determined by referring to the comprehensive research report published by the National Institute of Standards and Technology (NIST) [53]. Within the temperature range of -40°F to 40°F, the data obtained from this study were fitted to the following mathematical expression:

$$\mu_a = \frac{10^{-4}}{0.12764 + 124.38/T_{st}} \tag{59}$$

Thermal conductivity data is taken from works of NIST [53]. These data are fitted into the following formulation at 14.5 psia and temperature range of -40 to 40 Fahrenheit degree.

$$k_a = \left[-12.69 + 2.029 * \sqrt{T_{film}}\right] * 1.2 * 10^{-3} \tag{60}$$

The expression provided by Pruppacher et al. [54] describes the diffusivity of water vapor in air.

$$D_v = 0.211 \frac{cm^2}{s} * \left(\frac{T_{film}}{273.15\ K}\right)^{1.94} * \left(\frac{1.0132 * 10^5 Pa}{p_{st}}\right) \tag{61}$$

$$h_c = \frac{k_a * Nu_a}{d} \tag{62}$$

$$Nu_a = 1.14 * Pr_a^{0.4} * Re_a^{0.5} \tag{63}$$

Pruppacher and Klett derived a regression equation to fit the curve of the saturation pressure of vapor over water within the temperature range of -50°C to 0°C [54]. It should be noted that this equation is also applicable for estimating the vapor pressure over ice (p_{ww}).

$$p_w = a_0 + \Delta T(a_1 + \Delta T(a_3 + \Delta T(a_4 + \Delta T(a_5 + \Delta T * a_6))$$

$$a_0 = 610.78 \; Pa$$
$$a_1 = 44.365 \; Pa/K$$
$$a_2 = 1.4289 \; Pa/K^2$$
$$a_3 = 2.6506 * 10^{-2} \; Pa/K^3 \tag{64}$$
$$a_4 = 3.0312 * 10^{-4} \; Pa/K^4$$
$$a_5 = 3.0341 * 10^{-6} \; Pa/K^5$$
$$a_6 = 6.1369 * 10^{-9} \; Pa/K^6$$

Pruppacher and Klett provide the following equation to represent the latent heat of vaporization [54].

$$\Lambda_v = 597.3 * \left(\frac{273.15K}{T}\right)^E \frac{cal}{g} \tag{65}$$

In addition, it should be noted that the exponent E is dependent on temperature as well and expressed in the following equation.

$$E = 0.167 + 3.670 * 10^{-4} * T \tag{66}$$

Tribus et al. introduced a dimensionless parameter denoted as b, which is commonly referred to as the relative heat factor [47].

$$b = \frac{LWC * V * \beta_0 * c_{p,ws}}{h_c} \tag{67}$$

Where the β_0 (collection efficiency at the stagnation point) is defined as follows [43]:

$$\beta_0 = \frac{1.40 \left(K_0 - \frac{1}{8}\right)^{0.84}}{1 + 1.40 \left(K_0 - \frac{1}{8}\right)^{0.84}} \tag{68}$$

In Equation 51, all the necessary terms for calculation are provided in Equations 52 to 68, excluding the term LWC. The LWC is determined through a non-linear GRG solver process, allowing the solver to converge towards a calculated value by changing and fitting the depended parameters for optimal value. Once this is achieved, all scaling parameters are computed, thereby completing the scaling process. The resulting calculations for an example scenario are displayed in the table provided below.

Table 10: Scaling of a Test Conditions

	Chord (m)	T_{st} (°C)	T_{tot} (°C)	V_∞ (m/s)
Ref	0.530	-27.8	-26.12	58.10
Scaled	0.265	-28.2	-24.84	82.17
Change.	½	-1.4%	-4.9%	41.4%
	MVD (μm)	LWC (g/m³)	t_{exp} (s)	P_{tot} (kPa)
Ref	30.00	0.90	480.0	97921
Scaled	17.08	1.03	148.5	100000
Change.	43.1%	14.2%	69%	2.1%

Table 11: Scaling of Similarity Parameters

	K_0	β_0	A_c	n_0	b
Ref	3.398	0.791	1.633	1.326	**0.46**
Scaled	3.398	0.791	1.633	1.326	**0.44**
Change	0.0%	0.0%	0.0%	0.0%	**3.9%**
	ϕ (K)	θ (K)	Re_a	We_L	Mach
Ref	27.4	**35.6**	83811	8.70E+05	0.185
Scaled	27.4	**34.2**	59272	8.70E+05	0.262
Change	0.0%	**3.9%**	29.3%	0.0%	41.5%

Table 12: Scaling of Test Conditions with b and θ match

	$Chord$ (m)	T_{st} (°C)	T_{tot} (°C)	V_∞ (m/s)
Ref	0.530	-27.80	-26.12	58.10
Scaled	0.265	-28.20	-24.84	82.17
Change	1/2	-1.4%	-4.9%	41.4%
	MVD (µm)	LWC (g/m³)	t_{exp} (s)	P_{tot} (kPa)
Ref	30.00	1.30	480.00	97921
Scaled	16.54	1.44	152.96	87206
Change	44.9%	10.9%	68.1%	10.9%

Table 13: Scaling of Similarity Parameters with b and θ match

	K_0	β_0	A_c	n_0	b
Ref	3.398	0.791	2.358	1.025	0.662
Scaled	3.398	0.791	2.358	1.025	0.662
Change	0.0%	0.0%	0.0%	0.0%	0.0%
	ϕ (K)	θ (K)	Re_a	We_L	$Mach$
Ref	27.40	35.564	83811	8.70E+05	0.185
Scaled	27.40	35.564	51688	8.70E+05	0.262
Change	0.0%	0.0%	38.3%	0.0%	41.5%

The findings of the model scaling calculations are presented in Table 10 and Table 11. It is evident from Table 11 that all similarity parameters match, with the exception of the b and θ terms. As observed in the data presented in Table 12 and

Table 13, the matching of b and θ values has been successfully achieved but requiring altitude capability in the wind tunnel. However, the discrepancy in these values has been previously addressed in this dissertation that b and θ have infinitesimal effect on final ice accumulation. Consequently, it was determined that the wind tunnel to be constructed for this study should not incorporate an altitude control capability in order to optimize cost efficiency. Furthermore, the Modified Ruff method demonstrates satisfactory outcomes for this particular type of tunnel.

3.5   Icing Prediction

The in-house icing prediction code (AEROMSICE-2D) operates within a series of calculations and solving a physical state at each step. The calculations comprises, flow field, determining droplet trajectories and collection efficiencies, conducting thermodynamic analysis, and modeling ice accretion, consecutively.

3.5.1   Flow Field Solution

The in-house ice accretion prediction code uses the Hess-Smith panel method [55] in conjunction with a boundary layer solver. This code also calculates the flow velocities and pressure distributions on the airfoil, necessary to calculate the trajectories of the droplets. In addition, boundary layer calculations are performed, and heat transfer coefficients are obtained.

To explain this method in more detail, the airfoil is divided into a certain number (N) of line segments called panels. Each panel in the system is linked to a specific source and vortex singularity element. The source singularity strength remains constant for each panel, while the vortex singularity strength remains constant across all panels. The presence of N sources and a single vortex singularity strength introduces N+1 unknowns. These unknowns are determined by applying the flow tangency boundary condition at the collocation points, which correspond to the centers of the panels. The Kutta condition is then utilized to provide the necessary equation for the closure of the system.

Once the singularity strengths are known, the velocity potential can be established, and the components of the airflow at any location in the flow field, including the boundaries of the wing, can be calculated. Furthermore, the distribution of convective heat transfer around the wing is determined through the utilization of the integral boundary layer method, which involves the calculation of the inviscid velocity distribution obtained from the panel method. Further details are available in reference [56].

3.5.2   Droplet Trajectory

Droplet trajectories are calculated using the Lagrangian approach. These calculations are performed for droplets with 500 microns or smaller diameter under the following assumptions:

- Droplets are assumed to be spherical.
- Droplets do not affect the flow field.
- The only forces acting on the droplets are gravity and aerodynamic drag.
- Heat and mass transfer (evaporation) between the droplet and flow are neglected.
- The temperature of the droplets is the same as the temperature of the flow.

Governing equations for the 2-D droplet trajectories are as follows, [56]:

$$m\ddot{x}_p = -D\cos(\gamma) \tag{69}$$

$$m\ddot{y}_p = -D\sin(\gamma) + mg \tag{70}$$

$$\gamma = \tan^{-1}\frac{\dot{y}_p - V_y}{\dot{x}_p - V_x} \tag{71}$$

$$D = \frac{1}{2}\rho V^2 C_D A_p \tag{72}$$

$$V = \sqrt{\left(\dot{x}_p - V_x\right)^2 + \left(\dot{y}_p - V_y\right)^2} \tag{73}$$

where V_x, V_y are components of flow velocity, $\dot{x}_p$, $\dot{y}_p$, $\ddot{x}_p$, $\ddot{y}_p$ are droplet velocity and components of acceleration, respectively. A_p represents cross-sectional area of

the droplets, and C_D is the droplet drag coefficient. An empirical drug formulation is used to calculate the droplet drag coefficients [56]:

$$C_D = \frac{24}{Re}(1 + 0.197Re^{0.63} + 2.6x10^{-4}Re^{1.38}) \qquad Re_d \leq 3500 \qquad (74)$$

$$C_D = \frac{24}{Re}(1.699x10^{-5}Re^{1.92}) \qquad\qquad Re_d > 3500 \qquad (75)$$

The Reynolds number used in the calculation above is determined by utilizing the droplet Reynolds number.

Anderson et al, defines the β term as the local catch efficiency, or collection efficiency. This term can be defined by ratio of the projection of a stream tube (Δy_0) from the undisturbed flow upstream of the model to the model surface at the location of interest (Δs) and is formulated in Equation 65 can be visualized in Figure 22 [10].

$$\beta = \frac{\Delta y_0}{\Delta s} \qquad\qquad (76)$$
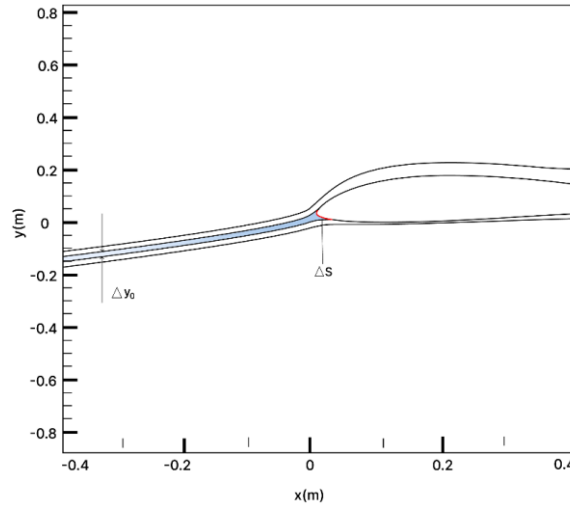
Figure 22: Collection Efficiency

3.5.3 Thermodynamic Analysis

The ice prediction method utilizes an Integral Boundary Layer Method to compute the convective heat transfer coefficients over the 2D geometry. Moreover, this approach facilitates the precise calculation of the characteristics of both laminar and turbulent boundary layers. Moreover, in the context of this icing prediction code, the Thwaites formulation is employed to analyze the boundary layer conditions for laminar boundary layer for the roughness Reynolds number lower than 600, while the Kays & Crawford formulation is applied for turbulent boundary layer conditions for the roughness Reynolds number greater than 600 [56].

3.5.4 Ice Accretion Modelling

Extended Messinger model could be utilized in order to yield ice accretion on the model. Phase change also known as the Stefan problem, is the foundation for ice formation. The governing equations for the phase change problem consist of the energy equations in the ice and water layers, the mass conservation equation, and the phase change condition at the ice/water interface [57].

The ice and water layers conservation of energy equations [56],

$$\frac{\partial T}{\partial t} = \frac{k_i}{\rho_i C_{pi}} \frac{\partial^2 T}{\partial y^2} \tag{77}$$

$$\frac{\partial \theta}{\partial t} = \frac{k_w}{\rho_w C_{pw}} \frac{\partial^2 \theta}{\partial y^2} \tag{78}$$

The conservation of mass equations for ice and water layers [56],

$$\rho_i \frac{\partial B}{\partial t} + \rho_w \frac{\partial h}{\partial t} = \rho_a \beta V_\infty + \dot{m}_{in} - \dot{m}_{e,s} \tag{79}$$

Ice-water phase change [56],

$$\rho_i L_F \frac{\partial B}{\partial t} = k_i \frac{\partial T}{\partial y} - k_w \frac{\partial \theta}{\partial y} \tag{80}$$

In Equations 77-78, θ, and T are the temperatures, k_i and k_w are thermal conductions, C_{pi} and C_{pw} are specific heats and B and h are the thicknesses of ice

and water layers [56]. Boundary conditions associated with these equations are as follows:

In this approach ice assumed to be in complete contact with the surface of the model, thereby ice having the same temperature as the ambient air temperature, T_a in this study [58]:

$$T(0, t) = T_s = T_a \tag{81}$$

The temperature is equal to the freezing temperature at the ice/water boundary [58]:

$$T(B, t) = \theta(B, t) = T_f \tag{82}$$

At the air/water (glaze ice) or air/ice (rime ice) interface, the heat flux is governed by various factors including convection (Q_c), radiation (Q_r), latent heat release (Q_l), cooling caused by incoming droplets (Q_d), heat carried by runback water (Q_{in}), evaporation (Q_e), sublimation (Q_s), aerodynamic heating (Q_a), and the kinetic energy of incoming droplets (Q_k) which are shown in Equation 83 and 84 [56].

$$Glaze\ ice{:}\ -k_w \frac{\partial \theta}{\partial y}$$
$$= (Q_c + Q_e + Q_d + Q_r) - (Q_a + Q_k + Q_{in}) \tag{83}$$
$$at\ y = B + h$$

$$Rime\ ice{:}\ -k_i \frac{\partial T}{\partial y}$$
$$= (Q_c + Q_s + Q_d + Q_r) - (Q_a + Q_k + Q_{in} + Q_l) \tag{84}$$
$$at\ y = B$$

The wing surface assumed to be completely clean at initial time.

$$B = h = 0, \ \ t = 0 \tag{85}$$

These equations are solved for rime ice and glaze ice using the numerical method defined in reference [56].

For rime ice growth.

$$B(t) = \frac{\rho_a * \beta * V_\infty + \dot{m}_{in} - \dot{m}_s}{\rho_r} * t \qquad (86)$$

The spatial distribution of temperature within the rime ice layer is of interest.

$$T(y) = T_s + \frac{(Q_a + Q_k + Q_{in} + Q_l) - (Q_c + Q_d + Q_s + Q_r)}{k_i} * y \qquad (87)$$

Ice growth equation for glaze ice,

$$\rho_i L_F \frac{\partial B}{\partial t} = k_i \frac{\partial (T_f - T_s)}{B} \\ + k_w \frac{(Q_c + Q_e + Q_d + Q_r) - (Q_a + Q_k + Q_{in})}{k_w} \qquad (88)$$

In the context of the upper surface of the airfoil, it is postulated that the water remains unfrozen and flows back to the adjacent downstream cell. Conversely, for the lower surface, all water is shed [59]. The thickness of the glaze ice is determined by numerically integrating equation 53 using the Runge-Kutta-Fehlberg method.

Ice layer temperature distribution

$$T(y) = \frac{T_f - T_s}{B} + T_s \qquad (89)$$

Temperature distribution within the water layer

$$\theta(y) = T_f + \frac{(Q_a + Q_k + Q_{in}) - (Q_c + Q_e + Q_d + Q_r)}{k_w} * (y - B) \qquad (90)$$

Threshold ice thickness where the transition from rime ice to glaze ice occurs.

$$B_g \\ = \frac{k_i(T_f - T_s)}{(\rho_a * \beta * V_\infty + \dot{m}_{in} - \dot{m}_e) * L_F + (Q_a + Q_k + Q_{in}) - (Q_c + Q_e + Q_d)} \qquad (91)$$

In the context of glaze ice formation, B_g represents the critical thickness of rime ice at which the initial formation of glaze ice occurs. Correspondingly, t_g denotes the time at which this glaze ice formation takes place.

$$t_g = \frac{\rho_r}{(\rho_a * \beta * V_\infty + \dot{m}_{in} - \dot{m}_s)} * B_g \qquad (92)$$

3.5.5   Langmuir Distribution Modification

One of the essential assumptions in all these sizing processes is to take the particle size as the particle size that is most abundant in the cloud environment. The actual droplet size distribution in clouds is conventionally represented by a simple variable which is the droplet MVD. When the actual size distributions of these particles are included in the calculations, it is possible to obtain results with higher accuracy. For this reason, the distributions were discretized, taking into account the CFR Part 25 Appendix C icing conditions [2]. Most commonly used droplet size distribution model is the Langmuir D, used for Appendix C conditions [26], [43]. An MVD=20-micron cloud 7-bin weight average and cumulative weight representation of the Langmuir D distributions are shown in Table 14.

Table 14: Langmuir D Distribution

index	d_i x MVD	Cumulative Mass (%)	Weight (%)
1	6.200	3%	5%
2	10.400	10%	10%
3	14.200	25%	20%
4	20.000	50%	30%
5	27.400	75%	20%
6	34.800	90%	10%
7	44.440	98%	5%

As can be seen in Figure 23, the probability of the size of the droplets in the cloud is used as a value in the weighted average calculation of collection efficiency in Equation 93 by using percentage values represented in Table 14. Equation 93 represents the overall droplet collection efficiency of the droplet size distribution by taking the contributions of the individual droplet sizes proportional to their weights in the distribution.
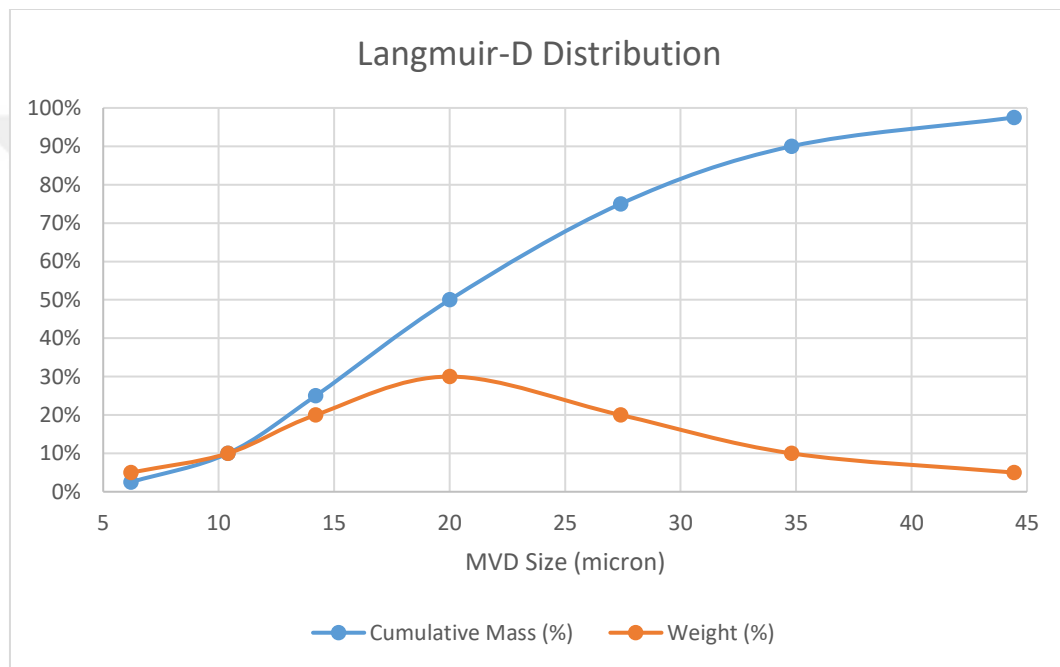
Figure 23: Langmuir-D for 20 Microns Droplet Size

$$\beta = 0.05 * \beta_1 + 0.1 * \beta_2 + 0.2 * \beta_3 + 0.3 * \beta_4 + 0.2 * \beta_5 + 0.1 * \beta_6 + 0.05 * \beta_7 \tag{93}$$

As clearly seen in Figure 24, the application of the Langmuir D distribution for the Case 27, increases the collection efficiency with the arrival of particles with larger diameters within the impingement zone of the particles, especially in the regions at close to the impingement limits at the top and bottom of the airfoil, while the maximum collection efficiency value remains almost unchanged.
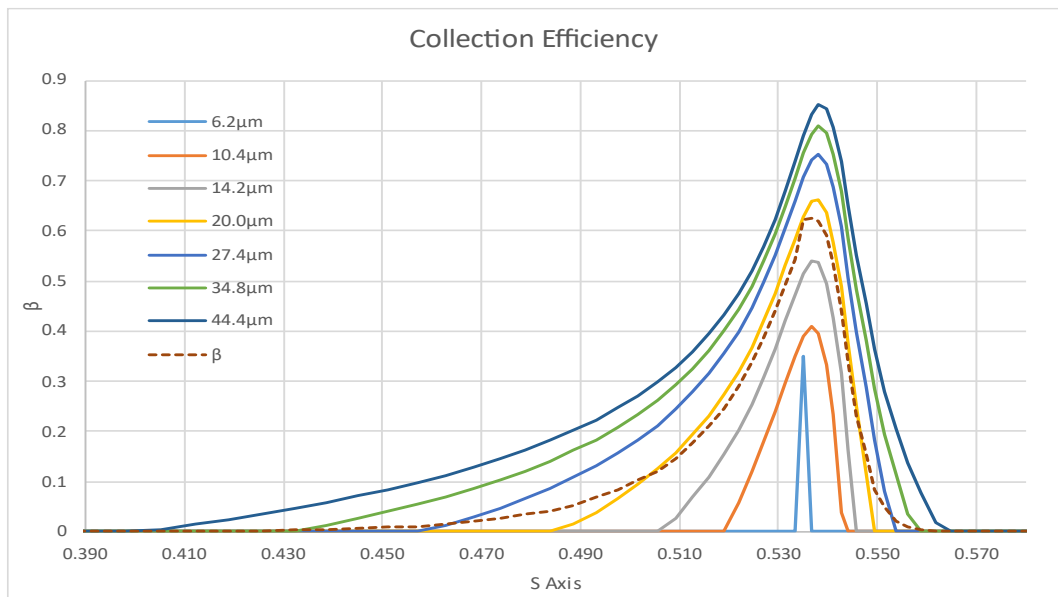
Figure 24: Langmuir D Implementation

Comparing the overall β distribution with the β distribution of a single droplet distribution (MVD=20 micron for this case) in Figure 24 highlights the effect of the distribution with brown dashed line and yellow line in comparison.

3.6 Case Study

3.6.1 Ice Prediction Analyses

In order to validate the icing software and the similitude model described above, six test cases were selected exhibiting sufficient variation in the icing parameters and also have experimental ice shape data. Modelling and scaling were performed to determine the limits of the numerical approach.

The test cases shown in Table 15 are well-known test cases widely used by researchers [60]. These cases were first solved and then downscaled. In some cases, upscaling was also attempted, because the reference geometry is already very small. The variation of the parameters presented by these cases provide valuable information for validation.

Table 15: Experimental Case Values [60]

| Figure | Airfoil | Chord | A.O.A. | Velocity | Static (Total) Temperature |
Cases	NACA	m.	Degrees	m/s	^0C
27	0012	0.530	4.0	58.10	-27.8 (-26.0)
28	0012	0.530	4.0	58.10	-19.8 (-18.0)
29	0012	0.530	4.0	58.10	-13.9 (-12.0)
30	0012	0.530	4.0	58.10	-6.7 (-5.0)
31	0012	0.530	4.0	58.10	-3.9 (-2.0)
35	0012	0.530	4.0	93.89	-12.2 (-8.0)

| Figure | Pressure | Humidity | LWC | MVD | Exposure Time |
Cases	kPa	RH %	g/m^3	Microns	Seconds
27	95.61	100.0	1.30	20.0	480.0
28	95.61	100.0	1.30	20.0	480.0
29	95.61	100.0	1.30	20.0	480.0
30	95.61	100.0	1.30	20.0	480.0
31	95.61	100.0	1.30	20.0	480.0
35	92.06	100.0	1.05	20.0	372.0

The aim of scaling these cases is to yield the exact icing contours in scaled conditions as in the reference conditions. However, the numerical scaling approach can perform satisfactorily only in some conditions. Therefore, these cases with different conditions were studied to comprehend the scaling method's limits.

3.6.1.1   Case 27

Reference and scaling conditions for case 27 are stated in Table 16 and Table 17. In this case, the temperature and velocity are low, suggesting incompressible flow and a typical rime ice condition.

Table 16: Physical Conditions for Case 27 [60]

Case	Type	NACA	AOA deg.	Chord (m)	T_{st} (°C)	T_{tot} (°C)	V (m/s)
27	Ref	0012	4	0.530	-27.8	-26.12	58.10
27	Scaled	0012	4	0.265	-28.20	-24.84	82.17

Case	Type	NACA	MVD (µm)	LWC (g/m³)	t_{exp} (s)	P_{tot} (kPa)	P_{st} (kPa)
27	Ref	0012	20.00	1.30	480	97921	95610
27	Scaled	0012	11.44	1.49	147	100000	95342

Table 17: Similitude Parameters for Case 27

Case	Type	K_0	β_0	A_c	n_0	b
27	Ref	1.807	0.684	2.358	1.129	0.572
27	Scaled	1.807	0.684	2.358	1.129	0.553

Case	Type	φ (K)	θ (K)	Reynolds	We_L	Mach
27	Ref	27.4	35.6	83811	869764	0.185
27	Scaled	27.4	34.4	71345	869764	0.262

As can be seen in Table 17, four of six similitude parameters are identically matched, and the remaining two (*b* and *θ*) are fairly well matched. The collection efficiency distributions and ice shapes presented in Figure 25 and Figure 26 show that the similitude approach successfully replicates the reference case. The ice shapes illustrated in Figure 26 show typical rime ice characteristics, with ice shape being generally smooth, following the contours of the airfoil leading edge.
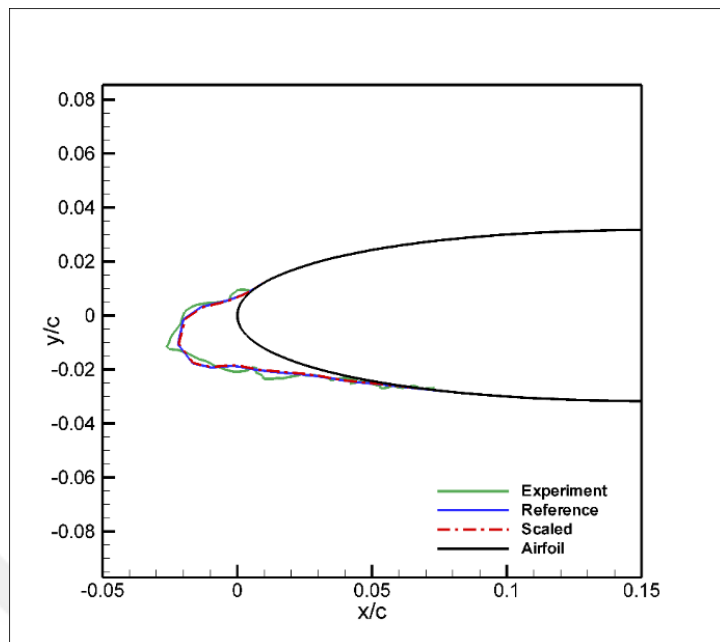
Figure 25: Case 27 Ice Shapes
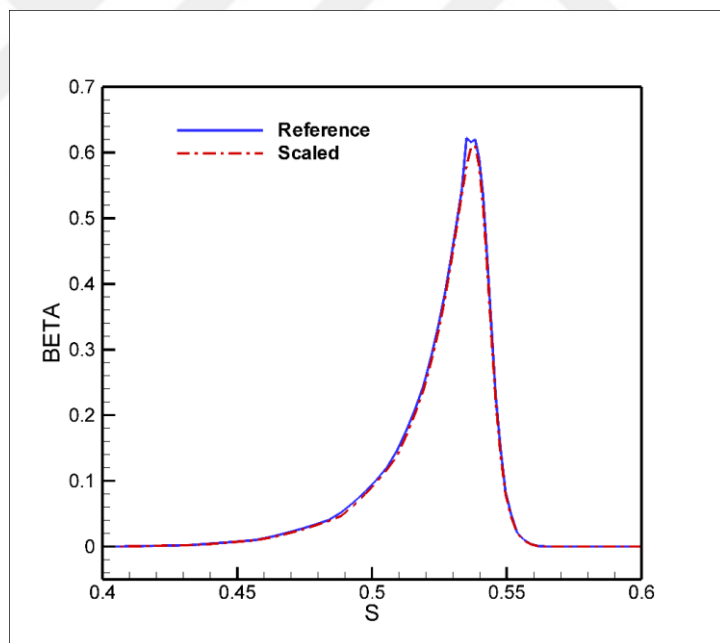
Figure 26: Case 27 Droplet Collection Efficiencies

The selected scaling parameters in Table 16 and Table 17 have been effectively aligned with the intended level of confidence, as evidenced by the findings presented in Figure 25 and Figure 26. The scaling technique has yielded ice shapes that is indistinguishable from the reference case. However, it is important to acknowledge

that the computed ice shape does not exhibit wavy contours present at the upper and lower part of the ice, which is prominently observed in the experimental ice shape but still, experimental ice shapes and ice shape predictions of scaled and reference case are in a good agreement. Besides, it can be easily said that collection efficiencies are in a perfect agreement on reference and scaled cases which can be seen in Figure 26, both in terms of impingement limits and droplet collection efficiency values. This affinity can be interpreted as an indication that the calculations of the scaling analysis work very well.

The computed ice shapes are also in very good agreement with the experimental ice shape. However, this is not a really challenging test case for the numerical method because all the droplets freeze upon impact, establishing energy balance is trivial.

3.6.1.2 Case 28

The reference and scaling conditions for Case 28 are listed in Table 18 and Table 19. In this case, the temperature and velocity are low again suggesting incompressible flow and rime ice conditions. The contour of Case 28 ice shape resembles Case 27 as shown in Figure 27 and droplet collection efficiencies are shown in Figure 28. However, according to the freezing fraction value, it is a mixed ice condition rather than rime ice.

Table 18: Physical Conditions for Case 28 [60]

Case	Type	NACA	AOA deg.	Chord (m)	T_{st} (°C)	T_{tot} (°C)	V (m/s)
28	Ref	0012	4	0.530	-19.80	-18.12	58.10
28	Scaled	0012	4	0.265	-20.20	-16.84	82.17
Case	Type	NACA	MVD (μm)	LWC (g/m³)	t_{exp} (s)	P_{tot} (kPa)	P_{st} (kPa)
28	Ref	0012	20.00	1.30	480	97848	95610
28	Scaled	0012	11.45	1.47	150	100000	95486

Table 19: Similitude Parameters for Case 28

Case	Type	K_0	β_0	A_c	n_0	b
28	Ref	1.799	0.683	2.358	0.828	0.573
28	Scaled	1.799	0.683	2.358	0.828	0.544

		φ (K)	θ (K)	Reynolds	We_L	Mach
28	Ref	19.4	26.4	79099	869764	0.182
28	Scaled	19.4	34.2	71345	869764	0.258
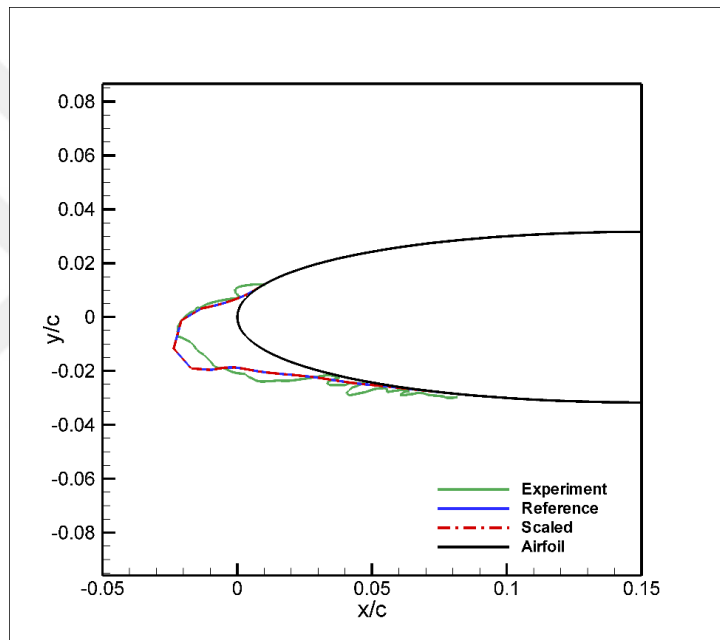
Figure 27: Case 28 Ice Shapes
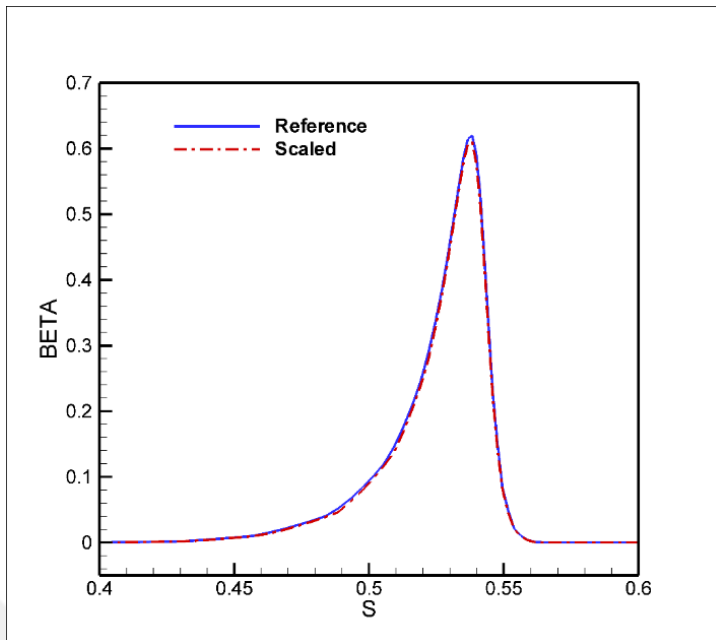
Figure 28: Case 28 Droplet Collection Efficiencies

The chosen scaling parameters have been successfully matched with the desired confidence level, as can be seen in Figure 27. The scaling calculation result is identical for ice shapes of the scaled case compared to the reference case. However, it should be noted that the computed ice shape does not exhibit a horn-like feature that is observed in the experimental ice shape. The experimental ice shape shows mixed ice characteristics, that is not reflected in the computed ice shapes. Although the ice shapes may not exhibit precise conformity, the graph of droplet collection efficiency demonstrate complete overlap, as depicted in Figure 28. This serves as compelling evidence that the scaling calculations have been accurately formulated.

3.6.1.3   Case 29

Reference and scaling conditions for Case 29 are presented in Table 20 and Table 21. In this case, the temperature is higher than in the previous cases, in the mixed ice range, while the velocity is still low, in the incompressible flow range. The freezing fraction of the stagnation point is below the unity; hence glaze ice characteristics are expected.

Table 20: Physical Conditions for Case 29 [60]

Case	Type	NACA	AOA deg.	Chord (m)	T_{st} (°C)	T_{tot} (°C)	V (m/s)
29	Ref	0012	4	0.530	-13.90	-12.22	58.10
29	Scaled	0012	4	0.265	-14.30	-10.94	82.17

Case	Type	NACA	MVD (μm)	LWC (g/m³)	t_{exp} (s)	P_{tot} (kPa)	P_{st} (kPa)
29	Ref	0012	20.00	1.30	480	97796	95610
29	Scaled	0012	11.46	1.44	153	100000	95586

Table 21: Similitude Parameters for Case 29

Case	Type	K_0	β_0	A_c	n_0	b
29	Ref	1.794	0.683	2.358	0.592	0.573
29	Scaled	1.794	0.683	2.358	0.592	0.534

		φ (K)	θ (K)	Reynolds	We_L	Mach
29	Ref	13.5	19.1	75879	869764	0.180
29	Scaled	13.5	34.2	71345	869764	0.255
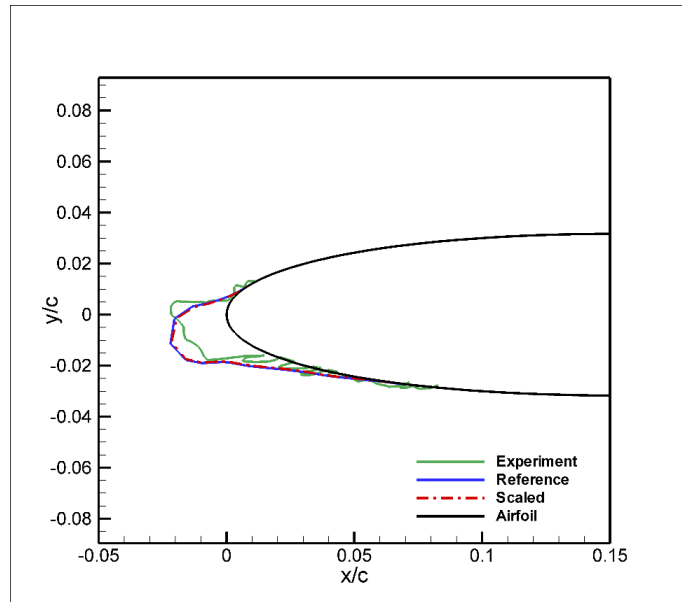
Figure 29: Case 29 Ice Shapes
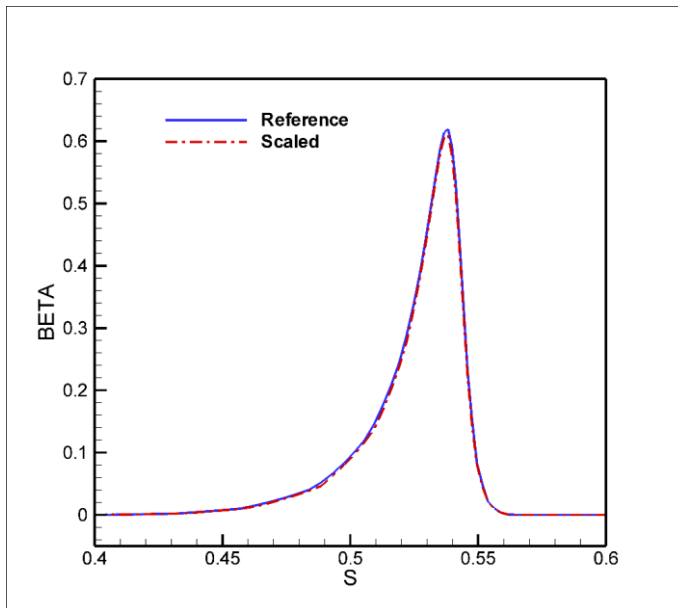
Figure 30: Case 29 Droplet Collection Efficiencies

The chosen scaling parameters were successfully matched with the desired confidence level, as shown in Figure 29 and Figure 30. The scaling method employed predicts identical ice shapes for the scaled case compared to the reference case. For this case, the horn-type ice formations in the experimental data were not evident in the computed ice shape. Furthermore, the droplet collection efficiencies show a high degree of agreement between the reference and scaled cases, as shown in Figure 30. This agreement can be interpreted as evidence of the effectiveness of the scaling analysis approach.

3.6.1.4   Case 30

Reference and scaling conditions for Case 30 are given in Table 22 and Table 23. In this case, the temperature is well within glaze ice range and the velocity is still low enough to be in incompressible flow range. The freezing fraction of the stagnation point is well below unity; hence glaze ice characteristics were indeed observed as shown in Figure 32.

Table 22: Physical Conditions for Case 30 [60]

Case	Type	NACA	AOA deg.	Chord (m)	T_{st} (°C)	T_{tot} (°C)	V (m/s)
30	Ref	0012	4	0.530	-6.70	-5.02	58.10
30	Scaled	0012	4	0.265	-7.10	-3.74	82.17

Case	Type	NACA	MVD (μm)	LWC (g/m³)	t_{exp} (s)	P_{tot} (kPa)	P_{st} (kPa)
30	Ref	0012	20.00	1.30	480	97737	95610
30	Scaled	0012	11.46	1.34	165	100000	95702

Table 23: Similitude Parameters for Case 30

Case	Type	K_0	β_0	A_c	n_0	b
30	Ref	1.787	0.682	2.358	0.280	0.574
30	Scaled	1.787	0.682	2.358	0.280	0.495

		φ (K)	θ (K)	Reynolds	We_L	Mach
30	Ref	6.300	9.10	72206.5	869764	0.178
30	Scaled	6.300	34.2	71345.9	869764	0.251
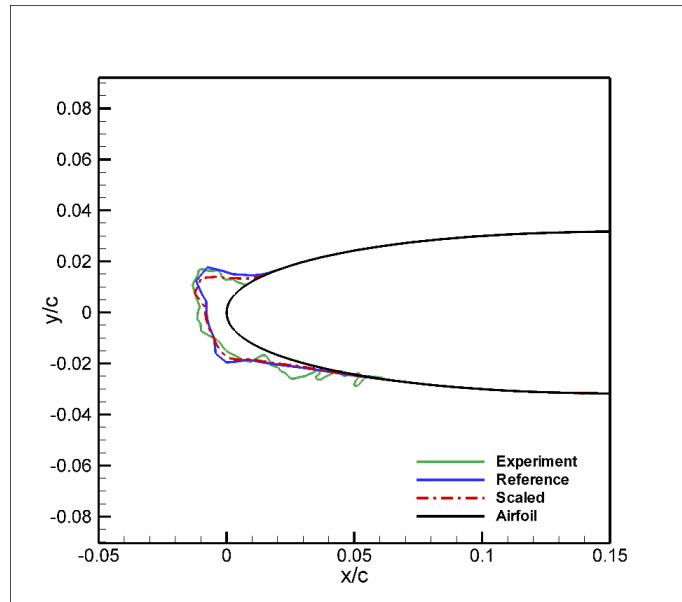
Figure 31: Case 30 Ice Shapes
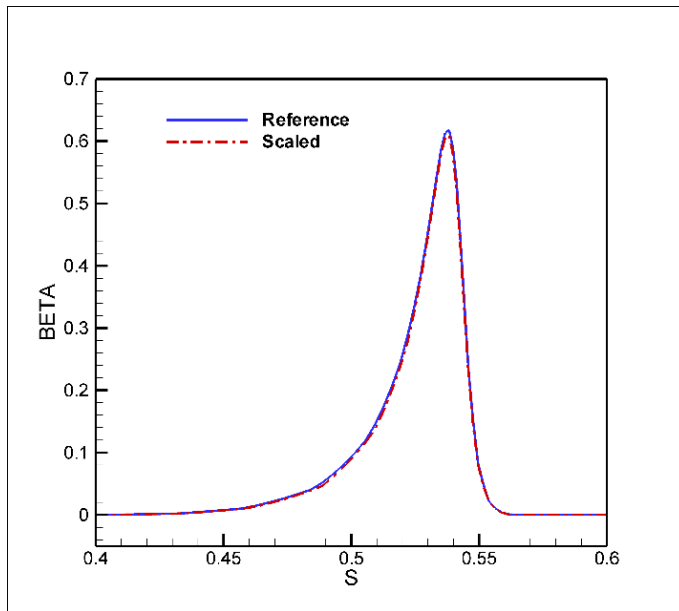
Figure 32: Case 30 Droplet Collection Efficiencies

The selected scaling parameters are successfully matched at the desired confidence level also for this case, as seen in Figure 31. The scaling method predicts the ice shape very closely for the scaled case compared to the reference case, including the prominent horn-like structure at the upper surface. The ice accretion prediction code accurately predicts the experimental ice shape, including the size and location of the above-mentioned horn-like structure. Furthermore, the droplet collection efficiency values also for this particular case exhibit a high level of consistency as shown in Figure 32.

3.6.1.5 Case 31

Reference and scaling conditions for Case 31 are provided and tabulated in Table 24 and Table 25. In this case, the temperature is close to the freezing temperature and velocity is still in incompressible range. The freezing fraction of the stagnation point is much below unity; hence glaze ice characteristics are expected.

Table 24: Physical Conditions for Case 31 [60]

Case	Type	NACA	AOA deg.	Chord (m)	T_{st} (°C)	T_{tot} (°C)	V (m/s)
31	Ref	0012	4	0.530	-3.90	-2.22	58.10
31	Scaled	0012	4	0.265	-4.30	-0.94	82.17

Case	Type	NACA	MVD (µm)	LWC (g/m³)	t_{exp} (s)	P_{tot} (kPa)	P_{st} (kPa)
31	Ref	0012	20.00	1.30	480	97715	95610
31	Scaled	0012	11.47	1.16	191	100000	95745

Table 25: Similitude Parameters for Case 31

Case	Type	K_0	β_0	A_c	n_0	b
31	Ref	1.785	0.682	2.358	0.149	0.574
31	Scaled	1.785	0.682	2.358	0.149	0.428

		φ (K)	θ (K)	Reynolds	We_L	Mach
31	Ref	3.5	4.70	70845	869764	0.177
31	Scaled	3.5	34.2	71345	869764	0.250
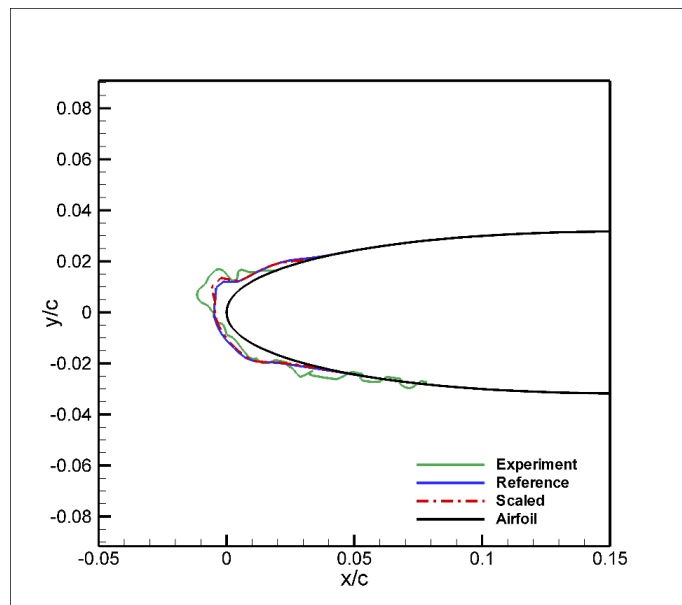
Figure 33: Case 31 Ice Shapes
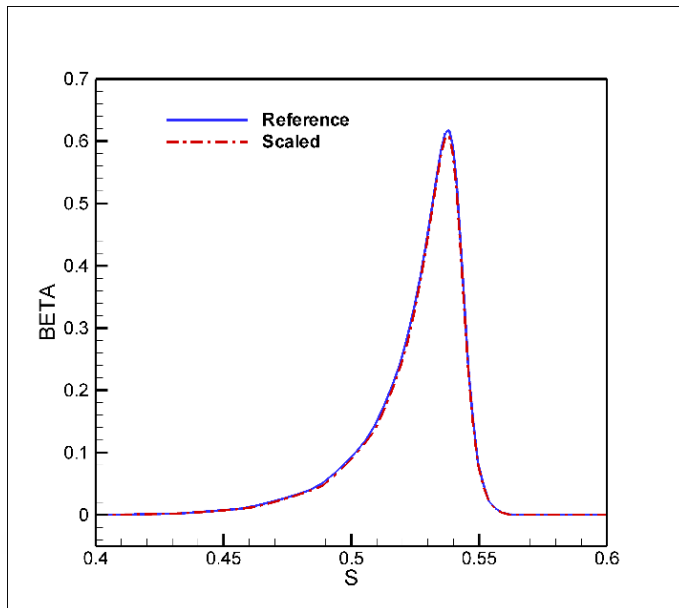
Figure 34: Case 31 Droplet Collection Efficiency

Within the selected scaling parameters, the reference and scaled ice shapes are very close, as seen in Figure 33. As a result of the n_0 value being well below unity, it is possible to say that this icing formation is glaze ice. Although the location of the horn-like structure is well predicted by the calculations, its size is underpredicted compared to the experimental ice shape. It is a known fact that glaze ice predictions usually are worse than rime ice predictions due to mixed characteristics of ice and water thermophysics.

3.6.1.6   Case 35

Reference and scaling conditions for Case 35 are given in Table 26 and Table 27. In this case, the velocity is sufficiently high for high-speed flow effects to be considered. The freezing fraction of the stagnation point is below unity; therefore, mixed/glaze ice characteristics are expected.

Table 26: Physical Conditions for Case 35 [60]

Case	Type	NACA	AOA deg.	Chord (m)	T_{st} (°C)	T_{tot} (°C)	V (m/s)
35	Ref	0012	4	0.530	-12.20	-7.81	93.89
35	Scaled	0012	4	0.265	-13.25	-4.47	132.78

Case	Type	NACA	MVD (μm)	LWC (g/m³)	t_{exp} (s)	P_{tot} (kPa)	P_{st} (kPa)
35	Ref	0012	20.00	1.30	372	97593	92060
35	Scaled	0012	11.32	1.18	145	100000	89027

Table 27: Similitude Parameters for Case 35

Case	Type	K_0	β_0	A_c	n_0	b
35	Ref	2.42	0.738	2.953	0.363	0.803
35	Scaled	2.42	0.738	2.953	0.363	0.621

| Case	Type	φ (K)	θ (K)	Reynolds	We_L	Mach
35	Ref	11.2	14.1	116678	2271372	0.290
35	Scaled	11.2	34.2	71345	2271372	0.411
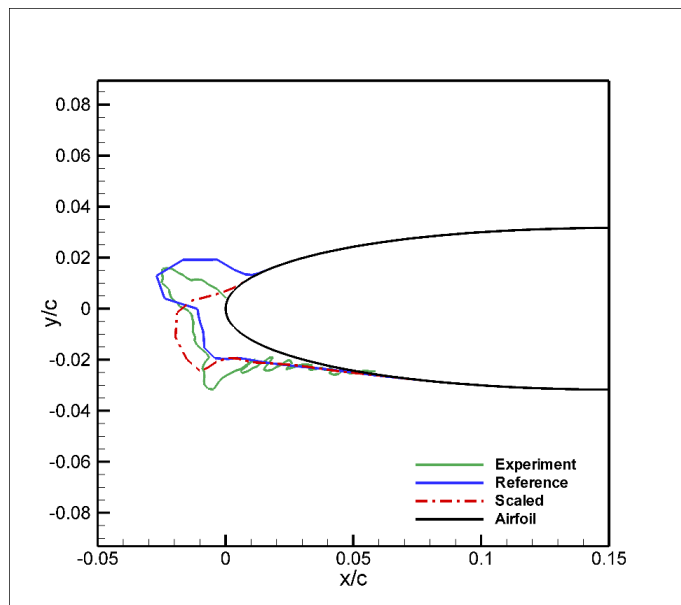
Figure 35: Case 35 Ice Shapes
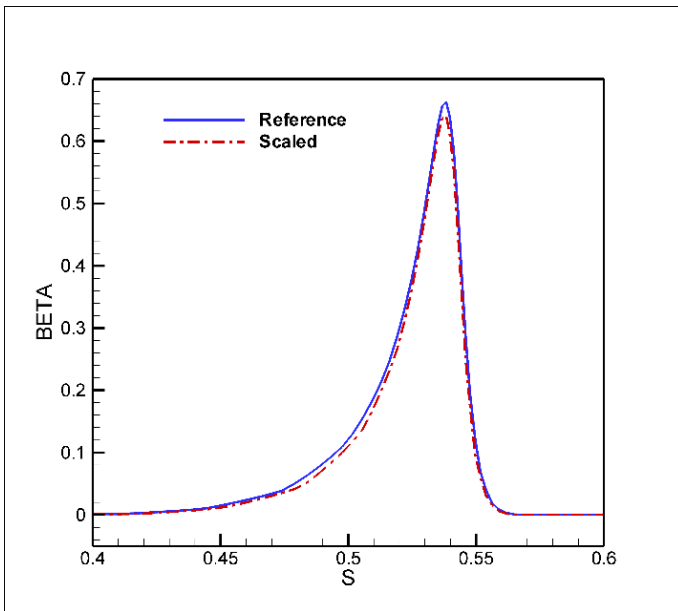
Figure 36: Case 35 Droplet Collection Efficiency

The selected scaling parameters could not be successfully matched at the desired confidence level for this case as can be seen in Figure 35. Although the solution of the reference model and the horn-shaped structure of the experimental data overlap approximately, they do not match exactly. Due to the physics of glaze ice and high velocity, these approaches give an approximate value but are only partially accurate. In this case, the droplet collection efficiency values also started to deviate slightly from each other as the difference in ice shapes started to become more noticeable as it can be seen in Figure 36. However, the droplet collection efficiency values of the reference and scale cases are still remarkably close to each other. This shows that the scaling calculations were performed successfully regarding droplet trajectory physics.

The ice accretion predictions do not show good agreement between the reference and scaled ice shapes; both predictions deviate from the experimental ice shape, especially regarding the horn angle. This discrepancy can be attributed to the limitations of the computational tool used, which may not be dependable in accurately calculating the amount of increased velocity in the scaling and, consequently, the high-speed effects. If one examines the similitude parameters

presented in Table 27, the reference freestream velocity is 93.89 m/s and the scaled freestream velocity is 132.78 m/s, corresponding to M=0.29 and 0.41 respectively. The reference condition is at the limit of the generally accepted threshold for compressibility, while the scaled condition is well-above the same threshold, rendering the flow regime different, which certainly contributes to the discrepancy.

3.7   Determination of Wind Tunnel Design Limitations

Requirements for wind tunnel that will be designed within this thesis, will be determined by ice formation testing needs. A vast parametric study will be conducted to finalize wind tunnel aerodynamic and mechanical variables. The present thesis presents the design of an icing wind tunnel that aims to replicate the majority of the icing conditions outlined in 14 CFR Parts 25, Appendix C. Therefore, wind tunnel must satisfy the conditions illustrated in Figure 4 and Figure 5. Besides, wind tunnels should be equipped with spraying nozzles to control LWC and MVD of the air in the wind tunnel. To accomplish this objective, this chapter discusses and identifies the constraints of the wind tunnel design and the specifications of necessary equipment. A table is provided, outlining the specific test conditions required to achieve the desired outcome, along with the factors that influence these conditions and the equipment that determines them. Furthermore, each contributing factor is individually analyzed and comprehensively described in subsequent sections. Unfortunately, as mentioned in the preceding sections, the pressure value will not be matched, thereby rendering the wind tunnel incapable of simulating altitude.

Table 28: Simulation Capability Determination

Test Condition	Determine	Limitation
c_S or L	Test Section size	Blockage
t_{st}	Icing capability	Cooling Power and Cost
p_{st}	Altitude and b and θ	Mechanical strength of wind tunnel walls and Cost
V_{inf}	motor power and compressibility effect.	Effect on droplets to inhibit particle impingement. Fail in scaling due to high-speed effects.
MVD	Icing capability	Spray bar type and calibration
LWC	Icing capability	Spray bar type and flow rate
τ	Cooling requirements	Liquid nitrogen capacity and cooling power
Turbulence intensity	Mesh screen size and quantity, heat transfer rate	Ice accretion on mesh, intrusive equipment of wind tunnel.

3.7.1   Scaling the Size of the Object

3.7.1.1   Blockage in Test Section

The speeds mentioned in the literature survey regarding wind tunnel test sections typically pertain to test sections that are not occupied. Therefore, the actual airspeed achieved in practice is contingent upon the level of blockage and the drag coefficient associated with the test assembly. For instance, in the case of the IRT (Institute for Research in Technology), it has been approximated that the maximum speed decreases from 192 m/s (430 mph) in an unoccupied test section to 156 m/s (350 mph) when a model in test section with 5 percent blockage and a drag coefficient of 1.7 is installed [61].

Hence, it is comprehensible that the calculation of blockage, a crucial factor in determining the dimensions of the test chamber, is undertaken. The maximum blockage was found to be 5 percent, and based on this rate, the optimal size of the model to be accommodated in the test chamber was determined. This size was deemed adequate for conducting icing flow field analysis and scaling.

Table 29: Test Section Blockage

Test Section Area	Allowed Blockage	Cross Section Area of Model	Utilization of Test section w/ span	Thickness	Chord
$1\ m^2$	5%	$0.05\ m^2$	100%	0.05 m	0.416 m
$1\ m^2$	5%	$0.05\ m^2$	75%	0.067 m	0.555 m
$1\ m^2$	5%	$0.05\ m^2$	50%	0.1 m	0.833 m

The chord length of 0.833 meters was determined as the largest model size for the icing wind tunnel to be designed. Considering the scaling limitations discussed earlier, when the maximum scaling reduction of 1/4 is utilized, this translates to a chord length of 3.33 meters under real conditions. This size is more than sufficient to test the icing characteristics of many aircraft with scaling, for example the ATR-72, in the wind tunnel.

3.7.2 Temperature

Temperature control in the icing wind tunnel is achieved through the utilization of cooling systems. These systems incorporate a heat exchanger positioned within the wind tunnel, enabling the air circulating through the closed-circuit wind tunnel to counteract the conditions that lead to temperature adjustment within the wind tunnel.

The majority of wind tunnels discussed in the existing literature are capable of cooling down to -30 ℃, which is the desired level of cooling for this particular study. Furthermore, as shown in Table 3, the data collected in the research conducted by 14 CFR Appendix C to Part 25 on clouds causing icing reveals that the required

temperatures within the icing envelope for stratiform and cumuliform clouds range from 0 to -30 °C. However, it is worth noting that occasionally, temperatures as low as -40 °C can be observed for cumuliform clouds. Therefore, in instances where additional cooling is necessary, the injection of liquid nitrogen into the wind tunnel is employed to temporarily lower the temperature below -30 °C. The specific duration for which this enhanced cooling is sustained will be comprehensively described and calculated in the design section of the wind tunnel. Nevertheless, for the present moment, taking into account cost considerations, it has been determined that a cooling system capable of maintaining a stable temperature of -30 °C within the test chamber is the most suitable option. For temperatures lower than -30 °C, the expected exposure time by injecting liquid nitrogen into the flow is planned to be at least 6 minutes, provided that the temperature of the test chamber is kept constant at -40 °C.

3.7.3   Velocity in Test Section

In addition to the aforementioned issues, it is important to consider the variations in ice shape and the effects of compressibility when the airspeed is high. Based on the literature and market research, the minimum MVD size that can be calibrated and applied is 10 microns [15]. Figure 38, shows MVD values as a function of scaling ratio, while the redline is the limitation of the minimum MVD generation; therefore, working below that line is impractical. Considering this and the results of the sizing studies, facility, and fundamental physical constraints, scaling below ¼ ($C_r/C_s = 4$) does not seem feasible. These outcomes are also in agreement with the works conducted by Anderson et al. [10].

Even if higher velocities than 155 m/s can be achieved, compressibility effects should be taken into account, and it needs to be kept in mind that the assumption made for scaling ignores the compressibility effects. Therefore, it is generally accepted that 150 m/s velocity in the test section is an upper limit for the icing test applications [62]. However, inconsistencies in scaling calculations have been observed after the flow velocity exceeds a value of 0.3 Mach. Hence, the airflow

velocity in the test chamber for this study has been determined to be 100 m/s. The reason for selecting this value is to ensure higher accuracy in scaling calculations and to enable cost-effective design of the wind tunnel for production purposes. This can be seen in Figure 37 and visualized with a dashed redline for the limitation of airspeed in the test section. Figure 37 also states that scaling factor lower than ¼ $(C_r/C_s = 4)$ scaling ratio is not feasible for wind tunnel applications. This scaling ratio is even reduced to 1/2 for the reference cases with airspeeds of 100 m/s and above.
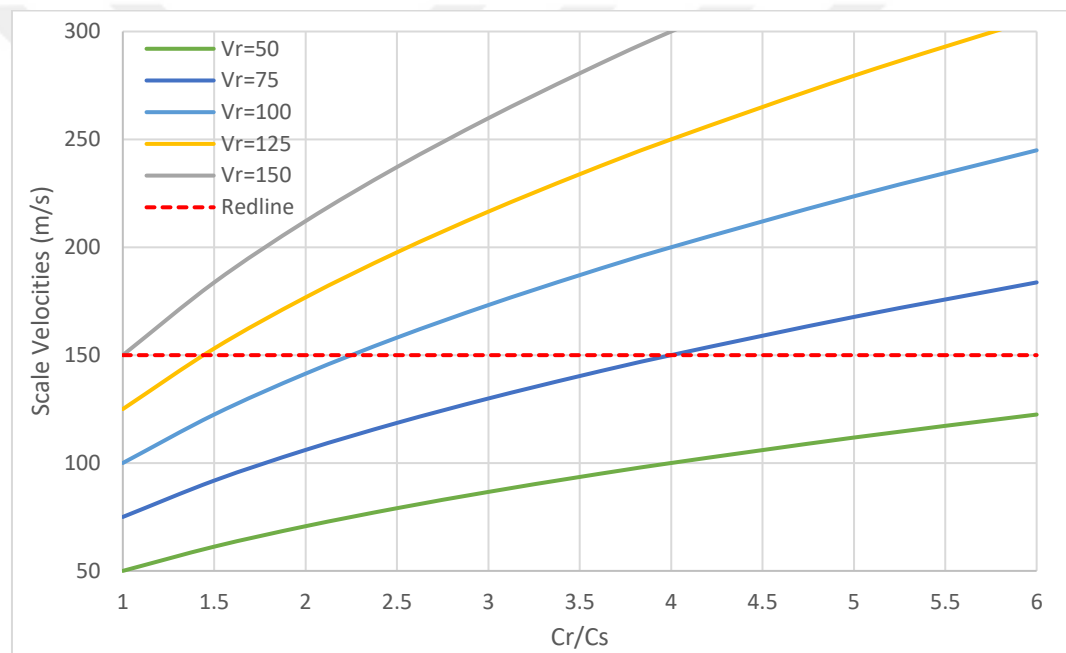
Figure 37: Velocity vs. Scaling Ratio

3.7.4   LWC

Comparison of Appendix C envelopes and generic spray bar calibration curve, highlights the limitations of current water spray nozzle technology used in icing wind tunnels. These air-atomizing nozzles, while allowing some control over water flow rate and droplet size, do not provide complete independence in achieving the desired LWC and MVD ranges. As a result, the capabilities of icing wind tunnels in reproducing certain ranges of LWC and MVD are restricted. In detail, spray bars

struggle to replicate the high LWC and small MVD of the intermittent maximum icing envelope, as well as the low LWC and large MVD conditions in the Appendix C envelopes. In theory, increasing the number of spray nozzles could enhance the LWC for low MVDs. However, incorporating a larger number of spray bars and nozzle locations into the system would be challenging, as it would significantly complicate the spray-bar system and potentially lead to increased flow blockage and distortion [63].

Furthermore, the challenges encountered in obtaining LWC values are evident. Previous studies in the literature have reported LWC values ranging from $0.1\ to\ 3.0\ g/m^3$ in various icing wind tunnels. It is believed that these values can be achieved using standard spray bars. Consequently, in order to comply to the envelops outlined in Appendix C, LWC values within the range of $0.1\ to\ 3.0\ g/m^3$ were chosen. The accuracy of these selected values will be assessed through subsequent calculations.

3.7.5   MVD Size

When the model size is reduced, the droplet size decreases, and freestream velocity needs to be increased accordingly. Depending on the test equipment, there are limits on the minimum droplet size and maximum velocity that can be achieved steadily, and if the droplet size is too small, the droplets may not even impinge the surface. Supplying a minimum-size MVD is a problem. However, this problem could be solved at a certain level by a spray system and nozzle calibration. Obtaining practical minimum MVD size is essential to get precise and validated icing conditions in an icing wind tunnel. If the required MVD size fails to be produced, large-scale geometries and high-speed velocities in the test section must be supplied. However, these two conditions have their own physical constraints as stated in prior sections. In addition to the above, the scaling size determines almost all the values of the wind tunnel, together with all the icing physics parameters.

Figure 38 illustrates the relationship between the MVD value and the scaling ratio. The decline in MVD values as the scaling ratio decreases indicates the limitations of

the scaling ratio in comparing the smallest droplet size that the spray bar can generate. The red line in Figure 38 represents the minimum droplet diameter achievable, and upon analysis, it can be determined that the limitation for this issue is approximately 1/3 ($C_r/C_s = 3$). In the reference case, the scaling ratio also increases for larger particle diameters. Consequently, an average scaling ratio of ¼ ($C_r/C_s = 4$) can be considered as an acceptable limitation when considering the Langmuir D droplet size distribution.
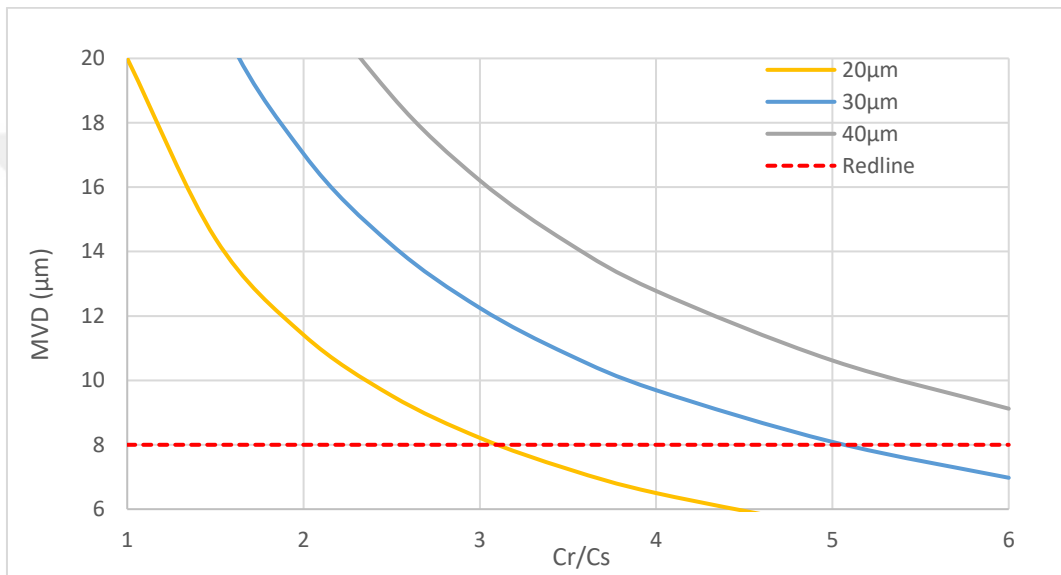
Figure 38: Droplet Size Distribution vs. Scaling Ratio

In addition, Figure 39 shows that the scaling calculations made in this graph has very little effect on MVD and LWC values with different chord length. When the reference dimensions with different reference lengths but with same scaling ratios, it is seen that the lines represents the similitude parameters overlapped exactly for each MVD value. If the same comment is to be made for another graph, it can be easily stated that the scaling values in Figure 41 are independent of the characteristic length but depend on the scaling ratio and the test section air velocity. The most challenging condition of the spraying nozzle envelopes represent in the same graph visualized with green dotted line, namely the highest velocity (100 m/s), has been taken into consideration. For lower airspeed values, the upper part of the nozzle LWC lines stretches to higher values.
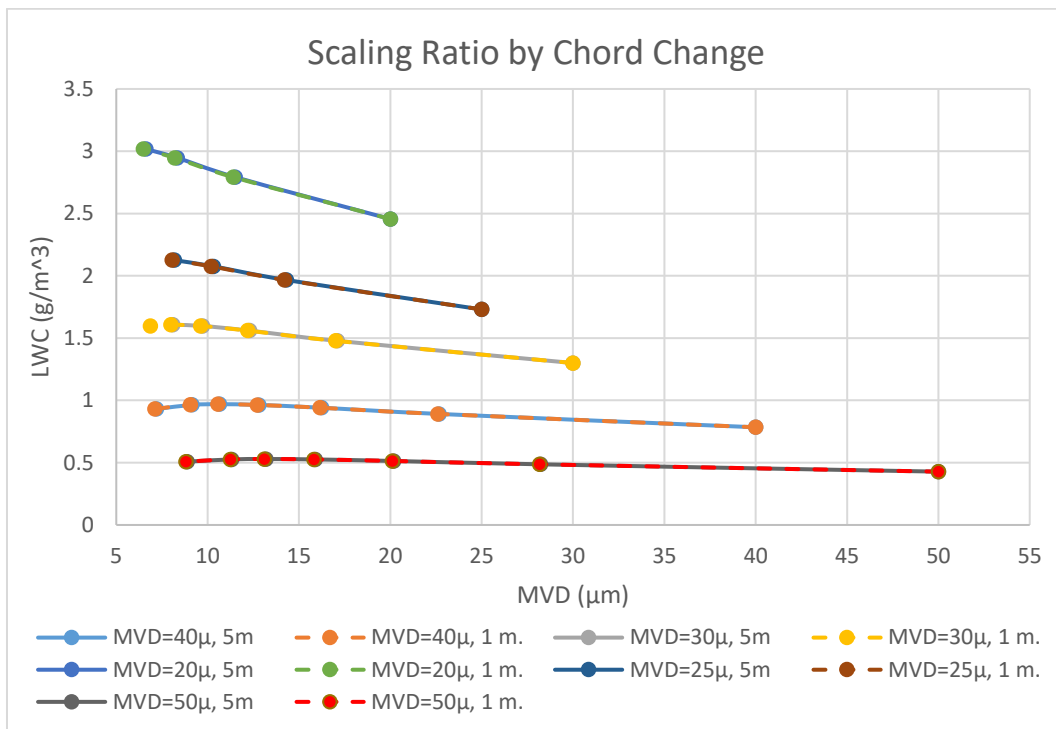
Figure 39: MVD and LWC Values for Different Length

The limitations of the wind tunnel are determined by the physical characteristics of the icing formation is shown in Figure 41. In addition, it is shown where it stands according to the cumuliform and stratiform envelopes defined by 14 CFR Parts 25 Appendix C. Here, 7 reference cases have been identified and scaling calculations were performed for different scaling ratios. Scaling calculations of these cases were made and shown on the graph according to MVD and LWC parameters. The closed curves with green dashed dots show two different spray nozzles of the NASA IRT. As can be clearly seen from the graph, for the low MVD and high LWC values, the spray bar capabilities cannot serve for scaling application for this issue second scaling calculation could be performed in order to fit the scaling condition inside of the wind tunnel spray bar specifications by matching $LWC * \tau$ for both conditions. This second scaling approach visualized in Figure 40. In order to fulfil the required specification for scaling application, a new spray bar design will be conducted. This will be analyzed and calculated in more detail under the wind tunnel design section and spray bar design subsection. It has been mentioned that the MVD value among the commercially available spray bars can go down to 10-micron levels. When this value is taken into account, it is seen that the scaling limitation is established around

1/3 or 1/4 for different MVD values at reference conditions. Appendix C has determined the range of MVD values for stratiform and cumuliform conditions to be between 15-40 and 15-50 microns, respectively. Taking these factors into consideration, the MVD lower and upper limits for the proposed icing wind tunnel are determined to be 10 microns as the lowest value for spray bar calibration, and 50 microns considering the App C conditions.
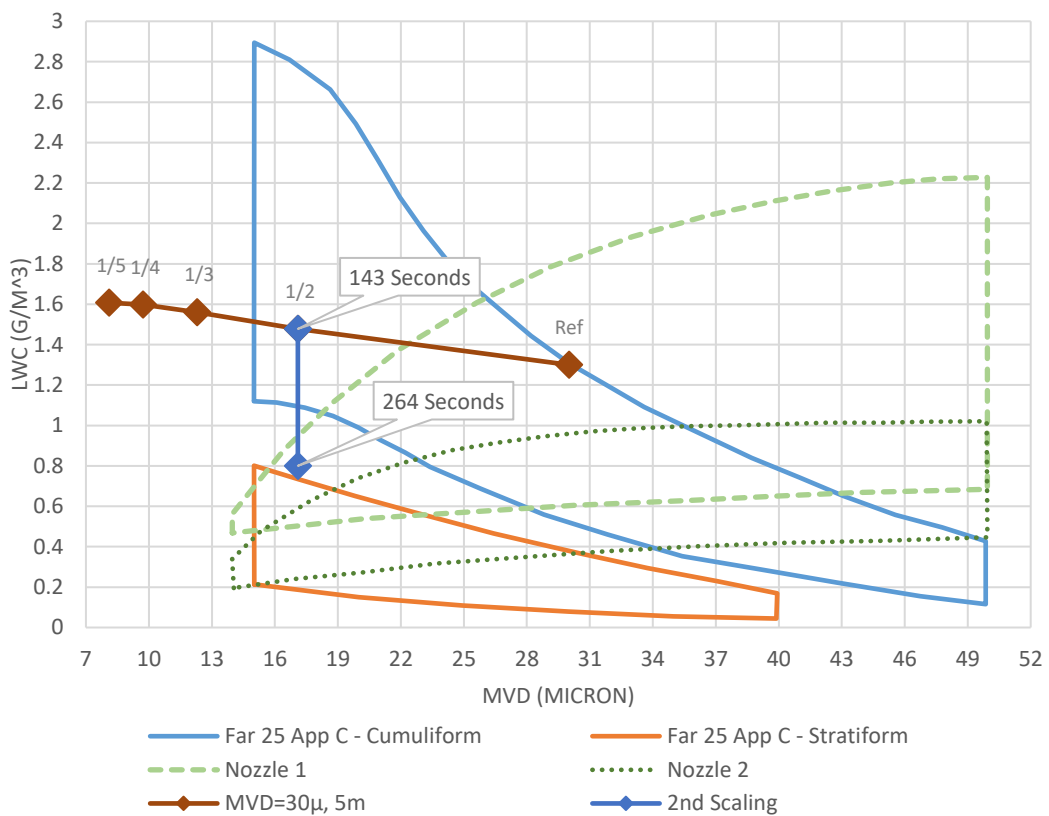
Figure 40: Secondary Scaling Approach
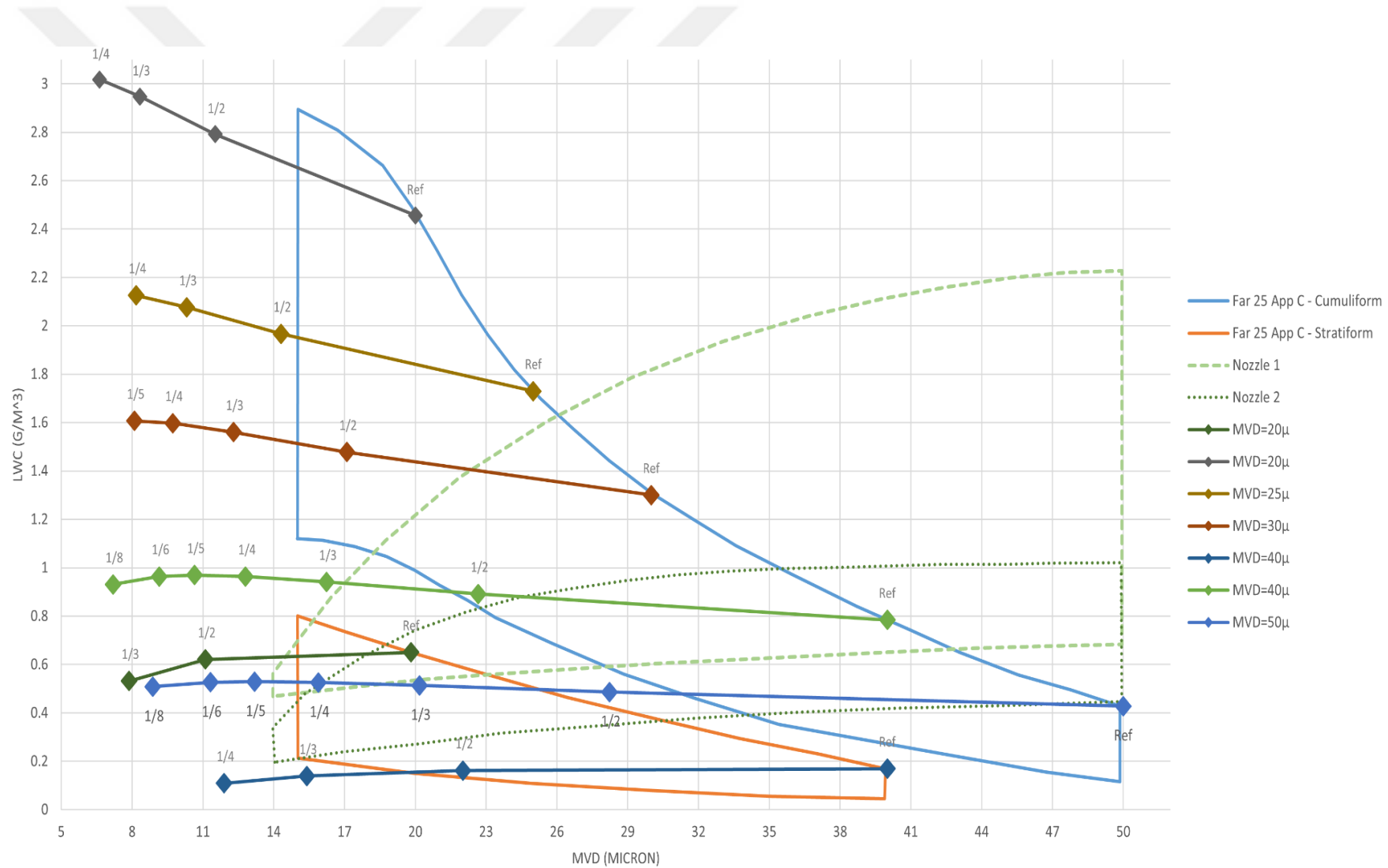
Figure 41: Limitation Regarding MVD and LWC

3.7.6   Turbulence Concerns

In the test chamber of wind tunnels, the measured turbulence values of the flow are found to be higher compared to conventional wind tunnels and flight conditions. Although turbulence levels in natural ice accretion clouds have not been measured, they are assumed to be lower than those in wind tunnels. In icing wind tunnels, the equipment present, such as spray bars and heat exchanger, contribute to the formation of turbulence more clearly, and mesh screens are not used to reduce turbulence levels in all tunnels due to the potential for ice accumulation. For example, mesh screens are not used in the IRT. Higher turbulence levels tend to aid in the mixing of particles and should therefore assist in cloud homogeneity, but likely do not fully mimic nature. For speeds below 134 m/s, turbulence intensity in the IRT has been measured between 0.5% and 0.9% by several researchers without the operation of spray bars [64], compared to values below 0.1% in flights under non-icing conditions [65]. An increase in turbulence can affect both aerodynamics (by increasing skin friction and advancing the boundary layer transition location) and ice accretion (by increasing local convective heat transfer rates). Therefore, heat transfer in wind tunnels has been shown to have higher heat transfer rates compared to flight conditions. The turbulence levels in icing wind tunnels and the resulting heat transfer values seem to impose a natural limit on their ability to fully simulate [63]. Although the use of mesh screens is not observed and common in icing wind tunnels, due to the reasons mentioned above, it is anticipated that a lower number of mesh screens with low mesh number values will be used to achieve a higher level of similarity, compared to the number used in high-standard wind tunnels.

3.7.7   Uncertainty for Scaling

When scaling, some similarity coefficients cannot be exactly matched, but the freezing rate and accumulation factor should be matched within ±10% [10]. In the calculations performed in this study, these parameters are precisely matched. Although the effect of ice formation on velocity change is not as sensitive as the

freezing rate and accumulation factor, the Weber number using the length L should be consistent within ±15% [62]. Again, in our calculations, the Weber number was precisely matched for both cases. Within our dissertation, almost all parameters are precisely equalized. However, θ and b values, which are thermal parameters, could not be always matched. It is possible to match these values precisely, but in the case of scaled, this requires the static pressure conditions to be reduced significantly. This requires a tunnel with altitude simulation capability, which boosts the costs of developing and implementing such a tunnel. As it can be seen in Table 11, change in parameters is zero for most parameters except b and θ. Changes in these parameters are infinitesimal for ice accretion prediction. The calculations for icing, in which all parameters are matched, are shown in Table 12, with a pressure variation of up to 20 kPa.

3.7.8   Wind Tunnel Parameters

Taking into account all the above-mentioned limitations, almost all the parameters necessary to determine the requirement characteristics of the wind tunnel have been determined. The few parameters that could not be determined are based on the values of the existing tunnels. In the following table most of the technical parameters are determined and introduced.

Table 30: Proposed Wind Tunnel Specification

Name	Value / Type	Unit
Company/Institute	Middle East Technical University	
Facility Name	Icing wind tunnel (IWT)	
Test Section	1000 x 1000	$milimeters$
Total Temperature	-30	$Celsius\ Degree$
Flow rate	360000	m^3/h
Test Section Type	Closed with transparent glass	
Max A/F Chord	0.833	$meters$
V_∞ at test section	100	m/s
Compressibility	Subsonic	
Humidity	100%	RH
MVD	$10 - 50$	μm
LWC	$0.1 - 3$	g/m^3
Exposure Time	(TBD in Chapter 4)	$second$
Mach	0.32	$unitless$
Reynolds Number	$3.09 * 10^6$	$per\ meter$
Pressure	Ambient	$Pascal$
Testing gas	Air & Liquid Nitrogen	
Type	Closed Circuit (Göttingen Type)	
Honeycomb	1 (TBD in Chapter 4)	$Quantity$
Mesh Screen	2 (TBD in Chapter 4)	$Quantity$
Turbulence intensity	<1% (without model and instrumentation)	$unitless$
Cloud Generation	Spray bar	
Cooling System	Heat exchanger with A/C unit and R744 gas. And liquid nitrogen injection	
Driver Unit	(Technical Specification derived in Chapter 4)	kW
Motor Control	Variable Frequency System	

CHAPTER 4

ICING WIND TUNNEL DESIGN

In this study, the wind tunnel is considered as a closed circuit type due to the reason that closed-circuit type wind tunnel allows for a controlled establishment of different climatic test conditions. Due to closed volume, climatic conditions can be easily controlled when no bleeding zone exists. However, protection of internal climate should be mandatory due to the effects of engine heating and air friction, and this protection will be ensured by strong insulation around the outer wall of the wind tunnel. Besides the abovementioned concerns, the air temperature inside the wind tunnel should be regulated tightly to simulate icing conditions. Because of this reason, the cooling exchanger and refrigerant control system will be equipped with close loop feedback temperature control, and this control system is capable of keeping the temperature threshold between 1 celsius degree.
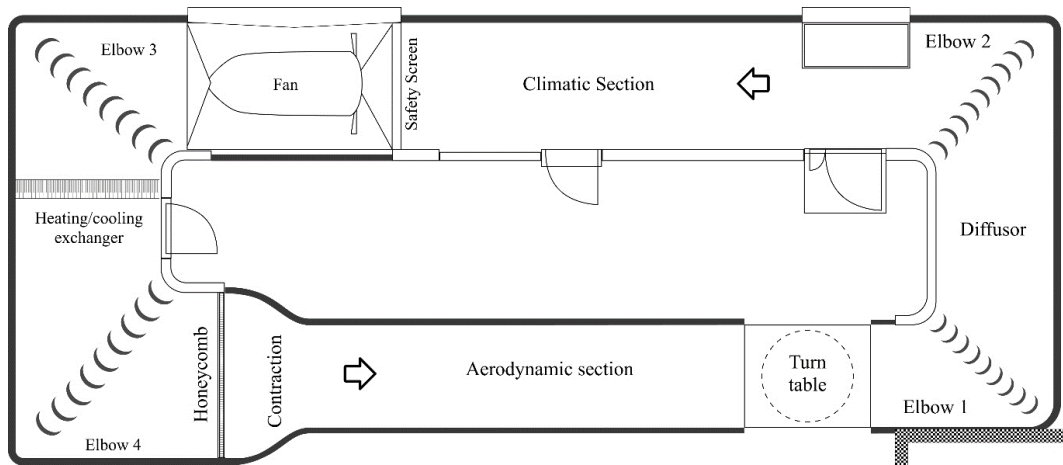
Figure 42: Generic Climatic CWT Top View [66]

Icing tunnels are constructed using principles derived from conventional sub-sonic wind tunnel designs. In addition to possessing the typical features of subsonic wind tunnels, these tunnels are equipped with two crucial supplementary components. Firstly, a cooling system (A/C) and heat exchanger are incorporated to regulate the air temperature below freezing. Secondly, a spray bar system is implemented to introduce water into the air stream, with precise control over drop size and water flow, thereby simulating an icing cloud. The test conditions created within icing wind tunnels are primarily intended to replicate the environments outlined in 14 CFR Parts 25 and 29, Appendix C.
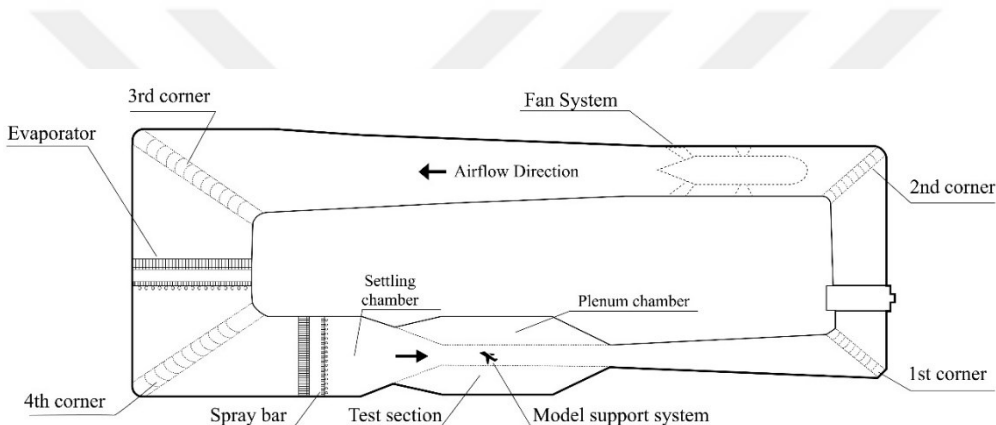
Figure 43: Generic Icing Wind Tunnel Top View [19]

A simple comparison of Figure 42, an environmental conditioning wind tunnel, and Figure 43, an icing wind tunnel, clearly shows the differences between them. An educated viewer can also recognize the design conditions required by icing conditions.

This chapter commences by providing an overview of the constituent elements of the icing wind tunnel. Subsequently, it delves into these elements' comprehensive design and pressure loss calculations. Finally, it culminates with a comparative analysis between the computational fluid dynamics (CFD) analysis and the design calculations..

4.1   Design Criteria

Wind tunnel design requires a lot of engineering discipline and organization. A general wind tunnel design starts with the design of the test chamber. Once the test chamber is determined, the Wind tunnel design requires a lot of engineering discipline and organization. A general wind tunnel design starts with the design of the test chamber. Once the test chamber is determined, the design progresses in two main branches. The first branch involves the design of the contraction section and diffuser, which are mechanically connected to the test flow. After the contraction section, the design of flow conditioning devices, such as honeycomb screens located in the settling chamber, is carried out. Subsequently, a corner diffuser is designed, which is then connected to the motor. During this stage, flow conditioning or conditioning device designs within the relevant components are also developed. If any component is found to be problematic or faulty during this process, the design is revised starting from the test chamber and continued accordingly. In the final stage, the pressure losses and other technical specifications of all the designed components are determined, along with the flow rate, to finalize the design of the motor fan section and its technical features. This design process is fully interconnected and iterative. During the design phase of each segment, controls and other physical phenomena need to be checked to ensure that they are met. For these reasons, the entire wind tunnel and each of its components is subjected to an iterative calculation. In the final stage, the calculations of the drive unit are performed to check whether the required conditions are met, and if so, the process is finalized. A simplified flowchart of a wind tunnel can be seen in Figure 44.
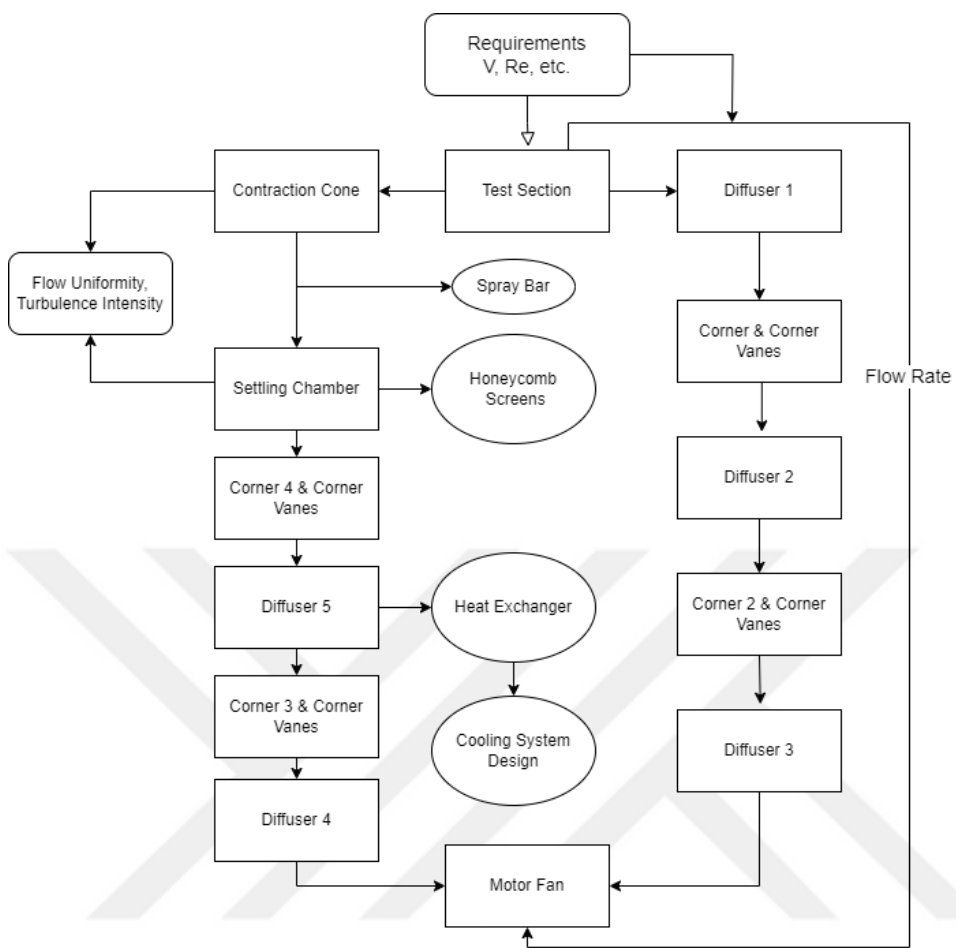
Figure 44: Wind Tunnel Design Flowchart

In designing wind tunnels, a crucial consideration is whether to opt for a closed or open circuit configuration. Open circuit wind tunnels are commonly preferred due to their cost-effectiveness and user-friendly nature, resulting in widespread usage. However, the specific conditions of the present study necessitate a departure from this norm. Given that the air within the icing tunnel experiences requires excessive cooling compared to the surrounding environment, adopting a closed-circuit wind tunnel becomes almost imperative to mitigate heat losses.

4.2   Wind Tunnel Components

The various components of the icing wind tunnel are briefly outlined in this section. Figure 45 displays the components on a generic cross-sectional diagram of the wind tunnel to provide a visual representation and facilitate comprehension. Elaborate calculations and dimensioning will be addressed in the subsequent chapter.
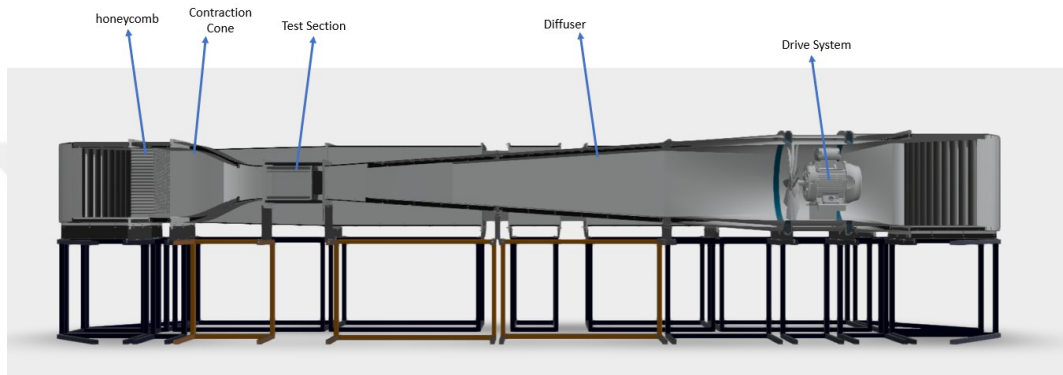
Figure 45: Generic Close Loop Wind Tunnel

4.2.1   Test Section

The test chamber holds significant importance within the wind tunnel as it serves as the primary location for all measurements. The cross-sectional area and length of the test chamber directly influence the cost and power requirements of the wind tunnel. Consequently, the size of the test chamber should be determined based on key characteristics of the wind tunnel, such as the operating speed and desired flow quality. The dimensions of the test chamber and the operating speed dictate the maximum size of the models that can be accommodated and the maximum Reynolds number that can be achieved. Consequently, the shape of all wind tunnels is designed in accordance with the sizing requirements of the test section. When designing the test section, consideration should be given to the interface of the model and the ease of access for instrumentation. It is preferable to have flat walls with rounded or chamfered edges to facilitate access and usage. Additionally, the test section should incorporate transparent windows or walls to allow for visual observation of the model. Figure 46 shows a subsonic test section with a transparent flat wall.
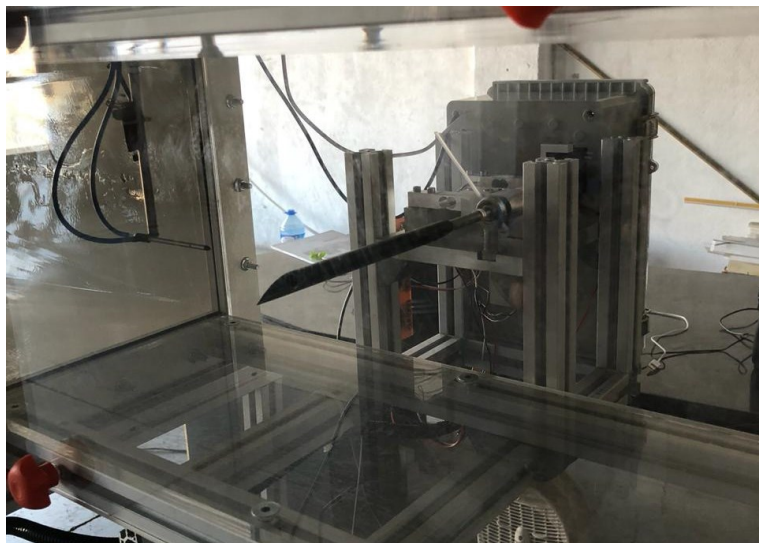
Figure 46: Test Section with Transparent Wall and Model.

4.2.2 Flow Conditioners

Most of the settling section in the wind tunnel comprises honeycomb (Figure 47) and screens (Figure 49). The purpose of the honeycomb is to align the flow in the direction of the wind tunnel axis, while the screens serve to homogenize the pressure along this axis. Flow conditioning equipment helps to reduce large-scale turbulent deviations and promote the formation of smaller-scale eddies, thereby decreasing the growth of the boundary layer. The combined use of screens and honeycomb effectively reduces turbulence intensity within the wind tunnel.
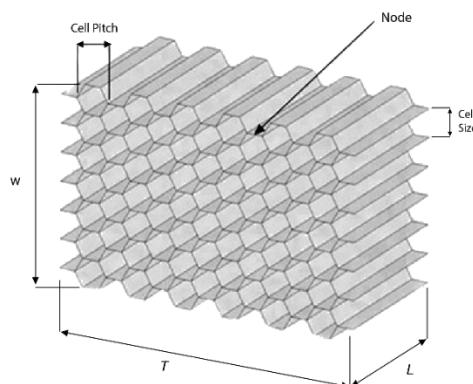
Figure 47: Generic Honeycomb
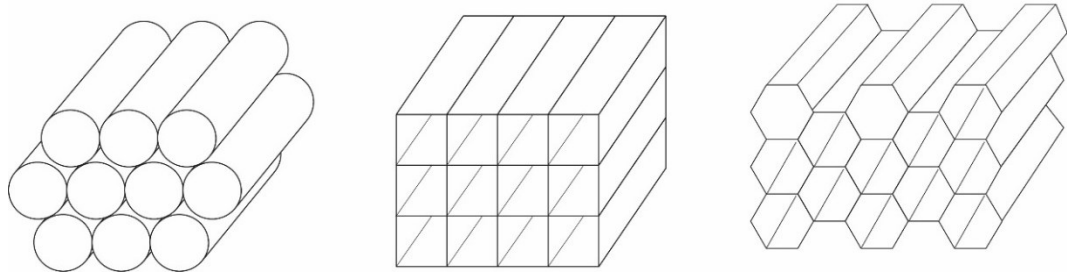
Figure 48: Honeycomb Types [67]

Although turbulence intensity is a significant technical feature for wind tunnels, there are wind tunnels where mesh screens are not used because they cause blockage in icing tunnels due to ice accumulation and other factors. Furthermore, they require a lot of maintenance and cleaning for this reason. For example, no screens are used in the NASA icing wind tunnel (IRT) [63]. Although not used in a few tunnels, the CIRA icing wind tunnel features a honeycomb and an optional screen mesh behind it for tests requiring high-quality flow [19]. In addition to these examples, the BRAIT icing wind tunnel incorporates a flow conditioning system consisting of 5 screens and one honeycomb. There is one coarse mesh screen upstream of the honeycomb, and there are four fine mesh screens [20]. Therefore, in this study, the design will be made with the presence of a screen mesh. However, it can be removed if requested. In this study, the need for this use will be rationalized and concluded in the calculations of the relevant section in the following sections.
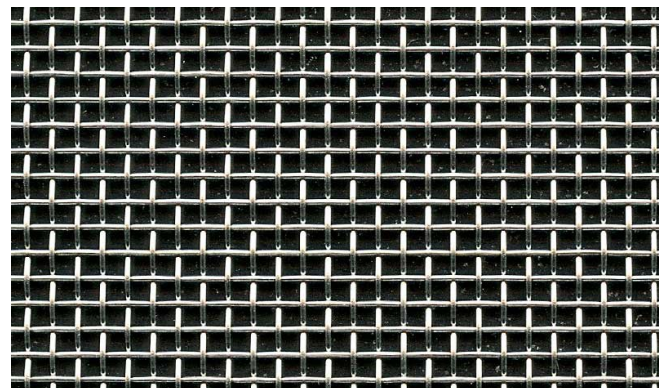
Figure 49: Mesh Screen

4.2.3   Contraction

An inlet contraction cone is a specialized component employed in fluid systems to decrease the cross-sectional area of a pipe or duct at the inlet of a device or system. This cone is typically designed with a smaller cross-sectional area at the outlet end and a larger cross-sectional area at the inlet end. Its purpose is to enhance the velocity of the fluid while maintaining a high level of desired flow quality as it enters the device or system. In the present study, the contraction cone is responsible for directing the flow from the settling chamber to the test chamber. Contraction ratios typically range from 4 to 10, with the most commonly used ratios falling between 6 and 9 to achieve optimal flow quality.

The shape and size of the inlet contraction cone can be designed to achieve specific flow characteristics, such as increasing the velocity of the fluid or reducing the pressure drop across the inlet. The contraction's size and shape control the test section's final turbulence intensity levels. A trade-off determines the length of the contraction. The contraction cone should be small enough to reduce boundary layer growth and long enough to prevent massive pressure drop. The cone can be made from various materials, including metal, plastic, or composite materials, depending on the specific application and the system's requirements [68].
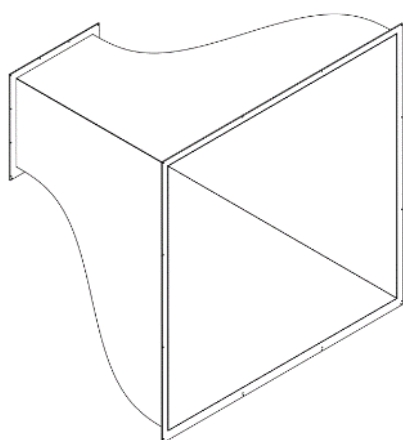
Figure 50: Generic Contraction Shape

4.2.4   Diffuser

The purpose of the diffuser is to decelerate the high-speed flow from the test section, resulting in the recovery of static pressure and a decrease in the load on the drive unit. The level of energy loss is directly proportional to the extent of pressure recovery, making it desirable to reduce the flow velocity over the shortest distance possible without causing flow separation. Various factors such as geometry, size, and wake development influence the diffuser inlet flow. To prevent flow separation, the cross-sectional area of the diffuser should gradually increase along its axis. This gradual increment ensures high efficiency and helps reduce construction costs by minimizing the overall size of the tunnel shell. The diffuser's performance is crucial for the tunnel's success, and extensive experimental work has led to the conclusion that the expansion half angle of the diffuser should not exceed 3.5 degrees [69]. This consideration will be incorporated into the design process of this thesis.

4.2.5   Corners

In the context of airflow management in wind tunnels, corners play a crucial role in deflecting the airflow. Without any additional features, a corner would cause the flow to rotate, resulting in an uneven flow at the outlet. In order to mitigate this issue and minimize losses, guiding vanes are commonly employed to maintain a relatively straight flow throughout the circuit. These corners are typically of constant area, and their dimensions are designed to match the connected components of the wind tunnel. Therefore, corners are designed in pairs and conjunction with neighboring components. In the specific case of this closed-circuit wind tunnel, the flow needs to be deflected by 90° four times while minimizing turbulence at the corners. In order to achieve enhanced flow at the corners, the corners are equipped with corner vanes. These vanes come in various shapes, ranging from bent plates to highly cambered airfoils. The most practical and cost-effective shape is a quarter of a circle, which a short, straight part can extend at the end to reduce vortices at the edges. The losses in the corner vanes can be minimized by selecting an efficient cross-sectional shape and an appropriate chord-to-gap ratio. Furthermore, vanes utilizing cambered airfoils

and relatively blunt leading edges are less susceptible to variations in the approaching air flow angle compared to vanes with sharp leading edges.
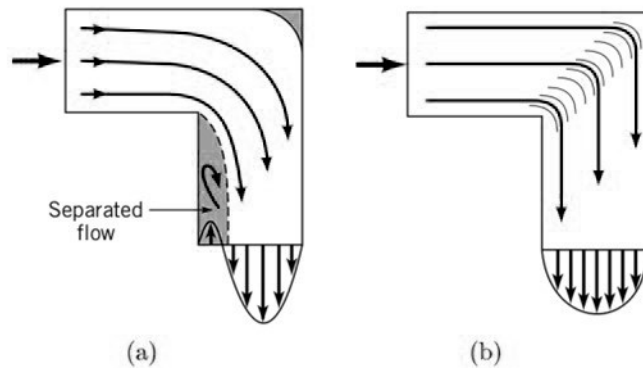
Figure 51: Corner with (a) and without (b) Corner Vanes [70].

4.2.6   Drive System

The drive unit consists of the motor, propeller, motor drive (VFD) and other electrical equipment that enables them to operate. It accelerates and pressurizes the airflow in the wind tunnel. The constant-flow wind tunnel conditions require the fan to compensate for the pressure drop across the elements of the tunnel. Calculating the fan power that exactly reproduces the pressure lost across the elements of the wind tunnel is a challenging and iterative task throughout the wind design process. An axial fan is the most common equipment used to direct flow in wind tunnels. Axial fans or propellers will produce swirls in their induced flow unless a utilization of guide and straightening vanes is present to overcome these vortices in the settling chamber.

4.2.7   Air Conditioning Units

Heat exchangers are the must-to-use component in close-circuit wind tunnels due to the heating induced by surface friction. Nevertheless, in this work, the heat exchanger will be used to climate the air volume contained by the wind tunnel ducts. For the icing wind tunnel requirements, the temperature should be equal to or lower

than about $-30^{\circ}C$. Hence, refrigerant gas (R407C, R410 etc.) will be used in the air conditioner [71].

Figure 52: Air Heat Exchanger

4.2.8 Spraying Units

As previously discussed in this research, the spray bar is a crucial component of icing wind tunnels that distinguishes them from other types of tunnels. Its primary function is to generate cloud formations that induce icing formation in the actual air environment within the icing wind tunnel. In a broader context, the spray bar involves injecting atomized or pulverized droplets into the airflow of the wind tunnel to achieve controlled LWC and MVD for controlled application. The droplets produced by the spray bar must possess consistent size and continuity, essential for accurately replicating real-world icing conditions. Otherwise, the data obtained from such studies will not accurately reflect reality.

Spraying units are designed to generate water droplets with defined diameters (MVD). LWC must have covered the overall envelope prescribed by FAR 25 and FAR 29 Attachment C for both continuous and intermittent operations introduced in Figure 4 and Figure 5 [72]. Furthermore, within the scope of this study, a specific spray bar and its associated components should cover at least the Appendix C conditions, and the spray bar will be specified and calculated in this manner. Moreover, calibration and fine-tuning will be of utmost importance at this stage, as they will significantly contribute to adjusting the LWC, MVD, and spray range and simulating icing conditions in order to fulfil the given requirements. Given its critical

role in the icing wind tunnel's performance, reliability, and accuracy, this component will be subject to meticulous examination and detailed optimization.

Figure 53: Spraying Units in Test Section [73]

4.3 Icing Wind Tunnel Design Calculations

In order to have an iterative design procedure and selection for wind tunnel design calculations, an in-house computer code is developed. This code calculates conceptual design sizing and pressure losses, and general design parameters are determined.

4.3.1 Power Analysis

In this part of the calculations, the worst case scenario should be considered in order to calculate the required power of the engine. In this work, air temperature of -30 °C, required maximum speed U and a cross-sectional area A_{tsec} of the tunnel test section, the required jet power P_{jet} can be calculated to the following equations [69]:

$$P_{jet} = \frac{1}{2} * \rho_{air} * U_\infty^2 * \dot{V}_{air} \qquad (94)$$

$$P_{jet} = \frac{1}{2} * \rho_{air} * U_\infty^2 * (U_\infty * A_{tsec}) = \frac{1}{2} * \rho_{air} * U_\infty^3 * A_{tsec} \qquad (95)$$

$$P_{jet} = \frac{1}{2} * 1.4515 \ \frac{kg}{m^3} * \left(100 \ \frac{m}{s}\right)^3 * 1 \ m^2 \qquad (96)$$

$$P_{jet} = 725.75 \ kW \qquad (97)$$

Power factor λ is introduced in order to calculate the wind tunnel's required power level. This factor includes the power of the fan and jet. For conventional wind tunnels, the value of this factor can be taken as 1.5. However, pressure losses and ice accretion are more severe in the icing wind tunnel than in conventional wind tunnels, so the power factor can be altered to 2.3, yielding a fan power of $P_{fan} \approx 1667$ kW. An axial fan with an efficiency $\eta_{fan} \approx 67$ % was selected for the tunnel drive, the electrical power input is therefore 2500 kW. Although these values have been calculated, when we look at the engine power of similar tunnels in the world and make a comparison, it can be seen that this value is overestimated. For this reason, technical data of existing similar tunnels are presented in the table below. When comparing the technical data in the table, it is evident that the power value has been overestimated. An average power coefficient was calculated based on the technical data obtained from existing tunnels, and the driver unit power of the wind tunnel was calculated according to this power coefficient. Based on these calculations, the maximum value of the power coefficient was taken as a reference point, and calculation were done. The power requirement of 322 kilowatts has been determined.

Table 31: Power Coefficient of existed tunnels [15]

	Test Section Height	Test Section Width	Test Section Velocity	MVD	Pow er	Power Coef.
	meters	*meters*	*m/s*	*μm*	*kW*	*unitless*
Nasa IRT	1.83	2.74	167.2	15 - 275	3730	0.220
CIRA	2.25	2.35	132.0	5-300	4000	0.450
Cox	0.71	1.17	98.3		149	0.260
METU IRT	1.00	1.00	100.0	8 - 100	322	0.450*

Average of existed tunnel presented in the table

Among industrial motor manufacturer catalogues, it is easy to find motors with 315 kW tri-phase motors with various RPM configurations. Also, It should be noted that these power values of the motors are the continuous power level, and utilization with surge conditions for a short duration can be applicable. Therefore, a 315 kW motor can be used for the requirement of 322 kW. In other ways, it can be divided into four quantities of 75 kW power motors with 2x2 configuration to simplify the implementation of the engines and fans with mechanical complexity. However, this configuration selection will be discussed in detail in the subsequent section. Using a VFD device, the fan drive motor can be controlled, allowing variable tunnel speeds from 5 to 100 m/s.

According to wind tunnel design parameters, test section airspeed should be at least 100 m/s. Therefore, power units comprising fans and engines should satisfy the flow rate needed to reach this speed.

$$Q = U_\infty * A_{tsec} \tag{98}$$

$$Q = 100\,\frac{m}{s} * 1\,m^2 = 100\,\frac{m^3}{s} = 360{,}000\,m^3/hour \tag{99}$$

After this calculation, the power unit should satisfy the 360,000 cubic meters per hour without any pressure loss. However, with pressure loss calculations, this parameter stays the same, but power needs to overcome the flow rate should be increased. There is commercial software for selecting motor, fan and other parameters belonging to engine units. The following figures are calculations for this work.
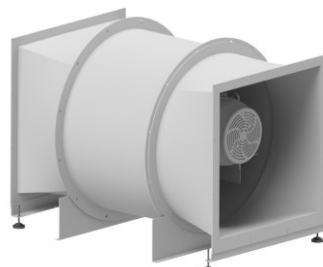
Figure 54: Power Plant

4.4   Design Calculations

The pressure drop calculations are a vital aspect of wind tunnel design because they help ensure that the tunnel can maintain the desired flow conditions for the tests to be conducted. Pressure drop refers to the pressure drop that occurs as air flows through the tunnel and its various components, like the contraction cone, test section, and diffuser. There are several factors that can affect the pressure loss in a wind tunnel, including:

Flow velocity: The flow velocity of the air within the tunnel can significantly affect the pressure loss. At higher velocities, the pressure loss tends to increase due to the increased kinetic energy of the air.

Hydraulic diameter and shape of the tunnel: The hydraulic diameter and shape of the tunnel can also affect the pressure loss, as smaller and more complex shapes can create additional resistance to the flow of air.

Surface roughness: The surface roughness of the walls and other components of the tunnel can also affect the pressure loss, as rough surfaces can create additional resistance to the flow of air.

Flow separation: Flow separation, which occurs when the air detaches from the walls or other surfaces of the tunnel, can also increase the pressure loss.

Engineers typically use CFD simulations or other analyses to calculate the pressure loss in a wind tunnel to predict the flow and pressure conditions. These calculations help to ensure that the tunnel can maintain the desired flow conditions for the tests being performed and can also be used to identify and resolve any issues or challenges that may arise.

Overall, pressure loss calculations are an essential aspect of wind tunnel design, as they help to ensure that the tunnel can maintain the desired flow conditions for the tests being performed.

Pressure loss for all components can be calculated by multiplying dynamic pressure with pressure loss coefficient. The pressure loss coefficient is constant and can be calculated for different types of channels..

$$\Delta p = K * q$$

$$\Delta = K * \frac{1}{2} * \rho * V^2 \qquad (100)$$

Where K is the pressure loss coefficient and q is dynamic pressure of related part of the wind tunnel. In the work of Idelchik, all of the pressure loss works and formulations are represented [74]. In the subsequent section, we will compute the various components of the icing wind tunnel individually, as outlined in the corresponding components section.

4.4.1   Test Section

In the process of designing a wind tunnel, the test section holds significant importance as it greatly influences other design factors. The Reynolds number and maximum flow velocity within the test chamber serve as crucial parameters that impact the overall design process. Consequently, the technical requirements of the test section play a vital role in determining the inputs for the entire design process. The dimensions of the test section and the air velocity within it dictate the size of the models that can be accommodated and the Reynolds number that can be achieved.
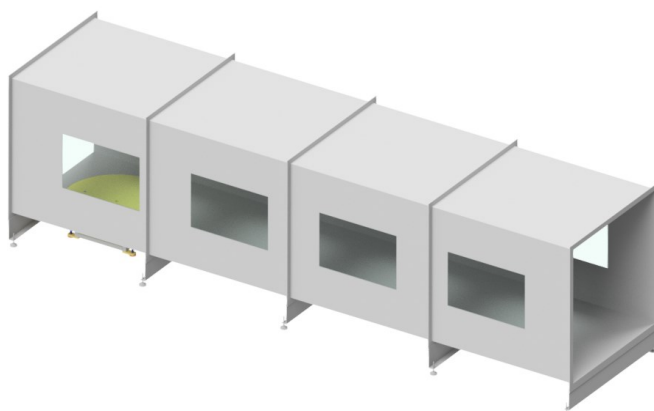
Figure 55: Test Section

The geometry of the test section is typically determined based on the intended application. In industrial settings, a square cross-section is commonly employed. To ensure unobstructed flow, the cross-sectional area of the test specimen should not exceed 10% of the test section's area. Additionally, the high air velocity within the test section leads to a decrease in static pressure. To address this, a small opening, constituting approximately 1.0% of the test section's length, should be incorporated on the surface of the test section.

As established in the preceding chapter, the desired velocity within the wind tunnel's test chamber is 100 m/s, while the dimensions of the square test chamber have been determined to be 1 meter by 1 meter. Given that the minimum temperature to be achieved within the test chamber is -30 degrees Celsius, all subsequent calculations will be conducted with these specified dimensions and temperatures.

The hydraulic diameter will be determined in the initial phase of the test chamber analysis. This parameter is computed using Equation 101, where the variable *A* represents the inlet area. Barlow et al. have suggested that length of the test section should range from 0.5 to 3 times the hydraulic diameter. After evaluating the available tunnels, it was determined that using a value of 2 times the length is appropriate [75].

$$D_h = 2 * \sqrt{A/\pi}$$
(101)

Measuring pressure loss in the test section is an important aspect of wind tunnel testing, as it can provide insight into the flow characteristics of the test section and the model being tested. It can also help to identify any issues or problems with the wind tunnel that may need to be addressed, such as blockages or roughness on the walls of the test section.

The expression gives the pressure loss coefficient formulation:

$$\xi = \lambda * \frac{L}{D_h}$$
(102)

Where,

- L ,   test chamber length
- λ,   friction factor
- K_{test},   pressure loss coefficient

$$\lambda = 1/(1.8 * \log(Re) - 1.64)^2 \tag{103}$$

$$K_{test} = \lambda * L/D_h \tag{104}$$

All calculated parameters for the wind tunnel test chamber are given in Table 32. These values will be used in the calculation of the next component.

Table 32: Test Section Sizing Parameters

	Input	Value	Unit
Dimensions	W_{in}	1.00	m
	H_{in}	1.00	m
	W_{out}	1.00	m
	H_{out}	1.00	m
	A_{in}	1.00	m^2
	A_{out}	1.00	m^2
	L	2.00	m
	α	0	rad
	β	0	rad
Aerodynamics terms	V_∞	100	m/s
	T_∞	243.15 (-30.00)	K (^0C)
	Q_{in}	100	m^3/s
	μ	1.56451E-05	$N * s/m^2$
	ν	1.078E-05	m^2/s
	D_h	1.000	$unitless$
	ρ_∞	1.452	kg/m^3
	Re	9.28E+06	$unitless$
	P_{total}	101,325	Pa
	P_{static}	94,065	Pa
	M_∞	0.320	$unitless$
Pressure Loss	λ	0.00841	
	K_{test}	0.01683	
	Δp_{test}	122.173	Pa

4.4.2 Settling Chamber

In order to decrease the turbulence level inside the test section of the wind tunnel, a settling chamber which comprises honeycomb and meshes is needed. It is a basic constant section channel without instruments inside the settling chamber. The settling chamber inlet pairs with the last corner before the test section and is connected to the spray bar part to match their mechanical interfaces. Flow quality and turbulence intensity levels should be lower than 0.1% for professional aerospace applications. These conditions can be satisfied by installing two or more screens and a proper honeycomb inside the settling chamber. Therefore, a combination of honeycomb–screen–screen was selected. The screens have a mesh size of 5 and 10. Moreover, the honeycomb size is 10.40 mm. This part discussed in detail the turbulence reduction factor part.
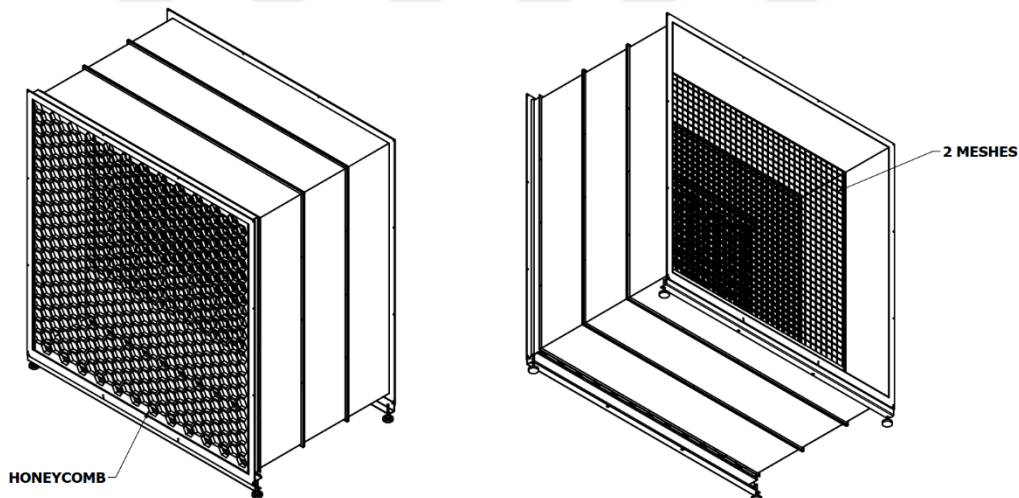
Figure 56: Settling Chamber

4.4.2.1 Honeycomb Calculations

Honeycomb structures have been found to effectively reduce lateral turbulence when fluid flows through long and narrow pipes. However, using a honeycomb also introduces axial turbulence, which limits the thickness of the honeycomb. It is

recommended that the length of the honeycomb should be at least six times greater than its diameter to mitigate this issue [75].

The honeycomb in the settling chamber aligns flow through the wind tunnel axis, reducing flow deviation in other directions. In order to select honeycomb size in the wind tunnel design procedure, hydraulic cell diameter (D_h), length (L), and porosity (β_h) are the important parameters. Porosity of the honeycomb can be easily calculated by geometric approach [76], [77].

$$\beta_h = \frac{A_{flow}}{A_{tot}} \tag{105}$$

Two important factors rely on the following equation for selecting honeycomb sizes [75].

$$6 \leq \frac{L_h}{D_h} \leq 8 \tag{106}$$

Porosity of the honeycomb should be greater that 0.8 value [75].

$$\beta_h \geq 0.8 \tag{107}$$
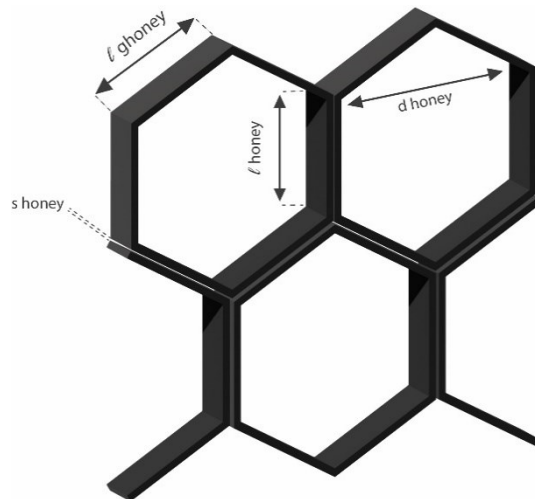
Figure 57: Honeycomb Schematics

Figure 57, the honeycomb cell side (l_{honey}) can be calculated with following formula.

$$l_{honey} = \frac{d_{honey}}{2\sin{(60^0)}} \tag{108}$$

the outer cell side ($l_{g\ honey}$) can be revised with following equation.

$$l_{ghoney} = l_{honey} + 2\frac{S_{honey}}{tan60^0} \tag{109}$$

The metal sheet parts of the honeycomb (z) can be computed with the following equation.

$$z = 2l_{honey} + l_{ghoney} \tag{110}$$

In order to calculate honeycomb's area subjected to flow, the following formula can be used.

$$A_{parallelogram} = l_{honey}S_{honey} \tag{111}$$

$$A_{trapeze} = \frac{(l_{honey} + l_{ghoney})S_{honey}}{2} \tag{112}$$

The porosity of the honeycomb is calculated in the order of height and width by the following formula.

$$n_z = \frac{L_1}{z} \tag{113}$$

Ratio can be calculated by the following formula.

$$n_{sheet} = \frac{L_2}{\frac{d_{honey}}{2} + S_{honey}} \tag{114}$$

Area of honeycomb in manner of cross section can be calculated as following equation.

$$A_{sheet} = 2\left(A_{parallelogram} + A_{trapeze}\right)n_z\, n_{sheet} \tag{115}$$

Solidity of honeycomb can be calculated as follows.

$$\sigma_h = \frac{A_{sheet}}{A_{total}} \tag{116}$$

Solidity and porosity combined together is 1.

$$\beta_h + \sigma_h = 1 \tag{117}$$

Honeycomb hydraulic diameter can be calculated by starting the computing cell area.

$$A_{cell} = 6\left(\frac{d_{honey}}{2}l_{honey}\frac{1}{2}\right) = 6\frac{d_{honey}}{2}\frac{d_{honey}}{\sqrt{3}}\frac{1}{2} = \frac{3}{2}\frac{d_{honey}^2}{\sqrt{3}} \tag{118}$$

Hydraulic diameter of the honeycomb can be calculated by imposing same size of cylinder geometric calculation [66].

$$\frac{\pi D_h^2}{4} = \frac{3}{2}\frac{d_{honey}^2}{\sqrt{3}} \tag{119}$$

$$D_h = d_{honey}\sqrt{\frac{6}{\pi\sqrt{3}}} \tag{120}$$

The contraction ratio was selected as 9 to obtain high-quality flow inside the test section. According to this parameter, the settling chamber dimensions were calculated as 3000 mm to 3000 mm rectangular. However, manufacturer standards of the honeycomb are limited, with a maximum length of 3000 mm and a maximum height of 1500 mm. Therefore, the honeycomb will be placed as two half pieces side by side. Another parameter for the honeycomb is foil thickness. Honeycomb can be

manufactured with various materials such as stainless steel, aluminum, and ABS plastics. In this thesis, aluminum is selected as the core material of honeycomb. In most case foil thickness of aluminum honeycomb foil thickness is 0.06 mm. Due to hostile conditions inside the tunnel, aluminum should be coated with the passivation method.
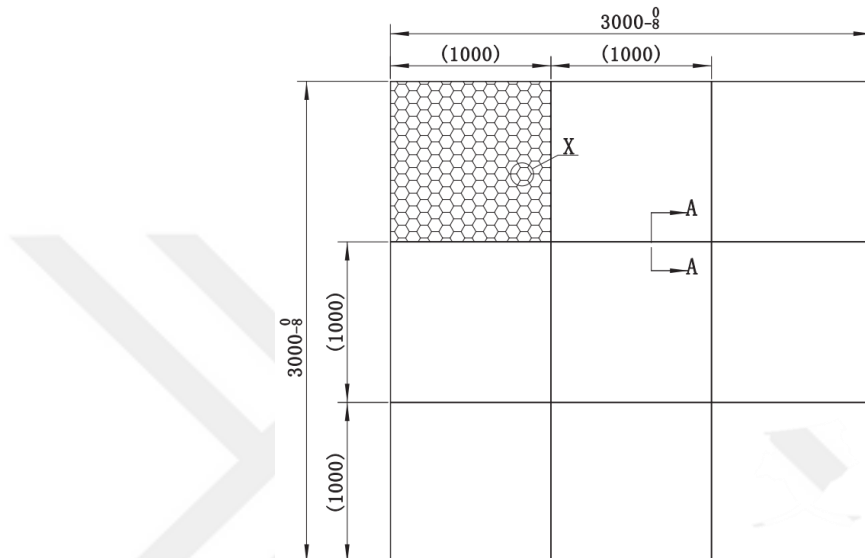
Figure 58: Honeycomb Technical Drawing

The empirical relations developed by Prandtl in 1933 continue to be employed for determining the pressure loss coefficient of the honeycomb [78].

$$K_h = \lambda_h * \left(\frac{L_h}{D_h} + 3\right) * \left(\frac{1}{\beta_h}\right)^2 + \left(\frac{1}{\beta_h} - 1\right)^2 \qquad (121)$$

$$\lambda_h = \begin{cases} 0.375 * \left(\frac{\Delta}{D_h}\right)^{0.4} Re_\Delta^{-0.1} & Re_\Delta \leq 275 \\ 0.214 * \left(\frac{\Delta}{D_h}\right)^{0.4} & Re_\Delta \leq 275 \end{cases} \qquad (122)$$

Based on the findings of previous experimental studies, Barlow et al. propose that a honeycomb cell diameter equal to the size of the settling chamber divided by 150 is optimal. Furthermore, they recommend a cell depth ranging from 8 to 12 times the

cell diameter for optimal performance. These considerations will be incorporated into the design process at this stage [69].

Table 33: Honeycomb Main Parameters

Description	Symbol	Value	Unit
Honeycomb Height	H_{honey}	3000	mm
Honeycomb Height	W_{honey}	3000	mm
Cell Diameter	d_{honey}	10.40	mm
Sheet Metal Thickness	s_{honey}	0.06	mm
Roughness	δ	15.00	μm
Length	L_h	120.00	mm
Cell Hydraulic Diameter	D_h	10.92	mm
Length to Hydraulic diameter ratio	$\dfrac{L_h}{D_h}$	10.99	
Honeycomb Cell Side	l_{honey}	6.00	mm
External Cell Size	l_{ghoney}	6.07	mm
Divisions	z	18.08	
Area of parallelogram	$A_{parallelogram}$	0.36	mm^2
Area of trapeze	$A_{trapeze}$	0.36	mm^2
Divisions height-wise	n_z	166	
Divisions width-wise	n_{sheet}	570	
Area of Sheet	A_{sheet}	136751	mm^2
Honeycomb Solidity	σ_h	1.52%	
Honeycomb Porosity	β_h	98.48%	
Area of Cell	A_{cell}	93.67	mm^2
Reynolds Number	Re_{honey}	7755.89	
Friction Factor	λ	0.0153	
Pressure Loss Coefficient	K_{hc}	0.2213	
Pressure Loss	ΔP	19.58	Pa

As indicated in Table 33, all of the essential empirical methodologies discussed earlier have been satisfied. Drawing from practical knowledge, it is evident that this honeycomb structure will effectively function in the regulating flow.

The honeycomb will be located at the entrance of the settling chamber. Although screens can be placed in front of the honeycomb to reduce swirl angles in wind tunnel experiments in ambient tunnels, using as few screens as possible for the icing tunnel is preferable. Therefore, the airflow will first pass through the honeycomb and enter the settling chamber. Sufficient space will be left behind for the screens to ensure

pressure recovery. It is generally recommended to leave a gap of 0.2 times the size of the settling chamber between the mesh screen combinations and the honeycomb. Hence, a gap of 600 mm will be ensured.

4.4.2.2   Mesh Screen Calculations

In order to mitigate the turbulence of the incoming flow, tension screens are employed within the settling chamber. These screens disrupt the large-scale turbulent eddies, breaking them down into smaller-scale eddies that dissipate. In other words, screens mainly reduce velocity fluctuations. It is recommended that the spacing between the screens be approximately equivalent to the length scale of the larger energetic eddies [79]. Moreover, screens have a minimal impact on lateral turbulence but are highly effective in reducing longitudinal turbulence. However, in the contraction chamber, the attenuation of lateral turbulence is not as significant as longitudinal turbulence. As mentioned earlier, a single screen can significantly reduce the level of longitudinal turbulence. In addition to that, combining more than two screens in an intermittent position in the settling chamber would be more advantageous [66]. However, by using a series of two or three screens, the turbulence level in both directions can be attenuated to as low as 0.15% [80]. Previous studies have demonstrated that incorporating multiple screens with varying porosities within the settling duct, with the coarsest screen positioned closest to the incoming flow and the finest screen positioned closest to the test section, leads to reduced turbulence levels within the test section. Following the screens, it is essential to include a settling chamber to allow for the dissipation of the small-scale fluctuations generated by the wires before they are intensified by contraction [76], [77].
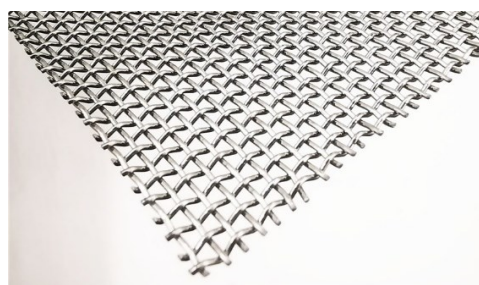
Figure 59: Mesh

The utilization of a mesh screen is widely recognized as advantageous for enhancing the flow quality within a wind tunnel. However, it is essential to note that this assumption does not hold true in the context of icing tunnels. The unique conditions in icing tunnels, characterized by high LWC and low temperatures, inevitably lead to ice accumulation on mesh screens. Consequently, the use of mesh screens is not favored in many icing wind tunnels. This preference is primarily attributed to the inability of mesh screens to effectively reduce the already elevated turbulence levels to levels representative of actual ambient conditions. This limitation arises due to the presence of intrusive equipment and instruments, such as the spray bar and heat exchanger, within the icing wind tunnel. However, despite these drawbacks, the use of this component and its implementation in a way that does not have a negative impact or can be removed if requested is planned in this study. For these reasons, using mesh screen combinations with high range values and low blocking values is planned.

Effective mesh porosity size should be between 0.58 – 0.8 [77].

$$0.58 \leq \beta_s \leq 0.8 \tag{123}$$

the screen wire can be calculated with following equation.

$$n_w l d_w + n_w l d_w - n_w (n_w d_w^2) \tag{124}$$

Where,

   d_w, is the wire diameter,

   n_w, is the generic wire number in the mesh,

   l, is the settling chamber cross-section side.

The last term in in the equation takes into account the areas where the wires cross.
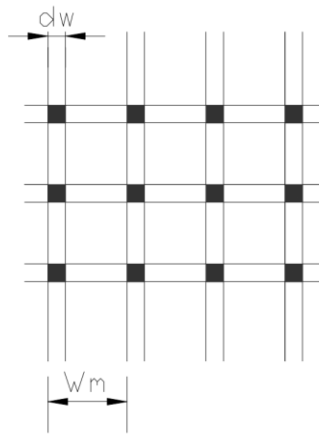
Figure 60: Mesh Schematic

Honeycomb screen porosity in following equation.

$$\beta_s = \frac{A_{flow}}{A_{total}} = \frac{l^2 - 2n_w l d_w + n_w^2 d_w^2}{l^2} = 1 - \frac{2n_w d_w}{l} + \frac{n_w^2 d_w^2}{l^2} \qquad (125)$$

Simplifying equation,

$$\beta_s = \left(1 - \frac{n_w d_w}{l}\right)^2 \qquad (126)$$

Following equation defines mesh density,

$$\rho_m = \frac{n_w}{l} \qquad (127)$$

Screen mesh division can be calculated (w_m) in following equation.

$$w_m = \frac{1}{\rho_m} \qquad (128)$$

Porosity can be written as in following equation.

$$\beta_s = (1 - d_w \rho_m)^2 \qquad (129)$$

In their comprehensive investigation, Groth et al. determined that a distance of 20 times of the mesh length is adequate for restoring the flow through the mesh screen [81]. This distance was duly considered during the placement of the mesh screens in the present study.

In the subsequent equations, the calculation of the pressure loss coefficient is presented. The terms included in the equation are defined as follows: K_{mesh} represents the smoothness coefficient, typically ranging from 1.0 to 2.1. However, Idelchik et al. have suggested a value of 1.0 for new metallic wires, 1.3 for metallic wires with a circular cross-section, and 2.1 for silk fibers. In most cases, a value of 1.3 is considered suitable [74].

$$K_m = K_{mesh} * K_{Rn} * \sigma_s + \frac{\sigma_s^2}{\beta_s^2} \tag{130}$$

$$K_{Rn} = 0.785 * \left(\frac{Re_{ew}}{241} + 1.0\right)^{-4} + 1.01 \quad for\ Re_{ew} \leq 400 \tag{131}$$

For the Re_{ew} higher that 400. K_{rn} is taken as 1.

As mentioned earlier, the pressure drop calculations conducted in the study were found to be close to existing experimental studies but have yet to be an exact match. Therefore, a new approach for these calculations is proposed in this study. In this approach, experimental data corresponding to the Reynolds values of the designed icing wind tunnel's relevant region were obtained, represented in Figure 61. Regression analysis was performed on this data to formulate an equation that could be used for curve-fitting calculations. As a result, more accurate pressure drop values could be calculated within the relevant range of Reynolds numbers.
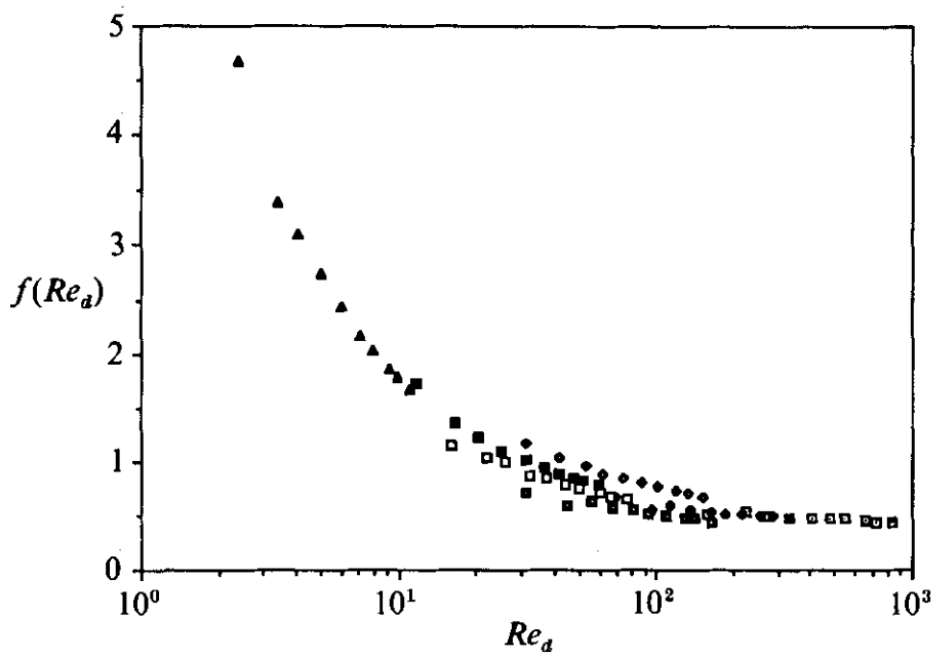
Figure 61: Experimental Values of Damped Screen Reynolds Function [81]

When the curve fitting calculation is performed on the graph shown in Figure 61, the equation shown in equation 132 and the coefficients listed below it are obtained.

$$f(Re) = \alpha + \theta * Re^{\eta}/(\kappa^{\eta} + Re^{\eta})$$
$$\alpha = 184.4489$$
$$\theta = -184.03969 \tag{132}$$
$$\eta = 0.794601$$
$$\kappa = 0.020280291$$

In the context of this calculation, the following formula is utilized to calculate the pressure loss coefficient [81]. By employing the Reynolds number function and the solidity function, which are calculated, the pressure loss calculation can be performed.

$$K_{f(Re)} = \left(\frac{1-\beta^2}{\beta^2}\right)^{f(Re)} \tag{133}$$

As observed in Table 34, the second approach yields results much closer to the experimental data. Therefore, calculations will proceed using the second approach due to these reasons.

Table 34: Screen Pressure Loss Comparison for Different Approaches

		Pressure Loss (Pa)		
No	Reynolds Number	Experimental [81]	1st Approach	2nd Approach
1	841.04	10.20	12.51	10.33
2	336.42	9.90	11.39	9.95
3	168.21	7.35	10.46	8.05
4	168.21	14.85	19.49	16.27
5	80.74	11.85	13.82	11.97
6	63.92	24.60	23.95	24.01
7	13.46	43.50	21.36	40.91

Firstly, this study proposes the use of a combination of a honeycomb structure and two mesh screens. The selection of mesh screens was determined through a series of experiments aimed at reducing non-uniformities. Initially, a low mesh value with a lower pressure drop coefficient (K<1.5) and higher porosity was used to decrease non-uniformities. Subsequently, a higher mesh value with a tighter weave was employed to minimize variations in the upstream flow. Therefore, commercial screens were chosen for this purpose.

Table 35 shows the mesh screen calculation for the case study. In this part, screens available in the market are listed in Table 35 , and mesh sizes selected for use in wind tunnels are highlighted in grey. In this stage, attention has been given to ensuring that the porosity values of the screens are as high as possible while minimizing pressure loss. Additionally, screens that are effective for turbulence have been selected.

The following table presents the mesh number, which is a measure of the fineness of a mesh and indicates the frequency of the mesh used. Additionally, the mesh number

represents the number of openings per inch in numerical terms. Therefore, as the mesh number increases, the fineness of the mesh also increases.

Table 35: Commercially Available Mesh Sizes

Mesh No.	Wire Dia	Porosity %	Pres. Loss Coefficient
4	1	71	0.4301
5	1	65	0.6129
6	1	58	0.8465
7	1	52	1.1488
8	0.65	63	0.6723
10	0.57	60	0.7993
12	0.47	61	0.7966
14	0.47	55	1.0669
16	0.37	59	0.8905
16	0.47	50	1.4140

The arrangement of screens is of great importance for the wind tunnel. Their placement in front of the test chamber and contraction cone is to achieve a high-quality and fast airflow in the test chamber. However, their relative positioning is also crucial for this airflow quality. Typically, screens are placed where there is a sudden change in the geometry of the area or pressure change, but in our case, the settling chamber has a straight wall. The positioning of the screens is essential to ensure static pressure recovery and a distance of 0.20 times each dimension of the settling chamber is considered satisfactory. Therefore, there will be a spacing of 600 mm between each screen.

4.4.2.3   Turbulence Reduction Factor

Turbulence reduction factor (TRF) is a measure of the effectiveness of a device or system in reducing the turbulence of a fluid flow. It is often used in the study of fluid dynamics. And it is defined as the ratio of the turbulence intensity of the flow after the device or system is applied to the turbulence intensity of the flow before the device or system is applied [81].

The turbulence intensity measures the strength of the turbulent fluctuations in a fluid flow. It is defined as the ratio of the root mean square (RMS) velocity of the

fluctuations to the mean velocity of the flow. The turbulence intensity is typically expressed as a percentage.

The TRF is often used to evaluate the performance of various devices or systems designed to reduce turbulence in a fluid flow, such as flow straighteners, vortex generators, and boundary layer control devices. It is also used to predict the effect of these devices on the performance and stability of systems sensitive to turbulence, such as aircraft, ships, and wind turbines.

Generally, a high TRF indicates that the device or system effectively reduces turbulence. In contrast, a low TRF indicates that the device or system is less effective at reducing turbulence. The TRF is an essential parameter in the design and optimization of systems that are sensitive to turbulence and is used to predict the impact of turbulence on the performance and stability of these systems [81].

Turbulence reduction is a phenomenon that is also provided by the pressure drop made by the screens, but which significantly improves the flow quality in the wind tunnel. It is also known as a damped screen. Looking at the work done by Groth et al. on this subject, they developed a method to determine how much the turbulence intensity is reduced in the flow [81]. Although this method underestimates the reduction of turbulence intensity, it does not pose a problem for our studies. Therefore, this method was calculated for screen meshes, and screen mesh types were selected accordingly.

Following the formula proposed by Dryden & Schubauer which is an empirical approach for the turbulence damping by screen combinations [82]. K_i is the respective pressure loss coefficient, and N is the number of the screens utilized in the test section.

$$(1 + K_i)^{0.5} * N \qquad (134)$$

The findings of the experiments conducted in this study indicate that walls with the lowest pressure loss coefficient should be selected. If multiple walls are utilized, choosing the walls with the least amount of loss is advisable. This recommendation is based on the observation that removing mesh screens with higher mesh numbers

had a negligible impact on the reduction of turbulence intensity, as demonstrated in the study. For this reason, our selections are made in the light of this information.

As mentioned before, mesh screens have a prominent effect on decreasing the velocity variation. The following equation represents the calculation of variation velocity. Δu_1 and Δu_2 are the streamwise velocity variations upstream and downstream, respectively.

$$\frac{\Delta u_2}{\Delta u_1} = \frac{1 + \alpha - \alpha * K_0}{1 + \alpha + K_0} \tag{135}$$

$$\alpha = \frac{1.1}{\sqrt{1 + K_0}} = \frac{\Delta v_2}{\Delta v_1} \tag{136}$$

All calculations regarding the mesh screen are conducted and turbulence reduction and velocity variation parameters come out as expected. But it should be noted that in icing wind tunnels, the presence of instruments and equipment, inherent to their nature, results in high turbulence levels. Despite this fact, this study calculates that the addition of two screen meshes reduces the existing turbulence values by one-third. Although this calculation underestimates the turbulence intensity, it is essential to note that a more significant reduction in turbulence is expected with higher levels. This finding significantly improves the performance of the designed wind tunnel for icing conditions. Upon careful examination of the graphs in Figure 63 and Figure 64, it is evident that the decrease in flow speed variation and turbulence intensity is sufficient and appropriate.
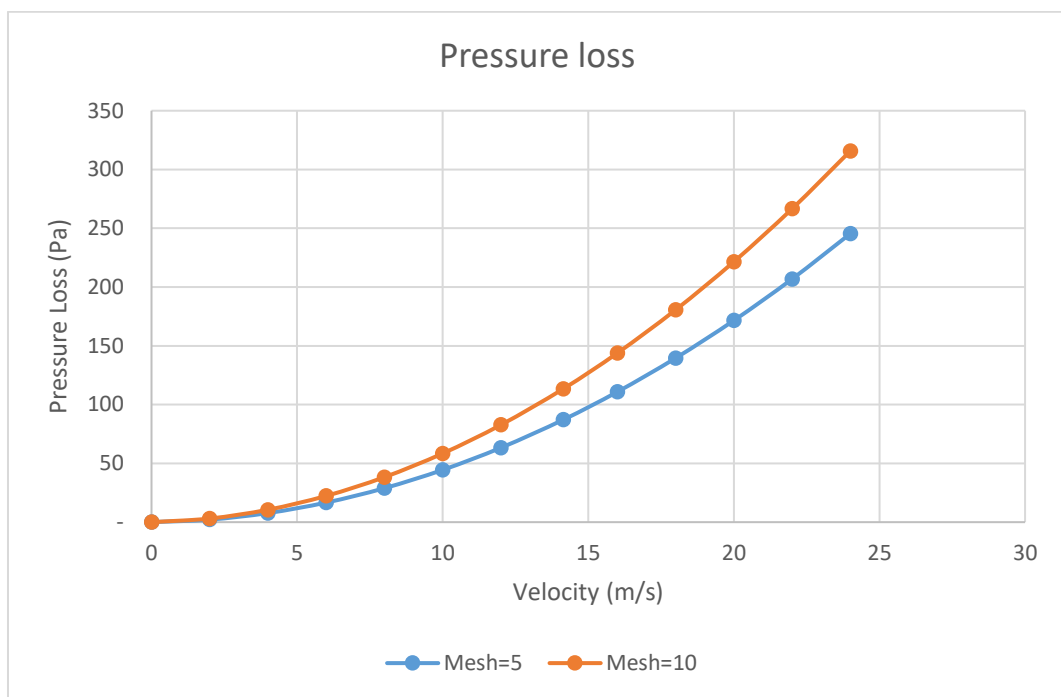
Figure 62: Mesh Screen Pressure Loss
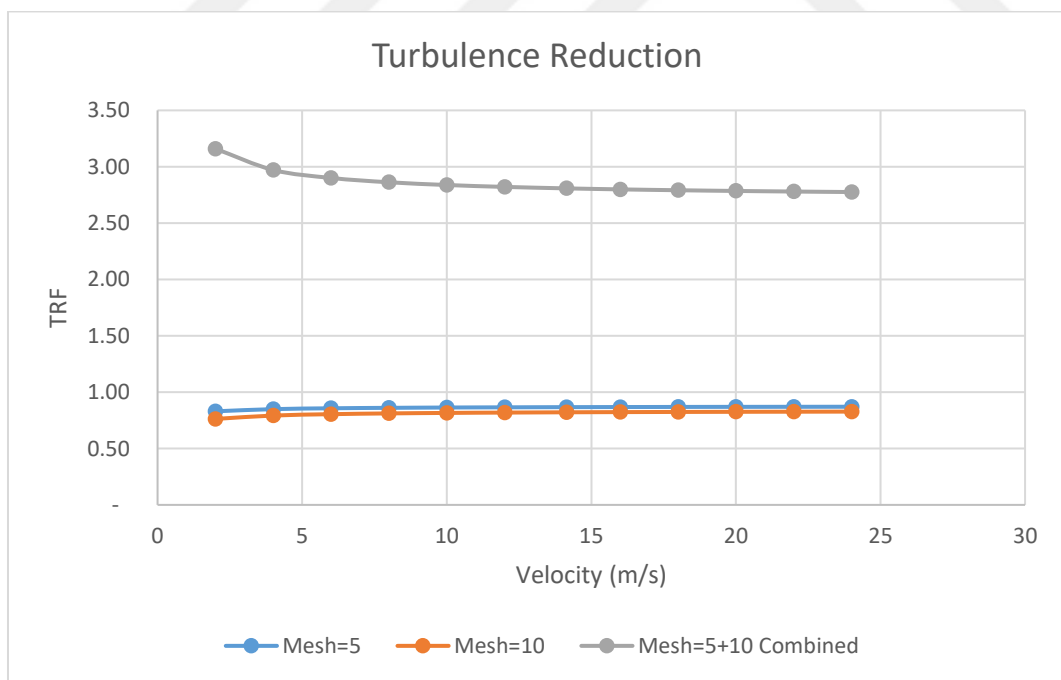
Figure 63: Turbulence Reduction Factor
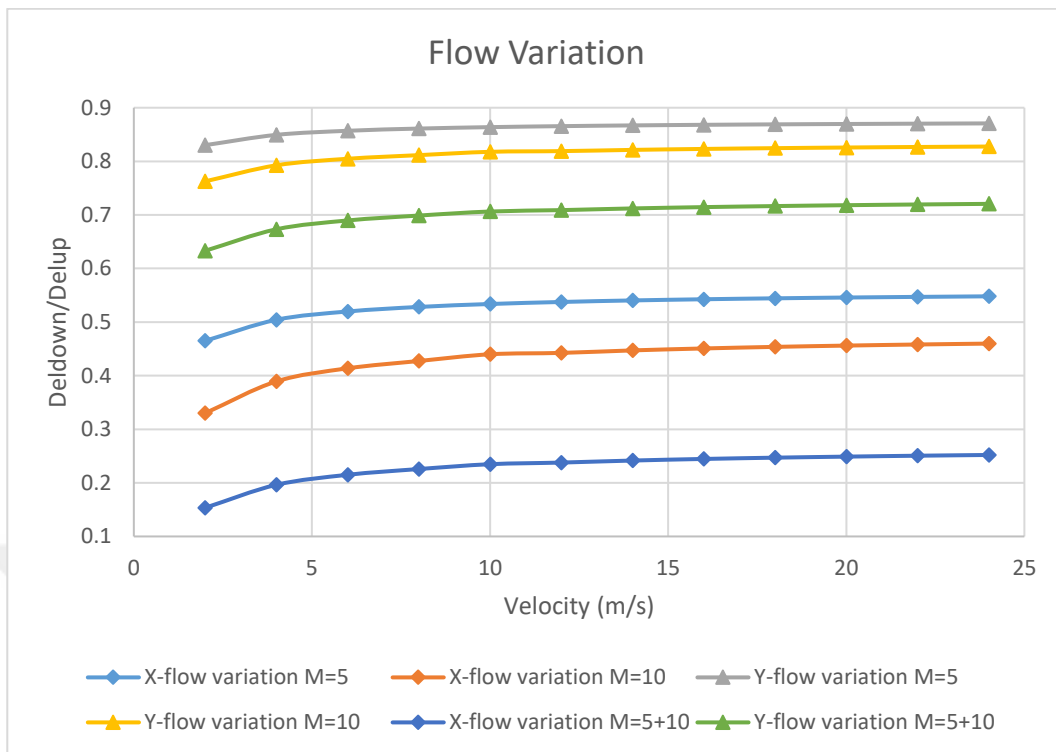
Figure 64: Flow Variation

Table 36: Mesh Screen Main Parameters

		Mesh #1	Mesh #2	Unit
Mesh	M	5	10	-
Mesh Wire Diameter	d_w	1.0	0.57	mm
Mesh Division	w_m	3.2	2.55	-
Screen porosity	β_s	0.65	0.60	-
Division	n_w	590	1189	-
Area of flow	A_{flow}	5,808,100	5,414,138	mm^2
Area of Settling Chamber	A_{total}	9,000,000	9,000,000	mm^2
Screen Mesh Density	ρ_m	0.20	0.39	-
Reynolds	Re	1280.4	729.83	-
Local Loss Coefficient	K_m	0.6129	0.7993	-
Pressure Loss	Δp	87.71	114.38	Pa
Velocity at Settling Chamber	V_∞	11.11	11.11	m/s
Damping Factor		0.79	0.75	-
Turbulence Reduction Factor	TRF	1.27	1.341	-
Flow variation damping x-axis	$\dfrac{\Delta u_2}{\Delta u_1}$	0.4649	0.3299	-
Flow variation damping y-axis	$\dfrac{\Delta v_2}{\Delta v_1}$	0.83	0.76	-

4.4.3 Contraction Cone

One of the most essential components in the wind tunnel is the contraction cone, which immensely affects flow speed and quality in the test section. Its primary role is to direct the flow from the settling chamber into the test chamber while reducing turbulence and flow inconsistency in the test chamber. The flow's acceleration and the unevenness reduction depend mainly on the contraction ratio. The contraction ratio is the ratio between the area of the inlet and outlet cross sections. Figure 65 shows typical contraction cone [83].

The component known as a contraction cone also referred to as a wide-angle diffuser, is distinguished by the semi-angle of its inlet and outlet. According to Mehda et al. [77]if the semi-angle is greater than 6 degrees, it can be classified as a wide-angle diffuser. Contraction cones can be used in conjunction with screens to minimize turbulence and prevent separation. However, this may not be the preferred option in cases involving icing wind tunnels due to the accumulation of ice.
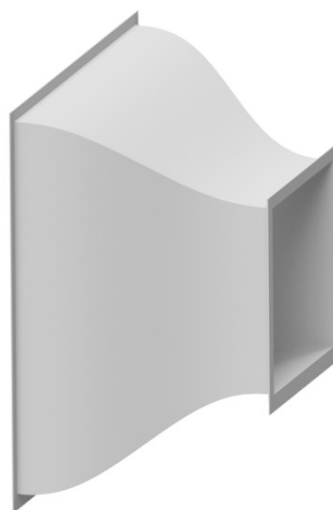
Figure 65: Contraction Cone

Although the contraction cone (N) ratio should be as ample as possible because of the improvement in flow quality, this part and coefficient decide the total dimensions

of the wind tunnel. Therefore, a compromise for this parameter should be found depending on the expected applications.

For most applications, the contraction cone ratio should be 4 and 6, accepted as a good ratio. However, turbulence intensity can be established around 2% with this contraction cone ratio, and these values can be deducted up to 0.5%. However, most applications suggest that the contraction cone ratio should be between 8 and 10. Using nine as the contraction ratio is a good compromise for a wind tunnel design.

The contraction should have reasonable length and good fluid dynamic behavior when the two half-angles of the contraction, $\alpha/2$ and $\beta/2$, assume values of the order of 12º. As for the shape of the contour, according to geometrical calculation, fifth-order polynomial curves are recommended. The profile of a wind tunnel contraction cone is typically described by a polynomial function, which is a mathematical expression consisting of terms combined using addition, subtraction, and multiplication. The polynomial function used to describe the profile of a contraction cone is typically a polynomial of the third or fifth degree, which means that it includes terms with exponents of up to 3 or 5. [83]

For example, the profile of a contraction cone might be described by a polynomial of the form:

$$y = ax^5 + bx^4 + cx^3 + dx^2 + ex + f \qquad (137)$$

where x is the distance along the axis of the cone and y is the height of the cone at that point. The coefficients a, b, and c are constants that are chosen to describe the specific shape of the cone.

Overall, the profile of a contraction cone is an essential factor in designing a wind tunnel, as it determines the flow conditions that will be present in the test section. Using a polynomial function to describe the profile of the cone allows engineers to accurately predict and control these flow conditions, which is essential for reliable and accurate testing.

$$Y_c = Y_{cl} - (Y_{cl} - Y_{c0}) * \left[6\left(\frac{X_c}{L_c}\right)^5 - 15*\left(\frac{X_c}{L_c}\right)^4 + 10*\left(\frac{X_c}{L_c}\right)^3\right] \quad (138)$$

Where,

$$Y_c = Y - axis\ coordinate$$

$$L_c = X - axis\ coordinate$$

$$Y_{c0} = Test\ section\ half - lenght$$

$$Y_{cl} = Settling\ Chamber\ half - lenght$$
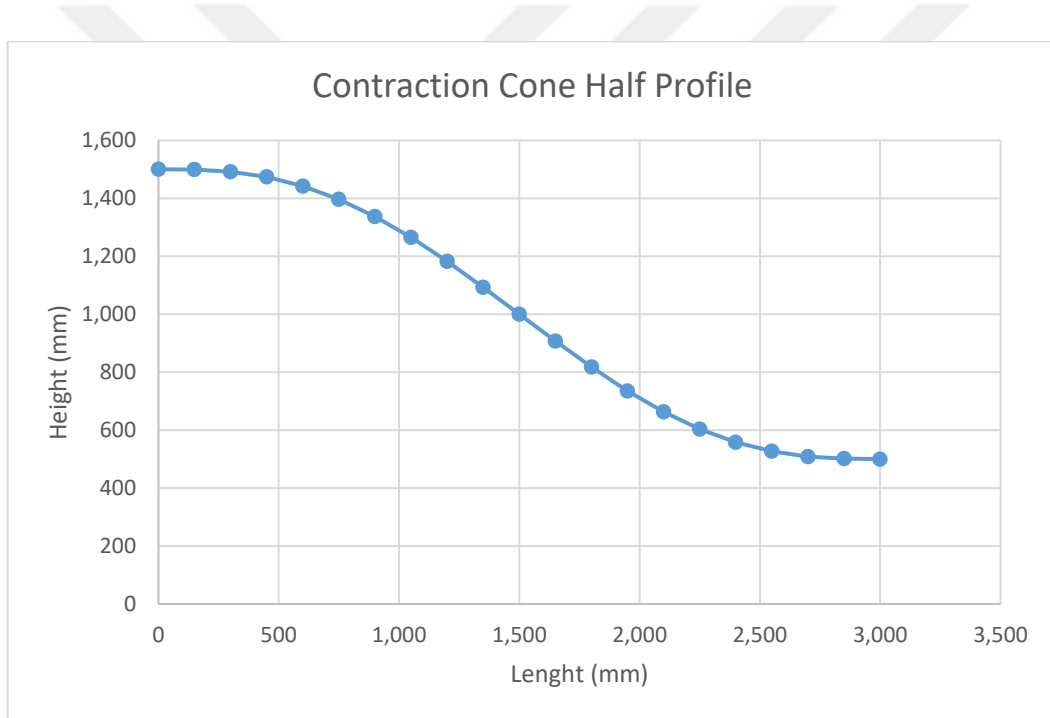
Figure 66: Contraction Cone Half Profile

Contraction Cone Pressure Loss

Contraction cone pressure loss can be calculated as in the following equation.

$$\xi = \left\{\frac{\lambda}{\left[16 * \sin\left(\frac{\alpha}{2}\right)\right]}\right\}\left(1 - \frac{1}{N^2}\right) + \left\{\frac{\lambda}{\left[16 * \sin\left(\frac{\beta}{2}\right)\right]}\right\}\left(1 - \frac{1}{N^2}\right) \quad (139)$$

134

where λ is:

$$\lambda = 1/(1.8\, logRe - 1.64)^2 \qquad (140)$$

In the equation above, Reynolds number is determined by the smallest section of the hydraulic diameter.

Table 37: Contraction Cone Design Parameters

	Input	Value	Unit
Dimensions	W_{in}	3	m
	H_{in}	3	m
	$Contraction\ ratio$	9	$unitless$
	W_{out}	1	m
	H_{out}	1	m
	A_{in}	9	m^2
	A_{out}	1	m^2
	L	3	m
	α	0.322	rad
	β	0.322	rad
Aerodynamics Terms	V_∞	11.111	m/s
	T_∞	243.15 (-30)	$K\ (^0C)$
	Q_{in}	100	m^3/s
	μ	1.56451E-05	$N*s/m^2$
	ν	1.09E-05	m^2/s
	D_h	1.000	$unitless$
	ρ_∞	1.433	kg/m^3
	Re	9.57E+05	$unitless$
	P_{total}	100000	Pa
	P_{static}	93474	Pa
	M_∞	0,312	$unitless$
P. Loss	λ	0.01201	$unitless$
	K_{cont}	0.00469	$unitless$
	Δp_{cont}	33.589	Pa

4.4.4 Diffuser

The primary function of diffusers is to recover static pressure to increase the performance of the wind tunnel and, of course, to close the circuit. For this reason, the half angle of the diffusers is limited to 3.5 degrees during the design step. The main purpose of this limitation is to maintain the flow quality high and the pressure drop minimal.
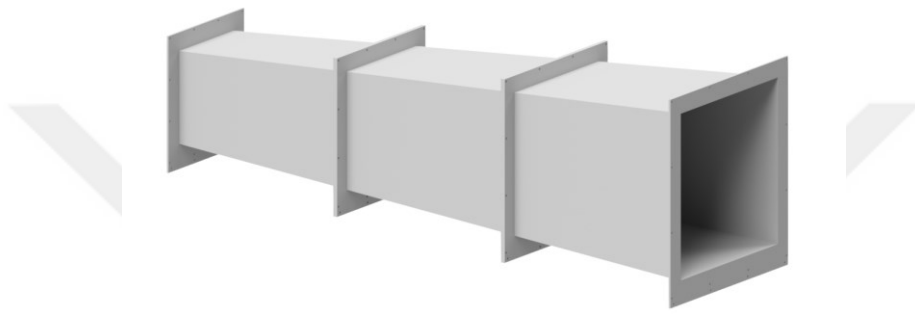
Figure 67: Diffuser

The diffuser semi-angle opening should be less than 3.5 degrees to prevent adverse flow effects. On the other hand, it is of great importance to reduce the dynamic pressure at the entrance of corner number 1 as much as possible to minimize the pressure loss.

Diffuser 2 is a transition channel where the dynamic pressure is still high. As a result, the design procedure that prescribes a maximum value for the semi-opening angle must also be applied here. The other parts of the wind tunnel determine the length of diffuser two.

The drive system is mechanically connected to diffusers 3 and 4. Therefore, the disturbed fluid by the fan flow mostly affected this part of the wind tunnel. Half of the semi-angle criteria still apply in this part.

Diffuser 5 connects corners, and it will be minimal in manner of dimensions, due to the low dynamic pressure. This is especially the case when the contraction cone ratio is high, and the diffuser semi-angle can be larger than 3.5°.

Diffuser Pressure Loss

Pressure loss coefficient is determined by the dynamic pressure in the smallest section of the diffuser. side of the diffuser, is presented by:

$$K_d = K_f + K_{exp} \tag{141}$$

$$K_f = \left(1 - \frac{1}{A_R^2}\right) * \frac{f}{8 * \sin \vartheta_e} \tag{142}$$

$$K_{exp} = K_e(\vartheta_e) * \left(1 - \frac{A_R - 1}{A_R}\right)^2 * \frac{f}{8 * \sin \vartheta_e} \tag{143}$$

$$K_{e(circle)} \begin{cases} A_1 + B_1\vartheta_e \\ A_2 + B_2\vartheta_e + C_2\vartheta_e^2 + D_2\vartheta_e^3 \\ +E_2\vartheta_e^4 + F_2\vartheta_e^5 + G_2\vartheta_e^6 \\ A_3 + B_3\vartheta_e \end{cases} \tag{144}$$

$$K_{e(square)} \begin{cases} A_1 + B_1\vartheta_e \\ A_2 + B_2\vartheta_e + C_2\vartheta_e^2 + D_2\vartheta_e^3 + E_2\vartheta_e^4 + F_2\vartheta_e^5 + G_2\vartheta_e^6 \\ A_3 + B_3\vartheta_e \end{cases} \tag{145}$$

$$\begin{aligned} & 0 < \vartheta_e < 1.5^0 \\ \text{If} \quad & 1.5^0 < \vartheta_e < 5^0 \\ & 5^0 < \vartheta_e \end{aligned}$$

Table 38: Coefficient of Geometric function [78]

Parameter	Circular	Square
A1	0.1033	0.09623
B1	-0.02389	-0.004152
A2	0.1709	0.1222
B2	-0.117	0.0459
C2	0.0326	0.02203
D2	0.001078	0.003269
E2	-0.0009076	-0.0006145
F2	-0.00001331	-0.000028
G2	0.0001345	0.00002337
A3	-0.09661	-0.01322
B3	0.04672	0.05866

Table 39: Diffuser Section Design Parameters

	Input	Diffuser 1	Diffuser 2	Diffuser 3	Diffuser 4	Unit
Dimensions	W_{in}	1.0	1.6	1.85	2.25	m
	H_{in}	1.0	1.6	1.85	2.25	m
	W_{out}	1.6	1.85	2.25	3.00	m
	H_{out}	1.6	1.85	2.25	3.00	m
	A_{in}	1	2.56	3.4225	5.063	m
	A_{out}	2.56	3.42	5.0625	8.994	m^2
	L	9.0375	3.6	5	10.1	m^2
	N	2.56	1.3369	1.48	1.78	m
	α	0.0332	0.0347	0.0400	0.0371	rad
	β	0.0332	0.0347	0.0400	0.0371	rad
Aerodynamics Terms	V_∞	100	39.06	29.22	19.75	m/s
	T_∞	243.15	243.15	243.15	243.15	K
	Q_{in}	100	100	100	100	m^3/s
	μ	1.56E-05	1.56E-05	1.56E-05	1.56E-05	Ns/m^2
	ν	1.09E-05	1.09E-05	1.09E-05	1.09E-05	m^2/s
	D_h	1.000	1.600	1.850	2.250	$unitless$
	ρ_∞	1.433	1.433	1.433	1.433	kg/m^3
	Re	6.39E+06	3.99E+06	3.46E+06	2.84E+06	$unitless$
	P_{total}	100000	100000	100000	100000	Pa
	P_{static}	92835	98906	99388	99720	Pa
	M_∞	0,312	0,312	0,312	0,312	$unitless$
Pressure Loss	η_f	0.0327	0.0151	0.0166	0.0232	$unitless$
	η_s	0.0210	0.0038	0.0075	0.0124	$unitless$
	η	0.0538	0.0189	0.0241	0.0356	$unitless$
	Δp_{diff}	121.630	15.160	9.557	9.950	Pa

4.4.5 Corners

There are four corners in closed-loop wind tunnels. These return channels are responsible for half of the total pressure loss. For this reason, the design of corner turns and the prevention of flow inhomogeneity due to centrifugal force are among the essential design criteria.

The radius of the corner turns is another critical design variable and is proportional to the width of the entrance. In addition, return vanes have been added to ensure the

air's return properly during turns. The spacing and number of return vanes have been calculated in terms of homogeneity and distribution of the returning air, and they have been designed in appropriate amounts and dimensions.
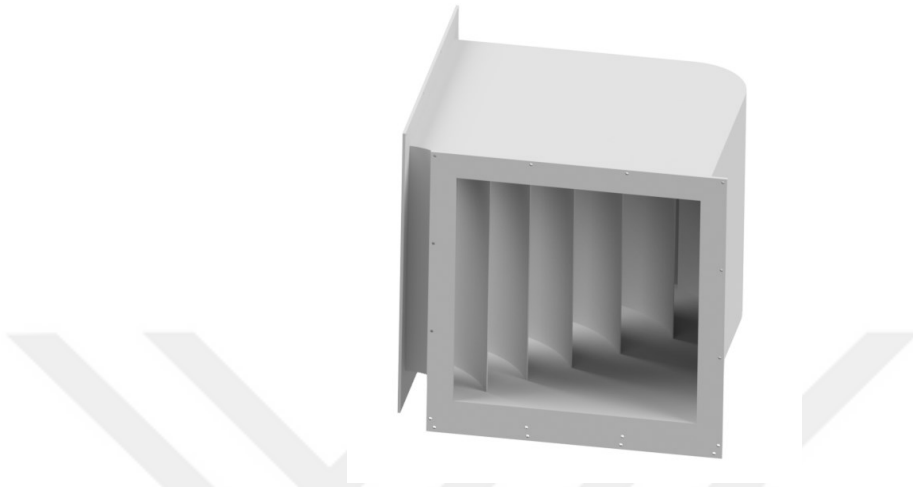
Figure 68: Corner

Pressure loss calculation for closed-loop wind tunnels should be taken into account that most of the pressure losses originated from the corners. Most losses come from the first corner, which is responsible for 30% of the pressure loss.

One of the most critical design parameters in corner design is corner radius. It is parametrically connected with the geometry of the rest of the wind tunnel. A big corner radius causes a pressure drop while a small corner radius causes spoiling homogeneity of the flow.

Corner Sections Pressure Loss

As mentioned in an earlier section, the corner and their vane design are discussed in the early chapters of this thesis. Optimized design is an essential factor due to minimizing the pressure drop and gaining homogeneity flow. Calculation of the pressure loss in the corners has been expressed in the following equations. In this approach, we assume an average number of vanes, $n = 1.4 * \dfrac{S}{c_{vane}}$, where S is the diagonal dimension of the corner, and c_{vane} is the chord of the vane. The pressure loss coefficient was obtained from the Equation 146.

$$K_c = 0.10 + \frac{4.55}{(\log_{10} R_{ec})^{2.58}} \tag{146}$$

Table 40: Corner Section Design Parameters

	Input	Corner 1	Corner 2	Corner 3	Corner 4	Unit
Dimensions	W_{in}	1.6	1.85	3.00	3.00	m
	H_{in}	1.6	1.85	3.00	3.00	m
	W_{out}	1.6	1.85	3.00	3.00	m
	H_{out}	1.6	1.85	3.00	3.00	m
	A_{in}	2.56	3.4225	9.00	9.00	m
	A_{out}	2.56	3.4225	9.00	9.00	m^2
	L	1	1.5	1.5	1.50	m^2
	R Ratio	0.25	0.25	0.20	0.20	$unitless$
	$Corner\ radii$	0.4	0.46	0.60	0.60	$unitless$
	N	1	1	1	1	m
	α	0	0	0	0	rad
	β	0	0	0	0	rad
Aerodynamics Terms	V_∞	39.06	29.22	11.11	11.11	m/s
	T_∞	243.15	243.15	243.15	243.15	K
	Q_{in}	100	100	100	100	m^3/s
	μ	1.56E-05	1.56E-05	1.56E-05	1.56E-05	Ns/m^2
	ν	1.09E-05	1.09E-05	1.09E-05	1.09E-05	m^2/s
	D_h	1.600	1.850	2.999	3.000	$unitless$
	ρ_∞	1.433	1.433	1.433	1.433	kg/m^3
	Re	3.99E+06	3.46E+06	3.05E+06	2.13E+06	$unitless$
	P_{total}	100000	100000	100000	100000	Pa
Pressure Loss	η_f	0.028	0.028	0.026	0.026	$unitless$
	η_s	0.165	0.165	0.201	0.201	$unitless$
	η	0.193	0.193	0.228	0.228	$unitless$
	Δp_{diff}	363.457	203.982	33.094	33.094	Pa

4.4.5.1   Corner Vanes Selection

Wind tunnel corner vanes are devices that are used to control the flow of air through a wind tunnel. They are typically located at the corners of the test section, and their

purpose is to guide the airflow around the corners of the test section and prevent flow separation.

There are several different types of wind tunnel corner vanes, and the specific type used will depend on the design of the wind tunnel and the specific requirements of the testing program. Some common types of corner vanes include straight vanes, curved vanes, and variable geometry vanes.

- Straight vanes are simple devices consisting of a flat plate mounted at an angle to the airflow. They are effective at guiding the airflow around the corners of the test section, but they do not provide any control over the flow.
- Curved vanes are similar to straight vanes, but they are shaped to follow the contour of the corners of the test section. This allows them to provide more control over the flow, as they can guide the airflow around the corners more smoothly.
- Variable geometry vanes are more complex devices that can be adjusted to change the shape of the vane and control the flow of air. These vanes are typically used in wind tunnels with more demanding flow conditions, and they allow engineers to fine-tune the flow around the corners of the test section.
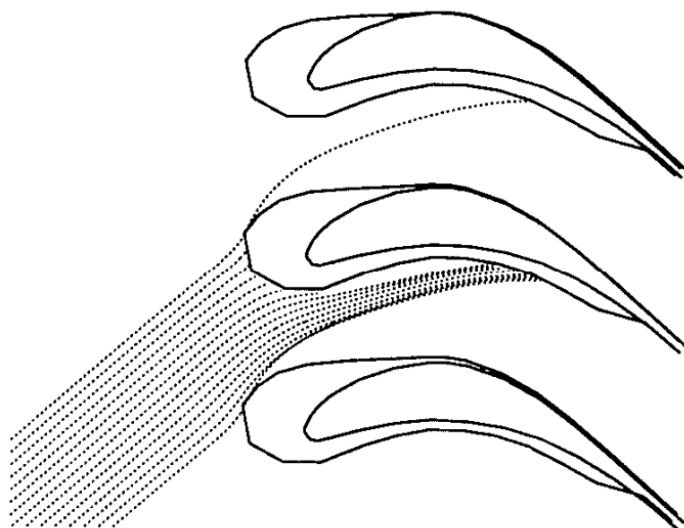

Figure 69: Ice Accretion on Corner Vanes [84].

The selection of sizing and spacing for the corner vanes is critical to the design process. It is crucial to consider the trade-off between the number of vanes and the resulting pressure drop. While a higher number of vanes can lead to a more significant pressure drop, a lower number does not guarantee uniform flow. Additionally, when designing icing tunnels, it is crucial to consider the number of vanes and sizes, aiming for the smallest possible selection. This consideration takes into account factors such as blockage and the potential for icing at the corners. Figure 69 illustrates the accumulation of icing at the corner valves, which can disrupt the flow. The specific choices made for Corner 1 can be found in Table 41. Additionally, all of the design aspects and technical specifications regarding corner vanes can be seen in Table 42.

Table 41: Vane Selection for Corner 1

	N	Gap	$\frac{Gap}{Chord}$	Total Vane Area	Solidity
Normal Vanes	9	0.226	2.5	0.144	5.63%
Optimum Vanes	6	0.323	1.75	0.096	3.75%
Min Vanes	4	0.453	1.25	0.064	2.50%

In addition, the evaluation of angles regarding the air intake and exit from the trailing edge of corner vanes is also essential. Therefore, it has been found to be ineffective when entering with a 0-degree angle of attack. However, Mehta et al. stated that it would be more accurate to place with a leading edge angle of 4-5 degrees [75]. This leading edge angle of attack for the corner vanes is selected as 5 degrees, and CFD analysis of the results represents the final section of this dissertation. Based on experimental tests, it was recommended to use a gap/chord ratio of 0.25 in order to achieve the lowest resistance coefficient (L/D max). However, slightly larger ratios could be employed in the third and fourth corners without causing vane stalling as long as the entry flow was adequately uniform.

Table 42: Corner Vane Calculations

Description	Input	Corner #1	Corner #2	Corner #3	Corner #4	Unit
Number of vane	n	6	6	7	7	
Diagonal length	S	2.263	2.616	4.241	4.243	m
Vane chord	c_{vane}	0.566	0.654	0.848	0.849	m
Gap length	D_{vane}	0.323	0.374	0.530	0.530	m
Vane height	h_{vane}	1.6	1.85	2.999	3	m
Arc length	arc_{vane}	0.628	0.726	0.942	0.942	m
Area of vane	A_{vane}	1.005	1.344	2.826	2.827	m^2
Reynolds of vane	Re_{vane}	2,023,948	1,750,442	863,839	863,551	
Solidity	β	1.75	1.75	1.6	1.6	
Gap/Chord ratio	$\dfrac{D_{vane}}{C}$	0.571	0.571	0.625	0.625	
Pressure loss Coefficient	K_c	0.14	0.14	0.15	0.15	
Pressure loss	P_{loss}	152.32	85.85	12.93	12.91	Pa
Thickness	t_{vane}	0.01	0.01	0.01	0.01	m

4.4.6 Cooling Section Selection

Cooling calculations are an essential aspect of wind tunnel design, as they help to ensure that the tunnel can maintain the required temperature and humidity conditions for the tests being performed. There are a number of factors that must be considered when performing cooling calculations for a wind tunnel, including:

Heat load: The heat load is the amount of heat that must be removed from the wind tunnel to maintain the desired temperature. The propulsion system's power determines the heat load, the heat generated by the test model, and the heat transfer through the tunnel's walls.

Cooling capacity: The cooling capacity is the ability of the cooling system to remove heat from the wind tunnel. The cooling capacity is determined by the size and efficiency of the cooling system, as well as the ambient temperature and humidity.

Temperature and humidity control: The temperature and humidity within the wind tunnel must be carefully controlled to ensure that the tests are conducted under the

desired conditions. This may involve heating and cooling systems, as well as humidifiers and dehumidifiers.

Airflow and ventilation: The airflow and ventilation within the wind tunnel must also be carefully considered, as the airflow can affect the tunnel's temperature and humidity.

In order to perform cooling calculations for a wind tunnel, the heat load and cooling capacity, and then design the cooling system and airflow and ventilation to ensure that the temperature and humidity within the tunnel can be maintained at the desired levels should be determined.

4.4.6.1   Heat Load Calculation

Before performing thermal load calculations for the wind tunnel, data about the wind tunnel and its external environment is required. The priority is to determine the specifications of the wind tunnel. Based on previous designs, the volume of the wind tunnel is approximately 270 cubic meters, and the surface area is around 730 square meters. Since the specific environment in which it will be used is not yet determined, approximate laboratory conditions will be assumed. Therefore, the external temperature will be set at 20 degrees Celsius, and the pressure will be considered as atmospheric pressure. Additionally, insulation will be utilized to minimize heat loss from the walls of the wind tunnel. Furthermore, it is necessary to calculate the heat generated by equipment such as the motor and spray bar located inside the wind tunnel, which is injected into the air.

The phenomenon of heat loss in a wind tunnel can be simplified by the following equation, which represents the balance of convective heat transfer.

$$Total\ Heat\ Loss = \ Q_{wall} + Q_{motor} + Q_{aero} + Q_{latent} + Q_{sens} \quad (147)$$

In the equation above, each term mentioned is sequentially explained as follows; Q_{wall}, heat transfer through the walls, Q_{motor}, heat injection due to motor, Q_{aero},

aerodynamic heating, Q_{latent}, the drop solidification heat, the latent heat, Q_{sens}, heat transfer of the spray bar

4.4.6.1.1 Heat Through Walls

The calculation of the amount of heat passing through the walls is essentially a conduction problem. In order to solve this conduction problem, it is necessary to determine the materials and insulation systems to be used and their technical specifications for the calculation. In order to prevent the flow between the cold and hot air, the wind tunnel design requires insulation. However, the inner wall will be made of sheet metal for production capabilities. Insulation will be applied on top of it to ensure heat preservation.

Additionally, there will be significant temperature changes inside the wind tunnel, which will result in repeated thermal cycling. The presence of excessive moisture and water inside also poses a rusting problem. Therefore, in order to prevent rusting, either galvanized steel or stainless steel must be used. When comparing the thermal conductivities of these two materials, stainless steel has a much lower thermal conductivity and a longer service life. Hence, the decision has been made to use stainless steel. Regardless of the quality and type of stainless steel, their thermal conductivities are around $16.2\ W/mK$, while galvanized steel has a range of $50 - 65\ W/mK$ [85], [86]. It is anticipated that the thickness of the sheet metal will be around 5 mm due to the structural requirements.

The exterior of the produced sheet metals will be fitted with insulation material. In the initial stage, elastomeric rubber insulation material will be utilized. This insulation material is preferred due to its resistance against water vapor diffusion, low thermal conductivity coefficient (0.032 W/mK at -20 degrees Celsius), flexibility, and ease of application. As the maximum thickness available for these materials from suppliers is 50 mm, a 50 mm application will be implemented [87].

Finally, the elastomeric rubber insulation material will be covered with cold room panels to provide superior insulation. This material is commonly used in cold rooms and warehouses and coated with a thin polyurethane sheet.

The following equation calculates the conductive calculation of three specific thickness materials that separate the cold air from the ambient air. The first layer is the sheet metal of the IWT which is 5 mm thick and thermal conductivity is $16.2 \, W/kg * K$. Then insulation layers are present, which are elastomeric rubber and insulation panel. Their thermal conductivity and thicknesses are 50, 100 mm and 0.032, 0.023 $W/kg * K$, respectively.

$$\lambda = \frac{1}{\left(\frac{d_1}{\lambda_1 d}\right) + \left(\frac{d_2}{\lambda_2 d}\right) + \left(\frac{d_3}{\lambda_3 d}\right)} \tag{148}$$

$$\lambda = \left(\frac{0.005 \, m}{16.2\frac{W}{kg*K}*0.155 \, m}\right) + \left(\frac{0.05 \, m}{0.032\frac{W}{kg*K}*0.155 \, m}\right) + \left(\frac{0.1 \, m}{0.023\frac{W}{kg*K}*0.155 \, m}\right) = \tag{149}$$
$$0.0266 \, \frac{W}{kg*K}$$

The amount of heat transferred into the tunnel through the surface area is calculated using the following equation, taking into account the cumulative conductive coefficient and the temperature difference. At this design point, the ambient temperature is assumed to be 20 °C, and air inside the wind tunnel should be -30 °C.

$$Q_s = \frac{\lambda}{d} * (T_{amb} - T_{air}) * S \tag{150}$$

$$Q_s = \frac{0.0266 \, \frac{W}{kg*K}}{0.155 \, m} * \left(20 \, ℃ - (-30 \, ℃)\right) * 270 \, m^3 \tag{151}$$
$$= 6.27 \, kW$$

In this study, the designed icing wind tunnel experiences a heat flux of 6.27 kilowatts from the walls of the wind tunnel under the most challenging operating conditions.

4.4.6.1.2 Heat Due to Spray Bar

The spray bar is an essential equipment within the wind tunnel due to its ability to inject a large amount of liquid into the flow. However, this can negatively affect the heat balance within the wind tunnel. There are two primary sources of heat loss that need to be overcome by the cooling device associated with the spray bar. These are referred to as sensible and latent heat. The first source involves water droplets that are excessively cooled from the temperature at which they exit the nozzle, approximately 20 ∘C, to the temperature of the air in the test section of the tunnel, resulting in heat transfer within the tunnel and is expressed as the sensible heat flow, Q_{sens}. The other heat flow, known as Q_{latent} or latent heat, occurs when the excessively cooled water droplet solidifies onto a solid surface in our case model placed in the test section within the wind tunnel due to droplet heterogenous nucleation, releasing latent heat. Both sensible and latent heat are functions of the liquid water content [15].

$$\dot{m}_{water} = LWC * \dot{V}_{air} = LWC * (U_\infty * A_{tsec}) \tag{152}$$

$$\dot{Q}_{sensible} = \dot{m}_{water} * c_{p,water} * \Delta T \tag{153}$$

$$\dot{Q}_{latent} = \dot{m}_{water} * c_{latent,water} \tag{154}$$

$$c_{p,water} = 4.183 \ kJ * kg^{-1}K^{-1} \tag{155}$$

$$c_{latent,water} = 334 \ kJ \ kg^{-1} \tag{156}$$

In this calculation, the values determined for the most challenging conditions of the icing wind tunnel are used, with a LWC of 3 g/m^3, a mass flow rate of 100 m^3/s, and a test section area of 1 m^2 . When these values are input into the calculation, the amount of heat lost is being calculated below.

$$\dot{Q}_{sensible} = 3\frac{g}{m^3} * 100\frac{m^3}{s} * 1 \ m^2 * 4.183 \ kJ * kg^{-1}K^{-1}$$
$$* 50 \ K = 62.75 \ kW \tag{157}$$

$$\dot{Q}_{latent} = 3\frac{g}{m^3} * 100\frac{m^3}{s} * 1\, m^2 * 334\, kJ\, kg^{-1} = 100.2\, kW \qquad (158)$$

According to the calculations performed for both heat sources, the selection of cooling equipment plays a significant role. Therefore, it can be confidently stated that the cooling capacity depends on the required LWC value in the icing tunnel.

4.4.6.1.3   Motor Heat

Electric motors are known for their high efficiency, making them one of the most efficient types of motors. As a result, they generate minimal heat. The motor used in this case is a three-phase motor that meets the IE3 standards. The catalog values indicate a 96% efficiency; however, in reality, this level of efficiency may not be achieved due to maintenance deficiencies or challenging environmental conditions. Additionally, the heat generated by airflow friction is converted entirely into heat, consuming the axial fan's power [88]. Furthermore, the heat generated by aerodynamic effects can be considered energy transferred to the air. Therefore, aerodynamic heating and the motor's heat load are included in the fan power calculation.

$$\dot{Q}_{motor} + \dot{Q}_{aero} = P_{fan} * \eta_{fan} = 315\, kW * 0.65 = 204.8\, kW \qquad (159)$$

$$Total\ Heat\ Loss = 6.72 + 204.8 + 100.2 + 62.75$$
$$= 373.97\, kW \qquad (160)$$

In addition to calculating the total heat loss and determining the cooling power requirement, it is also possible to determine the temperature increase within a wind tunnel. The calculations were performed using the equations shown below, and the temperature increase was determined as 2.61 Celsius degree for a particular design point. This temperature difference helps us to govern the heat exchanger specification.

$$Total\ Heat\ Loss = \dot{m} * \rho_{air} * \Delta T$$

$$373.97\ kW = 100\frac{m^3}{s} * 1.433\frac{kg}{m^3} * \Delta T \tag{161}$$

$$\Delta T = 2.61\ ℃ \tag{162}$$

Calculations have been made for each heat entering the wind tunnel. Based on the design point selected as the most challenging conditions for the wind tunnel, a total cooling capacity of 374 kW has been calculated. However, this calculation is based on a single point. Therefore, Figure 70 shows the required cooling capacity as the velocity value increases inside the wind tunnel. In this calculation, an LWC value of $3\ g/m^3$ has been assumed for all different velocities. Additionally, Figure 71 shows the required cooling capacity according to the change in LWC. Although the change in cooling capacity is not as significant as the change in motor speed, this graph allows for the examination of the cooling amount required for an LWC value at a velocity of 100 m/s in the test chamber.

Based on all these calculations, a cooling group calculation by component will be performed in the further stages of this study.
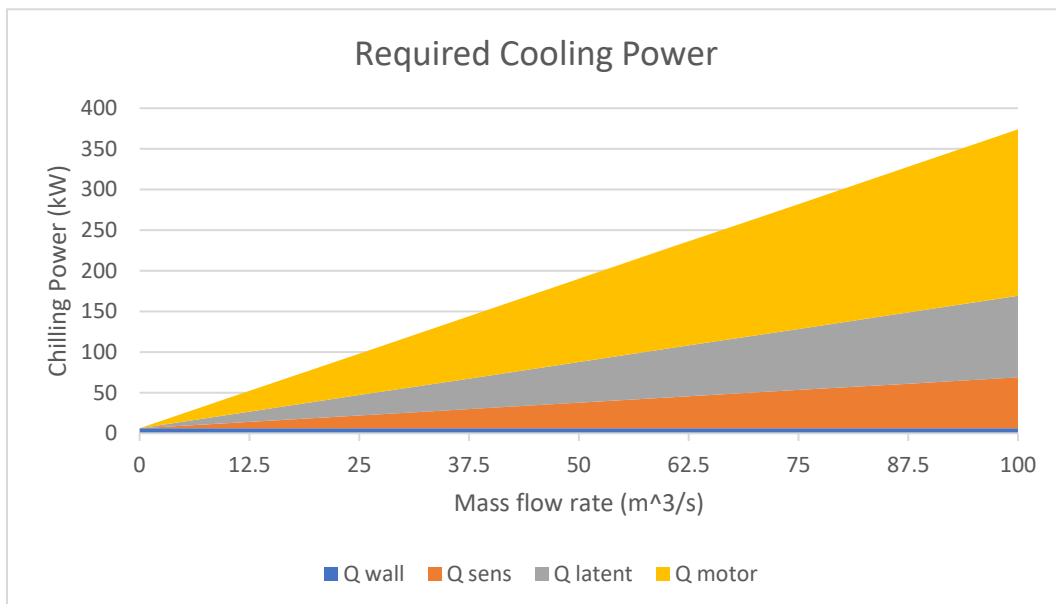

Figure 70: Cooling System Power vs. Mass Flow Rate
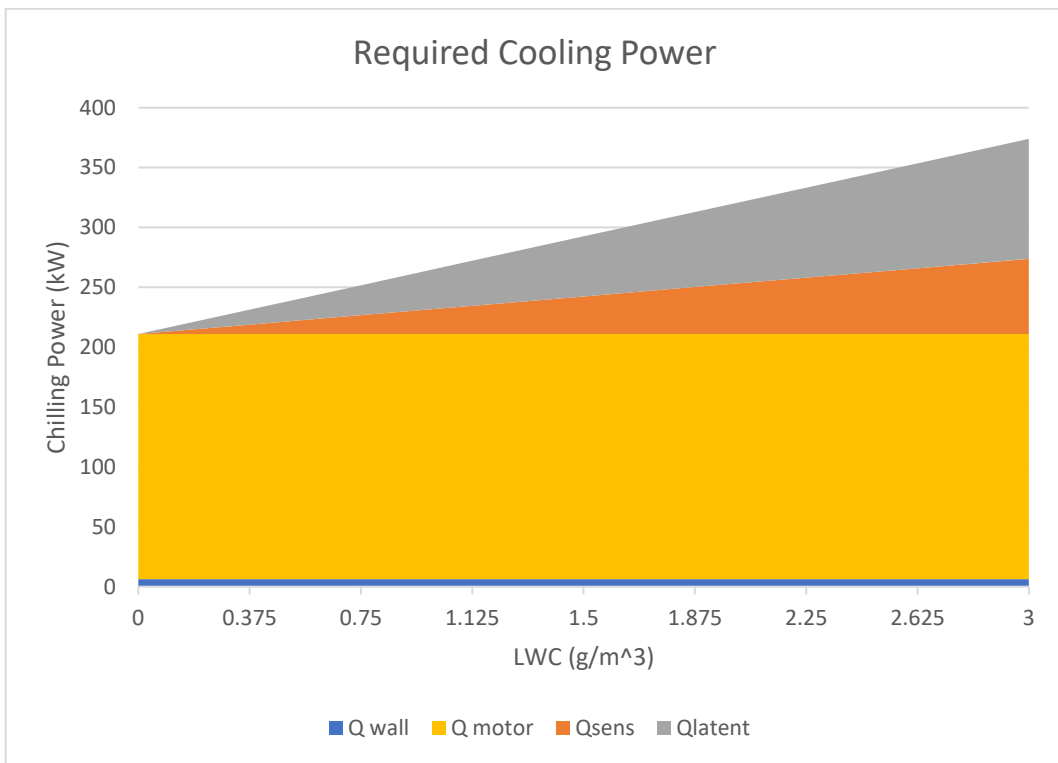
Figure 71: Cooling System Power vs. LWC

In the literature review of wind tunnels with cooling data, Table 43 compares the cooling performance of icing wind tunnels around the world. As evident from this table, the calculated values are in accordance with the existing tunnels, especially the fan-to-cooler unit power ratio aligned with the existing tunnels. At this stage, the accuracy of the calculations is assumed to be proven.

Table 43: Comparison of Icing Wind Tunnel Cooling Units [15]

Tunnel Name	Test Section (m x m)	V_∞ (m/s)	P_{fan} (kW)	P_{chill} (kW)	P_{fan}/P_{chill}
CIRA	2.35 x 1.15	225	4000	6400	1.60
NRC AIWT	0.57 x 0.57	100	450	420	0.93
METU IWT	1.00 x 1.00	100	315	374	1.19

REFRIGERANT

There are several factors to consider when choosing a refrigerant for a wind tunnel, including refrigerant-type cooling system compatibility.

The refrigerant should have the necessary thermodynamic properties to transfer heat from the wind tunnel effectively. This may include a high coefficient of performance (COP), a low saturation temperature, and a high latent heat of vaporization.

The refrigerant should be compatible with the materials and components of the cooling system and should not cause corrosion or other damage.

In general, selecting a cooling fluid for a wind tunnel depends on the specific requirements and constraints of the application, including desired efficiency, cost, and environmental impact. In this thesis, the selection of a cooling gas to be used in the wind tunnel was made considering the technical requirements. One of the most important requirements was the target temperature of -30 °C, which played a significant role in the selection of the cooling gas. As a result, the evaporation temperatures of various cooling gases were examined, and options such as R410A, R744, and R507A emerged as potential solutions. Among these gases, R744 was chosen based on its cost-effectiveness and applicability. To elaborate further, R744 is essentially carbon dioxide itself. Therefore, it does not pose risks such as flammability and greenhouse gas emissions. Additionally, as shown in the Table 44, it is abundantly available and has a low cost. Furthermore, CO2 stands out for its low critical point temperature (31.06 °C) and low evaporation temperature (-56.6 °C)[89].

Table 44: Common Coolant Gas Prices [89]

Gas Type	R134a	R404a	R407c	R410a	R507	R744 (CO_2)
Price (€/kg)	9.38	8.85	10.68	9.58	19.53	0.52

COMPRESSOR

A compressor is a mechanical device that increases the pressure of a gas or vapor by reducing its volume. Compressors are commonly used in cooling systems to

151

compress refrigerant gases and circulate them through the system. Overall, the compressor is a critical component of a cooling system, as it is responsible for compressing and circulating the refrigerant to transfer heat from the system.

DRYER

A dryer is a device that is used to remove moisture from gas or vapor. In a cooling system, a dryer is used to remove moisture from the refrigerant gas, as moisture can cause corrosion and other problems in the system.

In a cooling system, the dryer is typically located downstream of the compressor and upstream of the expansion valve or expansion device. The dryer helps to ensure that the refrigerant is dry and free of moisture, which can cause corrosion and other problems in the system. By removing moisture from the refrigerant, the dryer helps to improve the efficiency and reliability of the cooling system.

EXPANSION VALVE

An expansion valve is a device that is used to control the flow of refrigerant in a cooling system. It is typically located downstream of the evaporator and upstream of the compressor and is responsible for regulating the flow of refrigerant from the low-pressure side of the system to the high-pressure side.

HEAT EXCHANGER

In a cooling system in wind tunnels, the heat exchanger plays a critical role in transferring heat from the refrigerant to the surrounding air or to a secondary fluid. It helps dissipate the heat absorbed by the refrigerant, which allows the refrigerant to cool the system. The efficiency of the heat exchanger can significantly affect the overall efficiency of the cooling system.
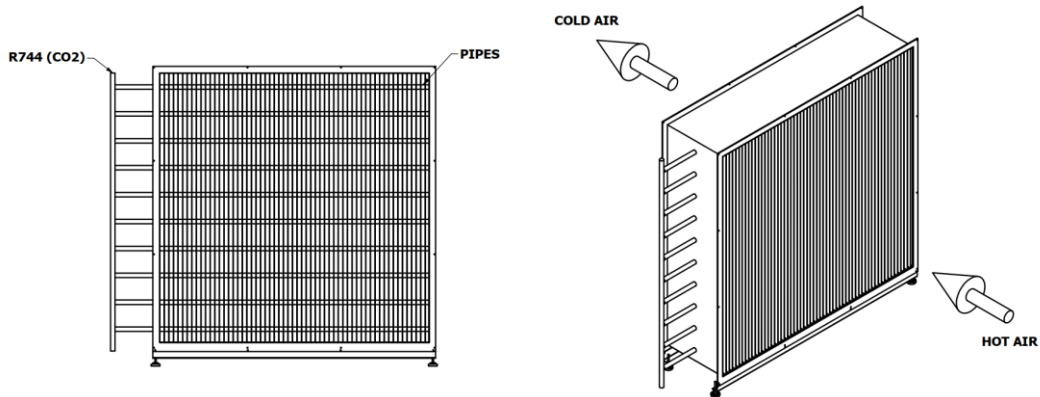
Figure 72: Air Type Finned Heat Exchanger

Although all of the heat exchangers to be used in the wind tunnel are practical and useful, it is necessary to use a heat exchanger system that is geometrically and mechanically suitable for the wind tunnel so that the airflow and the airflow momentum are not disturbed.

The cooling system component that is located within the wind tunnel and performs the cooling function independently within the tunnel is the airflow heat exchanger. From the perspective of heat transfer, it presents a forced convection problem that involves the solution of numerous parameters. Therefore, in order to be used in the wind tunnel, it was requested that the design calculations be provided to specialized companies, along with compliance with production conditions. Within the scope of this request, dimensions, temperature values, and environmental conditions were provided as input. The calculated values are presented in the table below as a result of this study.

Furthermore, the heat exchanger used for cooling purposes is an effective moisture absorber. For this reason, the fins of the heat exchanger are designed with a hydrophilic structure, allowing them to capture and accumulate moisture from the surrounding air. Therefore, the placement of this component has been moved before the settling chamber, specifically in diffuser 5, so that it can remove moisture from the flow inside the tunnel and prevent or decrease the possibility of ice accumulation on the honeycomb and mesh screens inside the settling chamber. Due to this reason,

an exhaust outlet will be added to the heat exchanger design process in order to discharge excess water retained from moisture.

Table 45: Heat Exchanger Technical Specifications

| Specification	Value	Unit
LL	3000	mm
LH	3000	mm
TH	88	mm
Capacity	377	kW
Heat	358	kW
Latent Heat	17.21	kW
Heat Transfer Area	394	m^2
Heat Transfer Coefficient	110	$W/m^2 * K$
Log. Temp. Difference	8.35	K
Dry Bulb in	-27.1	C
Dry Bulb out	-29.7	C
Volumetric Flow Rate	326000	m^3/h
Mass Flow Rate	472000	kg/h
Pressure Loss	751	Pa
Coolant Gas	R744	
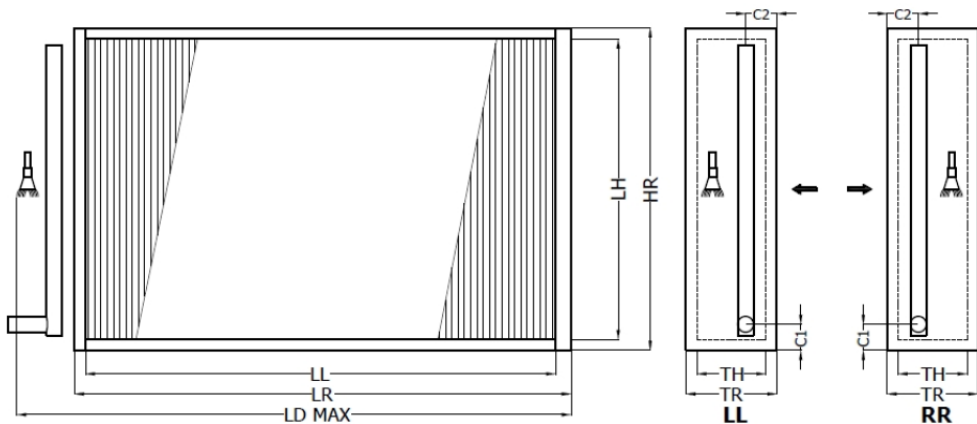
Figure 73: Heat Exchanger Technical Drawing

4.4.7 Exposure Time Calculation

Given the initial assumptions and calculations made for the wind tunnel, it was determined that the wind tunnel's speed would be maintained at a constant -30 °C. However, the decision to replace the cooling group with a more powerful version to accommodate lower temperature conditions was not taken into account in order to avoid an increase in costs. Consequently, in order to achieve the desired lower temperatures, liquid nitrogen will be introduced into the flow prior to entering the test chamber. Further calculations were conducted to determine the capacity of the tank and the duration for which the flow can be maintained at stable temperatures below the required -30 °C, taking into consideration exposure time.

The wind tunnel is effectively cooled by introducing pressurized liquid nitrogen into the settling chamber through spray nozzles. By injecting liquid nitrogen at a pressure of 5 bar, the wind tunnel can achieve temperatures as low as -40 °C when operating at its maximum speed. In the absence of nitrogen nozzles, the wind tunnel flow can be redirected through a cooler, resulting in temperatures ranging from -30 °C at low speeds to -20 °C at high speeds. Exposure time calculation with the liquid nitrogen injection can be calculated as follows.

Enclosed volume of wind tunnel: $250\ m^3$

Airflow rate: $100\ m^3/s$

Constant temperature of the wind tunnel: $-30\ °C$

Target air temperature at the test section: $-40\ °C$

Liquid nitrogen tank volume: $250\ liters$ [90]

Density of air at $-30\ °C = 1.453\ kg/m^3$

In the following equation, mass to be cooled is calculated.

$$\dot{m}_{air} = \rho_{air} * \dot{V}_{air} = 1.453\,\frac{kg}{m^3} * 100\,\frac{m^3}{s} = 145.3\,\frac{kg}{s} \qquad (163)$$

The energy needed to cool the mass airflow at the test section can be determined using the following equation.

$$\dot{Q} = \dot{m} * C_p * \Delta T = 145.3\frac{kg}{s} * 1.005\frac{kJ}{kg * K} * 10\ K$$
$$= 1460.265\frac{kJ}{s}$$

(164)

The flow rate of the liquid nitrogen can be determined using the following equation.

$$\dot{m}_{N2} = \frac{\dot{Q}}{L} = \frac{1460.265\frac{kJ}{s}}{200\frac{kJ}{kg}} = 7.301\frac{kg}{s}$$

(165)

Total available liquid nitrogen storage available.

$$m_{N2} = V_{N2} * \rho_{N2} = 0.25\ m^3 * 807\frac{kg}{m^3} = 201.75\ kg$$

(166)

The rate at which liquid nitrogen is consumed can be determined using the following equation.

$$\frac{m_{N2}}{\dot{m}_{N2}} = \tau = exposure\ time = \frac{201.75\ kg}{7.301\frac{kg}{s}} = 27.63\ seconds$$

(167)

In the context of liquid nitrogen tanks, the largest available tank on the market was calculated to determine the exposure time required for a 10 Kelvin temperature difference at -30 degrees Celsius. The resulting exposure time was found to be 27.63 seconds, which is considered to be relatively short for conducting icing experiments. To address this limitation, it is suggested that multiple tanks be combined using a manifold system in order to extend the time interval in a linear manner. Specifically, in order to achieve a 6-minute experiment time, which is proposed in the wind tunnel design phase, it is recommended to merge 12 liquid nitrogen tanks together. However, it should be noted that the occurrence of -40 degrees Celsius temperatures

is rare, making it a less common scenario for experimentation. Consequently, the exposure time can be extended up to 9 minutes for smaller temperature differences with one tank. For exposure time for further temperature differences, please refer to Figure 74 .
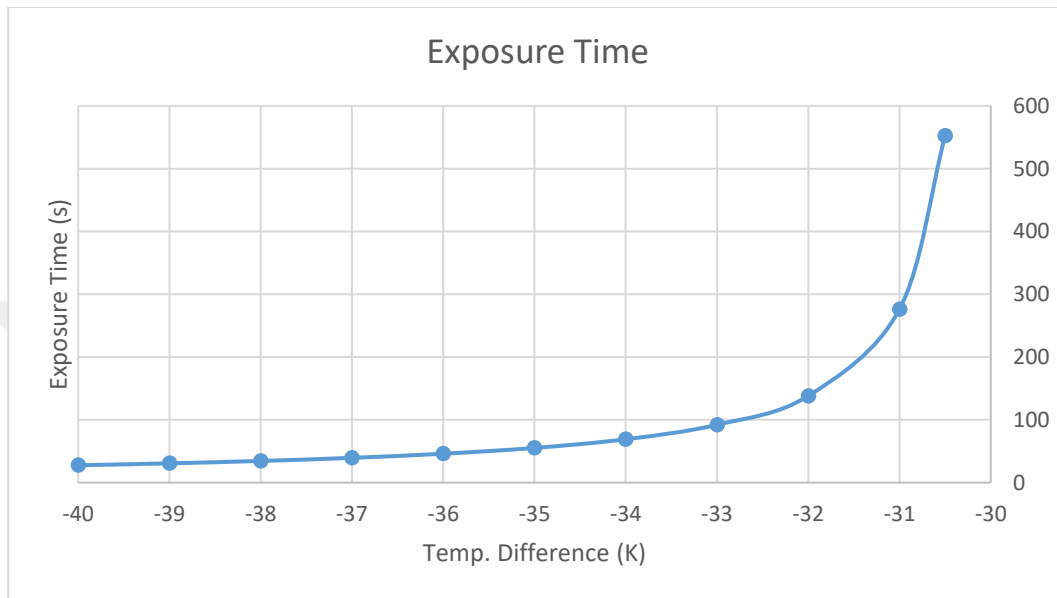

Figure 74: Time Exposure by Liquid Nitrogen Injection

4.4.8   Spray Bar

In an icing wind tunnel, a spray bar is a device that is used to dispense a spray of liquid into the airflow. The spray bar is typically part of the icing simulation system, and it is used to simulate the formation/accumulation of ice on the aircraft or structure being tested.

The design of a spray bar will depend on the specific requirements of the testing program and the type of liquid that is being sprayed. Some common design considerations for a spray bar include the size and shape of the bar, the number of nozzles, the spacing between the nozzles, and the spray pattern of the nozzles.

In general, the spray bar should be designed to deliver an even spray of liquid over the surface of the aircraft or structure being tested. This may involve using multiple nozzles with different spray patterns to ensure that the liquid is evenly distributed.

The size and shape of the spray bar will depend on the test section's size and shape and the tunnel's flow conditions..

In addition to these factors, the droplets' size and the nozzle's cone angle are also important. In this study, the droplet sizes range from 10 to 50 microns. Figure 75 illustrates that these values fall within the range of cloud droplet sizes.
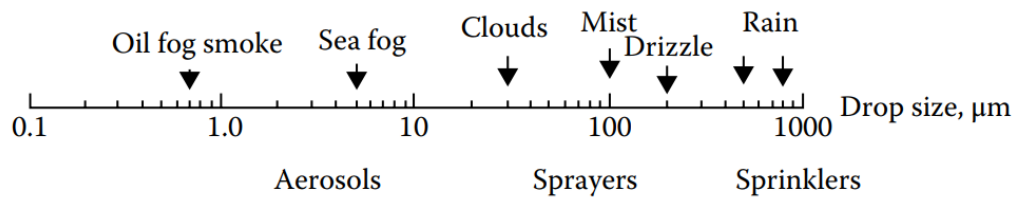

Figure 75: Classification of Droplet Size [91]

4.4.8.1   Nozzle

In the design and determination of the spray bar, the selection of nozzles is of primary importance because the selection of the nozzles is the most significant factor in determining the MVD dimensions and cone angle.

Therefore, it is necessary first to determine the type of nozzle. In literature, air-assisted nozzles are widely used. NASA named these nozzles as standard and Mod-1 nozzles; the only difference between them is that the standard nozzles cover the high LWC, and Mod-1 nozzles cover the low LWC zones. Furthermore, air-assisted nozzles can be chosen for wind tunnels due to their ability to provide the required MVD dimensions and their compatibility with the wind tunnel. This nozzle type is suitable because it injects droplets with flow, allowing for the formation of small sizes. Additionally, the supply of pressurized air and water is heated in order to modify particle sizes and prevent freezing within the wind tunnel. In Figure 76 types of air assisted nozzle are shown, both types of the nozzle's working principle are same however, the Mod-1 nozzle has a smaller inner diameter, this is the reason why it can supply smaller LWC with the required MVD.
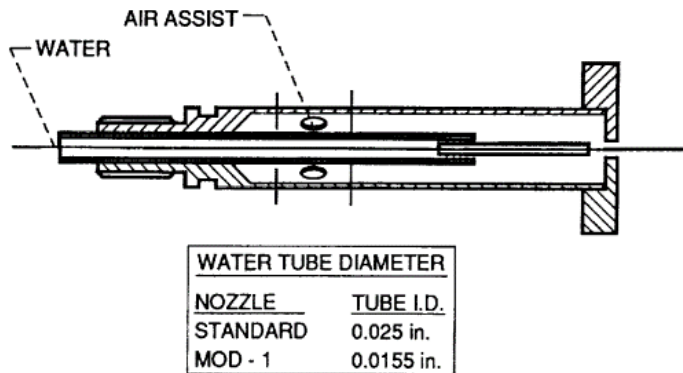
Figure 76: Icing Wind Tunnel Nozzle [92]

However, for further work, different types of nozzle could be utilized. The air-blasting nozzle is a type of nozzle that operates on the same working principle as air-assisted nozzles but with higher pressure and continuous air support in terms of air supply. In this following, SMD refers to Sauter Mean Diameter, which is commonly used as the ratio of the droplet volume to its surface area. However, SMD can also be used as the droplet diameter when assuming all droplets are ideal spheres. Also, $\dot{m}_L$ and $\dot{m}_A$, GLR represent the mass flow rate of the liquid and air and ratio of $\dot{m}_A$ to $\dot{m}_L$, respectively.
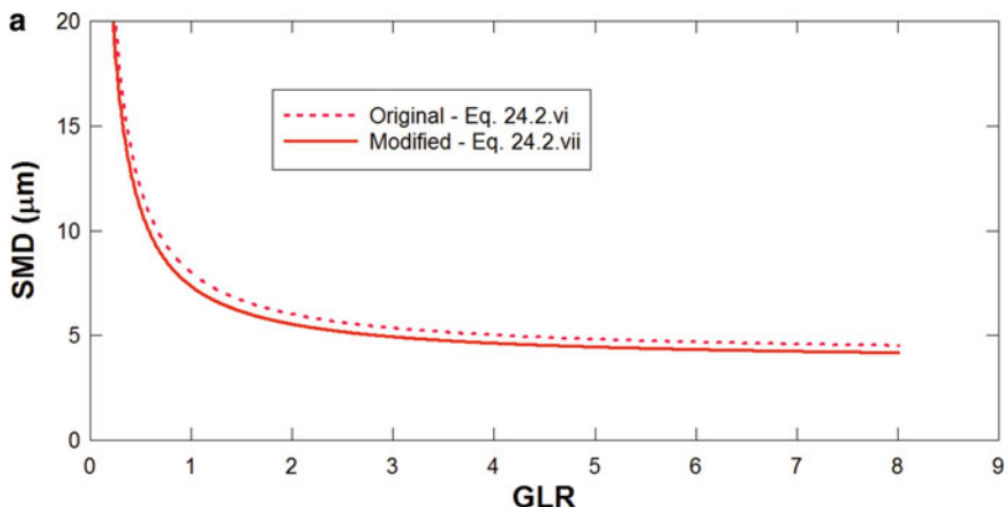

Figure 77: SMD vs. GLR Graph of Rizk–Lefebvre Equation [93]

As depicted in Figure 77, the graph drawn using the Rizk-Lefebvre equations demonstrates the ease of generating particles with a diameter up to 5 microns. The calculations for this graph were performed using a nozzle diameter of 0.5 mm and water as the fluid. Additionally, as shown in Figure 78, the droplet size decreases as the nozzle diameter decreases, as the droplet diameter graph indicates. In this calculation, the GLR value is assumed to be 1, and increasing of GLR value will cause the graph to move downwards. However, due to the lack of sufficient data and calculation parameters for the use of icing in wind tunnels, airblast nozzles is planned to be used in future studies.
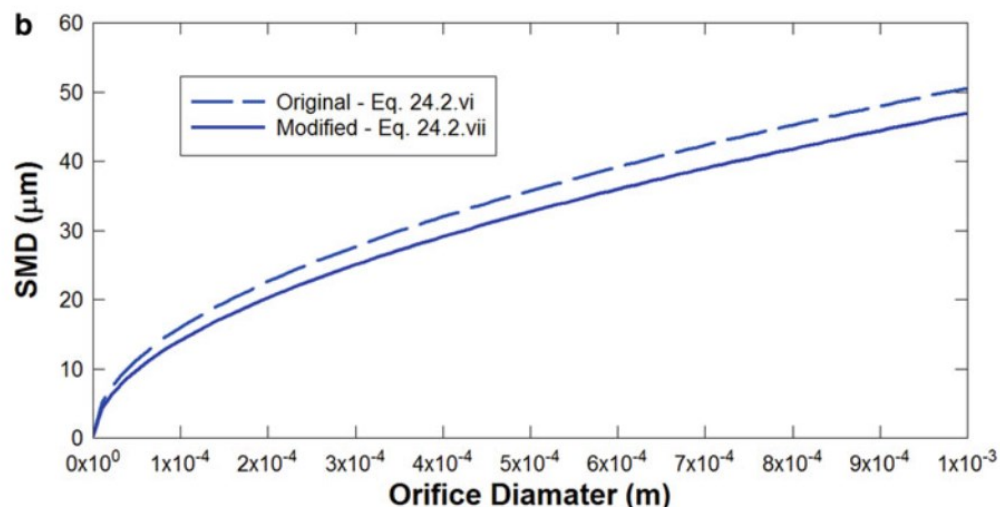

Figure 78: SMD vs. Orifice Diameter Graph of Rizk–Lefebvre Equation [93]

The spray bar system requires pressurized air, water, and a nozzle that can functionally manipulate these components. These enable the adjustment of the values of the relevant components to obtain different MVD and LWC values. NASA has conducted calibration studies using two different types of nozzles, namely standard and mod-1 nozzles. The data obtained from these calibration studies will be utilized in this research.

The collected MVD data for Mod-1 and Standard-type nozzles were analyzed in relation to air pressure and pressure difference between air and pressurized air. Curve fitting was performed using this data, resulting in the creation of a set of equations consisting of the equation below and coefficient relevant to equation 168 shown in Table 46 [94].

$$MVD = EXP(a + bx + cy + dx^2 + ey^2 + fyx + gx^3$$
$$+hy^3 + iy^2x + jyx^2)$$

(168)

Table 46: Coefficients for Spray Bar Calibration [94]

Coefficient	Mod 1	Standard
a	8.748044966	15.869868740
b	-5.758889866	-13.192403110
c	0.138821237	0.972293768
d	1.698096143	4.129758202
e	0.000048619	0.001586357
f	-0.067544202	-0.492910070
g	-0.165992209	-0.416788168
h	0.000000089	0.000000171
i	-0.000021458	-0.000386283
j	0.008648964	0.062787440

Requirements for equation 168 is stated in following part,

- P_{air} *should be* 10 *to* 70 *psig*

- ΔP should be 10 to 150 psid for standard nozzle

- ΔP should be 10 to 250 psid for mod-1 nozzle

- This is valid up to 50 micron MVD values

- x is the natural log of the air pressure in psig

The following equation is utilized for the calculation of LWC values of standard nozzles.

$$LWC = (14.2 * \ln V - 0.30 * P_{air} - 13.0 * \frac{\sqrt{\Delta P}}{V}$$

(169)

The following equation is utilized for the calculation of LWC values of mod-1 nozzles.

$$LWC = (4.45 * \ln V - 0.0475 * P_{air} - 4.8 * \frac{\sqrt{\Delta P}}{V}$$

(170)
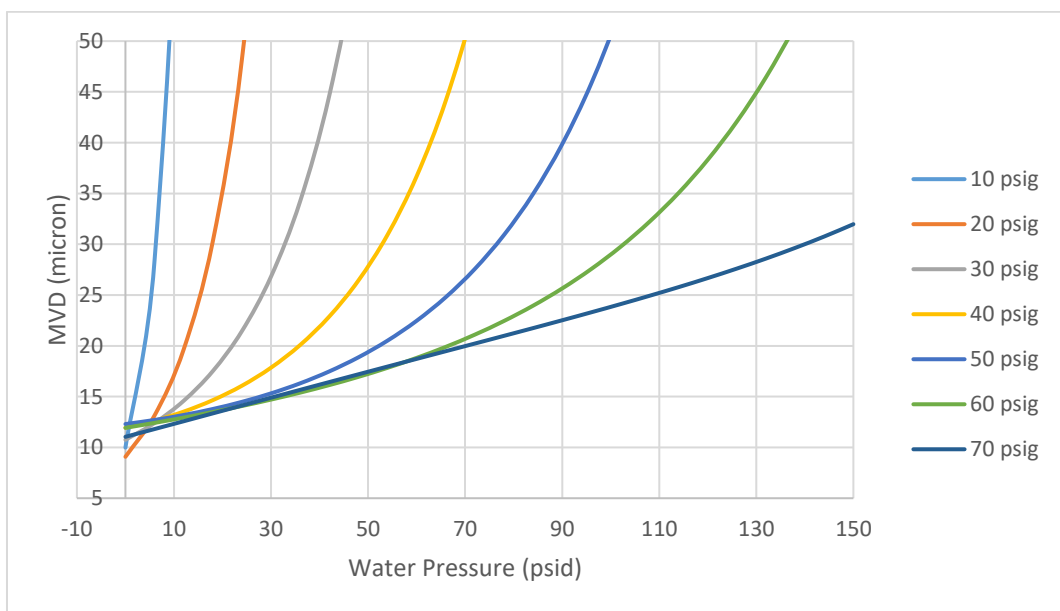
Figure 79: Standard Nozzle MVD vs. Water and Air Pressure

As depicted in Figure 79 and Figure 80, the spray bars created with two types of nozzles have the capacity to generate droplets at a level of 10 microns. Although they may not fully cover the high LWD and low MVD area for scaled cases, experiments can still be conducted using the hybrid scaling method seen in Figure 40.
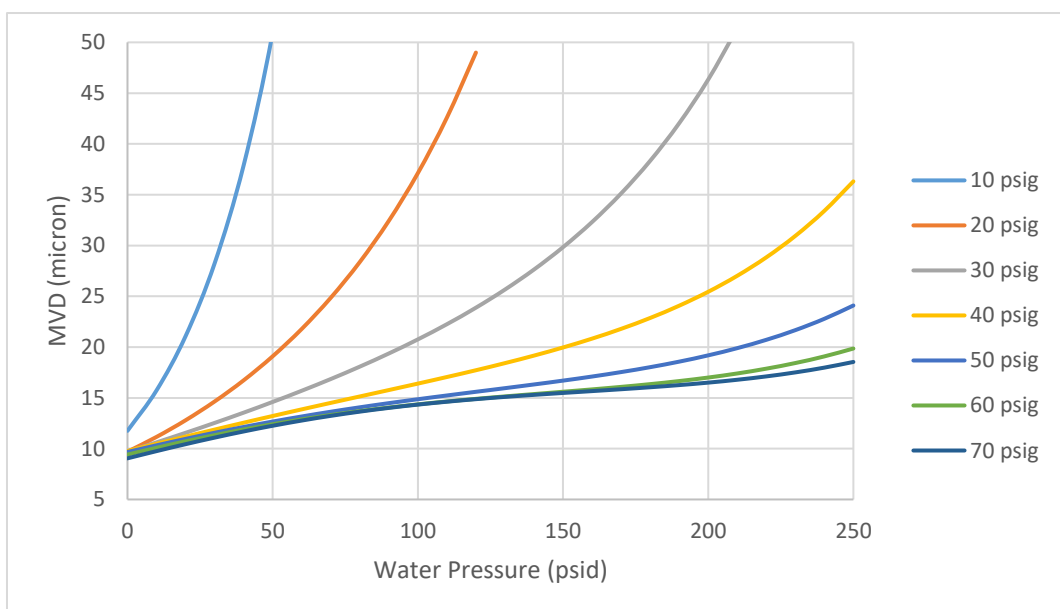

Figure 80: Mod -1 Nozzle MVD vs. Water and Air Pressure

In order to achieve a LWC water volume flux formulation can be established like following.

$$\dot{V}_{water} = \frac{LWC * \dot{V}_{air}}{\rho_{water}} = \frac{LWC * A_{tsec} * U_\infty}{\rho_{water}} \tag{171}$$

$$\dot{V}_{water} = 3.0 \ g/m^3 * 1 \ m^2 * \frac{100m/s}{1000kg/m^3} \tag{172}$$

$$\dot{V}_{water} = 1080 \ L/h \tag{173}$$

The calculated water flow rate is sufficient for a wind tunnel of this size for icing research. Additionally, the Braunschweig icing wind tunnel utilizes a spray bar with a 5 x 5 nozzle configuration for its 0.5 x 0.5 meter test section [15]. On the other hand, the NASA IRT tunnel uses an 18 x 12 nozzle configuration for its 2.75 x 1.8 meter test section [94]. Therefore, in the design of the proposed icing wind tunnel, the nozzle angle cones should also be taken into account, and it would be appropriate to use a 9 x 9 spray bar configuration with 65 nozzles on 5 x 5 bars in the settling chamber. Considering the above volumetric flow rate, a volume flow rate of 10.8 liters/hour per nozzle is observed. This is more than sufficient for a commercial pulsating type atomizer, which is capable of dispersing 59 liters/hour at 45 psi.
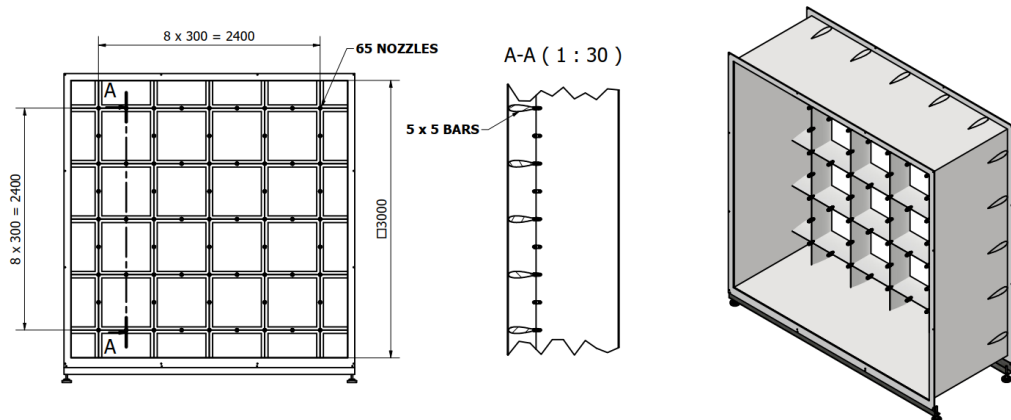

Figure 81: Spray Bar – Nozzle Layout

The atomizer used in the spray system is capable of pulsing up to 100 times per minute. The LWC can be adjusted without changing the pressure of the water and air supply by changing the duty cycle.

Water flow and air flow rates are measured and adjusted with flow controllers. In icing test facilities, where tunnel air temperatures can be set below -30 ˚C, the air duct of the spray atomizers is heated to prevent the droplets from freezing out.
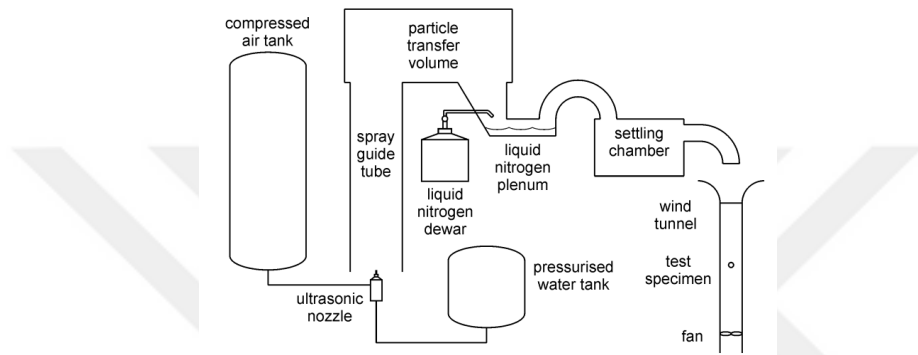

Figure 82: Spray Unit Schematic [95]

Furthermore, there is another test condition related to the spray bar in wind tunnels for icing. In order to prevent freezing, the droplets heated and injected into the icing wind tunnel from the nozzle must cool down to the ambient temperature until they meet the model in the test chamber. Otherwise, many of the assumptions and calculations made will be incorrect. Therefore, the placement and distance of the spray bar from the test chamber are of importance. In order to calculate this, the following equation was derived by Etteh et al. in 2019 [96].

$$m_p = \frac{D(c_{p,p}, T_p)}{Dt} = \dot{Q}_p + h_{phase} * \dot{m}_p \tag{174}$$

$$\frac{T_p(t) - T_{f@p}}{T_{p,t=0} - T_{f@p}} = \exp\left(\frac{12k_f * t}{\rho_p * d^2 * c_{p,p}}\right) = \exp\left(-\frac{t}{\tau_T}\right) \tag{175}$$

In this analysis, the properties of the wind tunnel design are outlined for the most challenging scenarios, which are -30 ℃, ambient temperature 20 ℃, and airflow velocity settling chamber velocity, corresponding to 100 m/s in the test chamber. These are the most severe and challenging conditions for the wind tunnel. The impact of particle size on temperature reduction is also assessed, determining the optimal distance between the spray bar and the test chamber within the wind tunnel. Figure 83 illustrates the temperature change experienced by a 20-micron particle as it travels streamwise from the spray bar in the wind tunnel, based on the Langmuir - D distribution.
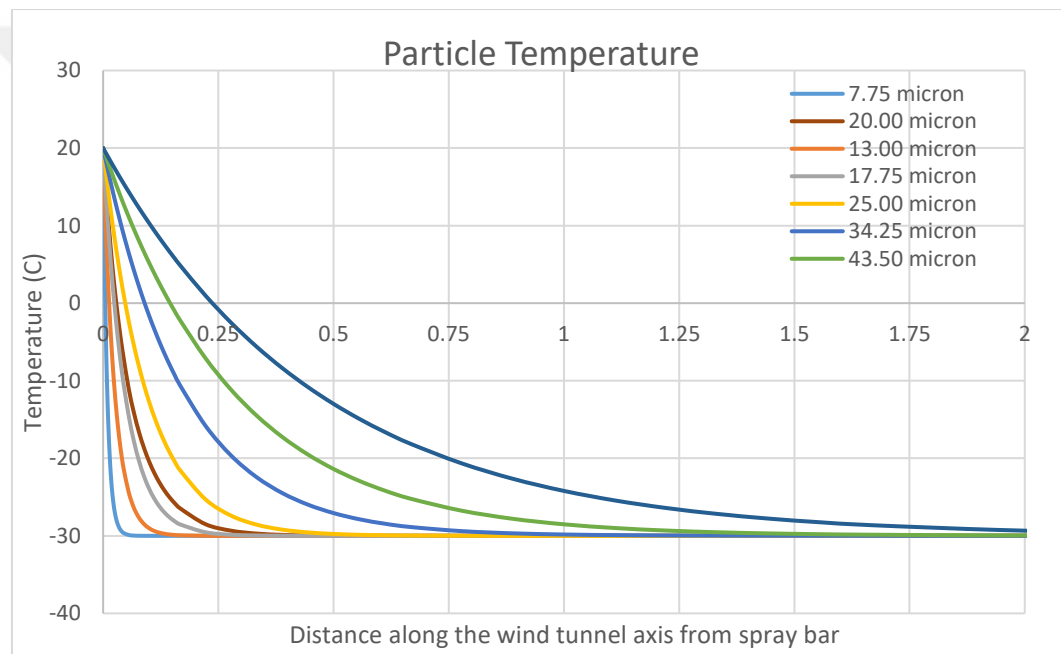

Figure 83: Droplet Temperature vs. Distance

As depicted in Figure 83, the process of cooling becomes progressively more challenging with an increase in particle diameter. Establishing the maximum particle diameter for experimentation purposes will provide valuable insights into the optimal placement of spray bars within the wind tunnel. Nevertheless, under the present circumstances, a distance of 1 meter between the spraying area and the test section will suffice.

As mentioned earlier in this study, MVD values have a certain physical limitation. As the literature studies show, the smallest achievable MVD value is around 10

microns. The size limit can be adjusted by pressure and other hardware variables. The calculations made in this regard are given in Figure 84 below Spray Bar -1 and Spray Bar - 2 in this graph refer to the spray bar designed and calibrated for this wind tunnel. Each line in the same color represents the different pressure values for the spray bar. Spray bar 1 is intended to operate for lower LWC values. Spray bar 2 is committed to high LWC and a more comprehensive range of MVD. These two spray bars' calculations are calculated for the wind tunnel's highest speed, 100 m/s. These values stretch upwards on the graph at lower speeds and cover a wider area. Even at these higher speeds, these calculated spray bars cover almost all of the 14 CFR Parts 25, Appendix C conditions, and most of the scaled results. As mentioned earlier in the study, MVD values can be produced by both spray bars from around 10 microns.

The upcoming spray bars are anticipated to possess a rectangular shape and an insulated semi-circular leading edge. This particular design has been derived from Bartlett et al.'s findings, who conducted spray distribution experiments [97]. Their research demonstrated that this configuration yields one of the most effective spray distributions when the air velocity passing the spray bar is low. The spray bars will consist of nine spray nozzles on each rod. These rods will be strategically positioned to horizontally cover the test chamber located directly downstream of the turbulence reducing grids.

The graphic presented in Figure 84 serves as a visual representation of the scaling studies and spray bar calculations conducted in this study. It displays two different nozzle configurations, with mod-1 nozzles depicted in blue lines and the standard nozzle in orange lines, each line for different air pressure levels. The spray bay configuration designed for this study is capable of achieving 10-micron MVD. Additionally, each line on the spray bar represents a combination of water pressure from the inside to atomize the droplets and air pressure to pulverize the water. The MVD size and the resulting LWC provided by the nozzle vary depending on the internal pressure. These values also fluctuate with the airflow velocity within the icing wind tunnel. However, the highest velocity represents the worst-case scenario for the area covered by the spray bar, which is why the graphic is plotted based on a wind speed of 100 m/s.
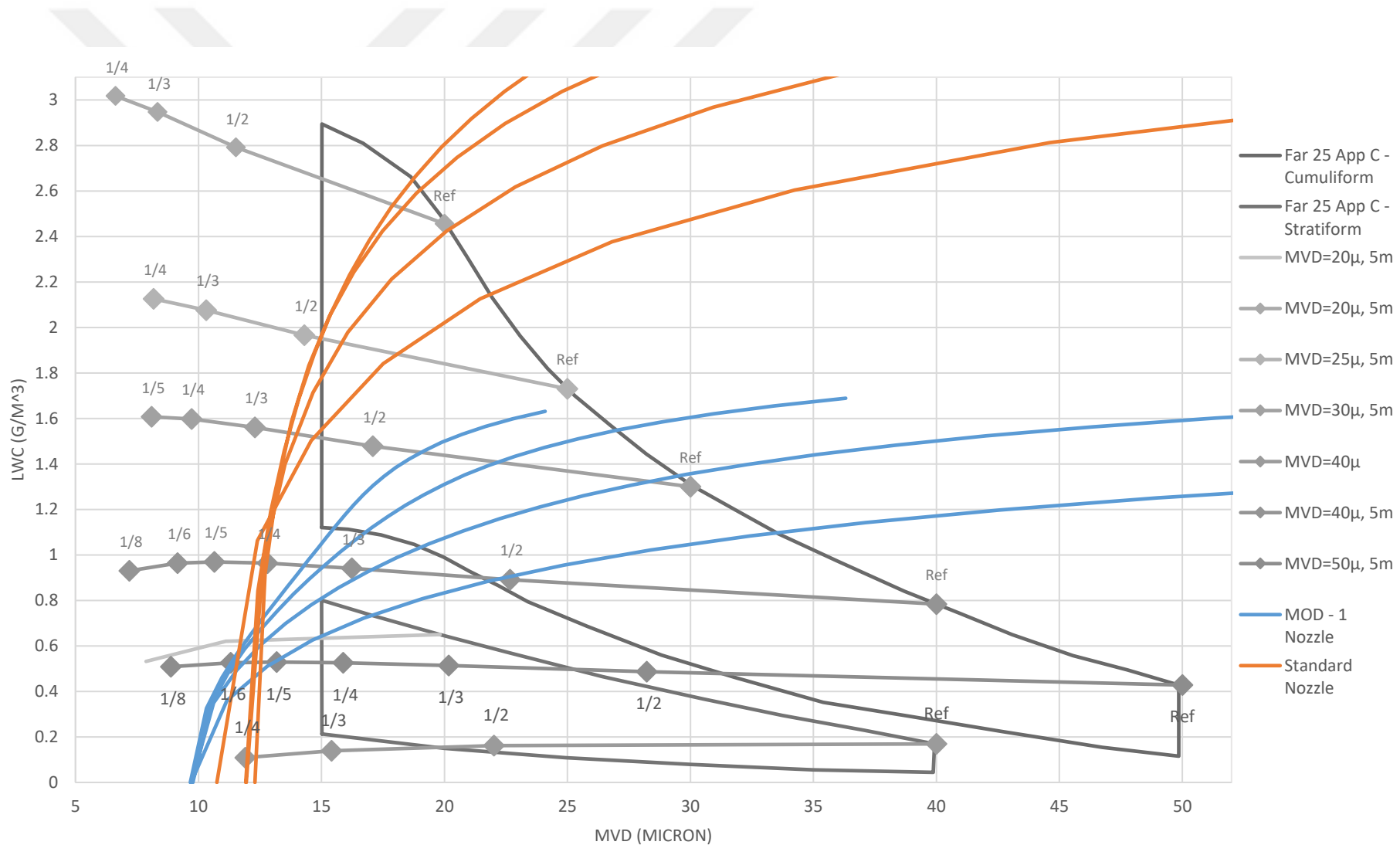
Figure 84: Spray Bar Envelope with Appendix C

4.4.9   Drive Unit Design

The rise in overall pressure across the fan must be equivalent to the cumulative pressure loss in other segments of the tunnel. Given that the fan section maintains a consistent cross-sectional area, the increase in total pressure across the fan is equivalent to the increase in static pressure.

Furthermore, the power of the fan, or the rate at which energy is added by the fan, must be equal to the rate at which energy is lost in other sections of the tunnel. The rate of energy loss is determined by the volumetric flow rate through the tunnel multiplied by the net decrease in total pressure.

In the field of wind tunnel testing, a widely employed metric for assessing performance is the energy ratio, which measures the ratio of energy flux in the test section to the power input supplied to the fan. This ratio can be expressed as follows.

$$ER = \frac{\frac{1}{2} * \rho * A * V^2}{power\ loss} = \frac{\eta_{fan}}{K} \tag{176}$$

As a result of the dimensioning process undertaken during the design stages of the wind tunnel, it was determined that the diameter of the engine is relatively large. In light of challenges associated with acquiring large engines, high power requirements, and the aerodynamically significant swirl and flapping effects downstream, alternative layout configurations were evaluated. After considering the dimensions and power of the engine, it was determined that a single fan and engine would be a suitable solution. This configuration offers advantages such as improved control over the speed of the test chamber, and a more efficient power unit.
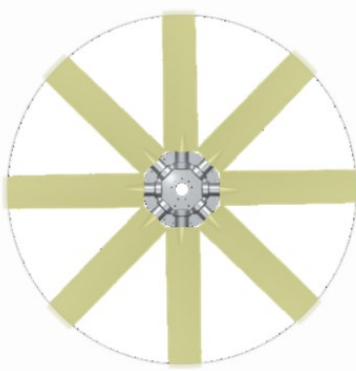
Figure 85: Fan Unit

Following this study and decision, the technical specifications of the wind tunnel's engine are detailed in the Table 47.

Table 47: Power Unit Technical Specifications

Specification	Value	Unit
Flow Rate	396,217	m^3/h
Pressure Loss	1,962	Pa
Blade Number	8	$Blade$
Propeller Type	Fiberglass Airfoil	
Pitch Angle	50	$degree$
Motor	315	kW
Motor RPM	1,440	RPM
Propeller Dia	2,135	mm
Noise	120	dBa
Working Temp.	-60/110	℃
Operational Tip Speed	160.2	m/s
Air Velocity	37.6	m/s
Torque	2,173.17	Nm
Moment of Inertia	5.95	$Kg.m^2$
Axial Thrust	8,784	$Newton$
Performance Per Blade	40,964	kW
Power Consumption	327	kW
Efficiency	65%	

The calculation of the engine power necessary to meet the specified requirements and account for pressure losses encountered in the wind tunnel was conducted. Furthermore, consultations were made with expert companies in the field to identify a suitable combination of propeller and motor capable of compensating for the power and pressure loss effects observed in the wind tunnel. The subsequent results obtained from this selection process are provided below in Figure 86.

In a fan system, the resistance to the flow of air, or pressure, increases as the flow of air is increased. The square of the flow describes this relationship. By determining the pressure required by the system at various flow rates, a "system performance curve" can be generated. This curve can be compared to the fan curve to identify the fan's actual operating point, represented by the intersection of the two curves. The operating point indicates the air flow delivered against pressure at that specific point. Other curves on the graph also represent the power consumption at the corresponding design point. This graph has been generated after determining all pressure losses, and the system performance graph can be observed in Figure 90.
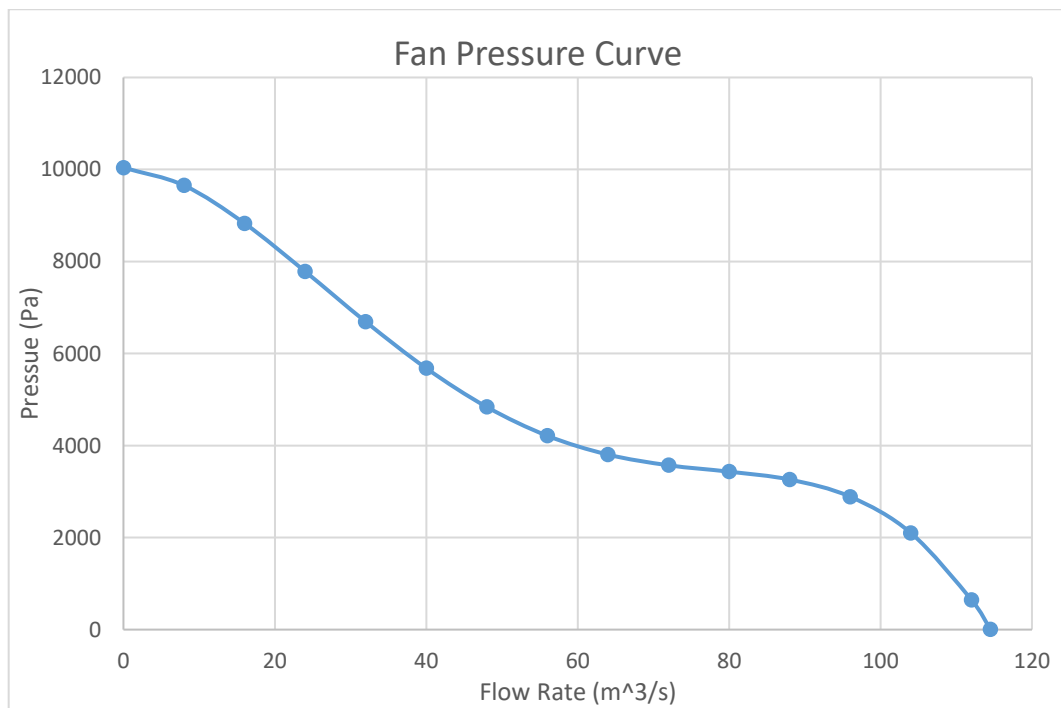

Figure 86: Fan Characteristics Curve by Vendor

As evident from the aforementioned information, the informed assumptions made during the initial stage of this investigation were validated. The proximity of the final value to the initial estimates resulted in time savings through the reduction of iterative computations. Furthermore, the decision to employ a motor configuration of a single fan-motor combination proved advantageous in terms of power reduction, reducing mechanical complexity, and facilitating the overall layout.

4.4.10 Overall Wind Tunnel Pressure Loss

Pressure losses were determined for the purpose of selecting an appropriate engine for use in the icing wind tunnel. The flow rate associated with these pressure losses, along with the design point at which the engine aligns with the pressure gain, will serve as the basis for our selection. The pressure loss values for each component of the wind tunnel are presented in Table 48. These pressure losses are also visually represented in Figure 87 for each respective component. As anticipated, the most tremendous pressure losses are observed in areas characterized by high velocities, flow regulators, and heat exchangers.

By utilizing the aforementioned criteria, it is possible to determine the loss coefficients for each component of the wind tunnel. The pressure drops for each of these components are presented in Table 48. The summation of the pressure drop values for all sections of the wind tunnel yields the total pressure drop, which in this instance amounts to 1906 Pa. It is imperative for the wind tunnel fan to compensate for this pressure drop.

Table 48: Wind Tunnel Pressure Loss of Components

V_∞	100	m/s	
Flow rate	360,000	$m^3/hour$	

|	**Pressure**		**Percentage**
Test Section	122.17	Pa	6.16%
Diffuser	121.63	Pa	6.13%
Corner	363.46	Pa	18.33%
Diffuser 2	15.16	Pa	0.76%
Corner 2	203.98	Pa	10.29%
Diffuser 3	9.58	Pa	0.48%
Motor	4.20	Pa	0.21%
Diffuser 4	9.95	Pa	0.50%
Corner 3	33.09	Pa	1.67%
Diffuser 5	0.64	Pa	0.03%
Heat Exchanger	885.74	Pa	44.67%
Corner 4	33.05	Pa	1.67%
Settling Chamber	1.09	Pa	0.05%
Honeycomb	19.58	Pa	0.99%
Mesh 1	54.59	Pa	2.75%
Mesh 2	71.53	Pa	3.61%
Contraction Cone	33.59	Pa	1.69%
Total	**1983.03**	**Pa**	
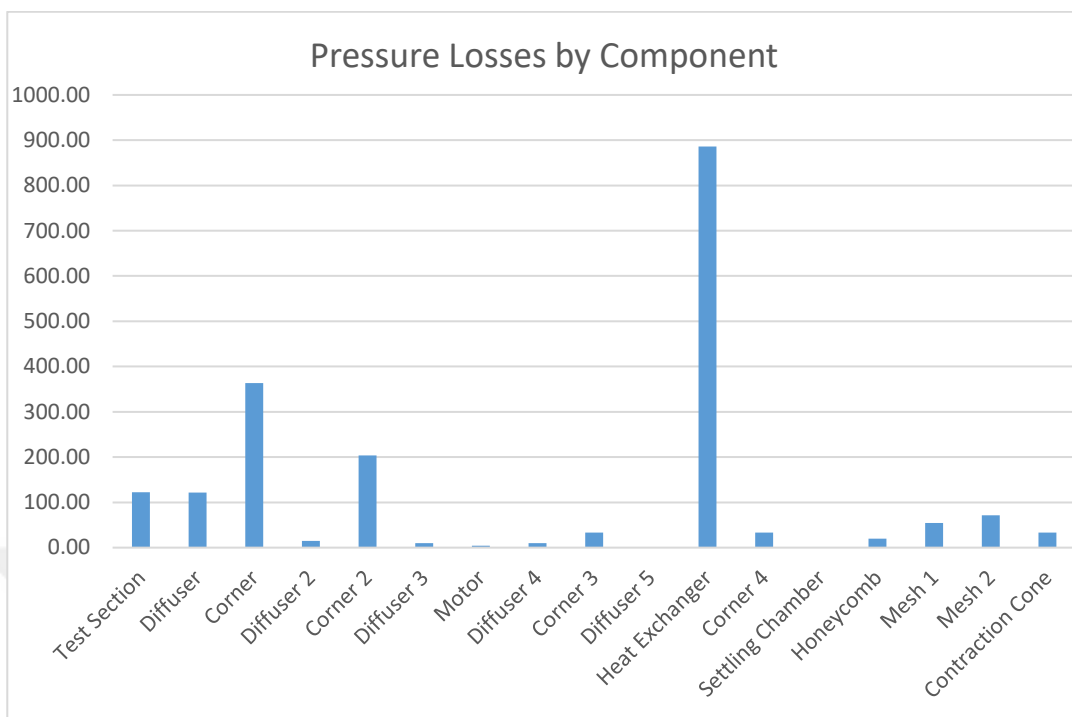
Figure 87: Pressure Losses by Component

The positioning and pressure loss calculations of the icing wind tunnel were performed on a component basis. This allowed for the determination of the contribution of each section to the total given pressure. Figure 87 and Figure 88 illustrate the pressure losses of each component and their cumulative total.

The primary observation in this graph is the significant pressure drop in the heat exchanger. To provide a more detailed explanation, the requirements for cooling a wind tunnel for icing calculations are extraordinarily demanding and advanced. Consequently, the cooling of such a tunnel necessitates a large and complex heat exchanger. As a result, the pressure drop in the exchanger is higher than expected compared to other components. However, this occurrence is quite natural.
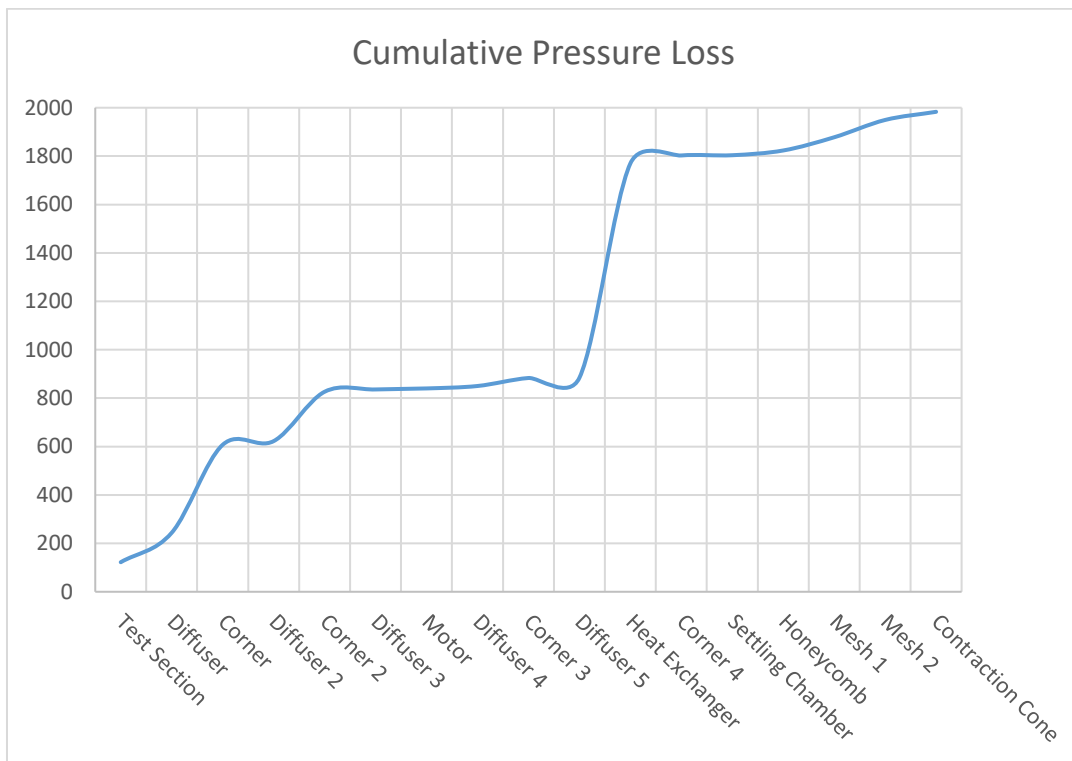
Figure 88: Cumulative Pressure Loss

Furthermore, the pressure loss in the icing wind tunnel has been shown relative to the design point up to this stage. However, when operating at different speeds, the required pressure amount is shown in Figure 89. This representation corresponds to the velocity value to be achieved in the test section. Naturally, the pressure increases in a quadratic manner with respect to this velocity value.

Additionally, the intersection point observed when the fan pressure jump and wind tunnel pressure loss figures are shown in the graph depicted in Figure 90, which indicates the operational point of the wind tunnel. This design point is slightly above a velocity of 104 m/s. Thus, we can conclude that the wind tunnel achieves the desired velocity of 100 m/s in its test chamber.

174
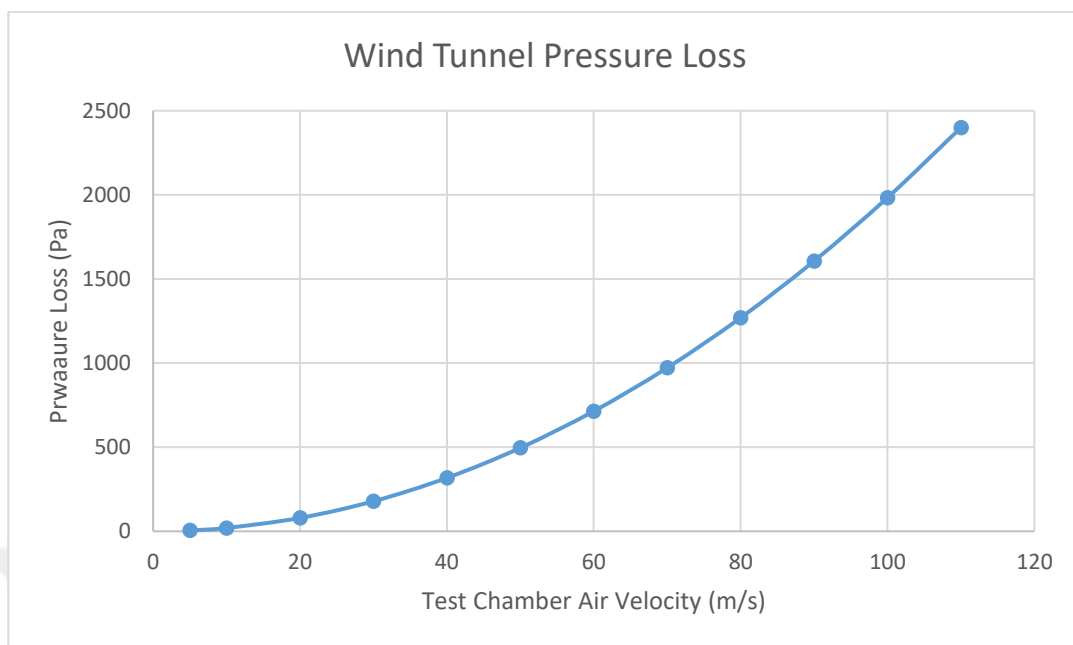
Figure 89: Wind Tunnel Pressure Loss vs. Air Velocity in Test Section
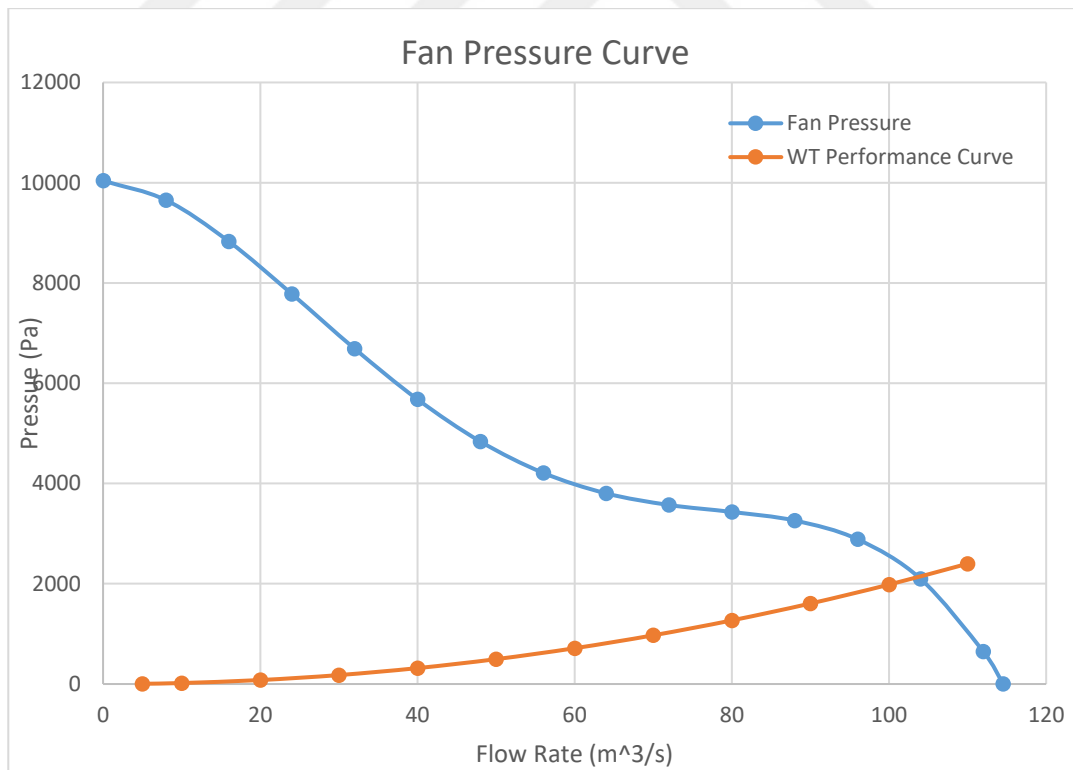
Figure 90: Fan and IWT Design Point

175
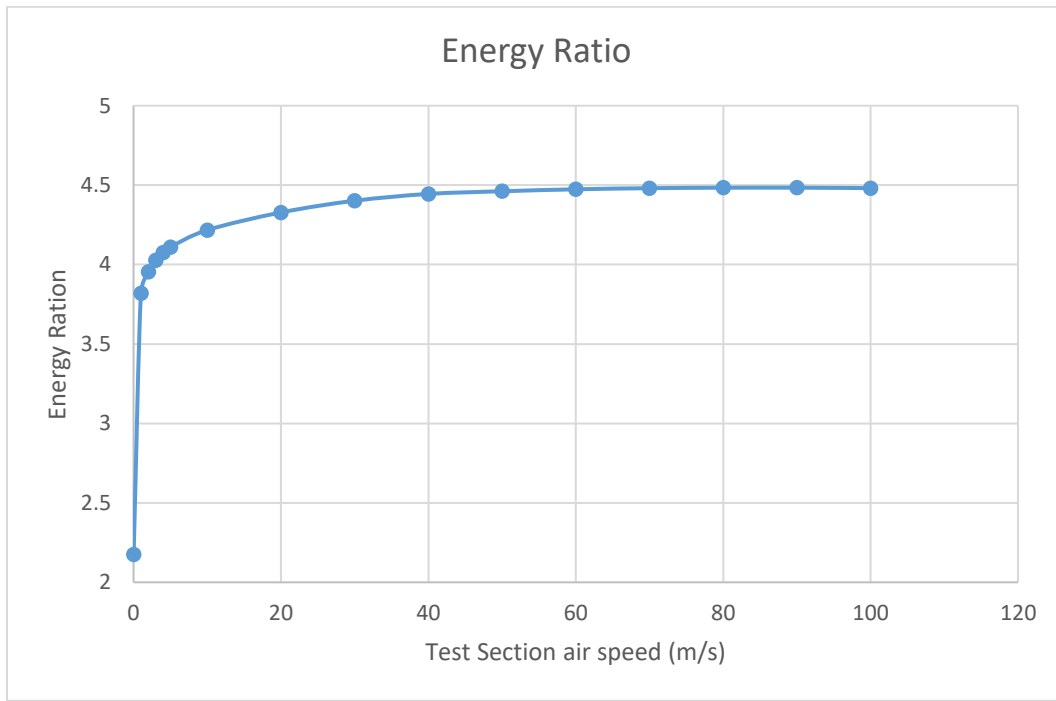
Figure 91: IWT Energy Ratio

In the wind tunnel, pressure losses, also known as energy losses, vary depending on the velocity. Therefore, a direct comparison between two tunnels may not be possible. For this reason, the most commonly used factor for comparing two types of tunnels is the energy ratio. The energy ratio can be defined as the ratio of the kinetic energy produced by the air passing through the wind tunnel to the work done by the motor. Additionally, this ratio indicates which component is more effective within the tunnel [98]. In most cases, for closed-loop tunnels, this ratio can range from 5 to 7, while in our case, it reaches levels of 4.5. Furthermore, as shown in Figure 91, the highest value occurs at a velocity of 90 meters per second in the Wind Tunnel test chamber. This means that the wind tunnel operates most efficiently in the 90 m/s range.

The general layout of the IWT is presented in Figure 92, from which the size of the IWT can be easily understood. In addition, the calculations, layout, and dimensioning analyses, as well as their results, have all been visualized in a single figure. Within this figure, the locations, dimensions, and shapes of the major components of the tunnel, such as the diffuser, motor contraction cone, and test chamber, are represented in a schematic manner.
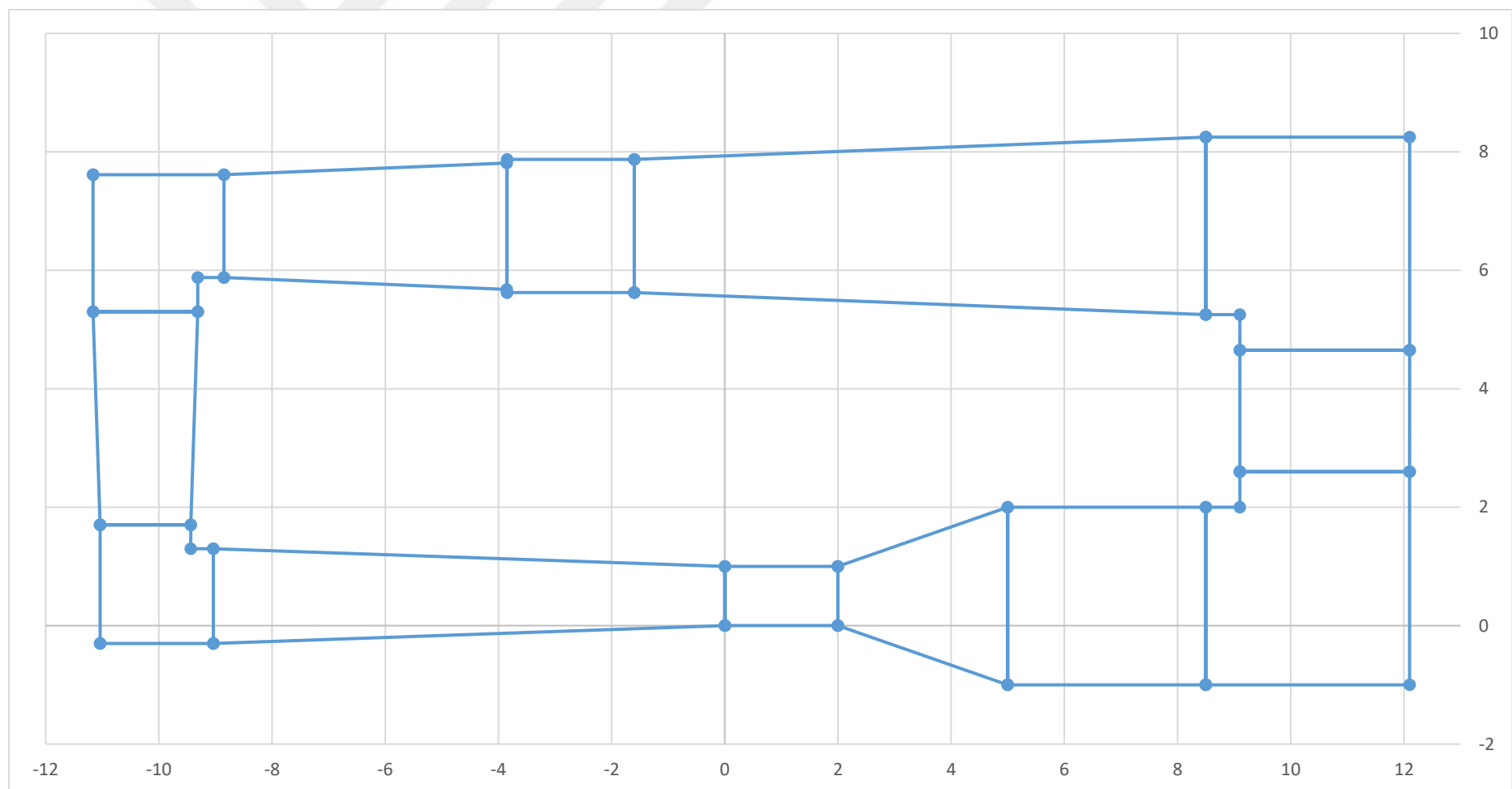
Figure 92: General Layout of Icing Wind Tunnel

4.5   CAD Design

In this study, two different designs have been made in the context of computer-aided design (CAD). The first is a more straightforward design in accordance with computational fluid dynamics. The second is a detailed design following production techniques and notions that can be suitable for production. In this study, two different designs have been made in the context of computer-aided design. The first is a more straightforward design in accordance with computational fluid dynamics, as seen in Figure 93.
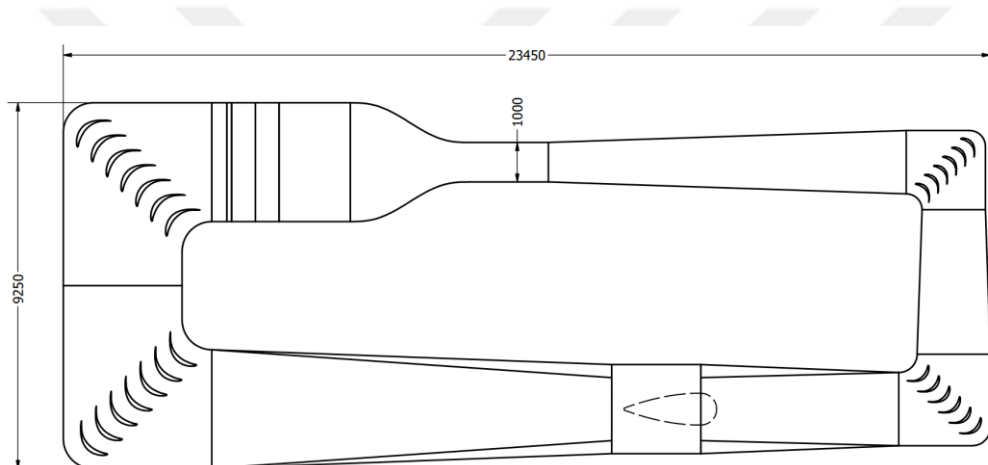

Figure 93: General Layout & Dimension of CFD CAD Design

The second is a detailed design in accordance with production techniques and notions that can be suitable for production. Drawings and visualizations of these designs are given below. In general, the difference between the two drawings is that in CFD studies, most parts and design details are removed from the design in order to ensure that the analysis results are accurate and do not create excessive processor load. In mechanical design, on the other hand, all detailed drawings with all the fasteners are present so that the manufacturer can properly manufacture this design. Drawings and visuals of these designs are given in Figure 94, Figure 95, and Figure 96.
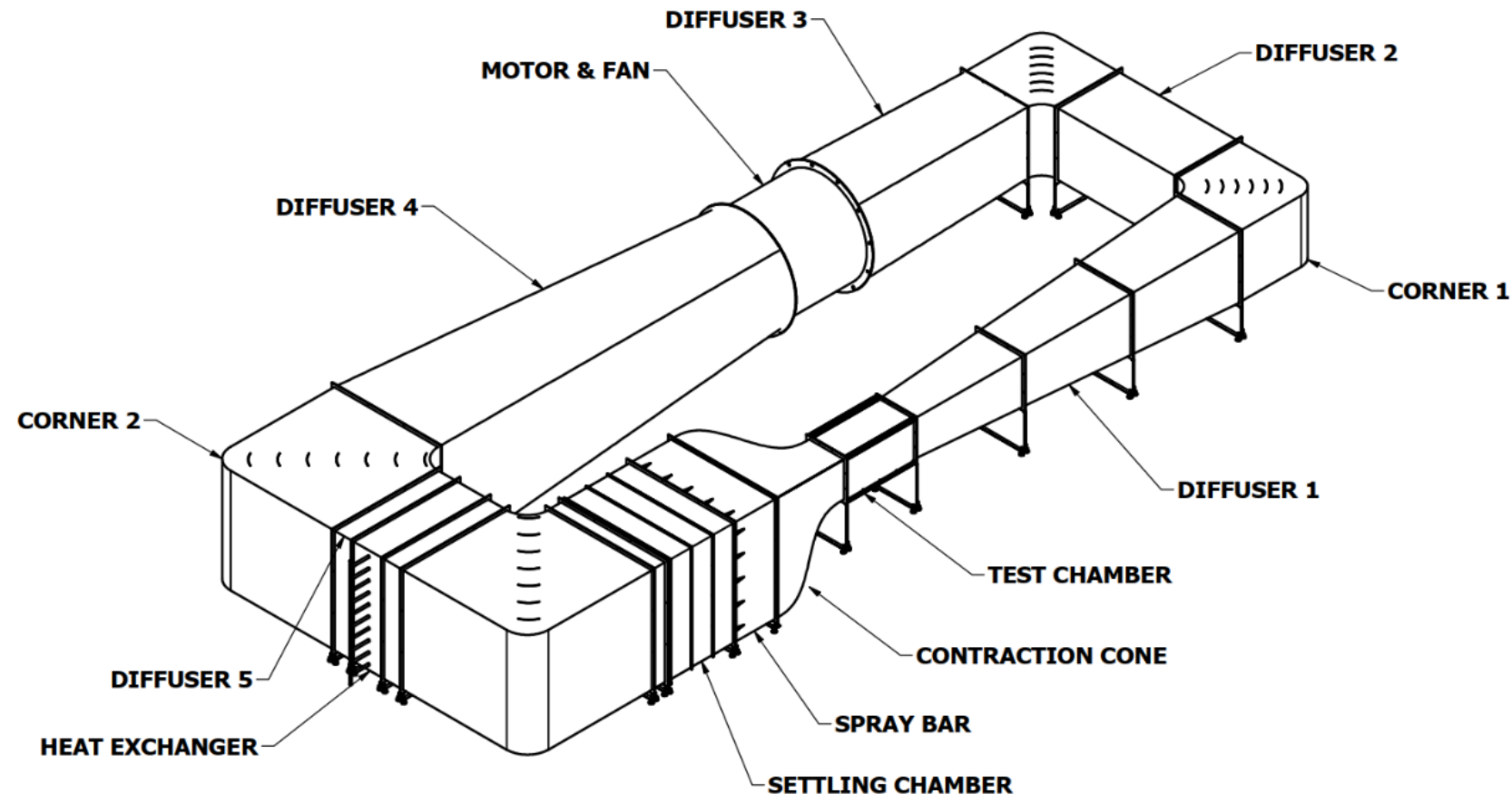
Figure 94: General Layout of IWT
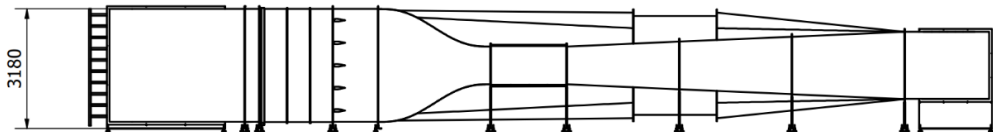
Figure 95:Side View of IWT
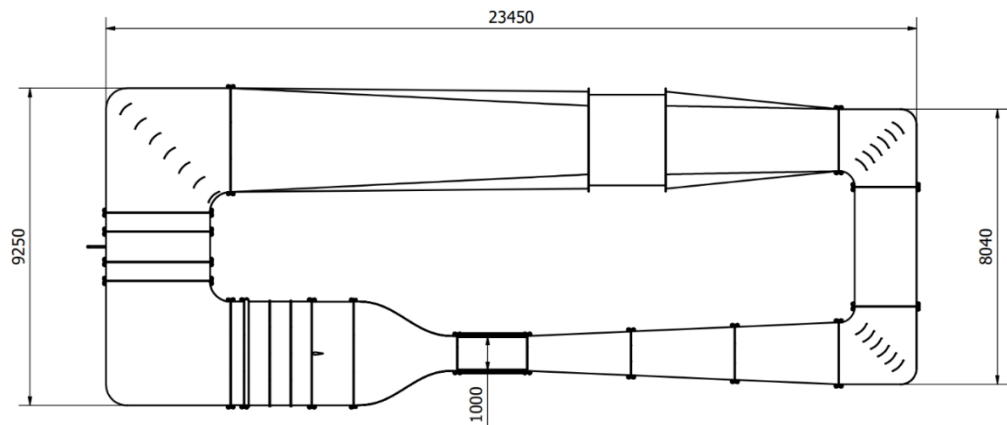
Figure 96: Top View of IWT

4.6   CFD Analysis

This section presents CFD simulations by the commercial software Ansys Fluent, conducted on the wind tunnel. These simulations were carried out to assist in the design process of the facility and were mostly completed before the development of the manufacturing plan discussed in other sections. However, the presentation of the CFD work has been postponed until this point in the dissertation to avoid redundant coverage of the facility's arrangement and geometry due to its iterative process, which has already been detailed in previous sections. The objective of this work is to assess the accuracy and dependability of the calculations through CFD simulations.

4.6.1   CFD Approach

ANSYS Fluent 2023 software was employed to conduct a CFD analysis of the flow characteristics within the wind tunnel. The simulation involved a full-scale CFD

model of the components of the icing wind tunnel. The flow field was assumed to be three-dimensional, steady, incompressible, and fully turbulent. In this case, the working fluid was air, which was treated as an ideal gas. The CFD model utilized a finite volume technique to solve the Reynolds-averaged Navier-Stokes (RANS) equations. A double precision standard SST k-omega $(k - \omega)$ turbulence model was selected. In this study, standard wall functions were employed to handle the boundary layers. The selection of the SST k-omega turbulence model is primarily influenced by its ability to closely approximate the results obtained from experimental data in wind tunnel analyses, making it the preferred choice over the SST $k - \omega$ and standard $k - \omega$ models [99].

The CFD simulation employed a solution method that incorporated an implicit approach for the pressure-coupled equations, a simple algorithm for the velocity-pressure coupling, and a second-order upwind approximation for all transport equations, except for the turbulence dissipation rate, which was approximated using a first-order scheme. The desired residuals for the continuity, momentum energy, and turbulence equations were set to be less than 1×10^{-5}.

4.6.2   Geometry

As mentioned before, the geometry was explicitly designed for CFD studies using a commercial CAD program. The designed geometry reflects all the features of the wind tunnel. Only the fan, the mesh screen, and the honeycomb were modeled mathematically due to the necessity of the application. In Figure 97, the CAD representation of the wind tunnel is depicted. Additionally, each component of the icing wind tunnel is assigned a distinct color to facilitate the analysis and interpretation of the results during the post-processing stage.
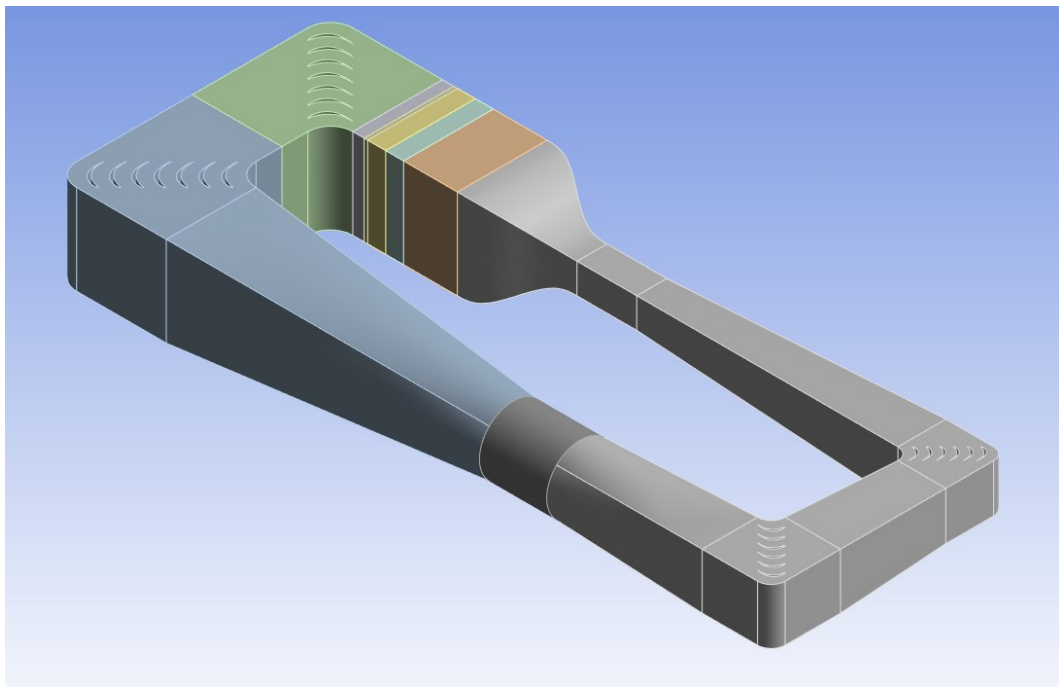
Figure 97: CFD CAD Layout

4.6.3   Meshing

The quality of the mesh is a crucial factor in achieving accurate and convergent solutions in CFD. Prismatic mesh elements are commonly employed for simple geometries, while tetragonal meshes are preferred for more complex geometries. In order to enhance the accuracy of the results, various options, such as fine meshing with high smoothing and enhanced meshing techniques, were employed. In order to resolve the boundary layers, an inflation parameter was set for all solid walls of the fluid computational domain, with twenty-five layers and a first layer thickness inflation option of $1 * 10^{-5}$ mm. Additionally, the element size was adjusted to increase the number of elements in the wind tunnel, and the mesh was refined in regions of particular interest. The average angle skewness of the cells was found to be 0.240. The overall mesh model consisted of 4,028,982 elements and 1,535,685 nodes. A significantly refined mesh resolution was implemented at the walls and motor section to enhance the precision of the flow analysis. In Figure 98 can be seen the meshing geometry in commercial software. Also, in Figure 99, section view of the meshing geometry represented to visualize inner meshes and inflation meshes.
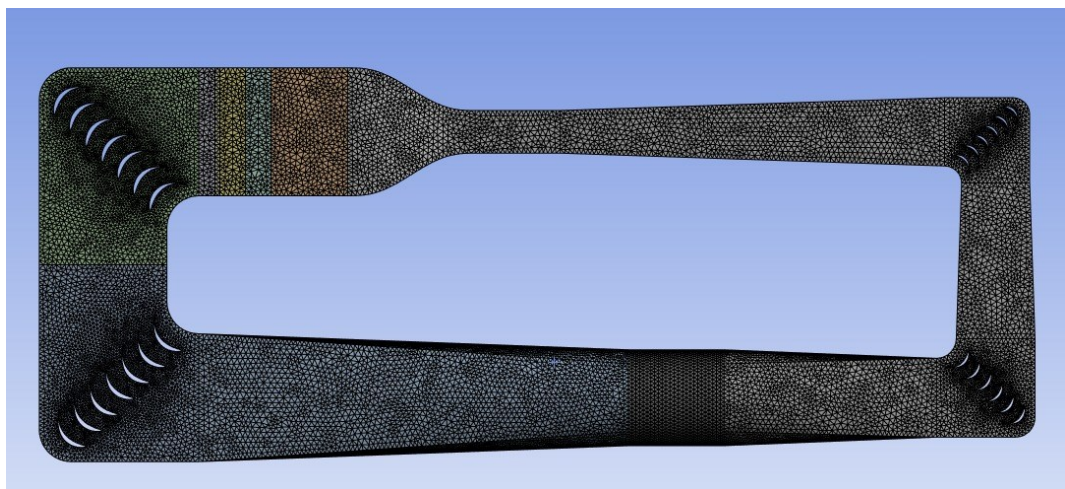
Figure 98: CFD Meshing
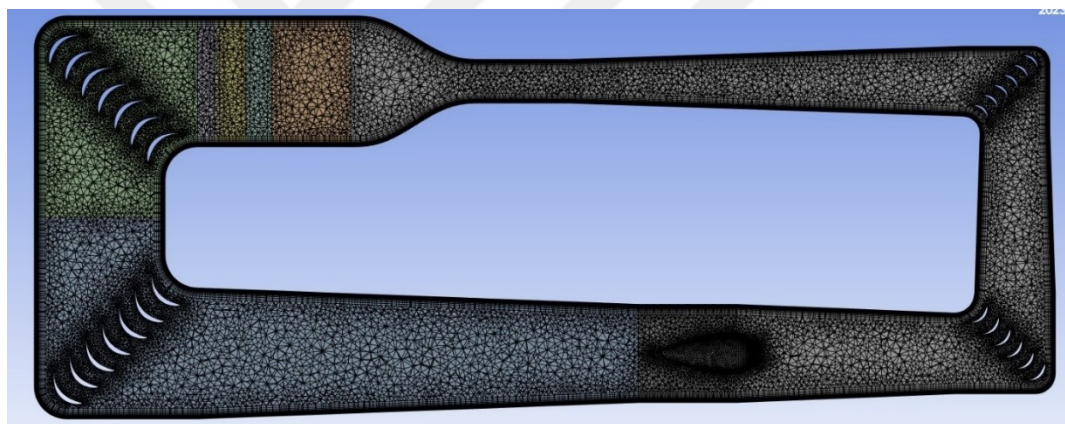
Figure 99: Mesh Section View

4.6.4   Boundary Conditions

In the numerical simulations of wind tunnel icing, two different approaches have been proposed. One approach involves leaving a gap in the geometry at the engine section and defining it as a boundary condition with a pressure outlet and velocity inlet. The second method involves keeping the geometry completely closed, adhering to the original design, and mathematically modeling the engine section to achieve a balance in terms of flow velocity. The second method has been deemed suitable in terms of accuracy and adherence to actual physical conditions.

In the wind tunnel simulations that incorporated screens and a honeycomb, the mesh screens were considered as a porous jump, resulting in a pressure jump or loss. The honeycomb, on the other hand, was treated as a porous zone. The boundary conditions for the wind tunnel in these cases consisted of a fan, porous jump zone, and radiator, as seen in Figure 100.
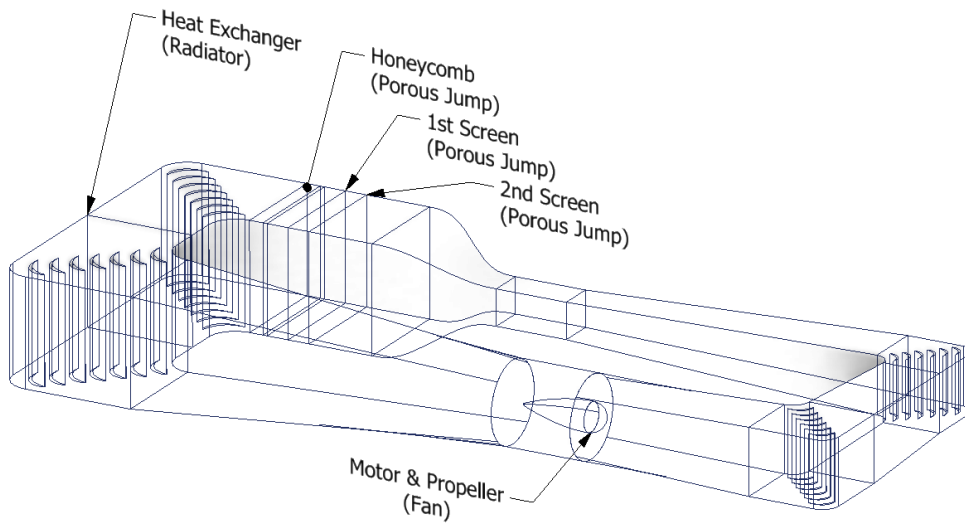
Figure 100: Boundary Condition for Icing Wind Tunnel

4.6.4.1   Porous Jump

Due to the complex nature of porous jump applications, the utilization of numerical modeling entails significant computational requirements. Consequently, flow instruments such as mesh screens, honeycombs, and heat exchangers are mathematically represented using their respective physical coefficients rather than being directly modeled in order to prevent intense CPU load originating from entangled and complex geometries. The specific intricacies of these calculations are elaborated upon in the subsequent sections.

To effectively govern the equations pertaining to this particular phenomenon, the momentum equation is established with the inclusion of a source term.

$$\nabla * (\rho \vec{v} \vec{v}) = -\nabla p * (\bar{\bar{\tau}}) + \rho * \vec{g} + \vec{S} \tag{177}$$

The term "S term," also known as the source term, encompasses two physical phenomena: viscous loss and inertial loss. The linear viscous loss term is more prominent at lower airstream velocities, while the quadratic term becomes increasingly dominant as the airstream velocity increases, representing the influence of viscous forces [100].

$$S_i = \left(\sum_{j=i}^{3} D_{ij} * \mu * v_i + \sum_{j=i}^{3} C_{ij} * \rho * |v| * v_i \right) \tag{178}$$

In equation 178, D_{ij} and C_{ij} are the diagonal matrices can be represented as $1/\alpha$ and C_2, respectively [101]. Hence, the equation becomes as follows where α is the permeability and C_2 is the inertial resistance factor.

$$S_i = \left(\frac{\mu}{\alpha} v_i + C_2 * \frac{1}{2} * \rho * |v| * v_i \right) \tag{179}$$

In order to obtain the necessary data, it is necessary to employ second-order curve fitting techniques to apply Darcy-Forchheimer's relation. The pressure drop of a specified mesh screen or honeycomb must be determined in relation to various freestream velocities, or alternatively, these values can be obtained from the manufacturer's technical data sheet.

$$S_i = \frac{\Delta p}{l} = a * V + b * V^2 = -\left(\frac{\mu}{\alpha} v_i + C_2 * \frac{1}{2} * \rho * v_i^2 \right) \tag{180}$$

a and b are the coefficients for flow characterization. In Figure 101, pressure loss of mesh screens is introduced for mesh no 10 and 5 with the curve fitting equation where the $a \ and \ b$ are equal to 0.5237 and 0.6158, 0.4139 and 0.3131, respectively. For the detailed and time-consuming process of the curve-fitting and graph approach, "Linest" command in Microsoft Excel could be used in order to achieve these multi-step calculations to gather these parameters.
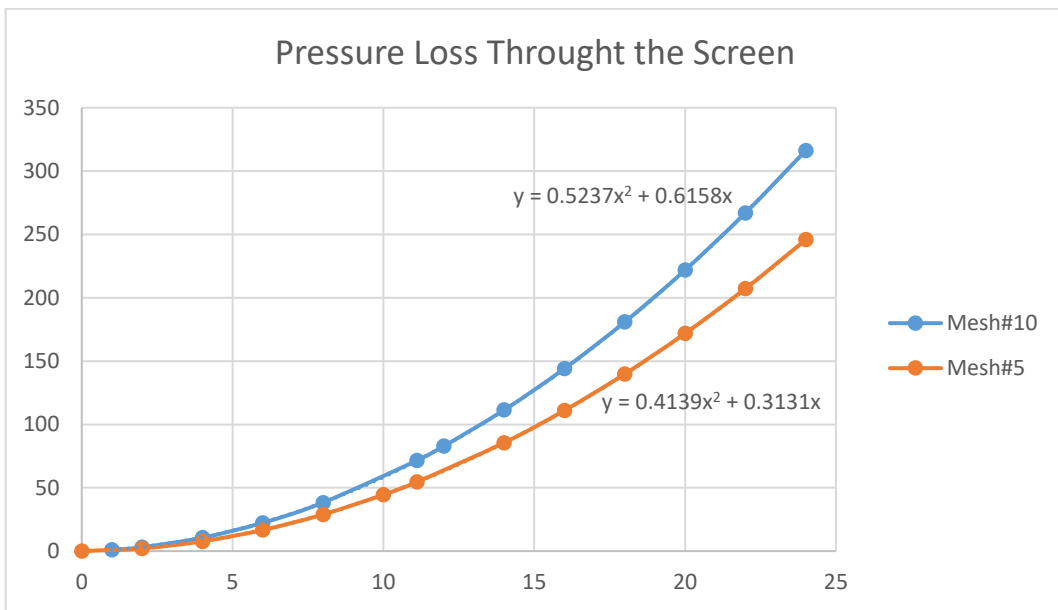
Figure 101: Pressure Loss of Mesh 5 Screen Pressure Loss

After above calculations, inertial coefficient and viscous coefficient calculated by utilization of following equations,

$$Inertial\ Resistance\ Coefficient = C_2 = \frac{2*b}{\rho*l} \qquad (181)$$

$$Viscous\ Resistance\ Coefficient = 1/\alpha = \frac{a}{l*\mu} \qquad (182)$$

Where the, α is permeability and, l is the porous medium thickness.

Table 49: Pressure Jump Coefficient for Screen Meshes

	Mesh #5	Mesh #10	HC	Unit
Face Permeability	4.714E-08	1.321E-08	2.74054E+11	m^2
Porous Medium Thickness	1.000E-03	5.700E-04	1.20E-01	m
Pressure Jump Coef.	5.768E+02	1.277E+03	1.845	m^{-1}
Porosity	64.64	60.30	98%	%

Figure 102 shows the places required to define porous boundary condition in the Ansys Fluent software. The porous jump is defined by entering the results of the calculations made using the above equations into the relevant boxes.
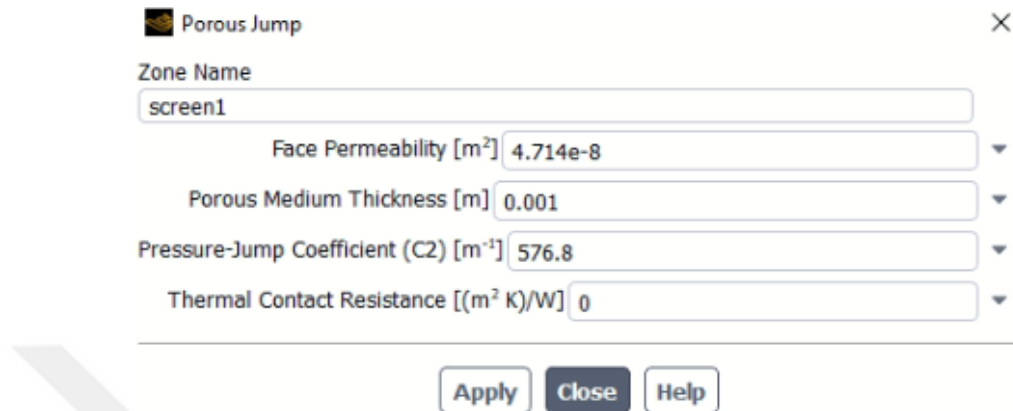
Figure 102: Porous Jump Domain Window

In order to verify the accuracy of the Porous Jump model and ensure that it has been correctly implemented, a comparative CFD study was conducted using experimental data from Groth et al.'s work [81]. A model case was created for different screens, each with a total of seven experimental data points seen in Table 50, and the calculated data was inputted into the porous jump boundary condition, which was modeled at the center of the geometry.

Table 50: Data for the Screens for 5 m/s ([81])

No	Mesh (in^{-1})	Wire Diameter (mm)	Solidity unitless	Re_d unitless	K unitless
1	2.1	2.50	0.37	830	0.68
2	4.9	1.00	0.35	330	0.66
3	7.9	0.50	0.29	170	0.49
4	12.1	0.50	0.42	80	0.99
5	19.0	0.24	0.33	80	0.79
6	34.0	0.19	0.44	65	1.64
7	147.0	0.04	0.41	13	2.90

For each of the seven cases with experimental data, calculations were performed. These calculations are presented in Table 51. Porous jump parameters required for CFD analysis were prepared and analyzed for each case.

Table 51: Screen Calculations for CFD Input

Screen No.	1	2	3	4	5	6	7
Mesh	2.1	4.9	7.9	12.1	19.0	34.0	147.0
Wire Diameter	2.5	1	0.5	0.5	0.24	0.19	0.04
Porosity	63%	65%	71%	58%	67%	56%	59%
Reynolds #	841.0	336.4	168.2	168.2	80.7	63.9	13.5
C_2	249.0	554.9	811.9	1648.5	2138.2	5080.4	22856.3
$1/\alpha$	4.2E+6	1.9E+7	4.8E+7	9.7E+7	2.2E+8	6.3E+8	8.6E+9
Permeability	2.4E-7	5.3E-8	2.1E-8	1.0E-8	4.5E-9	1.6E-9	1.2E-10
K	0.68	0.66	0.53	1.08	0.79	1.59	2.72

The results of the CFD analyses represented in Table 52 and conducted for these seven experimental conditions were compared with experimental and analytical calculations, and it was observed that the results were close to each other. However, CFD overpredicts the low Reynolds number regions. However, due to the already challenging nature of these regions, the deviations of the calculated values are moderately low. Nevertheless, the results still converge using both methods. Thus, it was concluded that the modeling performed was accurate, and the study continued based on this approach.

Table 52: Pressure Loss Comparison for Different Approaches

No	Pressure Loss (Pa)		
	Experimental	*CFD*	*Calculation*
1	10.20	11.39	10.33
2	9.90	11.14	9.95
3	7.35	9.30	8.05
4	14.85	17.92	16.27
5	11.85	13.58	11.97
6	24.60	26.46	24.01
7	43.50	45.92	40.91

When comparing the analyses of the honeycomb and mesh screens conducted using CFD, the pressure drops observed in Figure 103 are evident. The CFD results, represented by the blue line, and the analytical calculations, represented by the orange line, exhibit different trends in the change of pressure along the axis due to the distinct approaches of each method. However, there is minimal difference between the starting and ending points. Therefore, the accuracy of both methods has been demonstrated in this study, allowing for the continuation of the work with confidence in the subsequent sections.
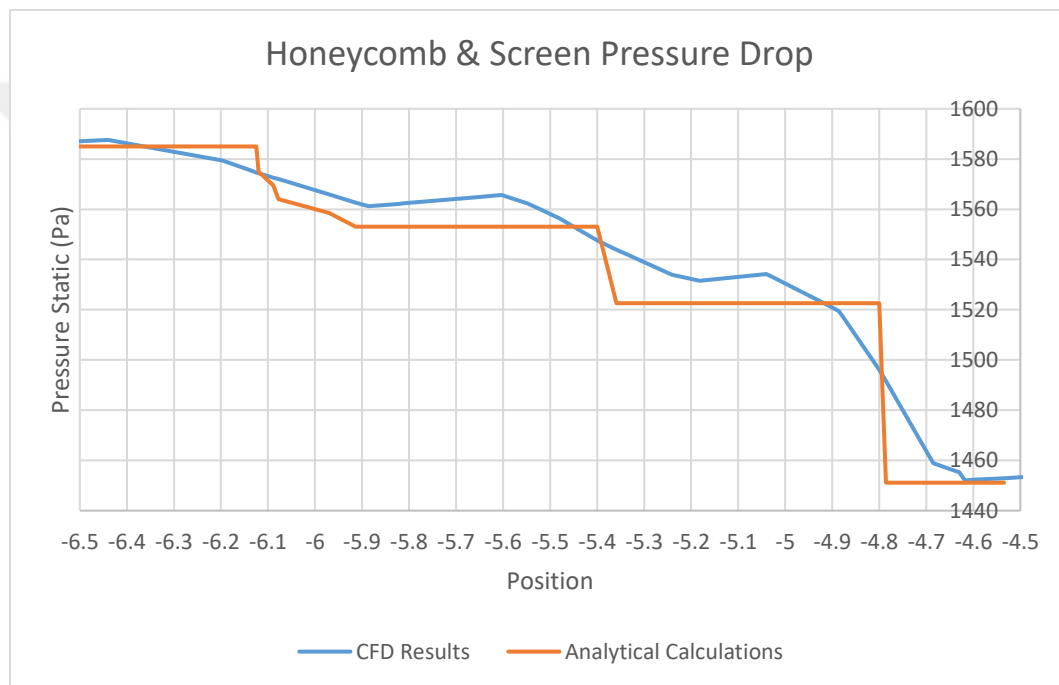

Figure 103: CFD and Analytical Calculation Comparison

4.6.4.2   Fan & Motor

The CFD analysis defined the porous jump region for the fan and motor, similar to the honeycomb or mesh application. However, this boundary condition is named as a fan. However, in this stage, the pressure and velocity graphics provided by the manufacturer for the motor were mathematically modeled. This formulation was defined as a polynomial in the CFD software's pressure jump section, represented in

Figure 105. This allowed for the estimation of the airflow quantity that the motor and fan components can generate based on pressure losses, through convergence in the CFD software. At this stage, it is essential to note that the velocity along the x-axis, as shown in Figure 104, represents the cross-sectional area of the region where the fan is located, and the velocity is calculated accordingly.
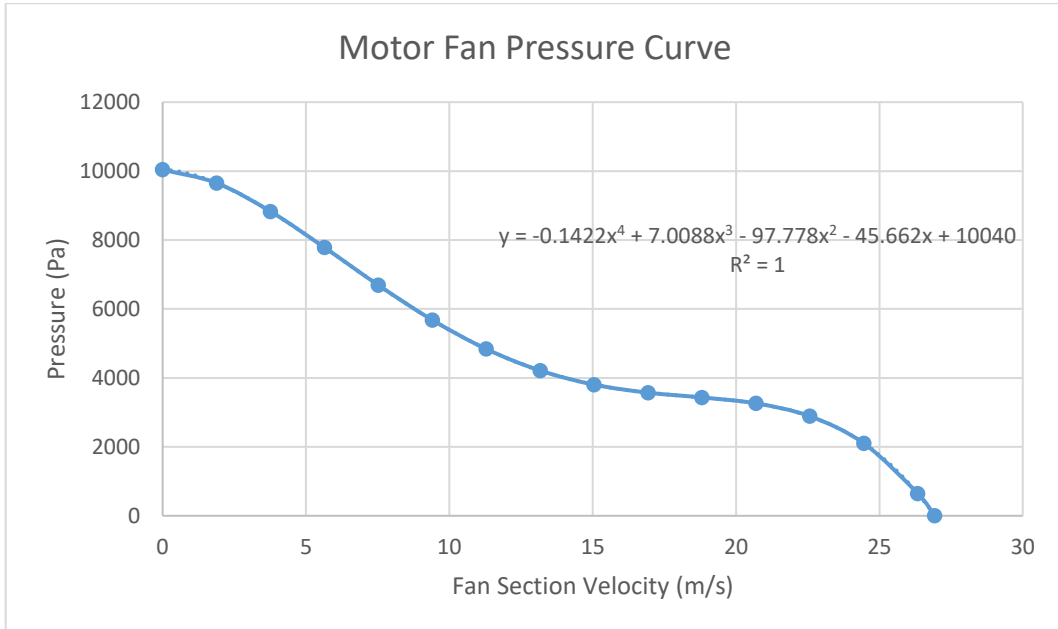

Figure 104: Motor & Fan Pressure Curve
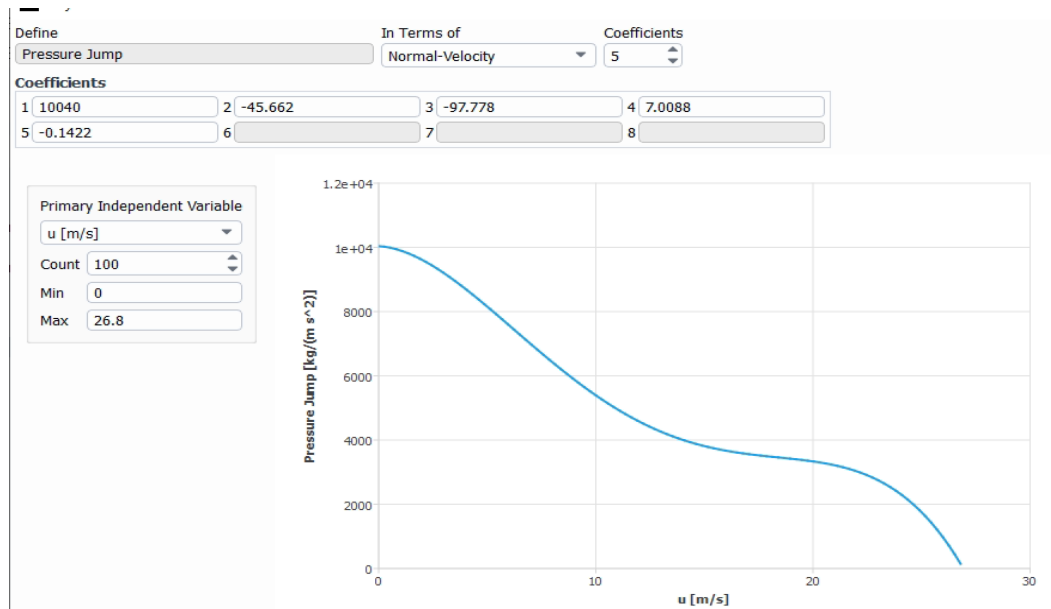
Figure 105: Fan BC Pressure Jump Polynomial Coefficients

In addition to the pressure values entered for the motor and fan, a heat definition has been made for the motor cowling section due to it being one of the significant sources of heat in the motor during icing wind tunnel tests. This heat definition is given by defining the cowling geometry, to which the motor is attached, as a wall and assigning a heat flux to this wall geometry. The total amount of heat emitted from the motor, together with aerodynamic heating, was previously found to be around 204.8 kW. However, here, only the heat emitted from the motor is calculated as the aerodynamic heating will be calculated using CFD methods. After taking heat dissipation from the motor, a value of 10 percent of motor power, the heat amount of 31500 watts, is divided by the area to obtain a value of 4075 W/m^2.
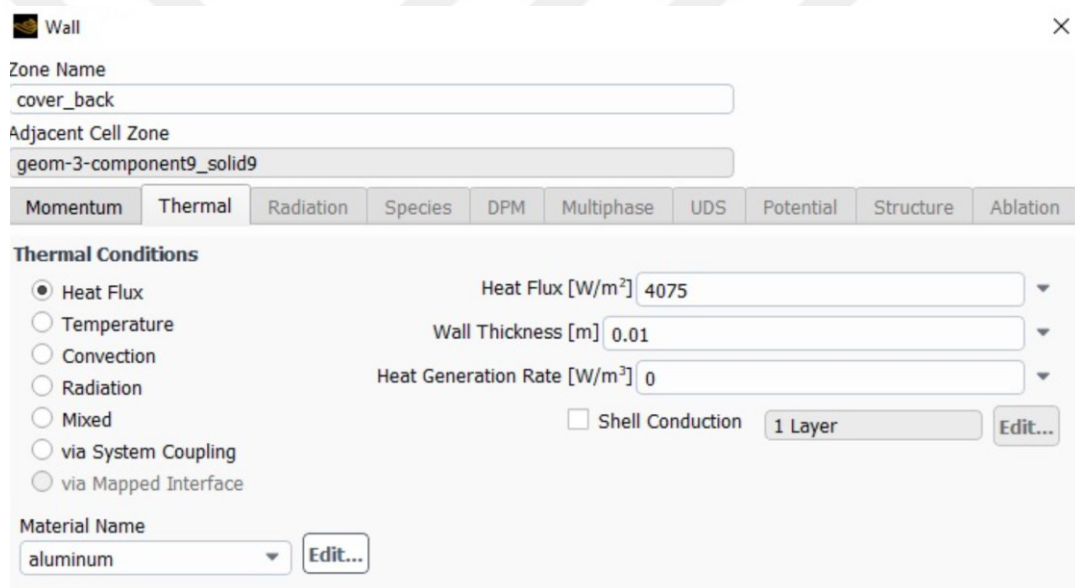
Figure 106: Motor Cowling Heat Definition

4.6.4.3   Radiator

Given that heat exchangers and porous medium share similar characteristics in terms of their detailed and repetitive microstructures, it is possible to employ the porous jump boundary condition approach to simulate heat exchangers. However, unlike the aforementioned porous jump approach, heat exchange coefficients are also added in this context. These coefficients can be determined using the equation provided below or by referring to the technical data sheet provided by the manufacturer.

$$Heat\ Transfer\ Coefficient = \frac{Q}{T_{a,d}-T_{ref}} \qquad (183)$$

The average temperature of the air between the inlet and outlet of the heat exchanger is denoted by the symbol T_{ref}.

Figure 107 depicts the interface of the commercial software program, which allows users to specify the parameters of the radiator domain. The mathematical representation of the heat exchanger will be finalized by inputting the appropriate coefficients into the designated fields.

$$HTC = \frac{q*v*c_p*(T_{a,u}-T_{a,d})}{T_{a,d}-T_{ref}} \qquad (184)$$

Where,

$T_{a,u}$ is upstream air temperature,

$T_{a,d}$ is downstream air temperature,

T_{ref} is ambient temperature,

In the motor and fan section, the software defines the variation of the heat exchanger's pressure drop with velocity as a polynomial. This variation is shown in Figure 108. Additionally, during the heat exchanger definition stage, the heat transfer coefficient is also mathematically modeled and defined as a polynomial due to its dependence on velocity. This polynomial definition is illustrated in Figure 109. Also, the radiator's temperature is governed by the analytical calculations and technical data provided by the manufacturer determined by the compressor and refrigerant of the system design.
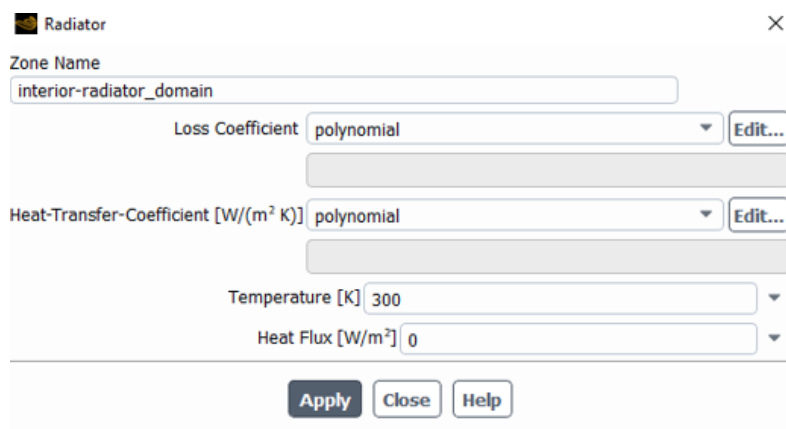
Figure 107: Radiator Domain Window
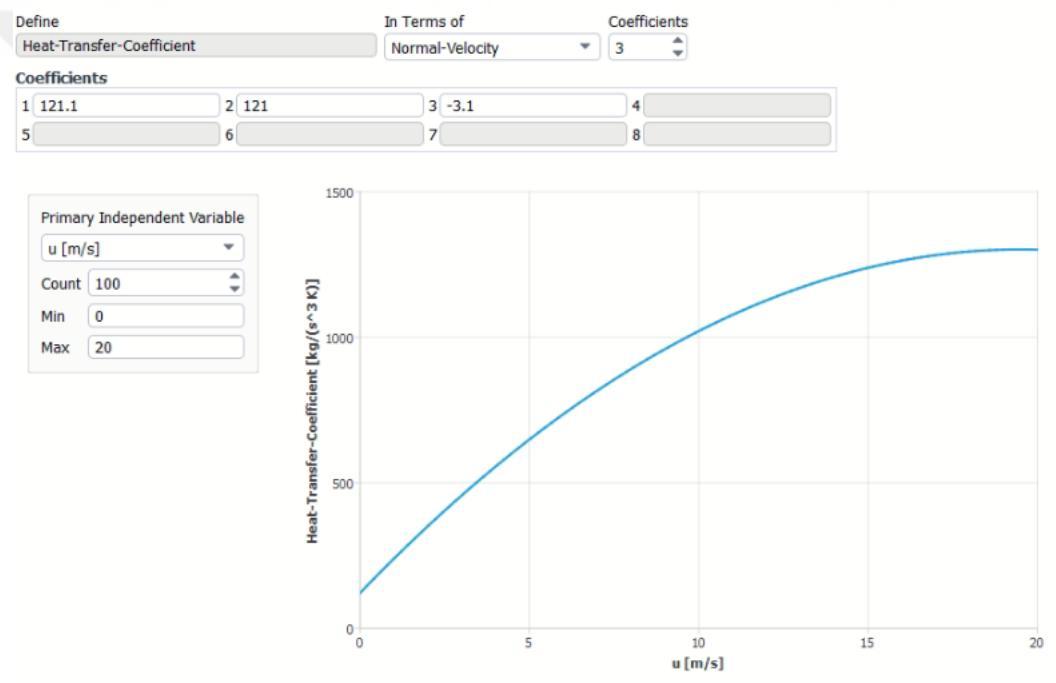
Figure 108: Heat Transfer Coefficient Polynomial Coefficients
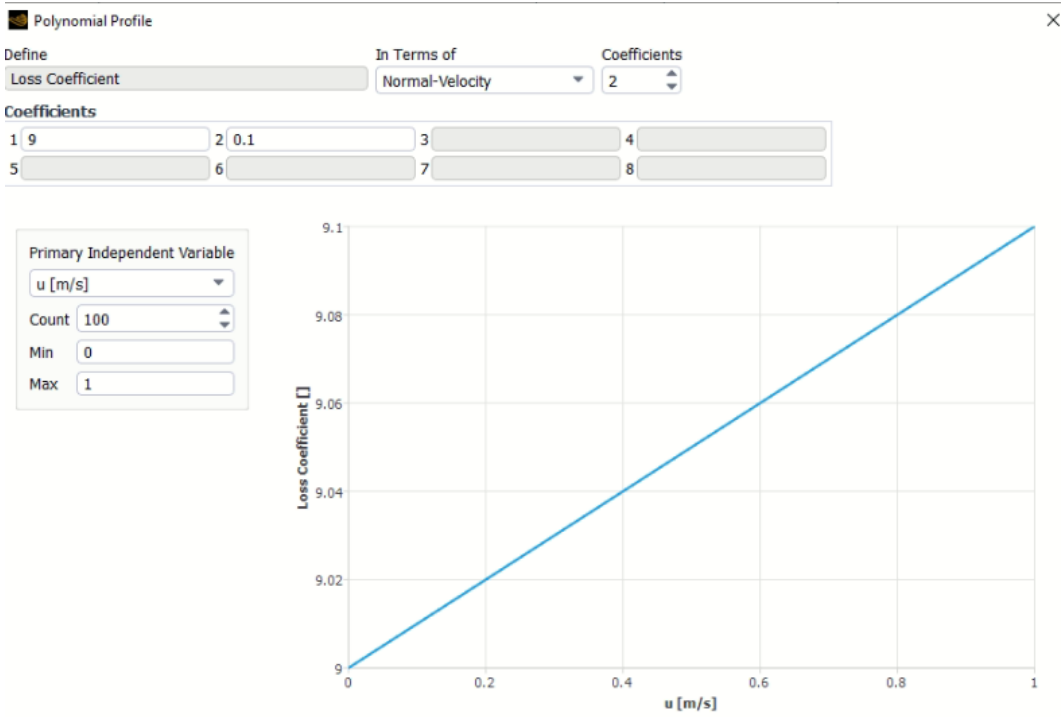
Figure 109: HTC BC Pressure Jump Polynomial Coefficients

4.6.5   Solution Controls

The solver used in the solution is a pressure-based and steady solver. Initially, this solver was defined for low-speed incompressible flows due to velocity values are low and temperature differences is negligible for being compressible. The solution domain is three-dimensional, and a solution is sought where convergence and residuals can be calculated with minimal error. Velocity definitions are not provided by the boundary conditions, as no velocity input is used. Instead, a fan that provides pressure increase is defined, and the pressure increase is entered as a polynomial function derived in the motor section. The turbulence model used in the solution is the k-omega model, which is a RANS model, as it has been shown to accurately solve turbulence and flow values in subsonic wind tunnels and provide better wall solutions. These assumptions were reached based on the studies conducted by Calautit et al.[99]. Also, energy equations are facilitated in order to calculate the thermal properties of the flow. For the solution methods, Second-order upwind

numerical schemes were selected for the pressure, momentum, turbulent kinetic energy, and turbulent dissipation rate equations in the solution. The Coupled algorithm was used for solving equations. The solution control panel is shown in Figure 110 . All parameters and relaxation factors in the viscosity panel of the FLUENT program were not modified and left as they were.
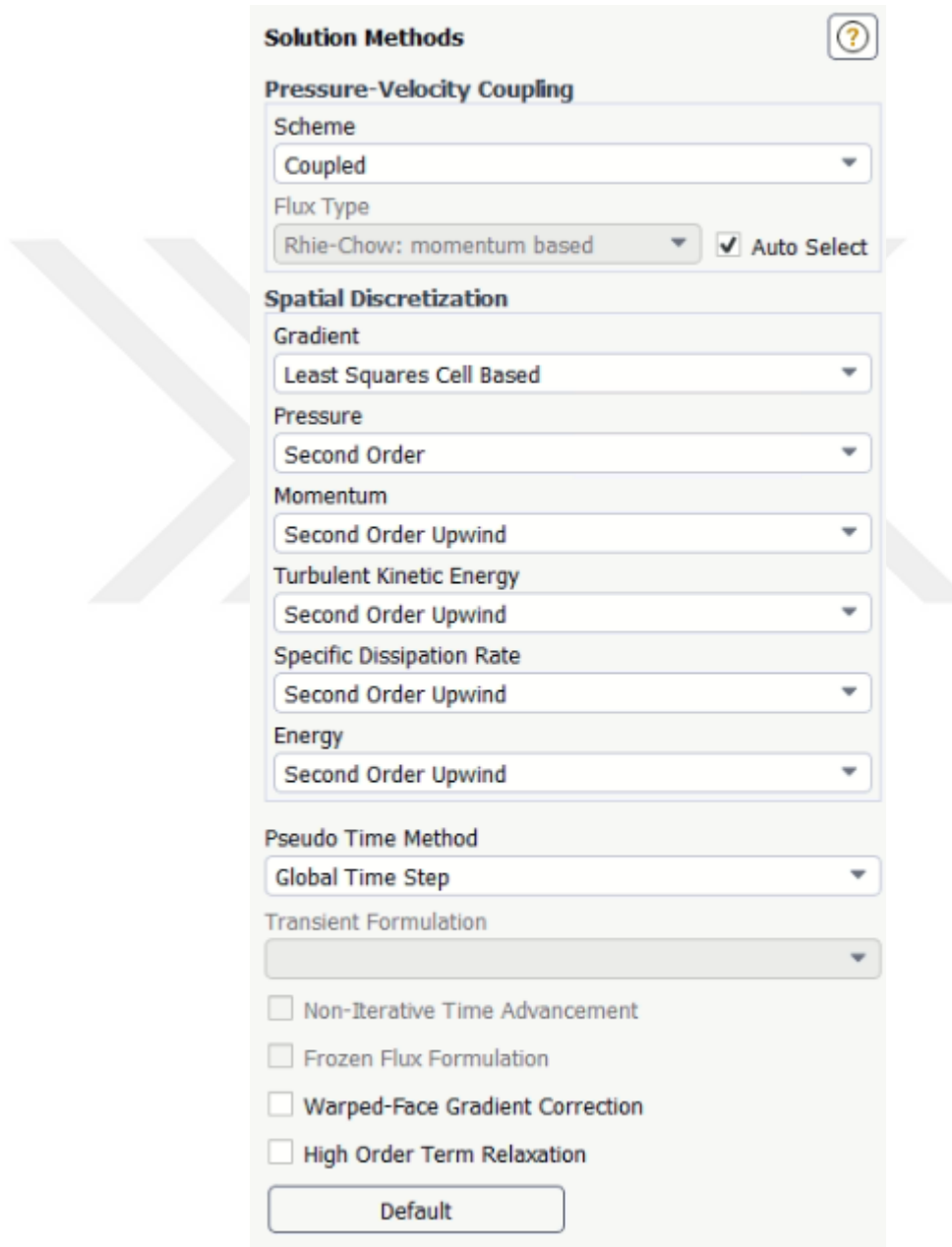
Figure 110: Solution Control Window

In addition to determining the software options, the insulation material and wall materials have been defined, as seen in Figure 111. This will play a significant role in the realism and accuracy of the thermal analyses to be conducted.
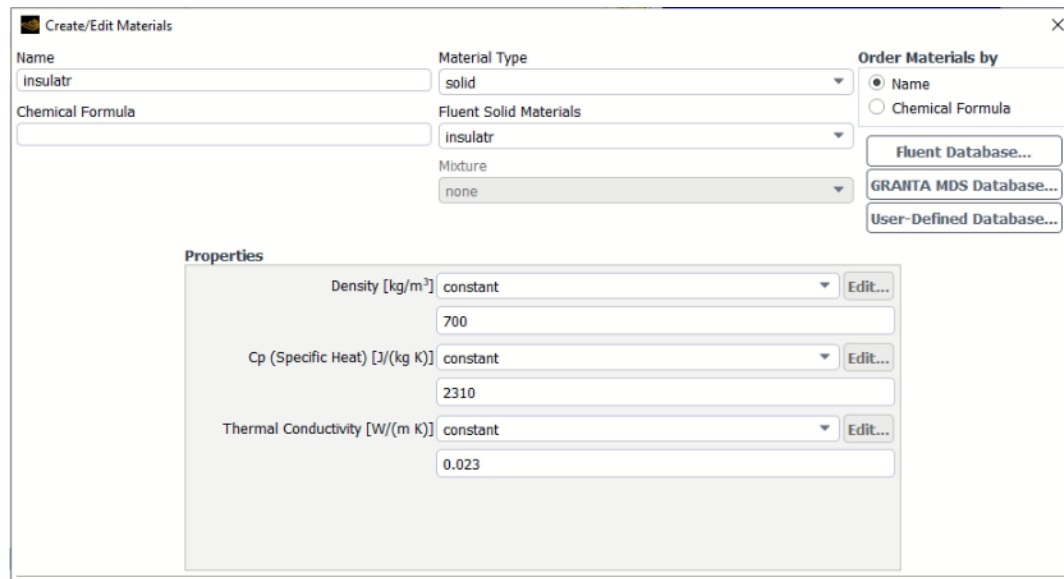
Figure 111: Insulation Material Definition

4.6.6   Results

The CFD calculations were conducted in this study to address the most challenging conditions of the icing wind tunnel, which are defined as the lowest temperature and highest velocity. The design point was determined based on these conditions. Both flow and thermal calculations were performed with a flow rate of 100 m^3/s and an ambient temperature of 20°C.

The CFD study initially focuses on the characteristics of corner valves, as they play a crucial role in directing the flow. The analysis of corner valves initially placed with a 0-degree angle of attack placement of the vanes, revealed the need for corrective measures. According to the results of the CFD analysis shown in Figure 112, it was observed that corner valves with a 0-degree attack angle did not effectively direct the flow as desired. Therefore, a design modification was implemented, and the attack angle was recalculated to be 5 degrees.
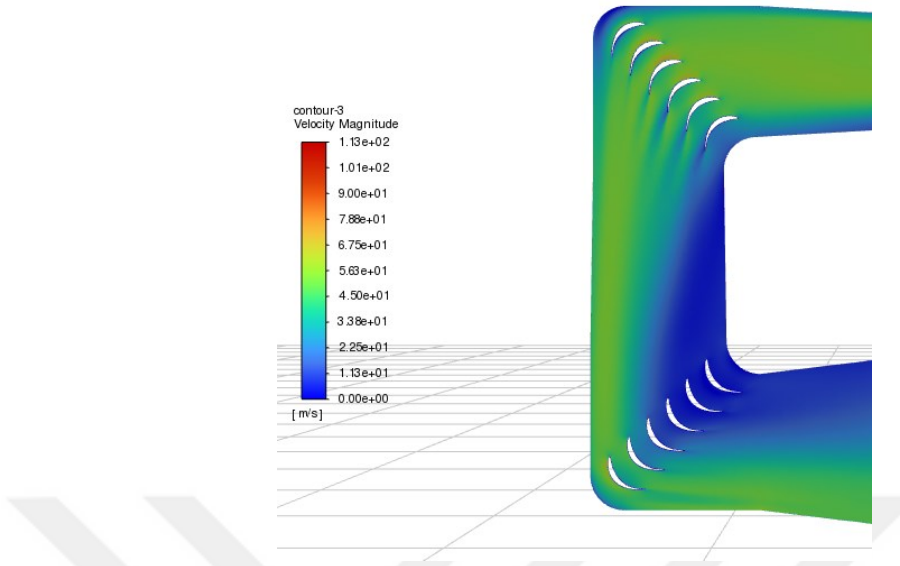
Figure 112: Velocity Magnitude of Corner Vanes LE=0 Degree

According to the contour plot of velocity magnitude observed in Figure 113, the redirection of flow has been achieved much more successfully compared to the previous condition. This study, conducted as intended for CFD analysis and verification of analytical design, has proven to be highly beneficial in design correction. Following this change in the angle of attack made throughout the entire design by means each corner vanes in the IWT, the remaining analyses have been carried out with this design modification.
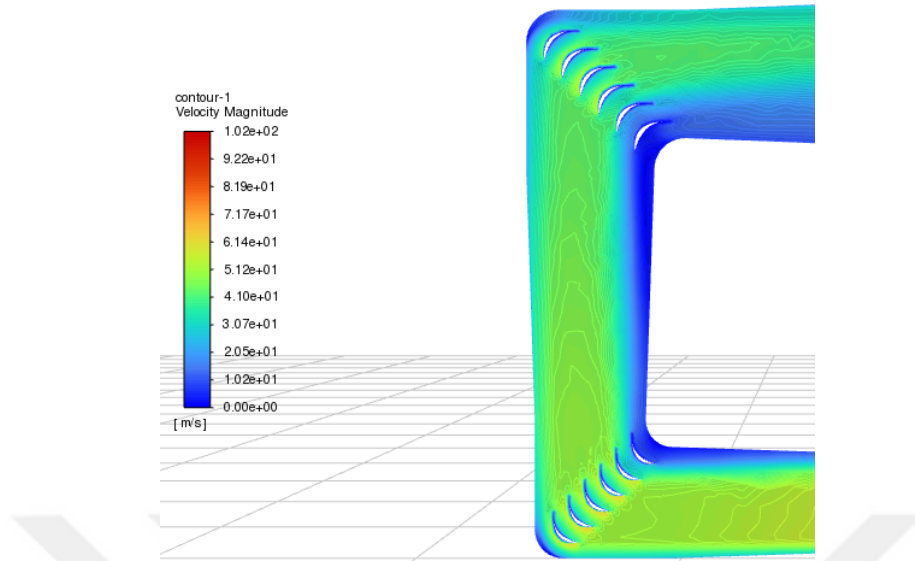
Figure 113: Velocity Magnitude of Corner Vanes LE=5 Degree

When examining the CFD results of the entire cross-section of the wind tunnel through the half axis, it is much easier to interpret the analysis results. Therefore, in order to facilitate the interpretation of the contour plots shown below, results of different physical parameters are presented.

Inspection of the velocity contour graph shown in Figure 114, it can be observed that the flow profile within the test chamber of the icing wind tunnel appears to be quite smooth, although a small separation has started at the diffuser exit. This separation subsequently grows and becomes more pronounced within the second corner, after which the flow is accelerated by the engine and accelerated within the icing wind tunnel. This distorted flow is rectified within the heat exchanger and subsequently within the settling chamber, ensuring that it enters the test chamber as a high-quality flow. Figure 115 illustrates the representation of the magnitude of velocity through particle tracking in the wind tunnel volume, where the color of the particles indicates their velocity. This visual aid serves the purpose of enhancing understanding in this area.
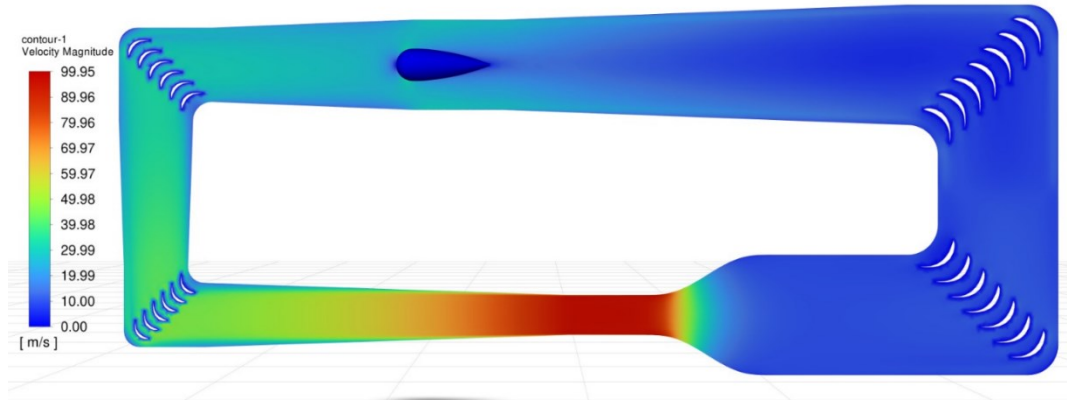
Figure 114: Top View of Velocity Magnitude Contour
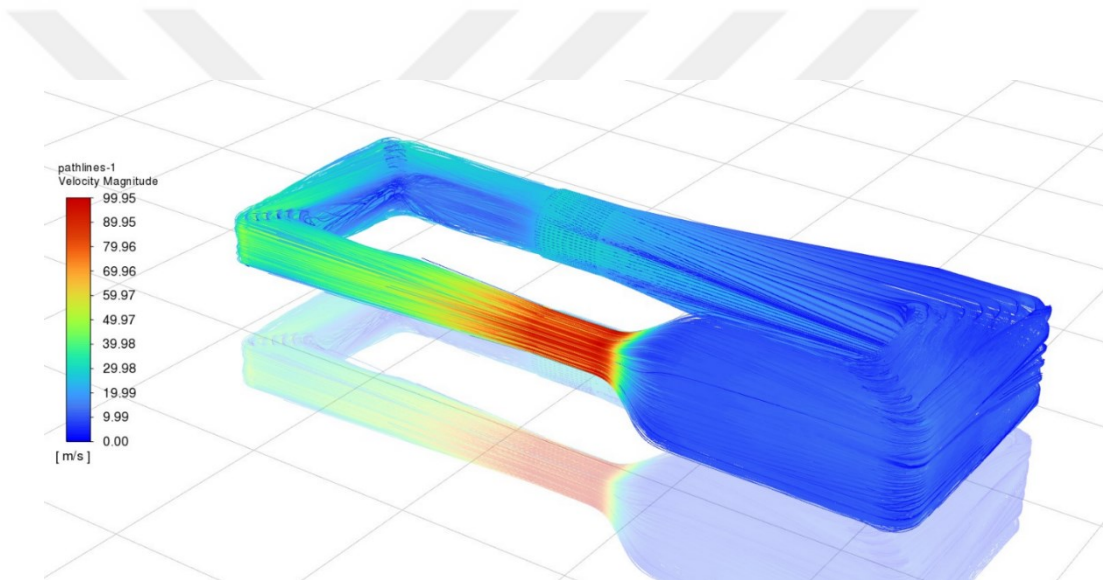
Figure 115: Velocity Particle Tracking Result for Whole Wind Tunnel

By inspecting the contours of velocity magnitude in the test chamber in more detail seen in Figure 116, it can be observed that there is no deviation of flow at the entrance of the test chamber or growth in the boundary layer after the contraction of the flow. However, as the flow progresses in the test chamber along the upstream direction, it is observed that the boundary layer propagates towards the end of the test chamber. This phenomenon is considered a regular occurrence within the context of wind tunnel testing. Subsequently, the separations in the diffuser continue to grow. Although the half-angle of the diffuser is kept as low as possible to prevent the formation of adverse pressure gradients, these separations are considered inevitable.
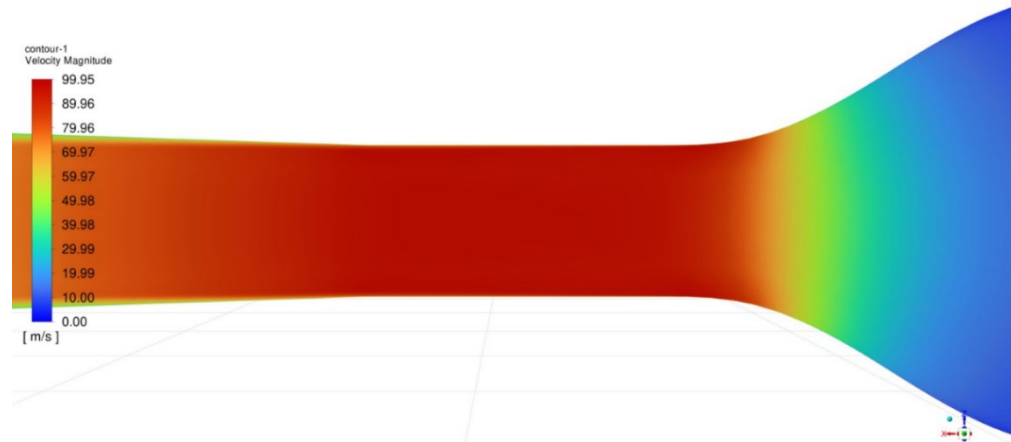
Figure 116: Velocity Section Result for Contraction and Test Section

The contour plots of velocity magnitudes provided within Figure 117 facilitate a more precise visualization of the propagation of the boundary layer conditions mentioned above. The cross-sections of the test chamber are dimensionless in this representation, with the first visual representing the inlet, the second visual representing the middle, and the third visual representing the outlet of the test chamber. Upon examining these cross-sections sequentially, it can be observed that, due to the presence of the diffuser towards the outlet of the test chamber, the contours of velocity are particularly distorted on the sides where the walls are located, indicating the growth of the boundary layer.
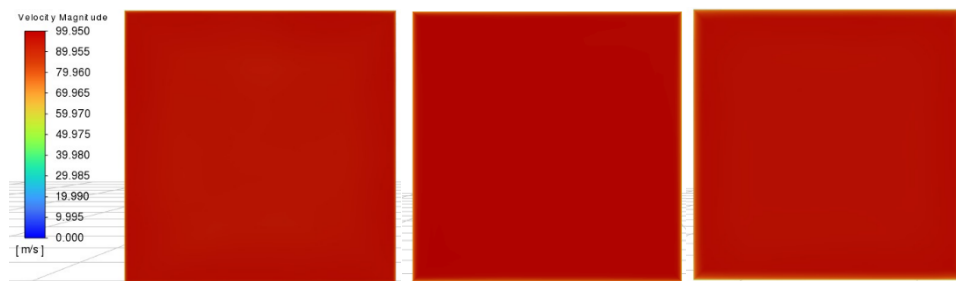
Figure 117: Test Section Velocity Magnitude Results for x/L= 0, 0.5 and 1.0

The section shapes sequence specified in Figure 117 are also applicable in Figure 118. However, Figure 118 provides turbulence intensity values according to the

sections of the test chamber, making these two graphs more meaningful when examined together. Also, Figure 119 represents the same condition with sections in more details with an isometric point of view. In both figures turbulence intensity increases in areas where the zero layer grows, as mentioned earlier, turbulence intensity values increase from the entrance to the exit of the test chamber, especially near the walls. Turbulence intensity values within the test chamber are observed to be below 1 percent. This value is sufficient to define flow as a high-quality flow. Therefore, it can be concluded that the design of the honeycomb and meshes placed in the settling chamber, followed by the design of the contraction cone, has been successfully accomplished.
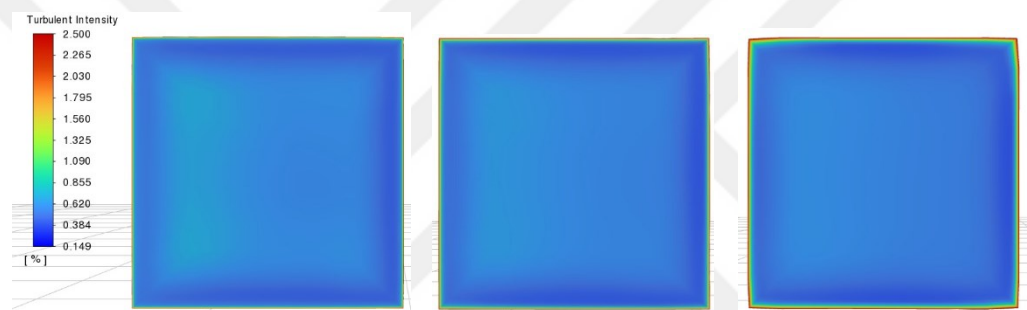
Figure 118: Test Section Turbulence Intensity Results for x/L= 0, 0.5 and 1.0
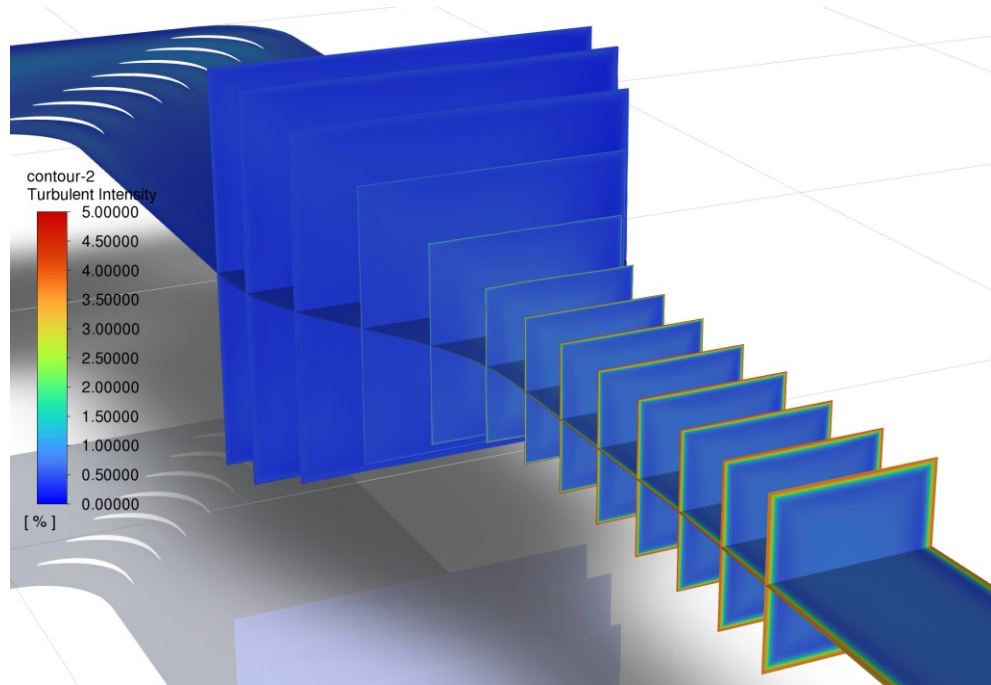
Figure 119: Turbulent Intensity Result for Different Sections

When the values observed in the previous analysis of the magnitude of the velocity contour are scrutinized by the attentive researcher, they become more meaningful when analyzed together with the static pressure values inside the icing wind tunnel. Therefore, Figure 120 displays the static pressure values that should be present in an ideal closed Wind Tunnel, which is consistent with the analysis. Specifically, examining the motor region will confirm the accuracy of the analytical calculations by comparing the pressure difference before and after the motor. The following detailed representation of the motor section will provide a more detailed and numerical presentation of this pressure difference, which is visually presented here.
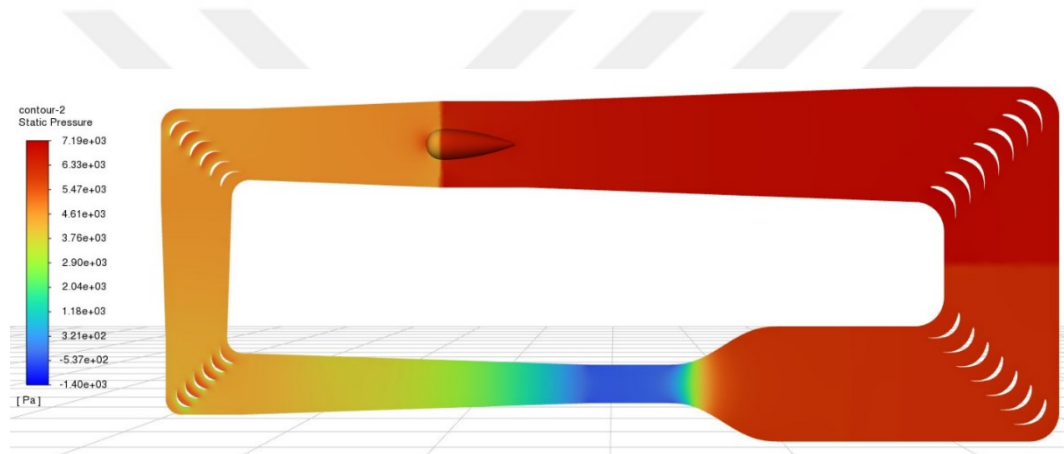
Figure 120: Top View of Static Pressure Contour

The static pressure values shown in Figure 121 have significance for the wind tunnel design and calculations. In the context of wind tunnel analysis, steady state equilibrium is presence, resulting in all physical parameters exhibiting convergence. Therefore, in order to elaborate further, the difference between the static pressure values in front of and behind the fan should be equal to the pressure loss in the wind tunnel. Upon careful examination of the values corresponding to the colors, a difference of approximately 2,000 pascals is noticeable. This is consistent with the analytical results; 1,983 pascals, previously conducted.
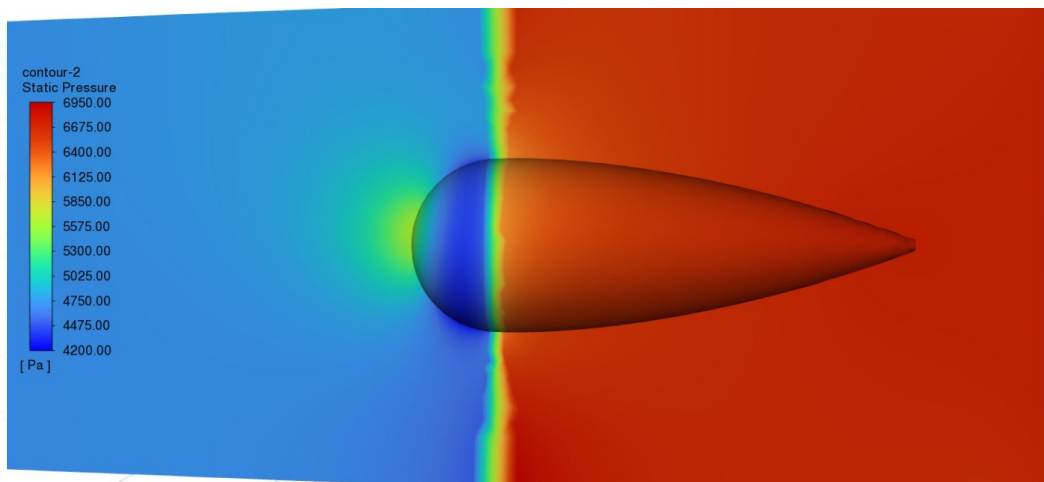
Figure 121: Static Pressure Through Fan

The turbulence intensity of the wind tunnel represented in Figure 122, shows that the turbulence intensity values increase significantly towards the ends of the diffuser. This increase leads to further elevation of turbulence intensity values during turns in corners. These turbulence intensity values, which reach their peak at the second corner, spread over a wider area towards the third corner with the effect of the motor. However, upon reaching the settling cone, turbulence intensity values decrease to levels well below one percent due to the functioning of the honeycomb and mesh screen equipment. As a result, the test chamber is provided with a high-quality flow.
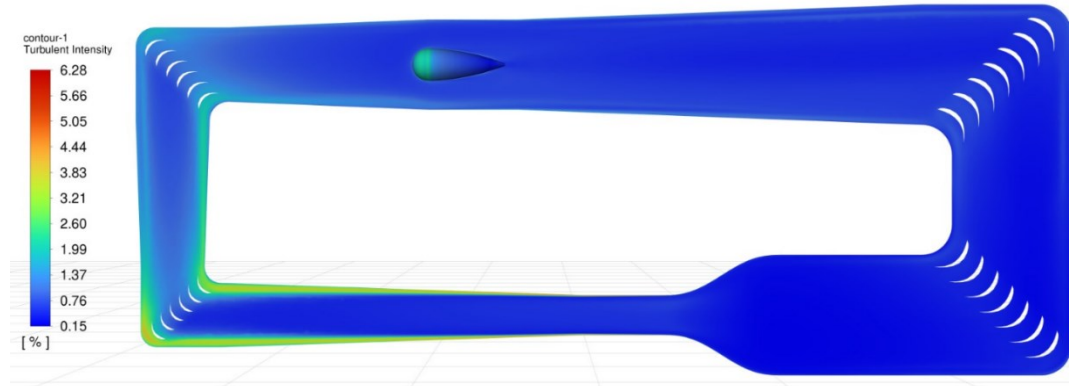
Figure 122: Turbulent Intensity Section Result for Whole Wind Tunnel

Figure 123, resents a cross-sectional view of honeycomb and meshes' static pressures. The numerical and graphical representation of this figure is also shown in Figure 103. The purpose of these equipment is to reduce irregularities in the flow and make each components of the flow more homogeneous in their direction by providing pressure damping. Therefore, it can be observed that the pressure decreases after each flow regulator device, indicating that the flow is being regulated. This is evident when examining the values of turbulence intensity, which also decrease with the pressure drop. Additionally, the pressure drop calculated as 134 pascals from the CFD results, as seen in Figure 103, shows consistent trend with the values inferred through color-based analysis in this context, as seen in Figure 123.
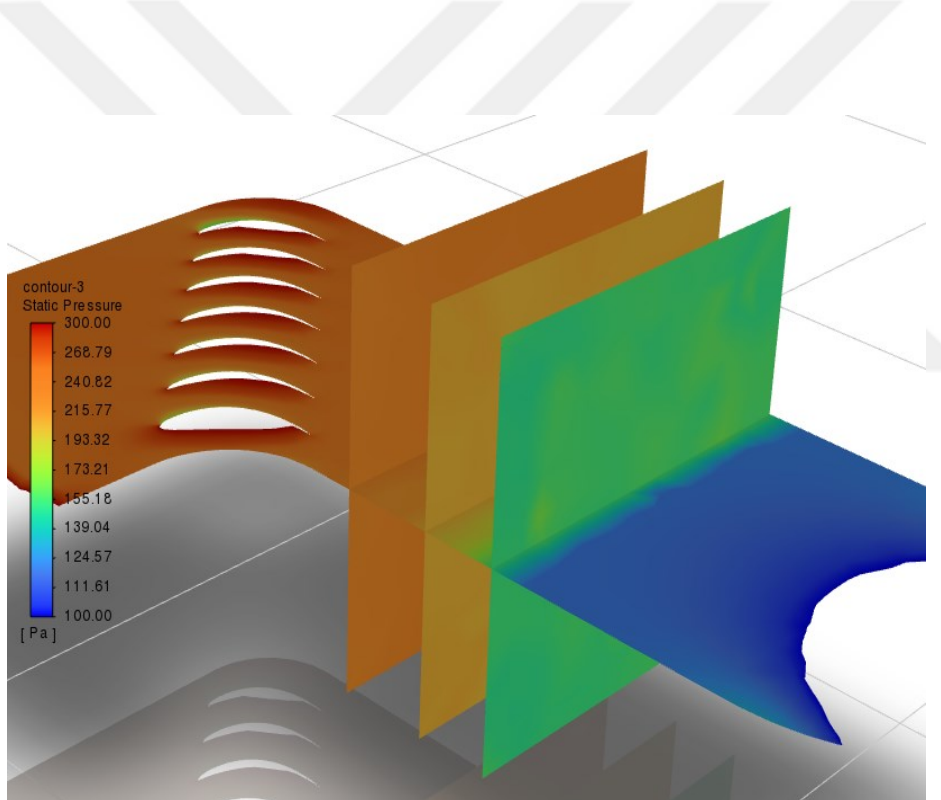
Figure 123: Static Pressure Results for Section of HC & Meshes

This dissertation examines the regulation of flow and the creation of high-quality flow within a wind tunnel, as well as the thermal properties associated with the requirements of the icing wind tunnel. In order to analyze these thermal properties, the energy equations within computational fluid dynamics solutions have been

solved, allowing for the calculation of temperature, heat flux, and other thermal parameters. Figure 124 illustrates the temperature distribution of the cross-section of the icing wind tunnel. Upon careful examination, it can be observed that the heat exchanger sufficiently reduces the temperature and that there is an aerodynamic heat input due to friction on the walls. Additionally, the temperature distribution in the test chamber is partially homogeneous due to heat losses from the walls. Therefore, it is being considered to close off the plenum chamber and this area in future studies. Furthermore, heat transfer is more effective in the interior walls due to the lower airflow velocity. As a result, there is more heat flux to airflow within the wind tunnel. Hence, the air temperature is elevated in this particular area. Additionally, the work generated by the motor placed inside the icing wind tunnel has been modeled. Additionally, the temperature differences observed in front of and behind the heat exchanger indicate a difference of approximately 3 degrees. This is consistent with previous analytical calculations, where the calculated difference was 2.61 degrees, which aligns with the approximately 3 degrees observed in this analysis.
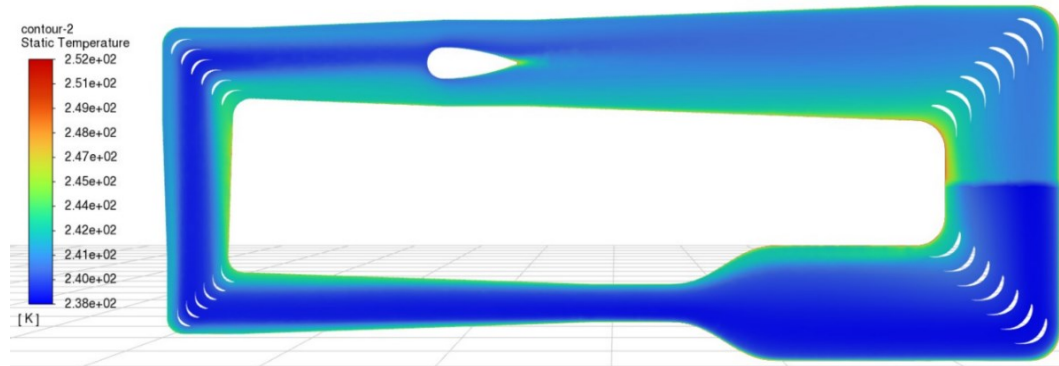
Figure 124: Temperature Result for Whole Wind Tunnel Half Section

In Figure 116, static temperature distributions are shown over the cross-sectional area within the test chamber. There is no significant variation in temperature distributions from the entrance to the exit of the test chamber. Based on the conducted analyses, the temperature within the test chamber ranges from 238 Kelvin to 245 Kelvin. Higher temperatures are observed in the wall region, which can be

attributed to the heat flow from the external environment into the tunnel. If the plenum chamber can be incorporated into the test chamber, its temperature distribution will be more homogeneous.
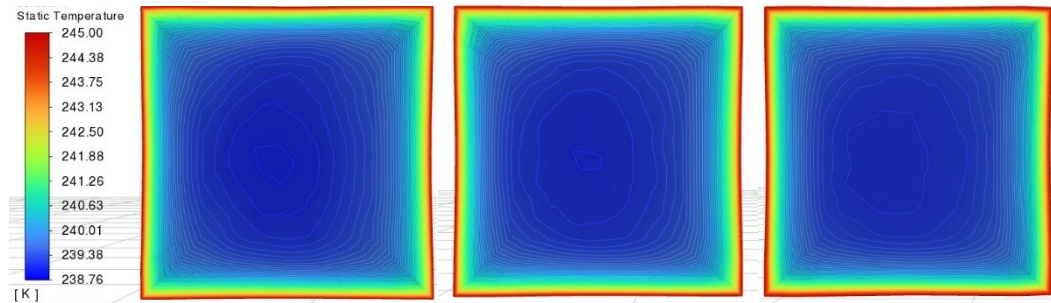
Figure 125: Test Section Static Temperature Plots for x/L= 0, 0.5 and 1.0

In terms of the analyzed results, all physical values, including temperature, pressure, turbulence, and velocity, align with the design requirements and conform to the analytical results of the design. Therefore, it can be stated that the calculations and the established model regarding the inputs are accurate and consistent.

CONCLUSION

In this dissertation, a scaling method for icing conditions was presented, which was used to scale the model size or the selected reference icing condition in order to test and better comprehend of icing conditions in icing wind tunnels or to achieve the same ice shape as the reference conditions. The limitations and challenges of this scaling method were identified in the study, providing input for the design of icing wind tunnels, mostly remaining within the boundaries of CFR 14 FAR 25, Appendix C conditions, presenting conceptual design and processes of an icing wind tunnel in the light of this information.

In the first chapter of the dissertation, the literature survey of the icing scaling studies was discussed in detail, and icing wind tunnels around the world were reviewed in order to shed light to this work.

Later, in the second chapter, the clouds that cause icing were discussed, including the formation, classification of clouds and cloud microphysics, in order to thoroughly understand the root causes and conditions of the icing phenomenon that prompted this study. In this section, the conditions in Appendix C were examined in detail, and the experimental data that study the conditions causing icing were carefully analyzed. Subsequently, the physical factors that cause icing or determining the severity of icing, were individually examined, and their specific effects on icing were expressed in depth.

In the following section, which can be considered the core of this study, an introduction was provided to modeling calculations and scaling studies related to icing. Initially, physical parameters that are assumed to contribute to icing are derived through similarity studies. Concepts such as geometric similarity, flow field, droplet trajectory, water capture, energy balance, and surface water dynamics

similarities were explained, and all calculations and formulations related to these terms were carried out.

In the same section, other competent methods for scaling ice accretion were compared, and it was decided to continue the study using the Modified Ruff Method, which yielded the highest accuracy in results. The Modified Ruff Method ensures similitude in terms of geometric similarity, flow field, droplet trajectory, water capture, energy balance, and surface water dynamics. However, certain parameters which are b and θ, were not selected to be matched, despite the solver's capability, due to the necessity of an icing wind tunnel with altitude capability. Due to the interdependence of multiple parameters affecting each other in these calculations, the GRG nonlinear solver was employed to perform the calculations, resulting in the calculation of similitude parameters with a high level of accuracy at a high resolution.

In order to test the results of the scaling studies, the in-house icing code AEROMSICE-2D was utilized in the present study. After providing a detailed explanation of the specifics and calculation methods of this icing prediction code, the Langmuir D distribution, which represents the droplet size distribution within the cloud rather than assuming the presence of only one droplet size, was incorporated into the code to enhance the resolution and accuracy of icing prediction. The results of this addition led to a negligible increase in the amount of icing at the top and bottom sections of the geometry exposed to ice close to the droplet impingement limit. However, the calculations of collection efficiency values have proven to be highly beneficial in improving accuracy.

In this study, scaling and icing prediction calculations were performed for six cases. For cases where experimental data were available, the accuracy of the resulting ice contours was validated by performing ice shape and droplet collection efficiency calculations of the reference and scaled conditions. This way, the scaling calculations' limitations and accuracy were understood. The interpretation of the results revealed the uncertainties and limitations of the modelling and scaling studies. This evaluation revealed that the particle sizes should not be below 10-micron size, and the velocities should not exceed 150 m/s (0.45 Mach) even limited to 100 m/s

(0.3 Mach) in the wind tunnel tests with these limitations, according to the calculations made in this study. Also, scaling should not be lower than ¼ or even ½ for some cases. Furthermore, it has been determined that the minimum temperature inside the wind tunnel is -30 degrees Celsius, and the size of the testing chamber is projected to be 1 x 1 meter.

In general, all parameters related to icing within the dimensioned models have been matched except for b and θ values. It is also possible to match b and θ values, but this requires the pressure values of the dimensioned environment to be much lower than ambient, requiring altitude capability. The results obtained are exactly accurate for rime ice, while they are mostly in good agreement for mixed and glaze ice conditions. Besides, droplet collection efficiency values are in perfect agreement for all cases. Interpretations of the missing parts in this regard were made, and it was stated that these calculations would not be entirely accurate for high-speed flows and elevated temperatures. In order to be specific, accurate results were not obtained if the total temperature was above -1^0C or high-speed effects were present.

Due to inherent issues related to glaze ice modelling and differences in flow regimes, additional similitude parameters to be matched and, mathematical models with higher fidelity regarding glaze ice are required. In spite of the shortcomings of the methods presented, the approach used in the current study can produce accurate and valuable data for the sizing and design of an icing wind tunnel within the limitations. In the subsequent chapter, all the limitations and requirements necessary for the design of the Icing Wind Tunnel were presented. This section began with a brief description of the components of the IWT, followed by a power analysis for the extended wind tunnel, where the motor power was initially estimated. Subsequently, design calculations were performed to individually size and characterize all the components, taking into account constraints such as pressure loss and their respective locations.

For the following components of the IWT, the calculations for the honeycomb and mesh screen within the settling chamber have been thoroughly conducted with a more detailed analysis and calculation. These calculations were conducted in order to enhance the flow quality while enhancing the turbulence reduction factor of the

IWT. Particularly, extensive research has been carried out on mesh screen designs to reduce turbulence intensity and accurately calculate pressure loss, resulting in valuable data in this regard.

In order to select the cooling equipment, it was necessary to perform thermal load calculations for the IWT. These calculations determined the amount of heat entering through the walls, the heat generated by the water injected into the flow by the spray bar, which consists of latent and sensbile heat, and the heat generated by the motor and fan combination placed inside the wind tunnel to facilitate pressure jump. The calculations for these factors were conducted in detail. As a result, a heat load of approximately 374 kW and, temperature rise of 2.61°C were determined. When comparing this result with the cooling capacities corresponding to the existing wind tunnel motors, it was found that the obtained result was satisfactory. In order to design a cost-effective wind tunnel that can maintain a constant temperature of -30°C for sessions, it has been calculated that the injection of liquid nitrogen into the air is necessary to achieve a temperature of -40°C in certain rare cases. Based on these calculations, a 250-liter liquid nitrogen tank can keep the wind tunnel at -40°C for approximately 27 seconds. However, in order to achieve a desired exposure time of 6 minutes, a proposed solution involves the implementation of a combined manifold structure consisting of 12 tanks.

The design of the spray bar, which is a crucial component of the Wind Tunnel, has been thoroughly examined and constructed. Firstly, the design and atomization of the liquid have been extensively studied, and the relevant parameters have been presented. Subsequently, the calibration curve of the air-assisted nozzle used by NASA has been calculated, and the quantities of droplets obtainable at different pressures have been investigated. Additionally, the temperature of the droplets injected into the tunnel has been analyzed until reaching the model, and the position of the spray bar within the IWT has been determined accordingly.

After calculating the pressure losses for each component of the wind tunnel, the total pressure loss was determined and used to select the appropriate motor fan combination. Once the design of this component was completed, all the components of the wind tunnel were identified, and a 3D CAD model was created based on this

information. Two different designs were produced, one for computational fluid dynamics analysis and the other for detailed design purposes with the intention of manufacturing.

In the final stage of this dissertation, CFD analyses were performed. The necessary boundary conditions for conducting these analyses were determined, and the computation of these boundary conditions was completed. Additionally, the quality of the flow was examined using the $k - \omega$ turbulence model. Furthermore, the results of the flow and thermal analyses were found to be in complete agreement with the analytical calculations, indicating that the design is adequate. Consequently, it can be observed that the results obtained from this design, taking into account the limitations of the IWT, are satisfactory in terms of the icing phenomenon.

REFERENCES

[1]   U.S. Government Publishing Office, "Airworthiness Standards: Transport Category Airplanes," *14 CFR Ch. I (1-1-16 Edition) Part 25*, 2016, [Online]. Available: https://www.govinfo.gov/content/pkg/CFR-2016-title14-vol1/pdf/CFR-2016-title14-vol1-part25.pdf%0Ahttps://www.govinfo.gov/

[2]   R. K. Jeck, "Icing Design Envelopes (14 CFR Parts 25 and 29 , Appendix C) Converted to a Distance-Based Format," *Regulation*, no. April. p. 55, 2002.

[3]   E. J. Sibley and R. E. Smith, "Model testing in an icing wind tunnel," *Lockheed Aircraft Corp., Inc., Rep. No. LR*, vol. 10981, 1955.

[4]   E. D. Dodson, "Scale model analogy for icing tunnel testing," *Document No. D6*, vol. 7976, 1962.

[5]   W. Olsen and J. Newton, "Experimental and Analytical Evaluation of Existing Icing Scaling Laws," *unpublished draft of NASA Technical Memorandum*, 1986.

[6]   D. N. Anderson and G. a. Ruff, "Scaling methods for simulating aircraft in-flight icing encounters," *NASA Technical Memorandum*, vol. 107538, no. October. 1997.

[7]   M. Ingelman-Sundberg, O. K. Trunov, and A. Ivaniko, "Methods for prediction of the influence of ice on aircraft flying characteristics," 1977.

[8]   C. Armand, F. Charpin, G. Fasso, and G. Leclere, "Techniques and Facilities Used At the Onera Modane Centre for Icing Tests.," AGARD-AF-127, November, 1977.

[9]   F. Charpin and G. Fasso, "Ising Testing In The Large Modene Wind-Tunnel on Full-Scale And Reduced Scale Models," in *Nasa Technical Memorandum*, 1972, pp. 23–42.

[10] D. N. Anderson, "Manual of scaling methods," *NASA CR*, vol. 212875, 2004.

[11] G. A. Ruff, "Analysis and verification of the icing scaling equations," 1986.

[12] M. G. Potapczuk, "Aircraft icing research at NASA Glenn research center," *J Aerosp Eng*, vol. 26, no. 2, pp. 260–276, 2013.

[13] Q. Wang and X. Yi, "A computational strategy for determining the optimal scaled wind speed in icing wind tunnel experiments," *Comput Fluids*, vol. 250, p. 105734, Jan. 2023, doi: 10.1016/j.compfluid.2022.105734.

[14] M. M. Oleskiw, F. H. Hyde, and P. J. Penna, "In-flight icing simulation capabilities of NRC's altitude icing wind tunnel," in *39th Aerospace Sciences Meeting and Exhibit*, 2001, p. 94. doi: 10.2514/6.2001-94.

[15] S. E. Bansmer *et al.*, "Design, construction and commissioning of the Braunschweig Icing Wind Tunnel," *Atmos Meas Tech*, vol. 11, no. 6, pp. 3221–3249, 2018, doi: 10.5194/amt-11-3221-2018.

[16] B. Chanetz, "A century of wind tunnels since Eiffel," *Comptes Rendus - Mecanique*, vol. 345, no. 8, pp. 581–594, 2017, doi: 10.1016/j.crme.2017.05.012.

[17] G. P. Klemenkov, Y. M. Prikhod'Ko, L. N. Puzyrev, and A. M. Kharitonov, "Modelling of icing of flying vehicles in climatic wind tunnels," *Thermophysics and Aeromechanics*, vol. 15, no. 4, pp. 527–536, 2008, doi: 10.1007/s11510-008-0001-7.

[18] P. Anton, E. Gritton, R. Mesic, and P. Steinberg, "Do NASA's Wind Tunnel and Propulsion Test Facilities Serve National Needs?," RAND NATIONAL DEFENSE RESEARCH INST SANTA MONICA CA, 2020. doi: 10.7249/rb9066.

[19] L. Vecchione, P. P. De Matteis, and G. Leone, "An overview of the CIRA Icing Wind Tunnel," in *41st Aerospace Sciences Meeting and Exhibit*, 2003, p. 900. doi: 10.2514/6.2003-900.

[20]   S. Chintamani, D. Delcarpio, and G. Langmeyer, "Development of Boeing Research aerodynamic icing tunnel circuit," in *AGARD conference proceedings*, 1997, pp. 1–8.

[21]   C. Of, "Icing wind tunnel," 2010. https://www.rta.eu/en/facility/customer-area/icing-wind-tunnel-iwt (accessed Oct. 18, 2022).

[22]   E. Herman, "Goodrich icing wind tunnel overview, improvements and capabilities," in *Collection of Technical Papers - 44th AIAA Aerospace Sciences Meeting*, 2006, pp. 10300–10307. doi: 10.2514/6.2006-862.

[23]   K. Ai-Khalil, L. Salamon, and G. Tenison, "Development of the Cox icing research facility," in *36th AIAA Aerospace Sciences Meeting and Exhibit*, 1998, p. 97. doi: 10.2514/6.1998-97.

[24]   J. J. Reinmann, R. J. Shaw, and W. A. Olsen, "Aircraft Icing Research At Nasa.," *NASA Tech Memo*, vol. 26, no. 2, pp. 260–276, 1982.

[25]   W. L. C. Alun Jones, "Technical Note No. 1855 : Recommended values of meterological factors to be considered in the design of aircraft ice-prevention equipment," NATIONAL   AERONAUTICS   AND   SPACE ADMINISTRATION MOFFETT FIELD CA AMES …, 1949. [Online]. Available:
https://www.google.com/url?sa=t&rct=j&q=&esrc=s&source=web&cd=&cad=rja&uact=8&ved=2ahUKEwjDvcLJkrnrAhUml4sKHawwBg8QFjAAegQIAxAB&url=http%3A%2F%2Fnaca.central.cranfield.ac.uk%2Freports%2F1949%2Fnaca-tn-1855.pdf&usg=AOvVaw1CI-FOBcC3Sr-YALq6frrn

[26]   A. Heinrich *et al.*, "Aircraft Icing Handbook, Volume 1 of 3," Gates Learjet Corp Wichita KS, 1991. [Online]. Available: ADA238040

[27]   P. T. Hacker and R. G. Dorsch, "a Summar Y of Meteorological Conditions Associated With Aircraft Icing and a Proposed Method of Selecting Design Criterions for Ice-Protection Equipment," 1951.

[28]   "EASA SLD Rule: Amendment 25-18 to CS-25, 'Airplane and Engine Certification Requirements in Supercooled Large Drop, Mixed Phase, and Ice

Crystal Icing Conditions.'" Accessed: Jul. 27, 2022. [Online]. Available: https://www.easa.europa.eu/en/document-library/certification-specifications/cs-25-amendment-18

[29] "FAA SLD Rule: CFR Title 14, Part 23 (amendment 64), Part 25 (amendment 145), and Part 33 (amendment 34), Appendix O, 'Supercooled Large Drop Icing Conditions,'" 2015. Accessed: Jul. 27, 2022. [Online]. Available: www.ecfr.gov

[30] M. S. Chappell and W. Grabe, *Icing Problems on Stationary Gas Turbine Powerplants*. National Research Council Canada, 1974.

[31] W. Lewis and W. H. Hoecker Jr., "Observations of Icing Conditions Encountered In Flight During 1948," 1948.

[32] W. Lewis and N. R. Bergrun, "A probability analysis of the meteorological factors conducive to aircraft icing in the United States," National Aeronautics and Space Administration Washington DC, 1952.

[33] I. Paraschiviou and F. Saeed, "Aircraft icing (unpublished book draft)," 2007.

[34] L. V Mitchell, "Aircraft Icing-A New Look," *Aerospace Safety. Published by the US Air Force*, pp. 9–11, 1964.

[35] L. Makkonen, "Estimating intensity of atmospheric ice accretion on stationary structures," *J Appl Meteorol Climatol*, vol. 20, no. 5, pp. 595–600, 1981.

[36] M. K. Politovich, "Predicting glaze or rime ice growth on airfoils," *J Aircr*, vol. 37, no. 1, pp. 117–121, 2000.

[37] T. Vukits, "Overview and risk assessment of icing for transport category aircraft and components," in *40th AIAA Aerospace Sciences Meeting & Exhibit*, 2002, p. 811.

[38] T. G. Myers, "Extension to the Messinger model for aircraft icing," *AIAA journal*, vol. 39, no. 2, pp. 211–218, 2001, doi: 10.2514/2.1312.

[39] "Objective Helicopter Icing Spraying System, U.S. Army, PEO STRI,." http://www.peostri.army.mil/PRODUCTS/OHISS/ (accessed Sep. 03, 2022).

[40] A. Bilanin and D. Anderson, "Ice accretion with varying surface tension," in *33rd Aerospace Sciences Meeting and Exhibit*, 1995, p. 538.

[41] Y. Han, "Theoretical and Experimental Study of Scaling Methods for Rotor Blade Ice Accretion Testing," 2011, doi: 10.13140/RG.2.1.2585.0485.

[42] "Dimensional Analysis and Similarity." https://www.me.psu.edu/cimbala/learning/fluid/Dim_anal/dim_anal.htm (accessed Jul. 08, 2023).

[43] I. Langmuir, *Mathematical Investigation of Water Droplet Trajectories*, no. 5418. Army Air Forces Headquarters, Air Technical Service Command, 1961. doi: 10.1016/b978-0-08-009362-8.50022-3.

[44] B. L. Messinger, "Equilibrium temperature of an unheated icing surface as a function of air speed," *Journal of the aeronautical sciences*, vol. 20, no. 1, pp. 29–42, 1953.

[45] E. Ayan and S. Özgen, "In-flight ice accretion simulation in mixed-phase conditions," *The Aeronautical Journal*, vol. 122, no. 1249, pp. 409–441, 2018.

[46] D. N. Anderson and J. C. Tsao, "Overview of icing physics relevant to scaling," *SAE Technical Papers*. 2003. doi: 10.4271/2003-01-2130.

[47] M. Tribus, G. B. W. Young, and L. M. K. Boelter, "Analysis of Heat Transfer Over a Small Cylinder in Icing Conditions on Mount Washington," *Asme*, vol. 70, no. 8, pp. 971 – 976, 1948.

[48] Y. Bourgault, W. G. Habashi, and H. Beaugendre, "Development of a shallow water icing model in fensap-ice," *37th Aerospace Sciences Meeting and Exhibit*, vol. 37, no. 4, pp. 640–646, 1999, doi: 10.2514/6.1999-246.

[49] D. N. Anderson and G. a. Ruff, "Scaling methods for simulating aircraft in-flight icing encounters," *NASA Technical Memorandum*, vol. 107538, no. October. 1997.

[50] D. N. Anderson, "Further evaluation of traditional icing scaling methods," *34th Aerospace Sciences Meeting and Exhibit*. 1996. doi: 10.2514/6.1996-633.

[51] G. O. Yanmaz, "Scaling for Icing Wind Tunnel Tests and Validation With," no. September. pp. 1–20, 2019.

[52] D. Anderson and J.-C. Tsao, "Additional results of ice-accretion scaling at SLD conditions," in *41st Aerospace Sciences Meeting and Exhibit*, 2003, p. 390.

[53] E. W. Lemmon, "NIST 72. NIST Thermophysical Properties of Air and Air Component Mixtures: AIRPROPS," 2003.

[54] H. R. Pruppacher, J. D. Klett, and P. K. Wang, "Microphysics of clouds and precipitation." Taylor & Francis, 1998.

[55] J. Katz and A. Plotkin, *Low-speed aerodynamics*, vol. 13. Cambridge university press, 2001.

[56] S. Özgen and M. CanIbek, "Ice accretion simulation on multi-element airfoils using extended Messinger model," *Heat and Mass Transfer/Waerme- und Stoffuebertragung*, vol. 45, no. 3. pp. 305–322, 2009. doi: 10.1007/s00231-008-0430-4.

[57] T. G. Myers, "Extension to the Messinger model for aircraft icing," *AIAA journal*, vol. 39, no. 2, pp. 211–218, 2001, doi: 10.2514/2.1312.

[58] S. Özgen, E. Tarhan, and M. Canıbek, "3-D in-flight icing simulations and use of parallel computing in Lagrangian droplet trajectory calculations," in *6th Ankara International Aerospace Conference, Ankara, Turkey*, Citeseer, 2011.

[59] G. Fortin, J.-L. Laforte, and A. Ilinca, "Heat and mass transfer during ice accretion on aircraft wings with an improved roughness model," *International Journal of Thermal Sciences*, vol. 45, no. 6, pp. 595–606, 2006.

[60]   W. B. Wright, R. W. Gent, and D. Guffond, "DRA/NASA/ONERA collaboration on icing research," 1997.

[61]   R. SOEDER, D. SHELDON, C. ANDRACCHIO, R. IDE, N. LALLI, and D. SPERA, "NASA Lewis icing research tunnel user manual," 1996.

[62]   D. N. Anderson, "Acceptable tolerances for matching icing similarity parameters in scaling applications," in *39th Aerospace Sciences Meeting and Exhibit*, 2001, p. 832. doi: 10.2514/6.2001-832.

[63]   F. A. A. A. C. N. J. A. A. N. D. A. S. R. A. N. D. DEVELOPMENT, "Capabilities and Prospects for Improvement in Aircraft Icing Simulation Methods: Contributions to the 11C Working Group," 2001.

[64]   C. Henze, M. Bragg, and H. Kim, "Freestream turbulence measurements in icing conditions," in *36th AIAA Aerospace Sciences Meeting and Exhibit*, 1998, p. 96.

[65]   P. E. Poinsatte, "Heat transfer measurements from a NACA 0012 airfoil in flight and in the nasa lewis icing research tunnel," NASA, 1990.

[66]   S. Brusca, R. Lanzafame, and M. Messina, "Low-speed wind tunnel: design and build," *Wind Tunnels: Aerodynamics, Models and Experiments*, pp. 189–220, 2011.

[67]   J. Kurian, "Wind tunnels Wind tunnel." pp. 1–19, 2010.

[68]   H. S. Tsien, "On the Design of the Contraction Cone for a Wind Tunnel," *Collected Works of Hsue-Shen Tsien (1938-1956)*. pp. 231–235, 2012. doi: 10.1016/B978-0-12-398277-3.50013-0.

[69]   J. B. Barlow, W. H. Rae, and A. Pope, *Low-speed wind tunnel testing*. John wiley & sons, 1999.

[70]   B. R. Munson, T. H. Okiishi, W. W. Huebsch, and A. P. Rothmayer, *Fluid mechanics*. Wiley Singapore, 2013.

[71]   A. N. Tifford, "Wind Tunnel Cooling.pdf," 1942.

[72] E. M. Gates, W. Lam, and E. P. Lozowski, "Spray evolution in icing wind tunnels," *Cold Reg Sci Technol*, vol. 15, no. 1, pp. 65–74, 1988.

[73] Spraying Systems Co, "Wind Tunnel Spraying System," 2023.

[74] I. E. Idelchik, "Handbook of Hydraulic Resistance, 2nd Edition," *J Press Vessel Technol*, vol. 109, no. 2, pp. 260–261, 1987, doi: 10.1115/1.3264907.

[75] R. D. Mehta and P. Bradshaw, "Design Rules for Small Low Speed Wind Tunnels.," *Aeronautical Journal*, vol. 83, no. 827, pp. 443–449, 1979.

[76] L. Prandtl, "Attaining a Steady Air Stream in Wind Tunnels," 1933.

[77] R. D. Mehta, "The aerodynamic design of blower tunnels with wide-angle diffusers," *Progress in Aerospace Sciences*, vol. 18, no. C, pp. 59–120, 1979, doi: 10.1016/0376-0421(77)90003-3.

[78] W. T. Eckert, K. W. Mort, and J. Jope, "Aerodynamic design guidelines and computer program for estimation of subsonic wind tunnel performance.," 1976.

[79] P. Moonen, B. Blocken, S. Roels, and J. Carmeliet, "Numerical modeling of the flow conditions in a closed-circuit low-speed wind tunnel," *Journal of Wind Engineering and Industrial Aerodynamics*, vol. 94, no. 10, pp. 699–723, 2006, doi: 10.1016/j.jweia.2006.02.001.

[80] M. A. Gonzalez Hernandez, A. I. Moreno Lopez, A. A., J. M. Perales Perales, Y. Wu, and S. Xiaoxiao, "Design Methodology for a Quick and Low-Cost Wind Tunnel," *Wind Tunnel Designs and Their Diverse Engineering Applications*, vol. 1, pp. 3–26, 2013, doi: 10.5772/54169.

[81] J. Groth and A. V Johansson, "Turbulence reduction by screens," *Journal of Fluid Mechanics*, vol. 197. pp. 139–155, 1988. doi: 10.1017/S0022112088003209.

[82] H. L. Dryden and G. B. Schubauer, "The use of damping screens for the reduction of wind-tunnel turbulence," *Journal of the Aeronautical Sciences*, vol. 14, no. 4, pp. 221–228, 1947.

[83]   J. H. Bell and R. D. Mehta, "Contraction Design for Small Low-Speed Wind Tunnels.," 1988.

[84]   F. De Gregorio, B. Esposito, G. Mingione, and A. Vicini, "Experimental and computational aerodynamics applications for an icing wind tunnel design," *Italian Aerospace Research Center, Aerodynamics of Wind Tunnel Circuits and their Components p(SEE N 97-27840 01-09)*, 1997.

[85]   MatWeb, "ASTM A525 Galvanized Steel." https://www.matweb.com/search/DataSheet.aspx?MatGUID=abbf07b7f93a4 c358a0ddd194f5c18be&ckck=1 (accessed Jul. 02, 2023).

[86]   MatWeb, "304 Stainless Steel." https://www.matweb.com/search/datasheet.aspx?MatGUID=abc4415b0f8b4 90387e3c922237098da&ckck=1 (accessed Jul. 02, 2023).

[87]   IZOCAM Comp., "OPTIFLEX SHEET." IZOCAM Company. Accessed: Jul. 02, 2023. [Online]. Available: https://www.izocam.com.tr/images/product/technical-image/optiflex-sheet849.pdf

[88]   L. Shi, F. Feng, W. Guo, and Y. Li, "Research and development of a small-scale icing wind tunnel test system for blade airfoil icing characteristics," *International Journal of Rotating Machinery*, vol. 2021, pp. 1–12, 2021.

[89]   F. Kasap, H. Acül, H. Canbaz, and S. Erbil, "R744 (CO2) soğutucu akışkanlı soğutma sistemleri, kanatlı borulu R744 (CO2) evaporatör ve gaz soğutucu tasarım esasları," *X. Ulusal Tesisat Mühendisliği Kongresi*, vol. 1, pp. 369–389, 2011.

[90]   Wolf Laboratories © 2010-2023. All rights reserved. (n.d.)., "Liquid Nitrogen Tank (250L)," *Taylor Wharton / Worthington XL240PB Cryostorage Equipment - Liquid Nitrogen Storage XL240PB-12*, 2023. https://www.wolflabs.co.uk/laboratory-products/cryostorage-equipment-liquid-nitrogen-storage/10481439#tab-1 (accessed Aug. 06, 2023).

[91]   A. H. Lefebvre and V. G. McDonell, *Atomization and sprays*. CRC press, 2017.

[92]   R. IDE, "Liquid water content and droplet size calibration of the NASA Lewis Icing Research Tunnel," in *28th Aerospace Sciences Meeting*, 1990, p. 669.

[93]   K. Omer and N. Ashgriz, "Spray nozzles," *Handbook of Atomization and Sprays: Theory and Applications*, pp. 497–579, 2011.

[94]   R. Ide and J. Oldenburg, "Icing cloud calibration of the NASA Glenn icing research tunnel," in *39th Aerospace Sciences Meeting and Exhibit*, 2001, p. 234.

[95]   R. I. Saeed, "NEW WIND TUNNEL FACILITY FOR ICING EXPERIMENTS ON MODELS OF TURBOFAN COMPRESSOR SURFACES," University of Southern Quennsland, 2019.

[96]   E. Tetteh, N. Lilly, E. Loth, J. Loebig, J. Cummings, and J. Harvell, "A compact icing research tunnel," *AIAA Propulsion and Energy Forum and Exposition, 2019*. 2019. doi: 10.2514/6.2019-4002.

[97]   C. S. Bartlett, "Turbine engine icing spray bar design issues," in *Turbo Expo: Power for Land, Sea, and Air*, American Society of Mechanical Engineers, 1994, p. V002T02A008.

[98]   E. P. Warner, F. H. Norton, and C. M. Herbert, *The design of wind tunnels and wind tunnel propellers*, no. 73. US Government Printing Office, 1919.

[99]   J. K. Calautit, H. N. Chaudhry, B. R. Hughes, and L. F. Sim, "A validated design methodology for a closed-loop subsonic wind tunnel," *Journal of Wind Engineering and Industrial Aerodynamics*, vol. 125, pp. 180–194, 2014.

[100] M. Musto, N. Bianco, G. Rotondo, F. Toscano, and G. Pezzella, "A simplified methodology to simulate a heat exchanger in an aircraft's oil cooler by means of a Porous Media model," *Appl Therm Eng*, vol. 94, pp. 836–845, 2016.

[101] A. FLUENT, "12.0 User's Guide-7.2. 3 Porous Media Conditions," *ANSYS, Inc., Jan*, 2009.

APPENDICES

A. Wind Tunnel Sizing Code

```
1    area
21   ninh=ninarea**0.5
22   #0.667<nlyratio<1.79
23   nlyratio=0.9848
24   nl=ninh*nlyratio
25
26   #second diffuser
27   sdifoutarea=ninarea
28   sdifouth=sdifoutarea**0.5
29   #2<sdifintestar<3
30   sdifintestar=2
31   sdifinarea=sdifintestar*tarea
32
33   fandim=2*((sdifinarea/math.pi)**0.5)
34
35   sdifoutinar=sdifoutarea/sdifinarea
36
37   vf=vt/sdifintestar
38   #0<sdifexpangd<6
39   sdifexpangd=3
40   sdifl=fandim/2*(sdifoutinar**0.5-
1)/(math.tan(sdifexpangd*math.pi/180))
41   #adaptor
42   adtl=0.3*sdifl/6.58
43
44   #fanhub
45   fanhubl=0.9
46
47
48   #first diffuser
49   vfdifin=vt
50   fdifinarea=tarea
51   fdifoutarea=sdifinarea
52   fdifoutinar=fdifoutarea/fdifinarea
53   fdifouth=fandim*(math.pi**0.5)/2
54   vfdifout=vfdifin*fdifinarea/fdifoutarea
55   vfdifave=(vfdifin+vfdifout)/2
56
dhfdifave=(2*((fdifinarea/math.pi)**0.5)+2*((fdifoutarea/math.pi)**
0.5))/2
57   #0<sdifexpangd<2
58   fdifexpangd=2
59   fdifl=dh/2*(fdifoutinar**0.5-
1)/(math.tan(fdifexpangd*math.pi/180))
60
61   #settlingchamber
62   seth=ninh
```

```
63    setl=sdifl+fanhubl+adtl-(fdifl+tl+nl)
64    #print(seth,"seth")
65    #small corner
66    #corner division 10<cordiv12<40
67    cordiv12=25
68    gap12=fdifouth/cordiv12
69    #0<gapchrat12<0.25
70    gapchrat12=0.25
71    ch12=gap12/gapchrat12
72    #up +angle
73    fpleang12=5
74    fpteang12=0
75    fpcang12=90-fpleang12-fpteang12
76    fprad12=ch12/(2*math.sin(fpcang12*math.pi/180/2))
77    #large corner
78    #corner division 10<cordiv34<40
79    cordiv34=25
80    gap34=0.75*sdifoutarea/cordiv34
81    #0<gapchrat34<0.25
82    gapchrat34=0.25
83    ch34=gap34/gapchrat34
84    #up +angle
85    fpleang34=5
86    fpteang34=0
87    fpcang34=90-fpleang34-fpteang34
88    fprad34=ch34/(2*math.sin(fpcang34*math.pi/180/2))
89    #honeycomb
90    honeyareatot=ninarea
91    dhoney=0.009
92    shoney=0.00006
93    rouhoney=0.000015
94    lhoney=dhoney/(2*math.sin(math.pi/3))
95    lghoney=lhoney+2*shoney/math.tan(math.pi/3)
96    zhoney=2*lhoney+lghoney
97    honeyparlogramarea=lhoney*shoney
98    honeytraparea=(lhoney+lghoney)*shoney/2
99    nzhoney=seth/zhoney
100   nshhoney=seth/(dhoney/2+shoney)
101
honeysharea=2*(honeyparlogramarea+honeytraparea)*nzhoney*nshhoney
102   tauhoney=honeysharea/honeyareatot
103   betahoney=1-tauhoney
104   dhhoney=dhoney*(6/(math.pi*(3**0.5)))**0.5
105   #6<honeyldhratio<8
106   honeyldhratio=6.56
107   honeyl=honeyldhratio*dhhoney
108
##print(lhoney,lghoney,zhoney,nzhoney,nshhoney,tauhoney,betahoney,d
hhoney,honeyl)
109   #Screen1
110   #0.58<betascr1<0.81
111   betascr1=0.61
112   dwscr1=0.0007
113   rhoscr1=(1-(betascr1)**0.5)/dwscr1
114   wscr1=1/rhoscr1
115   nscr1=seth*rhoscr1
116
117   #Screen2
```

```python
118  #0.58<betascr2<0.81
119  betascr2=0.6
120  dwscr2=0.00056
121  rhoscr2=(1-(betascr2)**0.5)/dwscr2
122  wscr2=1/rhoscr2
123  nscr2=seth*rhoscr2
124
125  #Screen3
126  #0.58<betascr3<0.81
127  betascr3=0.61
128  dwscr3=0.00015
129  rhoscr3=(1-(betascr3)**0.5)/dwscr3
130  wscr3=1/rhoscr3
131  nscr3=seth*rhoscr3
132
133
134
135  rho=1.225
136  mu=1.81/100000
137  #Test section
138  Ret=rho*vt*dh/mu
139  fnew=1
140  error=100
141  while (error>0.001):
142      fold=fnew
143      ##print(fnew)
144      fnew=(1/(2*math.log10(Ret*fnew**0.5)-0.8))**2
145
146      error=abs(fnew-fold)/fold
147
148  dpt=rho*fnew*tl*vt**2/(2*dh)
149  #print(dpt)
150  #Smaller corner connection
151  vscc=vt*fdifinarea/fdifoutarea
152  dhscc=2*((fdifoutarea/math.pi)**0.5)
153  Rescc=rho*vscc*dhscc/mu
154  sccl=fdifouth*1.5
155
156  fnew=1
157  error=100
158  while (error>0.001):
159      fold=fnew
160      ##print(fnew)
161      fnew=(1/(2*math.log10(Rescc*fnew**0.5)-0.8))**2
162
163      error=abs(fnew-fold)/fold
164
165  dpscc=rho*fnew*sccl*vscc**2/(2*dhscc)
166  #print(dpscc)
167
168  #Adapter
169  vadt=vscc
170  dhadt=dhscc
171  Readt=Rescc
172
173
174  fnew=1
175  error=100
```

```python
176  while (error>0.001):
177      fold=fnew
178      ##print(fnew)
179      fnew=(1/(2*math.log10(Readt*fnew**0.5)-0.8))**2
180
181      error=abs(fnew-fold)/fold
182
183  dpadt=rho*fnew*adtl*vadt**2/(2*dhadt)
184  #print(dpadt)
185
186  #fanhub
187  Refanh=rho*vf*fandim/mu
188  fnew=1
189  error=100
190  while (error>0.001):
191      fold=fnew
192      ##print(fnew)
193      fnew=(1/(2*math.log10(Refanh*fnew**0.5)-0.8))**2
194
195      error=abs(fnew-fold)/fold
196
197  dpfanh=rho*fnew*fanhubl*vf**2/(2*fandim)
198  #print(dpfanh)
199
200  #Larger corner connection
201  vlcc=vf*sdifinarea/sdifoutarea
202  dhlcc=2*((sdifoutarea/math.pi)**0.5)
203  Relcc=rho*vlcc*dhlcc/mu
204  lccl=sdifouth*1.5
205
206  fnew=1
207  error=100
208  while (error>0.001):
209      fold=fnew
210      ##print(fnew)
211      fnew=(1/(2*math.log10(Relcc*fnew**0.5)-0.8))**2
212
213      error=abs(fnew-fold)/fold
214
215  dplcc=rho*fnew*lccl*vlcc**2/(2*dhlcc)
216  #print(dplcc)
217
218  #Settling chamber
219  vset=vlcc
220  dhset=dhlcc
221  Reset=rho*vset*dhset/mu
222
223  fnew=1
224  error=100
225  while (error>0.001):
226      fold=fnew
227      ##print(fnew)
228      fnew=(1/(2*math.log10(Reset*fnew**0.5)-0.8))**2
229
230      error=abs(fnew-fold)/fold
231
232  dpset=rho*fnew*setl*vset**2/(2*dhset)
233  #print(dpset)
```

```
234  #square
235  A1=0.09623
236  B1=-0.004152
237  A2=0.122156
238  B2=-0.045896
239  C2=0.02203
240  D2=-0.003269
241  E2=-0.0006145
242  F2=0.0000280
243  G2=-0.00002337
244  A3=-0.01322
245  B3=0.05866
246  #first diffuser
247  Refdif=rho*vfdifin*dh/mu
248
249  fnew=1
250  error=100
251  while (error>0.001):
252      fold=fnew
253      ##print(fnew)
254      fnew=(1/(2*math.log10(Refdif*fnew**0.5)-0.8))**2
255
256      error=abs(fnew-fold)/fold
257
258  #fdifoutinar=1/fdifoutinar
259
260  fdifkf=(1-
1/(fdifoutinar**2))*fnew/(8*math.sin(fdifexpangd*math.pi/180))
261  fdifexpangd=fdifexpangd*math.pi/180
262
fdifkexp=A2+B2*fdifexpangd+C2*fdifexpangd**2+D2*fdifexpangd**3+E2*f
difexpangd**4+F2*fdifexpangd**5+G2*fdifexpangd**6
263  fdifkexp=fdifkexp*((fdifoutinar-1)/fdifoutinar)**2
264  dpfdif=(fdifkexp+fdifkf)*0.5*rho*vfdifin**2
265  print(vfdifin,vt,"asasa")
266
267  #circular
268  A1=0.1033
269  B1=-0.02389
270  A2=0.1709
271  B2=-0.1170
272  C2=0.03260
273  D2=0.001078
274  E2=-0.0009076
275  F2=-0.00001331
276  G2=0.00001345
277  A3=-0.09661
278  B3=0.04672
279
280  #square
281  A1=0.09623
282  B1=-0.004152
283  A2=0.122156
284  B2=-0.045896
285  C2=0.02203
286  D2=-0.003269
287  E2=-0.0006145
288  F2=0.0000280
```

```python
289  G2=-0.00002337
290  A3=-0.01322
291  B3=0.05866
292
293
294  #second diffuser
295
296  Resdif=rho*vf*fandim/mu
297
298  fnew=1
299  error=100
300  while (error>0.001):
301      fold=fnew
302      ##print(fnew)
303      fnew=(1/(2*math.log10(Resdif*fnew**0.5)-0.8))**2
304
305      error=abs(fnew-fold)/fold
306
307  sdifkf=(1-
1/(sdifoutinar**2))*fnew/(8*math.sin(sdifexpangd*math.pi/180))
308  sdifexpangd=sdifexpangd*math.pi/180
309
310
sdifkexp=A2+B2*sdifexpangd+C2*sdifexpangd**2+D2*sdifexpangd**3+E2*s
difexpangd**4+F2*sdifexpangd**5+G2*sdifexpangd**6
311
312  sdifkexp=sdifkexp*((sdifoutinar-1)/sdifoutinar)**2
313
314  dpsdif=(sdifkexp+sdifkf)*0.5*rho*vf**2
315  #print(sdifkf,sdifkexp,vf**2,dpsdif)
316
317  #Nozzle
318  vnozin=vt*noutarea/ninarea
319
320  Renozave=rho*((vnozin+vt)/2)*((dhset+dh)/2)/mu
321
322
323  fnew=1
324  error=100
325  while (error>0.001):
326      fold=fnew
327      ##print(fnew)
328      fnew=(1/(2*math.log10(Renozave*fnew**0.5)-0.8))**2
329
330      error=abs(fnew-fold)/fold
331
332  nozk=0.32*(fnew)*nl/dh
333  dpnoz=nozk**0.5*rho*vnozin**2
334  #print(dpnoz)
335
336  #smaller corner
337  Resc=rho*vfdifout*ch12/mu
338  sck=0.1+4.55/(math.log10(Resc))**2.58
339  dpsc=sck*0.5*rho*vfdifout**2
340  #print(dpsc)
341
342  #larger corner
343  Relc=rho*vset*ch34/mu
```

```python
344    lck=0.1+4.55/(math.log10(Relc))**2.58
345    dplc=lck*0.5*rho*vset**2
346    #print(dplc)
347    #Honeycomb
348    Rehoneyr=rho*vnozin*rouhoney/mu
349    if (Rehoneyr>275):
350        lamdah=0.214*(rouhoney/dhhoney)**0.4
351    else:
352        lamdah=0.375*((rouhoney/dhhoney)**0.4)*(Rehoneyr**-0.1)
353
honeyk=lamdah*((honeyldhratio+3)*(1/betahoney)**2)+(1/betahoney-
1)**2
354    dphoney=honeyk*0.5*rho*vnozin**2
355    #print(dphoney)
356    #Screen1
357    Rescr1=rho*vnozin*dwscr1/mu
358
359    #print(Rescr1)
360
361    if (Rescr1>400):
362        krnscr1=1
363    else:
364        krnscr1=0.785*(1-Rescr1/354)+1.01
365
366    scr1k=1.3*krnscr1*(1-betascr1)+(1-betascr1)**2/betascr1**2
367
368    dpscr1=scr1k*0.5*rho*vnozin**2
369    #print(dpscr1)
370    #Screen2
371    Rescr2=rho*vnozin*dwscr2/mu
372    #print(Rescr2)
373    if (Rescr2>400):
374        krnscr2=1
375    else:
376        krnscr2=0.785*(1-Rescr2/354)+1.01
377
378    scr2k=1.3*krnscr2*(1-betascr2)+(1-betascr2)**2/betascr2**2
379
380    dpscr2=scr2k*0.5*rho*vnozin**2
381    #print(dpscr2)
382
383    #Screen3
384    Rescr3=rho*vnozin*dwscr3/mu
385    #print(Rescr3)
386    if (Rescr3>400):
387        krnscr3=1
388    else:
389        krnscr3=0.785*(1-Rescr3/354)+1.01
390
391    scr3k=1.3*krnscr3*(1-betascr3)+(1-betascr3)**2/betascr3**2
392
393    dpscr3=scr3k*0.5*rho*vnozin**2
394    #print(dpscr3)
395    dpfanscr=1
396    dp[1]=dpt
397    dp[2]=dpfdif
398    dp[3]=dpsc
399    dp[4]=dpscc
```

```python
400   dp[5]=dpsc
401   dp[6]=dpadt
402   dp[7]=dpfanscr
403   dp[8]=dpfanh
404   dp[9]=dpsdif
405   dp[10]=dplc
406   dp[11]=dplcc
407   dp[12]=dplc
408   dp[13]=dpset
409   dp[14]=dphoney
410   dp[15]=dpscr1
411   dp[16]=dpscr2
412   dp[17]=dpscr3
413   dp[18]=dpnoz
414
415
416
417   dpsum=0
418   for i in range(1, 19):
419       print(dp[i])
420       dpsum=dpsum+dp[i]
421       print(dpsum)
```

CIRRICULUM VITAE

Harun Özkanaktı

Education

2015- Still   Middle East Technical University (METU), Ankara, Turkey

- PhD in Aerospace Engineering

2012-2015   Middle East Technical University (METU), Ankara, Turkey

- M. S. in Aerospace Engineering
- CGPA: 3.07/4.00
  - Master Thesis Title: Measurement of lift and drag in morphing wings using a high precision load cell

2006-2011   Middle East Technical University (METU), Ankara, Turkey

- B. S. in Aerospace Engineering
- CGPA: 2.45/4.00

Publications

- Özkanaktı, M. H., Körpe, S., & Özgen, S. (2015, June). Measurement of Lift and Drag Force in Morphing Wings Using High Precision Load Cell. In *6th European Conference for Aerospace Sciences and Space Sciences*.

- Özkanaktı, M. H. (2015). Measurement of Lift and Drag Force in Morphing Wings Using High Precision Load Cell.(Master's Thesis)

Work Experience

05/2015- Still   Alti Dynamics, Founder & Aerospace Engineer, M.Sc., Ankara
09/2012-05/2015   Gate Electronic - TR-Technology Joint Venture, Aerospace Engineer, Ankara
09/2010-09/2011   TAI, Assistant Design Engineer, R&D (ATAK T-129), Ankara, Turkey
08/2010-09/2011   TEI, Internee, Assembly Line and R&D Departments, Eskisehir, Turkey

Term based projects

06/2013   METU – RUZGEM, Consultant, Wind tunnel testing setups
03/2012-12/2011   Boeing & HAVELSAN, Consultant, Peace Eagle Project, Ankara, Turkey
06/2012-06/2014   Tübitak, Experimental Aerodynamicist, 111M731 Scientific Research Project

Projects and Products

09/2011-12/2011   Design and Control of Tri-tilting Rotor, Experimental Aerodynamics Class, METU, Ankara, Turkey
08/2011   Air Cargo Challenge'11, EUROAVIA, Stuttgart, Germany (Leader)
04/2011   Design Build Fly Contest 10/11, American Institute of Aeronautics and Astronautics, Tucson, Arizona, USA (ranked 6th among 94 teams) (Leader)
05/2011   Designing and Manufacturing of a Fully Composite Aircraft, Experimental Aerodynamics Laboratory Class, METU, Ankara, Turkey
06/2010   Tasarla Yap Uçur, Turkish Air Force Academy, İstanbul, Turkey (ranked 1st among 18 team) (Leader)

| 04/2010 | Design Build Fly Contest 09/10, the American Institute of Aeronautics and Astronautics (AIAA), Wichita, Kansas, USA (ranked 6th among 76 teams) |

Training and Workshops

01/2014	Composite Design Workshop, STANFORD University, USA
01/2014	Work Safety and Health Specialist, Work and Labor Government of Turkey
06/2013	Project Management and Development Workshop, KOSGEB
09/2010	CATIA V5 Training, CADEM and TAI, Ankara, Turkey
06/2008	Numeca™ CFD Training, Pars Machine, Ankara, Turkey
06/2007	Project Management Training, METU Tech., Ankara Turkey

Skills

Management Skills
- Project and Corporation Management
- Aircraft and Subparts Certification Process
- Aircraft Design and Manufacture Process

Computer Skills
- CATIA V5, Autodesk Inventor
- Ansys Fluent, Fluent, Abaqus (composite FEA), Xflr5
- Fortran77, MATLAB, Simulink, MATLAB Aerospace toolbox
- TeamCenter, Labview

Hardware Skills
- Manufacture of UAV and Model Airplanes
- Highly skilled on aerodynamic and structural experiment set-ups
- Extensive command on electronic equipment & setups of A/Cs (ESC, FPV, Telemetry, Gimbal)
- Highly experienced on composite manufacturing and technologies
- Highly experienced about manufacturing methods and industry zone manufacturing capabilities.

Languages

	Listening	Reading	Writing skills	Spoken Production
English	Proficient	Proficient	Proficient	Proficient
French	Basic	Basic	Basic	Basic
Turkish (Native)				

Exams

09/2015	Pearson PTE	67
12/2011	Toefl IBT	90 (Reading: 25, Listening: 24, Speaking: 23, Writing: 18)
04/2011	ALES	90.5

Research Interest
- Aircraft Design and Unmanned Aerial Vehicles technologies (UAV)
- Multi-Disciplinary Optimization
- Aerodynamics (Numerical and Experimental) and Computational Fluid Dynamics (CFD)
- Morphing Aircraft (Aero-elastic structures)
- Computer Aided Drawing (CAD)

Organization
- Former Player of Turkish National Rugby Team
- METU Rugby Player (2010 and 2011 Turkish Rugby League Champions)
- Former Administrative Board Member in student society of *"Creativity And Social Innovation"*